Universidad de Valencia - CSIC
Departamento de Física Atómica, Molecular y Nuclear
Instituto de Física Corpuscular

New radiative neutron capture measurement of ^{207}Pb and ^{209}Bi

César Domingo Pardo
Tesis Doctoral
Diciembre de 2004

Universidad de Valencia - CSIC
Instituto de Física Corpuscular

Departamento de Física Atòmica,
Molecular i Nuclear

New radiative neutron capture measurement of ^{207}Pb and ^{209}Bi

César Domingo Pardo

Tesis Doctoral

Diciembre de 2004

A Berta,

a mi familia.

José Luis Taín Enríquez, Colaborador Científico del Consejo Superior de Investigaciones Científicas (CSIC),

CERTIFICA: Que la presente memoria **"New radiative neutron capture measurement of ^{207}Pb and ^{209}Bi"** ha sido realizada bajo su dirección en el Instituto de Física Corpuscular (Centro Mixto Universidad de Valencia - CSIC) por **César Domingo Pardo** y constituye su Tesis Doctoral dentro del programa de doctorado del Departamento de Física Atómica, Molecular y Nuclear.

Y para que así conste, en cumplimiento con la legislación vigente, presenta ante el Departamento de Física Atómica, Molecular y Nuclear la referida memoria, firmando el presente certificado en Burjassot (Valencia) a 21 de diciembre de 2004.

Fdo. José Luis Taín Enríquez

Abstract

This new measurement of the (n,γ) capture cross sections of ^{207}Pb and ^{209}Bi has been motivated by *i*) the aim to achieve a better understanding of the *s*-process stellar nucleosynthesis in its termination region and *ii*) the design of accelerator driven systems (ADS) based on a lead-bismuth eutectic spallation core.

The measurement has been performed using the total energy detector technique, since the lower neutron sensitivity achievable with such a detection system represents a clear advantage versus the alternative total absorption method. However, the former technique has been a source of controversy between experimentalists and therefore, an important part of the present work has been dedicated first to the review and further development of the so called Pulse Height Weighting Technique (PHWT). Performing dedicated measurements at the CERN n_TOF installation we have experimentally validated this technique, determining that a systematic uncertainty better than 2% can be achieved.

Once the measuring technique has been demonstrated to be well under control, the measurement of the radiative capture cross section of ^{207}Pb and ^{209}Bi was carried out. Experimental sources of systematic uncertainty have been thoroughly treated by means of Monte Carlo simulations. An R-matrix analysis of the resolved resonance region has been performed for both nuclides, deriving the total resonance radiative capture cross section and resonance parameters where possible.

Previous measurements of these isotopes were affected by large systematic corrections mainly due to the neutron sensitivity of the detection system used. In the present work these isotopes have been measured by employing an optimized detection setup, which permitted the determination of their cross sections with a practically negligible neutron sensitivity deviation.

A comparison between the results obtained here and current evaluated data files is also presented, revealing high deviations mainly on *s*-wave resonances. These are to be ascribed to the high systematic uncertainty of the previous measurements, in which these evaluations are based.

Implications of the new results in the field of stellar nucleosynthesis as well as in ADS engineering are studied and discussed.

Contents

List of Abbreviations

ADS	Accelerator Driven System
CDR	Central Data Recording
DAQ	Data AcQuisition system
DST	Data Summary Tape
EM	ElectroMagnetic
FADC	Flash Analog to Digital Converter
FWHM	Full Width at Half Maximum
GDR	Giant Dipole Resonance
GS	Ground State
LLFF	Long Lived Fission Fragments
LWR	Light Water Reactor
MACS	Maxwellian Averaged Cross Section
MC	Monte Carlo
PHWT	Pulse Height Weighting Technique
PM	PhotoMultiplier
PS	Proton Synchrotron
RBS	Rutherford Back-Scattering
RF	Resolution Function
RMS	Root Mean Square
SiMon	Silicon Monitor
SP	Single Particle
TAC	Total Absorption Calorimeter
TOF	Time Of Flight
TRU	TRans-Uranium isotopes
WCM	Wall Current Monitor
WF	Weighting Function

List of Figures

List of Tables

Chapter 1

Introduction

The understanding of the nucleosynthesis of heavy elements in the stars has progressed with the course of time, in the measure that observations of stellar isotopic abundances, as well as neutron capture measurements, have evolved. Combining the observational information of the abundances, with the experimentally determined cross sections, modelers have developed consistent and sophisticated stellar scenarios, which yield vast and detailed knowledge about the star evolution and its inner mechanisms.

Stellar models have been constructed, which account for the observed isotopic abundances in the mass region $60 < A < 205$ with a remarkable success [1]. However, for the synthesis of nuclei with masses between 205 and 209, the precise stellar scenario and mechanisms have not been addressed, partially due to the insufficient accuracy of experimental data reported in this region. Therefore, accurate measurements of the neutron capture cross section in these isotopes become crucial points in order to further develop the stellar nucleosynthesis models. A deeper description of the synthesis of the heavy elements in the stars will be given in section 1.1.

The measurement of the neutron capture cross section data of lead and bismuth has, on the other side, a very practical application [2]. The main disadvantage in the employment of nuclear power plants for the energy production resides, as is broadly known, on the nuclear waste yielded in the fission cycles of ^{235}U or ^{239}Pu inside the nuclear reactor. For many years, people have thought about using neutrons in order to, in a similar way as happens in the core of the stars, transmute these radioactive isotopes into other stable elements [3]. The precise knowledge of nuclear data achieved up to date indicates that such a project will be feasible within 10-15 years. The current designs of a nuclear waste transmutator usually include an accelerator, a liquid heavy-metal target for neutron production, surrounded by a subcritical blanket containing the actinide and fission products. One of the most thoroughly developed designs [4] uses a mixture of lead and bismuth as neutron source and coolant. Radiative capture reactions, unlike sometimes fission and other types of reactions, do not show an energy threshold, thus becoming a parasitic process which can continuously affect the neutron balance in the reactor core. Therefore, a precise

knowledge of the cross section of the lead and bismuth isotopes is required for the final design of an hybrid reactor. On the other hand, capture on bismuth leads to the production of the metastable ^{210m}Bi isotope, which is an α-emitter with a very long decay time (3×10^6 y), thus determining the long term radiotoxicity of the Pb/Bi-spallation target. The radiative capture cross section of bismuth is also needed in order to estimate the production of ^{210}Po, another α-emitter, which determines the short term radiotoxicity of the target. The issue of the advanced nuclear reactors and the role of the Pb and Bi (n,γ) cross section will be further discussed in section 1.2.

From the experimental viewpoint, the radiative capture cross section of the lead and bismuth isotopes are not known to an accurate level. The main difficulty arises from the nuclear structure of these isotopes, where most of the nuclear levels show a dominant neutron scattering channel. This creates contaminations due to sample-scattered and setup-captured neutrons, which have to be minimized. In this sense, the lower volume of the total energy detectors technique, described in chapter 2, becomes an advantage versus the total absorption method. The present work aims to overcome this experimental difficulty by using an optimized total energy detector [5].

A further experimental difficulty for the measurement of these (n,γ) cross sections resides on the feature that they are very small. Indeed, ^{208}Pb shows the smallest cross section of the heavy nuclei because it is a double magic nuclei with both proton and neutron closed shells. The proximity of the other lead isotopes and bismuth to this configuration, makes their cross section also rather small.

The energy differential cross section measurements described in this work, have been performed at the n_TOF installation [6] sited at CERN (Geneva). This installation offers an excellent instantaneous neutron flux, combined with a very good energy resolution due to its very long flight path length of 185 m. A description of the n_TOF installation as well as the experimental setup used in this capture measurements will be shown in chapter 3. Chapter 4 is dedicated to describe the (n,γ) capture data reduction procedure, previous to the analysis of the cross section.

As will be discussed in chapter 5, the total energy detector technique has been a source of controversy. For this reason, prior to the measurement of the cross section of the lead and bismuth isotopes, a validation experiment [7] was carried out in order to determine the systematic precision which can be achieved with the Pulse Height Weighting Technique (PHWT). This experiment was used at the same time in order to establish a resilient analysis procedure, able to account for the different experimental sources of systematic uncertainty.

The present work covers the measurement and analysis of two of the isotopes which are more relevant for the motivations introduced at the beginning of this section. The measurement of the ^{209}Bi (n,γ) cross section with a discussion of its stellar nucleosynthesis and ADS implications, will be given in chapter 6. The results obtained in this experiment will be compared with previous work and the evaluated data files.

The ^{207}Pb capture measurement will be described in chapter 7, where the results

will be also compared with previous work and the evaluations.

A final discussion of the more relevant results obtained across this work, and the scope of these measurements will be given in chapter 8.

1.1 Stellar nucleosynthesis

Light nuclei ($A < 60$) are easily built by fusion reactions in the hot core of the stars, where the very high temperature allows thermonuclear reactions. But beyond iron, the Coulomb barrier is too high for charged particle reactions to occur. At this point, neutrons may play a major role in the reactions which build up higher isotopes [8]. Nevertheless, neutrons are unstable, with a half life of about 10 minutes, therefore a neutron source is required.

Under some simplifying assumptions it is possible to establish mathematical models to calculate the abundances of elements produced by neutron reactions. Let us start first with the stellar scenario, where a neutron source is able to generate a "small" neutron density of $n_n \sim 10^8$ n/cm^3. This happens during the He burning in the cores of stars, where neutrons can be produced as a side effect of fusion reactions like ^{13}C(α,n)^{16}O or ^{22}Ne(α,n)^{25}Mg. The stellar neutron flux is given by $\Phi = n_n v_T$, being $v_T = \sqrt{2kT/m}$ the thermal neutron velocity determined by the temperature T at the stellar site.

Given the small neutron flux Φ, a neutron capture occurs in a slow time scale (1-10 yr), so that when a beta-unstable nucleus is built, the probability λ_β to beta decay to a higher Z element is much larger than the probability to capture another neutron. The latter is given by $\lambda_n = \Phi\sigma$, σ being the neutron capture cross section. In this way, elements across the line of beta stability are built. This is referred to as slow neutron capture process or s-process.

The abundance of an isotope with mass A has a time dependence that can be written as,

$$\frac{\mathrm{d}N_s(A)}{\mathrm{d}\tau} = \sigma(A-1)N_s(A-1) - \sigma(A)N_s(A), \tag{1.1}$$

where the neutron exposure τ is the time integrated neutron flux, $\tau = \int \Phi \mathrm{d}t$. In the previous equation, it has been assumed that either the nucleus is stable $\lambda_\beta \ll \lambda_n$ or that it is beta unstable with a decay probability $\lambda_\beta \gg \lambda_n$. In addition, the assumption of a constant temperature at the s-process site, T_s, is needed in order to have well defined capture cross sections $\sigma(A)$.

When the equilibrium has been reached after long irradiation τ, the product $\sigma(A)N_s(A)$ shows a smooth behaviour. In order to describe the observed abundances, an exponential exposure was required,

$$\rho(\tau) = \frac{fN_{56}}{\tau_\circ} e^{-\tau/\tau_\circ}. \tag{1.2}$$

N_{56} is the number of iron seed nuclei, whereas the values of f and $\tau_\circ$ are adjusted using the observed abundances of s-only isotopes. These are nuclides which are shielded of any other synthesis process by its isobar, so that the observed abundances can be only due to the s-process. There exist about 27 s-only nuclei, such as ^{80,82}Kr, ^{96}Mo, ^{134,136}Ba or ^{204}Pb.

However, different mass ranges need to be considered in order to explain the observed abundances. f and $\tau_\circ$ are adjusted in three different mass regions, thus designing the so called main component in the region $90 < A < 204$, weak component for $A < 90$, and strong s-process component to explain the ^{208}Pb and ^{209}Bi abundances.

Once these parameters have been empirically fixed, the isotopic s-process abundances in the stars, N_s are only determined by the neutron capture cross section of the corresponding isotope. With the neutron exposure given by equation 1.2, equation 1.1 has the solution,

$$\sigma(A)N(A) = fN_{56}\tau_\circ \prod_{i=56}^{A} [1 + (\tau_\circ \sigma(i))^{-1}]^{-1}. \tag{1.3}$$

From the previous equation, one can easily conclude that the abundance of a given isotope of mass A, is roughly proportional to the inverse of its cross section $\sigma(A)$. There are points across the nuclides chart, where large abundances accumulate as a consequence of the low neutron capture cross section, thus acting as bottle-neck in the s-process chain. This is the situation for the nuclides with closed neutron shells N =50, 82 or 126. The opposite situation occurs for elements showing a high cross section.

The situation becomes more complicated at nuclides whose beta decay probability, $\lambda_\beta = ln2/t_{1/2}$, is comparable with that of the neutron capture λ_n. A branching occurs in the s-process chain, since in some cases the nuclide will β-decay to a higher isotope, whereas in other cases it will capture another neutron. This situation becomes at the same time very interesting, since the temperature dependence of the β-decay process combined with s-only isotopes abundances, can lead to a determination of the characteristic temperature for the s-process T_s and to an estimation of the neutron density n_n in such scenarios.

A completely different stellar scenario where an intense source of neutrons occurs corresponds to supernova explosions. In such an environment a large neutron flux is available, thus causing the neutron capture reactions to happen at a much faster rate than the beta decay. It is the so called rapid neutron capture process or r-process. As a consequence, neutron rich nuclei can be built up through a series of nuclei that would decay if given enough time. This process is the characteristic progenitor of isotopes like uranium or thorium, but also of some r-only isotopes, such as ^{80,82}Se.

In general, the total abundances observed in the stars are basically the contribution of the two processes described above, but in addition, there are neutron poor isotopes attributed to the so called p-process, where p stands for proton capture. This contributes about one order of magnitude less than the other two contribu-

tions described above and the corresponding p-process enhancements can be simply interpolated from p-only isotopes or neglected.

The "observed" r-abundances can be calculated [1] as the difference between the total observed solar abundance $N_\odot$ and the s-process contribution N_s,

$$N_r = N_\odot - N_s. \tag{1.4}$$

The value of N_s can be obtained from the well known (within 10% uncertainty) σN_s curve, whereas the solar abundances have been also precisely measured. The so obtained r-process residuals curve (figure 1.1), shows remarkably good agreement with the r-only measured abundances. Nevertheless, by the end of this distribution for $A = 206, 207, 208$ and 209, the need of a strong component to reproduce the smooth trend of the σN curve becomes necessary.

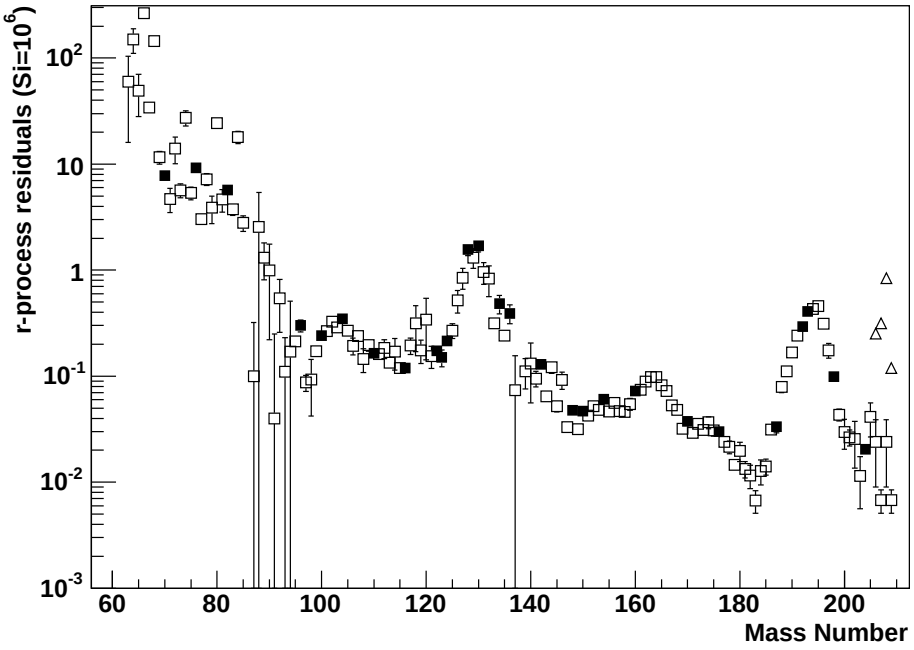

Figure 1.1: *r-process residuals [1] obtained as the subtraction of the s-process contribution to the observed solar abundances. Solid symbols designate r-only isotopes. Triangles at $A = 206, 207, 208$ and 209 correspond to the residual calculated without strong component [9].*

After developing improved stellar evolution models, the observed lead and bismuth abundances could be explained in terms of the main s-process component operating in low mass, low metallicity, thermally pulsing AGB stars [10, 11]. At this stage of the evolution, the He intershell suffers short (12 year) recurrent thermal pulses each $\sim 3\times10^3$ years. After each pulse, the H envelope shrinks back absorbing freshly s-processed material, which ultimately reaches the stellar atmosphere. The

neutron source which operates during the He flash is ^{22}Ne(α,n)^{25}Mg, activated by the higher temperature $T_8 \sim 3$ (in units of 10^8 K), whereas at the lower temperature of $T_8 \sim 0.9$ of the interpulses period, the ^{13}C(α,n)^{16}O produces the neutrons. Such models predicted that the *s*-process abundances of the Pb and Bi isotopes show a maximum production efficiency in stars of metallicity [Fe/H] ≈ -1. This picture has been confirmed by the lead abundances observed in some metal-poor stars.

The end of the *s*-process path becomes complex for several reasons. Neutron capture on the last stable isotope, ^{209}Bi, leads to ^{210}Bi or ^{210m}Bi. Here several reactions leading to ^{210}Po, ^{211}Po and ^{211}Bi may occur (figure 1.2). α-recycling from the former isotope would directly contribute to the enhancement of ^{206}Pb, whereas the other two contribute to the build up of ^{207}Pb. The effect of the two branchings

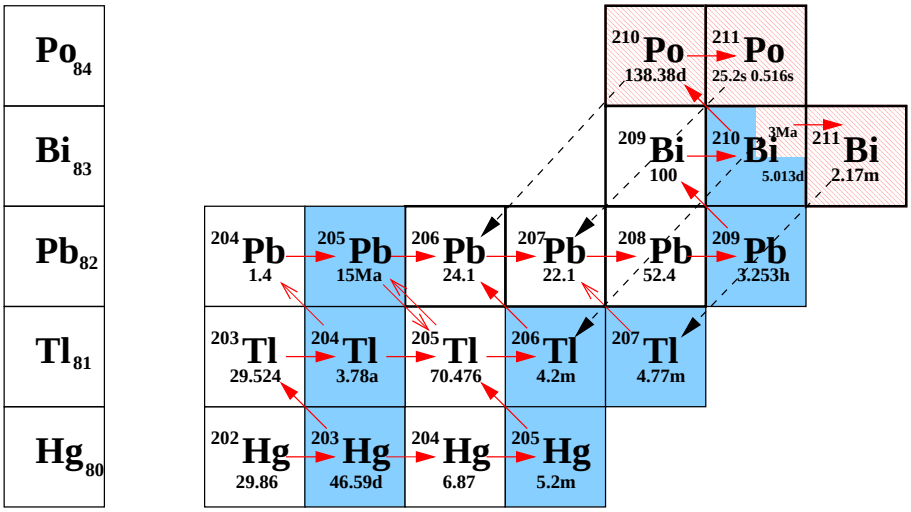

Figure 1.2: *Termination region of the s-process path. The top-right dashed boxes designate α-unstable nuclei, whereas dark boxes denote β-unstable nuclides. Arrows describe the s-process flow.*

at ^{210}Bi and ^{210}Po, strongly depends on the stellar conditions of neutron density and temperature. At the temperature and neutron density of the main and weak *s*-process components, the ^{210}Po with subsequent α-decay to ^{206}Pb would become the most probable. In order to extend these conditions to the strong component, the observed abundance ratio ^{206}Pb/^{207}Pb could be used.

Unfortunately, the *s*-process abundances of ^{206,207}Pb are difficult to estimate, since in the separation of the *r*-process contribution, the radiogenic component (not shown in figure 1.2) from the decay of various trans-bismuth progenitors and of ^{235,238}U needs to be included. The latter of course is difficult to determine. As can be observed in figure 1.1, the uncertainties beyond $A = 204$ are too large in order to determine which recycling path is dominating at the termination region of the *s*-process. This constitutes a motivation to improve the measurement of the capture cross sections of the lead and bismuth isotopes.

Furthermore, if the s-process abundances can be well determined independently of the r-process contributions, they can be employed in order to better isolate the radiogenic part from the direct r-process contribution [12, 13]. Since the Pb/Bi isotopes constitute the decay products of the long lived thorium and uranium nuclides, which are only build by means of the r-process mechanism, one could therefore use their radiogenic abundance, in order to derive estimates for the ages of the underlying r-process. Indeed, the radiogenic contribution to the Pb/Bi isotopes in old metal poor stars constitutes a constraint for the actinide abundances and therefore yield information about the time in which the first generations of stars could be built up in the Galaxy.

1.2 Radioactive waste transmutation

Radioactive waste can be considered as the main disadvantage of the energy production in nuclear power plants. These residues are of concern for all living creatures, therefore they should be stored in geological repositories. However, it is not a very comfortable situation to guard indefinitely a repository protecting it against criticality rearrangement, plutonium recovery for nuclear weapons, etc.

The waste is mainly composed of transuranium isotopes (TRU) built in the reactor through neutron capture in the fuel, and long lived fission fragments (LLFF), which result from the fission of the fissile isotopes in the reactor core. For many years, people have thought of destroying this waste in a similar way as it was created, by inducing further neutron reactions [3].

The TRU can not be effectively transmuted in the thermal neutron flux of a conventional Light Water Reactor (LWR) because there is a strong odd-even neutron number effect [14] so that ^{233,235}U, ^{239,241}Pu, etc show a large fission probability, whereas ^{236,238}U, ^{238,242,240}Pu have instead a larger capture probability. After a long neutron irradiation, the elements with an even number of neutrons tend to accumulate and reduce intolerably the neutron flux in the reactor.

The neutron reaction cross sections in the keV-MeV energy range are in general much lower than in the thermal region, however the fission to capture ratio for TRU is much more favorable in this higher energy range. Therefore, an incineration engine based on a high energy neutron flux has been thought to be a possible solution for this problem [4]. To compensate for the lower cross section, a large waste inventory must be present in such a transmutation machine as well as an intense neutron flux.

Another possibility [15] is based on using a thermal neutron flux, similar to that inside a reactor, but more intense $\sim 10^{16}$ n/cm^{2}s, so that the capture probability is enhanced and by means of a two step capture process, a nucleus with a higher fission probability is reached. An example would be n+^{237}Np$\rightarrow$^{238}Np. The ^{238}Np nucleus is β-unstable ($t_{1/2}$ = 2.1 days decaying to ^{238}Pu), but given its high fission cross section, provided a large enough neutron flux, the burn-up period becomes 0.5 days, thus undergoing mostly fission (n+^{238}Np$\rightarrow$ fission) before β-decaying.

A high neutron flux can be produced by means of an Accelerator Driven System

(ADS) in which protons coming from an accelerator impinge on a heavy metal target. When a proton impinges on the target, it ejects neutrons and protons in the forward direction with a lower energy than the energy of the incident particle. These neutrons, and sometimes protons, then strike other nuclides, which in turn eject other forward moving lower energy particles. The cascade continues until the energy is spent. The cascade length is of about 1 meter in lead for a 1 GeV proton beam energy. In any of these nuclear collisions, the struck nucleus is always excited to some degree and these hot nuclides boil-off neutrons isotropically. About 90% are boiled-off neutrons, whereas the remaining 10% come from the direct reactions. Around 30 neutrons are produced by each incident proton of 1 GeV. This prolific mechanism is referred to as spallation. By choosing the appropriate proton beam energy and current the spallation can be employed for the purpose described above of achieving a high neutron flux for incinerating radioactive waste.

Once the high intensity neutron flux is provided, the appropriate neutron energy spectrum (fast or thermal) to effectively achieve the transmutation can be obtained by moderation.

The possibility to eliminate the LLFF also exists as has been demonstrated experimentally for ^{99}Tc and ^{129}I in an experiment carried out at CERN [16]. The mechanism consists on the so called transmutation by means of adiabatic resonance crossing (TARC). In the experiment, a proton beam of 2-3.57 GeV/c with an intensity of 10^7-10^{10} protons per bunch impinges onto a 334 ton lead target. Due to the properties of lead, the initially high energetic neutron flux (few MeV), after having been quickly moderated by (n,xn), (n,n') reactions down to energies of a few hundred keV, starts to slow down, quasi-adiabatically with small isolethargic steps until it reaches a capture resonance energy of an element to be transmuted, where the neutrons have a high probability of being captured.

Such an accelerator driven engine could also be used the other way around, in order to produce radio-diagnosis isotopes with the required activity for medical applications. In the TARC experiment, the short-lived ^{99m}Tc, was activated from natural molybdenum by irradiating it inside the lead assembly.

A practical design of an ADS transmutator is still technically uncertain, but one of the most fully developed designs [4] consists of an annular core (containing the fuel and radioactive waste to be transmuted) immersed in molten lead-bismuth eutectic. The latter serves as primary coolant (moderator) and spallation target and represents a considerable amount of the total engine's volume.

In a first sensitivity study of the neutron cross sections of the main materials used in this type of incinerator [17], severe discrepancies where found between different evaluated nuclear data files. As a consequence, a list of isotopes were tagged as high priority to the on-going neutron cross section measurements. Most of the requested cross sections correspond to the fuel and cladding materials, and mainly elastic, inelastic and (n,xn) channels were asked for. However, in a recent extension of the same study [18], the request has been also extended to capture in the spallation/coolant material lead and bismuth. Comparing two evaluated data files,

ENDF/B-VI.8 and JENDL 3.3, discrepancies in the neutron balance of 24% and 12.5% were found respectively due to the poorly known (n,γ) capture cross section of ^{208}Pb and ^{209}Bi.

Therefore, the precise knowledge of the radiative neutron capture cross sections of the lead and bismuth isotopes turns out relevant for the design of an ADS for the transmutation of radioactive residues and energy production.

Furthermore, capture on bismuth leads to the build up in the liquid Pb/Bi coolant of the metastable ^{210m}Bi, which is a long term (3×10^6 years) α-emitter, thus contributes to the long term radiotoxicity of the target. Also, the production of ^{210}Po, a short term α-emitter with a half-life of 138 days contributes to the short term radiotoxicity of the spallation core. Both short and long term hazards can be only evaluated with precise knowledge of the (n,γ) capture cross section of bismuth.

1.3 Radiative neutron capture

The purpose of this section is to describe briefly the radiative neutron capture process and to define the nomenclature which is going to be used across the whole work. A detailed description of the physics involved can be found somewhere else [19, 20].

The radiative capture reaction is believed to proceed through the formation of a compound nucleus and subsequent decay emitting one or several gamma rays,

$$(Z, A) + n \rightarrow (Z, A+1)^* \rightarrow (Z, A+1) + \gamma. \tag{1.5}$$

This neutron reaction is sketched in figure 1.3. On the right side, the two observables of this reaction are shown. These correspond to the measured neutron time of flight, which is equivalent to the neutron energy E_n, and to the gamma ray spectrum. The gamma rays of this spectrum deposit their energy E_{dep} in radiation detectors, which in the present work are C_6D_6 detectors.

Following the neutron capture, the compound nucleus is excited to a level with an energy given by,

$$E^* = S_n + \frac{A}{A+1} E_n, \tag{1.6}$$

where S_n is the neutron separation energy of the nucleus (Z,A+1) and E_n is the energy of the incident neutron. The compound nucleus decays after a very short time $\tau_\gamma \sim 10^{-14}$ s by emission of one or more gamma rays E_j^γ to reach the ground state. Neglecting the recoil energy of the nucleus, one can write in very good approximation,

$$E^* = \sum_j E_j^\gamma. \tag{1.7}$$

The total cross section is related to the probability for the compound nucleus to occur. This probability is best described by the R-matrix theory [21], which in the

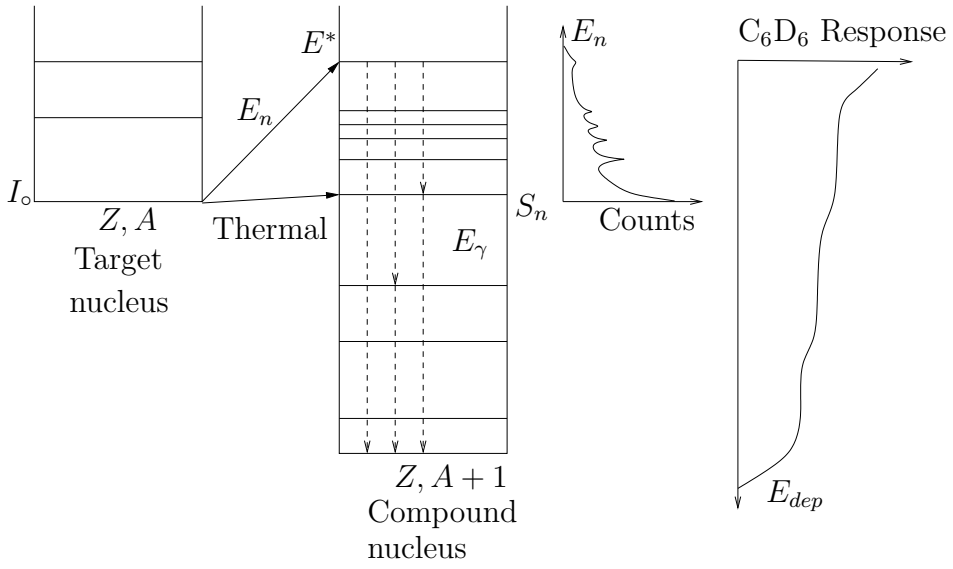

Figure 1.3: *Scheme of the radiative capture process and the two observables measured in the experiment, the neutron energy and the gamma-ray spectrum.*

isolated resonance region simplifies into the Breit-Wigner dispersion formula,

$$\sigma_{c^*}(E_n) = g\frac{\pi}{k_n^2}\frac{\Gamma_n\Gamma}{(E_n - E_\circ)^2 + (\Gamma/2)^2}, \tag{1.8}$$

where,

$E_\circ$ energy of the resonance.

$g = (2J+1)/((2s+1)(2I+1))$ is the spin factor, being,

I spin of the target nucleus,

J spin of the compound nucleus, and

s spin of the neutron.

$k_n = 2.196771 \times 10^{-3}\frac{A}{A+1}\sqrt{E_n}$.

Γ total width.

Γ_n neutron scattering width,

$$\begin{cases} s-\text{wave}: & \Gamma_n(E_n) = \Gamma_n^0\sqrt{E_n} \\ p-\text{wave}: & \Gamma_n(E_n) = \Gamma_n^1\sqrt{E_n}\,k_n^2\frac{a^2}{(1+k_n^2a^2)}, \quad \text{with} \quad a = 0.80 + 1.23A^{1/3}\ \text{fm}. \end{cases}$$

The total width Γ designates the sum of the individual reaction widths,

$$\Gamma = \Gamma_n + \Gamma_\gamma + \Gamma_f + \Gamma_p + \ldots \tag{1.9}$$

The radiative capture width Γ_γ is generally of the order of 0.1-1 eV and smaller for heavy nuclei (0.1-0.03 eV). These widths imply, through the uncertainty principle $\Gamma_\gamma \tau_\gamma \approx \hbar$, mean radiative lifetimes of about $\tau_\gamma \sim 10^{-14}$ seconds. In the energy range and for the nuclei under study in the present work, 1 eV-1 MeV, only the neutron scattering channel, Γ_n, shows a similar lifetime, all other possible reactions being excluded by their orders of magnitude larger lifetimes. The probability of the compound nucleus to decay by any of these two channels is given by,

$$P_r = \frac{\Gamma_r}{\Gamma} \qquad r = n, \gamma \tag{1.10}$$

and the corresponding cross section,

$$\sigma_r = \sigma_{c^*}(E_n) P_r. \tag{1.11}$$

In the case of (n,γ) capture, equation 1.11 reduces to,

$$\sigma_\gamma(E_n) = g \frac{\pi}{k_n^2} \frac{\Gamma_n \Gamma_\gamma}{(E_n - E_\circ)^2 + (\Gamma/2)^2}. \tag{1.12}$$

The peak cross section, at $E_n = E_\circ$, is given by,

$$\sigma_\gamma(E_\circ) = \sigma_\circ \frac{\Gamma_\gamma}{\Gamma}, \tag{1.13}$$

being $\sigma_\circ$ the peak value of the total cross section,

$$\sigma_\circ = \frac{4\pi}{k_n^2} g \frac{\Gamma_n}{\Gamma}. \tag{1.14}$$

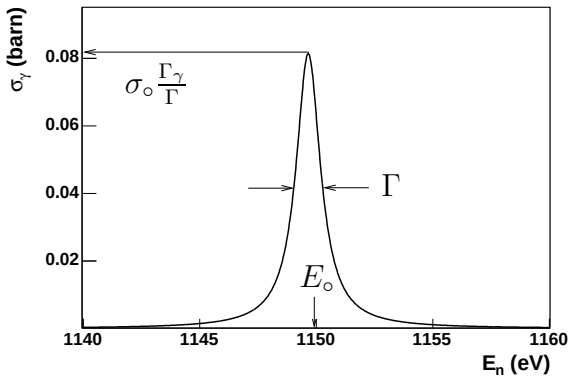

Figure 1.4: *Resonance in ^{56}Fe+n, with $I = 0$, $J = 1/2$, orbital angular momentum $l = 1$, $E_\circ = 1149.7$ eV, $\Gamma_\gamma = 0.574$ eV and $\Gamma_n = 0.0617$ eV.*

The total radiative area of a resonance is given by integrating equation 1.12 between $E_\circ - \frac{\Gamma}{2}$ and $E_\circ + \frac{\Gamma}{2}$,

$$A_r = \frac{2\pi^2}{k_\circ^2} g \frac{\Gamma_n \Gamma_\gamma}{\Gamma} = \frac{4.09 \times 10^6}{E_\circ} \left(\frac{A+1}{A} \right)^2 K_r \tag{1.15}$$

where K_r is the so called radiative kernel,

$$K_r = g \frac{\Gamma_n \Gamma_\gamma}{\Gamma}. \tag{1.16}$$

Chapter 2

Measuring technique

In the present work, we are interested in the accurate measurement of the capture cross section of the ^{209}Bi and ^{207}Pb isotopes in the energy region of resolved resonances. As these two nuclides are neighbours of the double magic ^{208}Pb, their neutron capture cross sections are also very small, thus requiring a measuring technique of high detection sensitivity or signal to background ratio.

On the other hand, the capture cross section of these isotopes is dominated by resonances, which show in general a much larger scattering than capture probability. Therefore at each resonance there are usually many more neutrons being scattered than captured in the sample. These scattered neutrons can be captured in the materials of the experimental setup and mimic a capture signal, thus artificially enhancing the apparent capture yield and contributing as a source of time of flight dependent background.

The common technique of measuring the number of cascades by using a 4π detector with high efficiency would show, in this type of measurements, a prohibiting contamination due to the neutron sensitivity effect mentioned above.

In the early 60's, the Moxon-Rae detector [22] was a first approach to solve this problem. It makes use of the fact that a plastic scintillator with a thick converter wall of a low Z material has a gamma ray detecting efficiency which increases nearly linearly with gamma ray energy. This feature makes the efficiency for the detection of a capture event independent of the particular gamma ray cascade emitted.

Maier-Leibnitz showed [23] that for a wide class of radiation detectors one can generate an average response function proportional to energy by applying to each pulse from the detector a certain weight, which is a function of the pulse size only. This is the basic idea of the so called **Pulse Height Weighting Technique** (PHWT) and has the big advantage of considerable freedom in optimizing the detection system in terms of insensitivity to scattered neutron backgrounds, shielding, efficiency, time resolution, etc. A detailed description of the technique itself is given in the following section.

Macklin and Gibbons applied the PHWT for the first time to measure the neutron capture cross section of several isotopes [23]. By calculating an accurate Weight-

ing Function (WF), one can in principle obtain a better proportionality between gamma ray efficiency and energy than with the Moxon-Rae method.

The PHWT employed with low neutron sensitivity detectors has been used for the measurement of isotopes, like ^{209}Bi and ^{207}Pb, whose cross sections are dominated by resonances with large scattering to capture ratios. Nevertheless, the neutron sensitivity of the experimental setup used in previous measurements of these isotopes [24, 25], was still a source of high systematic uncertainty and the measured cross section needed in some cases corrections larger than 50%.

Moreover, systematic errors arose also in previous experiments from the delicate procedure of obtaining the weighting factors [26]. Discrepancies larger than 20% in some measurements of the 1.15 keV resonance of ^{56}Fe triggered many doubts about the accuracy of this technique.

Our aim in this work is to overcome these two difficulties, by *i*) performing a validation and exhaustive study of the technique itself and its different sources of (mathematical and experimental) systematic uncertainty, and *ii*) making use of the PHWT with an optimized experimental apparatus characterized by a negligible neutron sensitivity.

In this chapter we will concentrate only on the description of the technique, and the mathematical procedure used to obtain weighting functions.

The optimized experimental setup will be described in the following chapter, while chapter 5 has been dedicated to the validation of the PHWT, the study of the different sources of systematic uncertainty and the calculation of correction factors related with those uncertainties.

The other common technique for capture measurements, the total absorption method (figure 2.1), is better suited for the measurement of other type of materials like radioactive samples, rare earths (available only in small amounts) and materials with higher capture to scattering ratio. In these cases, a better detection sensitivity is achieved by using a high efficiency detector. The **Total Absorption Calorimeter** (TAC) technique is based on the use of a 4π detector with an efficiency of about 100%. It has evolved from the original large liquid scintillators to more optimized crystal calorimeters, which show a better energy resolution and lower intrinsic background.

With this type of detector, all the prompt gamma rays of the nuclear cascade which follows a neutron capture are registered. Adding the energy of all the gamma rays registered in coincidence, one obtains a sum peak at the energy of the cascade which is proportional to the number of capture events occurred (right part of figure 2.1).

The good energy resolution and the possibility to perform n/γ-discrimination are some additional advantages of this technique. It also allows some other studies like gamma ray multiplicities, angular distributions and gamma ray spectra.

The main general disadvantage of the TAC-technique resides on its much more complex setup and higher cost.

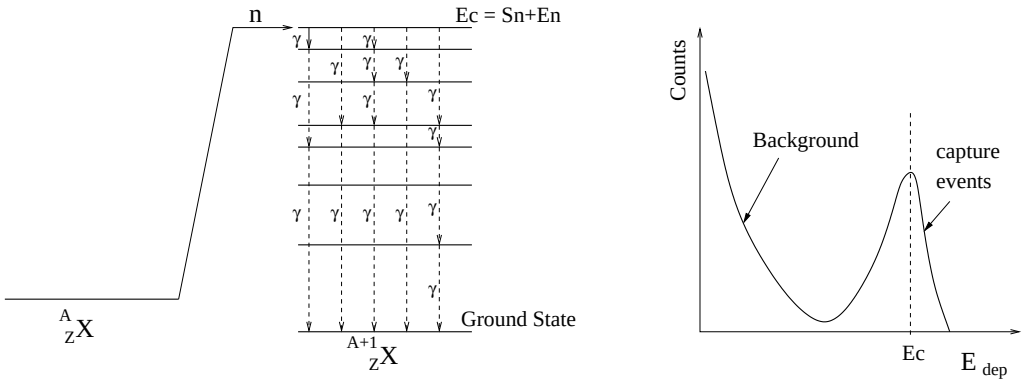

Figure 2.1: *(Left) Schematic draw of the capture process, with representation of several deexcitation paths. (Right) Sum peak of all the gamma rays detected in coincidence.*

2.1 Pulse Height Weighting Technique

The PHWT is based on the use of a gamma ray detection system with **very low efficiency**, so that at most only one gamma ray of the capture cascade is registered,

$$\varepsilon^{\gamma} \ll 1. \tag{2.1}$$

But since ε^{γ} varies with the gamma ray energy E^{γ}, such a detection setup would show a detection efficiency for a capture process depending on its particular nuclear deexcitation path. One can avoid this dependence by introducing a **proportionality condition** into the detection efficiency,

$$\varepsilon^{\gamma} = \alpha E^{\gamma}. \tag{2.2}$$

If the last equation is also fulfilled, then the probability to detect a cascade will be independent of the particular deexcitation path, as is shown in the following.

Mathematically, the efficiency of detecting a nuclear cascade composed of $j = 1, \ldots, N$ gamma rays of energies E_j^{γ}, can be expressed as

$$\varepsilon^{c} = 1 - \prod_{j=1}^{N} (1 - \varepsilon_j^{\gamma}), \tag{2.3}$$

where ε_j^{γ} designates the efficiency to register a gamma ray of energy E_j^{γ}. The latter equation describes the probability of detecting at least one of the cascade gamma rays, which has been written as the complementary of not detecting any of these gamma rays.

Given both initial conditions (2.1 and 2.2), the previous equation can now be written in good approximation as

$$\varepsilon^c \approx \sum_{j=1}^{N} \varepsilon_j^\gamma = \alpha \sum_{j=1}^{N} E_j^\gamma = \alpha E_C. \tag{2.4}$$

Hence, as the cascade detection probability ε^c is now proportional to the constant value of the neutron capture energy E_C, it does not depend any more on the particular nuclear deexcitation path or prompt gamma ray registered, as one wanted to prove.

While the first condition (2.1) of having a very low gamma ray detection efficiency can be easily achieved by utilizing small volume and low Z gamma ray detectors, the second condition (2.2) is slightly more complicated to fulfill.

Assume R_i^γ, with $i = 1, \ldots, n$, to be the response function of the detection system for a capture gamma ray of energy E^γ, normalized to the efficiency for detecting that gamma ray, i.e., $\sum_{i=1}^{n} R_i^\gamma = \varepsilon^\gamma$. The proportionality condition (2.2) between detection probability and gamma ray energy can be now achieved by appropriately weighting the response function R_i^γ for the registered gamma ray,

$$\sum_{i=1}^{n} W_i R_i^\gamma = E^\gamma. \tag{2.5}$$

In the last equation, the proportionality constant α has been chosen equal to one in inverse energy units. The weighted response function, $R'^\gamma_i = W_i R_i^\gamma$, fulfills now the proportionality condition 2.2 between efficiency and gamma ray energy,

$$\varepsilon'^\gamma = \sum_{i=1}^{n} R'^\gamma_i = \sum_{i=1}^{n} W_i R_i^\gamma = E^\gamma. \tag{2.6}$$

It is important to note here, that the systematic accuracy of this technique depends directly on the two assumed conditions of low efficiency 2.1 and proportionality 2.2.

The detection of at most one gamma ray of the nuclear cascade, condition 2.1, is sufficiently well fulfilled with the low efficiency experimental setup used for the measurements presented in this work. The efficiency depends on the details of each experimental setup and therefore will be presented together with each measurement (chapters 5, 6 and 7). Moreover, the probability to detect more than one gamma ray in coincidence has been investigated for the different experimental setups and corrections for this effect have been accurately calculated, as is described in the chapters mentioned above.

The mathematical procedure to calculate the WF is described in the two following subsections. Once the WF has been determined, one should check how well the proportionality condition 2.2 is achieved, by substitution of the WF back into equation 2.5 for a set of gamma ray energies E^γ in the energy range of the capture cascade. However, deviations in equation 2.5 reflect also deviations in the calculated WF at the corresponding gamma ray energies, but they do not give any information about the uncertainty introduced in the capture experiment by the WF itself. In

order to determine the WF uncertainty, we have developed a new procedure based on the Monte Carlo simulation of realistic nuclear cascades with fixed total energy E_C, where at most one of the prompt gamma rays is registered. Let W_i be the calculated WF and $R_{i,c}$ the response distribution of each simulated cascade c. Then, for a large number of cascades N and an exact WF it should be fulfilled that the weighted sum is equal to the number of cascades times the capture energy,

$$\sum_{c=1}^{N}\sum_{i=1}^{n} W_i R_{i,c} = NE_C. \tag{2.7}$$

Deviations of the weithed sum (left term in eq. 2.7) from NE_C indicate the uncertainty due to the calculated W_i. As the nuclear cascades depend on the sample's material, this method will be shown in more detail in chapter 5, which is dedicated to the validation of the experimental technique.

2.2 Weighting function calculation

In this section we describe two different mathematical methods that have been used in the present work to calculate the WF. The first one corresponds to the common approach of obtaining the WF assuming a polynomial behaviour and deriving its coefficients by performing a minimization of eq. 2.5. However, using this method we were not able to find accurate WF for the thicker samples of ^{209}Bi and ^{207}Pb, as it will be shown in chapter 6 and chapter 7. Therefore, a more general procedure based on the Tikhonov Linear regularization method has been developed [27]. This new procedure is described in section 2.2.2.

2.2.1 Polynomial weighting function

In order to calculate the WF one can start from eq. 2.5. Since we need a WF valid in the whole energy range of the capture process, E_C, one usually calculates by Monte Carlo simulation a set of response distributions $R_{i,j}$ for $j = 1, \ldots, l$ gamma rays in that energy range. About the calculation of these response functions for our experimental setups will be discussed in section 5.3. Here we will concentrate only on the mathematical procedure to derive W_i, given the efficiency normalized response functions $R_{i,j}$.

It has been always assumed in previous experiments that the energy dependence of the WF can be approximated by a polynomial function,

$$W_i \approx \sum_{k=0}^{q} a_k E_i^k, \tag{2.8}$$

where E_i designates the energy of the bin i in the response function and a_k has energy inverse units to the power of k.

The common procedure to determine the coefficients a_k is based on a least squares minimization,

$$min\left(\sum_{j=1}^{l}\left(\sum_{i=1}^{n}\sum_{k=0}^{q}\frac{a_k E_i^k R_{i,j}}{p_i} - E_j^{\gamma}\right)^2\right). \tag{2.9}$$

Usually a polynomial of degree $q = 3$ to 5 gives a satisfactory solution of the WF. The exact shape of the WF depends on the details of the experimental setup like the sample itself and type of detector, as will be shown in chapter 5.

Macklin and Gibbons [23] found for a detection system based on two plastic scintillators that the best weighting function was given by the ratio of two polynomial functions of degrees 2 (numerator) and 3 (denominator), while for a detector with two NE-226 hydrogen free liquid scintillator cells, the weighting function was the quotient of two polynomials with degree 3 (numerator) and 4 (denominator).

The estimators p_i in equation 2.9 can be arbitrary set to a value which gives a better convergence and solution for W_i. We have used $p_i = 1$, but a power of the energy E_i gives sometimes a better convergence.

From eq. 2.5, one can calculate the goodness of the obtained polynomial WF at each gamma ray energy E_j^{γ} by performing the weighted sum of its response function and checking how much the ratio with the energy differs from the unity, i.e., in which proportion the following equation is fulfilled,

$$\frac{\sum_i W_i R_{i,j}}{E_j^{\gamma}} = 1. \tag{2.10}$$

The accuracy of the WF however will be determined from equation 2.7, performing Monte Carlo simulations of the nuclear cascades as is described in detail in section 5.6.

2.2.2 Pointwise weighting function

The previous assumption of having a polynomial behaviour worked well for not so thick samples (with high neutron capture cross section) like gold, silver or iron but failed to give a valid WF for thick samples of heavy materials (with low capture cross section) like lead or bismuth. It should be pointed out that rather thick samples were necessary at n_TOF in order to keep the amount of measuring beam time within reasonable limits.

The reason why a polynomial WF did not perform well with the thicker samples is due to the gamma rays absorption inside the sample. These isotopes have a low neutron capture cross section, which in a thick sample means deeper penetrability of neutrons, having more capture reactions occuring in the inner core of the sample under study. This effect, together with the high Z of the sample, produces that a lot of capture gamma rays are scattered and absorbed before exiting outside the sample. The absorption of gamma rays in the sample is an experimental effect that we were not able to take into account with a polynomial WF. On one side, equation 2.10

showed in this case large deviations at lower energy. On the other side, the estimated uncertainty of the polynomial WF with equation 2.7 was of few per cent, while it is usually of only a few per mil compatible with the statistical uncertainty of the Monte Carlo simulated response functions $R_{i,j}$. In section 6.2.1 the calculation of a polynomial WF for the ^{209}Bi sample is shown, just to give an idea of how inaccurate results in this case the polynomial approximation.

We investigated this issue trying higher degree polynomial functions and several minimization methods, obtaining in all the cases inaccurate solutions of the WF.

Since we wanted to measure neutron capture cross sections with a systematic uncertainty down to few per cent, we had to work out a better solution for W_i. Therefore, a more general mathematical approach to obtain the WF has been developed [27]. The latter is based on the calculation of an approximate pointwise solution, W_i, for the system of equations,

$$\sum_{i=1}^{n} R_{ji} W_i = E_j \qquad \text{with} \quad j = 1, \ldots, l \quad \text{gamma rays.} \tag{2.11}$$

To understand the difficulty of this problem, let us consider first the situation from a general point of view. The previous system of equations can be written using vector notation as,

$$\mathbf{R}\vec{W} = \vec{E}. \tag{2.12}$$

Mathematically, this equation has a solution if the matrix $\mathbf{R}$ is not singular (i.e., has non zero determinant $|\mathbf{R}| \neq 0$) and its inverse matrix exists, (i.e., $\mathbf{R}$ need to be a square matrix). From the algebra's viewpoint, fulfill the last condition is not a problem, thus one can simulate as many gamma rays l as n bins are in the response function, in which case $l = n$ and $\mathbf{R}$ is a square matrix.

Then, the solution $\vec{W}$ is given by

$$\vec{W} = \mathbf{R^{-1}}\vec{E}. \tag{2.13}$$

Note that the response matrix $\mathbf{R}$, which is normalized to the efficiency, consists of small elements which are always lower than 1 (usually orders of magnitude smaller).

Inverting the matrix $\mathbf{R}$ is impossible from the computational viewpoint. The reason is that, given the real elements of the matrix and the restricted numerical precision of any computer (numbers of finite size length), at some point rounding effects take place. Therefore, the floating arithmetic operations in a computer, unlike the integer arithmetic operations, are not exact. In a system with so many equations[1] as 2.12, a small change in any of them (due to the mentioned roundoff errors), produces unpredictable effects on the result. Typical results oscillate between negative and positive values, giving an artificially oscillating and divergent

[1] At least 180 equations are needed in order to cover the energy interval up to 9 MeV with a bin width of 50 keV.

result. Obviously this result is unphysical and usually completely wrong, as can be checked by direct substitution back into the original equations.

The closer the set of equations 2.12 is to being singular, the more likely this is to happen, since increasingly close cancellations will occur during the solution. Indeed, our matrix $\mathbf{R}$ becomes easily singular for several reasons, which are explained in the following.

Let us observe first that the matrix $\mathbf{R}$ is almost triangular [28], hence its determinant will be in the order of magnitude of the product of the diagonal elements,

$$|\mathbf{R}| \approx \prod_{i=1}^{n} R_{ii}. \tag{2.14}$$

In our case, given the required small efficiency of the detection system, the product of such a series of small numbers (diagonal matrix elements) becomes easily zero for a computer. On the other side, using the raw response matrix of integer elements (not yet normalized to the efficiency), the product of the diagonal elements tends to infinity.

A floating type number (4 bytes memory are allocated for each `float`) on a normal machine has an approximate precision of 6 significant digits and a range of about 1E-38 to 1E38. This means that a number smaller than 1E-44 is taken as zero in a computer (larger than 1E44 would be taken as infinity). With this constraint, the maximum number of diagonal matrix elements which can be multiplied in our case is of around 10 (and only with one significant digit in the result!) and a matrix of higher dimension becomes already singular for the computer. Using higher precision variables (`double` of 8 bytes or `long double` of usually 12 bytes) also does not solve our problem, since the number of significant digits are still very small and roundoff errors accumulate rapidly.

Furthermore, the matrix $\mathbf{R}$ is composed of very similar columns, because the response function of the detection system for an energy E^{γ} is very similar to the next one of energy $E^{\gamma}+\Delta E$. While there is no exact linear combination of each other, some of the columns may be so similar that roundoff errors in the machine render them linearly dependent at some stage in the solution process. This contributes also to the rapid singularity of the system.

From the computational point of view an exact solution does not exist and we are treating with the so called *ill-posed* problem. A problem is ill-posed, when at least one of the following conditions is not fulfilled,

- a solution exists,
- the solution is unique,
- it depends continuously on the initial data.

The so called inverse problem has to be solved and this is much more complicated since the well-posedness must be restored by restricting the class of admissible

solutions using a priori knowledge, which of course depends on the particular type of the problem itself.

In order to solve our inverse problem and find a reasonable solution for $\vec{W}$, there exist several mathematical methods of different types, regularization, iterative, bayesian, maximum entropy, etc.

We have tested some of them with our problem, but finally the "Tikhonov"-Linear regularization method [29] was giving a better convergence and was easier to implement. Its algorithm can be derived from minimization principles,

$$min(\chi^2[\vec{W}] + \lambda\varsigma[\vec{W}]), \tag{2.15}$$

where λ is a Lagrange multiplier to be determined by some criteria. χ^2 measures the agreement of the model to the data whereas ς is a regularization functional related with "a priori" information. The last determines the smoothness or stability of the solution $\vec{W}$ and can be written as:

$$\varsigma[\vec{W}] = \vec{W}\mathbf{H}\vec{W} \qquad \text{with} \quad \mathbf{H} = \mathbf{B^T B} \tag{2.16}$$

$\mathbf{B}$ is the $(n-1) \times n$ matrix (in first order):

$$\mathbf{B} = \begin{pmatrix} -1 & 1 & 0 & 0 & 0 & 0 & 0 & \dots & 0 \\ 0 & -1 & 1 & 0 & 0 & 0 & 0 & \dots & 0 \\ \vdots & & & \ddots & & & & & \vdots \\ 0 & \dots & 0 & 0 & 0 & 0 & -1 & 1 & 0 \\ 0 & \dots & 0 & 0 & 0 & 0 & 0 & -1 & 1 \end{pmatrix} \tag{2.17}$$

so that $\mathbf{H}$ is the square matrix $n \times n$,

$$\mathbf{H} = \mathbf{B}^T\mathbf{B} = \begin{pmatrix} 1 & -1 & 0 & 0 & 0 & 0 & 0 & \dots & 0 \\ -1 & 2 & -1 & 0 & 0 & 0 & 0 & \dots & 0 \\ 0 & -1 & 2 & -1 & 0 & 0 & 0 & \dots & 0 \\ \vdots & & & \ddots & & & & \vdots & \\ 0 & \dots & 0 & 0 & 0 & -1 & 2 & -1 & 0 \\ 0 & \dots & 0 & 0 & 0 & 0 & -1 & 2 & -1 \\ 0 & \dots & 0 & 0 & 0 & 0 & 0 & -1 & 1 \end{pmatrix} \tag{2.18}$$

With the preceding definitions it can be demonstrated that equation 2.15 is equivalent to

$$(\mathbf{R}^T\mathbf{R} + \lambda\mathbf{H})\vec{W} = \mathbf{R}^T\vec{E}, \tag{2.19}$$

which can be solved by the standard techniques, e.g., LU decomposition. The λ parameter prevents the last equation of being ill-conditioned.

The best value for the regularizator λ is determined by the optimal agreement between sharpness (χ^2) of the solution and stability of the solution ($\vec{W}\mathbf{H}\vec{W}$). When these two quantities are represented for several values of λ (see figure 2.2), one obtains a figure with the shape of an "L". The best solutions to our inverse problem can be obtained for the values of λ in the corner region of this "L". There are therefore different valid solutions, which depend on the exact value of λ.

Nevertheless, the solution $\vec{W}$ is not positive definite in general. This means that the possible values of λ need to be also restricted in order to obtain a positive solution $\vec{W}$.

A practical view of this method will be given in chapters 6 and 7, where the pointwise WF of ^{209}Bi and ^{207}Pb are calculated.

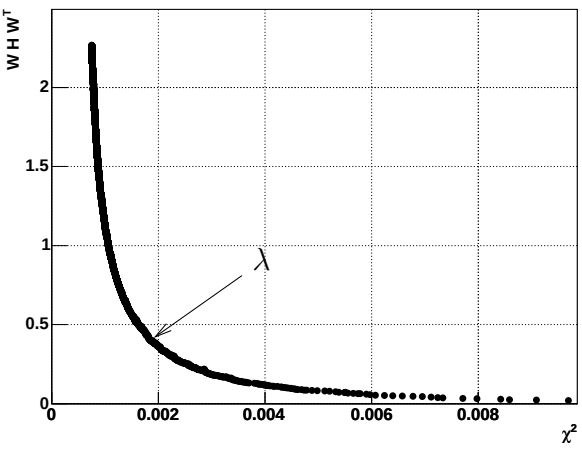

Figure 2.2: *L-plot to find the value of the Lagrange multiplier* λ.

Chapter 3

Experimental setup

Neutron energy differential capture cross sections can be measured with high resolution using the time of flight technique at the CERN n_TOF installation. A description of the main features of this facility, focusing on the relevant elements for the capture experiments, is given in section 3.1.

As has been shown in the previous chapter, the accurate measurement of the (n,γ) cross sections of ^{209}Bi and ^{207}Pb, requires a minimization of the neutron sensitivity in the experimental apparatus. Therefore, the PHWT has been chosen for these measurements, which enabled us to use a very optimized detection system. The "complexity" of the involved analysis procedure described in the previous chapter, has on the other hand the advantage of a very simple experimental setup, based on two C_6D_6 detectors as will be described in detail in this chapter.

3.1 The CERN time of flight installation

n_TOF[6, 30, 31, 32] is a time of flight installation based on a spallation source. Neutrons are produced by spallation reactions induced by a sharply pulsed, 6 ns wide (RMS), 20 GeV/c proton beam impinging onto a high purity lead block of $80\times80\times60$ cm^3. This prolific mechanism, generates in average about 600 neutrons per incident proton.

The protons are provided by the CERN Proton Synchrotron (PS)[33], which is able to produce a total of 3×10^{13} protons per 14.4 s supercycle. The supercycle is divided into sub-intervals, delivering a bunch of protons every 2.4 s (or multiples of this quantity). The PS proton beam can operate in dedicated mode, delivering 7×10^{12} protons per bunch, or in the parasitic mode, delivering 4×10^{12} protons per bunch.

The very low duty cycle is an advantage for the measurement of radioactive samples with a greatly improved signal to background ratio. Moreover, the 2.4 s time between each two PS-events have permitted the implementation of a zero deadtime acquisition system, described in section 3.3.

A calibrated wall current monitor (WCM), with a precision in the determination

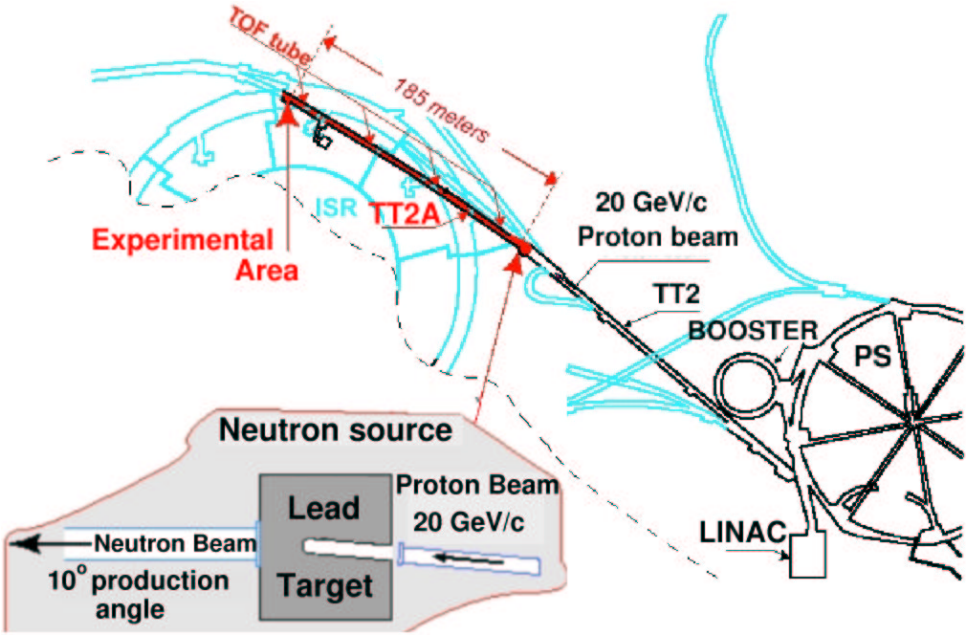

Figure 3.1: *General view of the n_TOF installation with a detail of the lead spallation target.*

of the proton current better than 1%, is located at the proton beam line right before the lead block. The induced Pickup signal can be utilized to accurately monitor the number of protons per bunch impinging on the spallation source. This Pickup signal is also used to trigger the n_TOF data acquisition system.

The lead spallation target is immersed in water contained in an aluminum tank. The water serves both as coolant and as moderator of the initially fast neutron spectrum, providing a wide energy spectrum from 1 eV up to 250 MeV, with a nearly $1/E$ flux dependence up to about 1 MeV (see section 4.5 for more details on the neutron flux). An aluminum alloy window of 1.6 mm thickness is the only interface between the moderator and the vacuum of the n_TOF tube. The last is shifted by an angle of 10° with respect to the incident proton beam direction, in order to reduce the amount of charged particles and gamma rays which are scattered preferably in the forward direction. Furthermore, a 2 m long dipole magnet has been located 120 m upstream in order to fully clean the neutron fluence of any secondary charged particle. A 3 m thick iron shielding [34, 35] placed after the magnet minimizes the background due to negative muon capture in the experimental area. A two collimators system [36] has been build, consisting of two tubes 2 m×11 cm ⊘ and 2.5 m×1.8 cm ⊘ located at 135.54 m and 175.35 m respectively from the lead target. This results in a Gaussian beam profile at the sample position with approximately 2 cm FWHM, as is described in section 4.6.1. Finally, the measuring station starts 182.5 m upstream, the capture sample being positioned usually at 185.05 m from the exit window of the spallation target. Thanks to this very long flight path, a high

neutron energy resolution of about $\Delta E/E = 1\times10^{-4}$ can be achieved up to energies of ∼100 keV.

A detailed description of the experimental apparatus for neutron capture measurements is given in section 3.2. The neutron guide extends 12 m beyond the sample position. In order to minimize the background due to back-scattered neutrons, a concrete wall separates the measuring station from the end of the escape line where neutrons are finally dumped.

3.2 Neutron capture experimental setup

The relevant feature of the (n,γ) capture experiments performed at n_TOF is the experimental setup itself. A large effort has been devoted to build a low mass setup, characterized by a very low neutron sensitivity. Figure 3.2 shows a schematic view of the experimental setup.

In the subsequent sections, each component of this setup is described in detail.

3.2.1 C_6D_6 detectors

The prompt gamma rays following the neutron capture are registered by means of two C_6D_6 liquid scintillator detectors. The detector itself is the most delicate element in terms of neutron sensitivity, since any scattered neutron which is captured in the detector materials has a high probability to be registered as background. For this reason, the neutron sensitivity of these detectors has been subject of careful investigation [5]. A quantitative measure of this effect and the corresponding yield correction factors will be given later in section 4.8.

In the measurements described in this work we always make use of neutron sensitivity improved detectors. Depending on the degree of optimization, one can classify the detectors employed at n_TOF into two groups:

- Commercial C_6D_6 detector. A set of four Bicron detectors with some improved neutron sensitivity features were available. Two of them have been used for the validation of the PHWT described in chapter 5.

  The photomultiplier tube, type XP4508B, has been especially built with a non borated glass window, in order to lower its neutron sensitivity. The C_6D_6 container has a volume of 618 cm^3 and is coupled with the PM by means of a quartz window.

  The detector is provided with a thin aluminum housing and a removable Teflon tubing coiled around the C_6D_6 cell. The latter is used for expansion of the scintillation liquid. A detailed scheme of this detector is provided in appendix D.1.

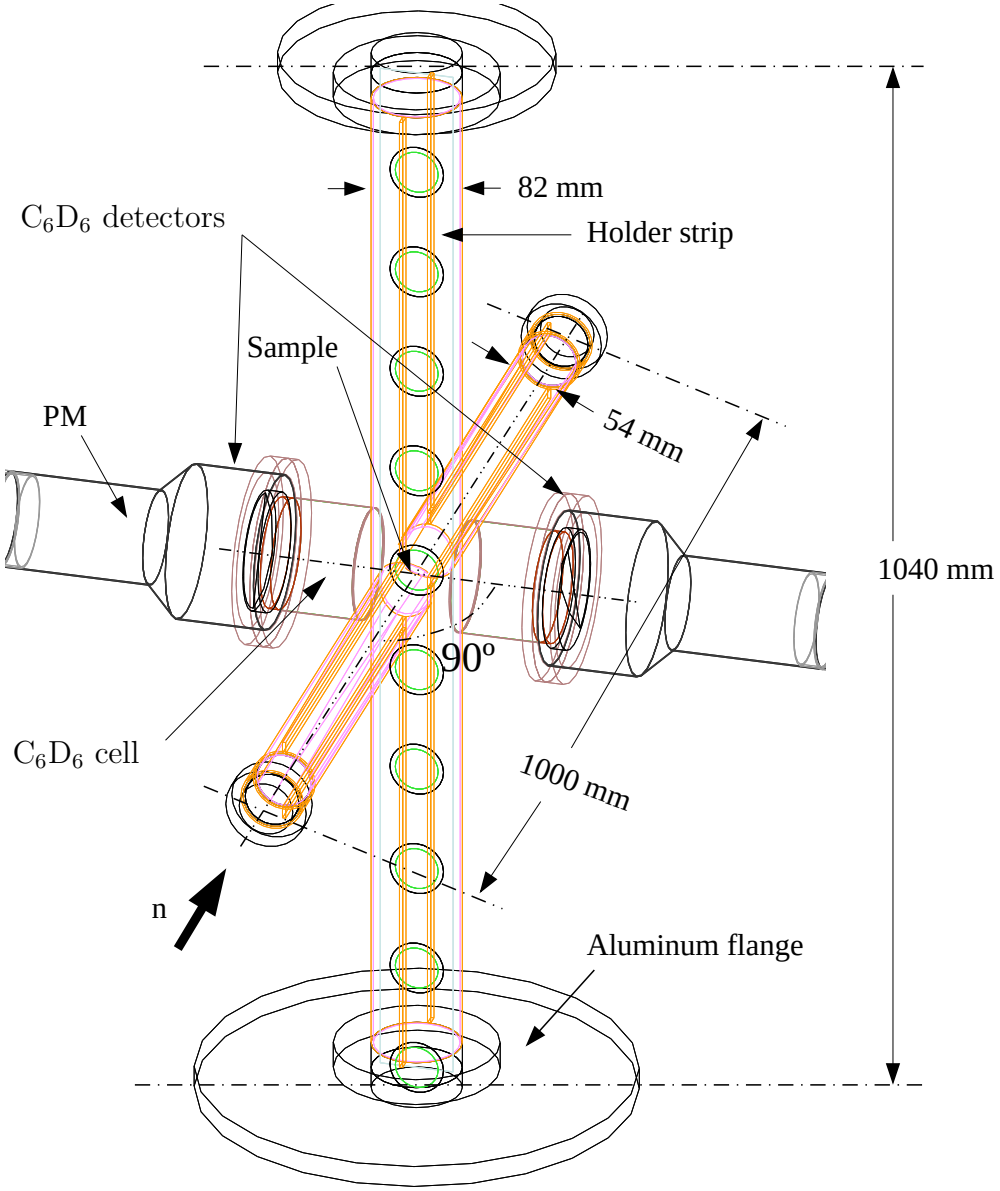

Figure 3.2: *Schematic view of the n_TOF (n,γ) experimental setup with the sample changer and two C_6D_6 detectors.*

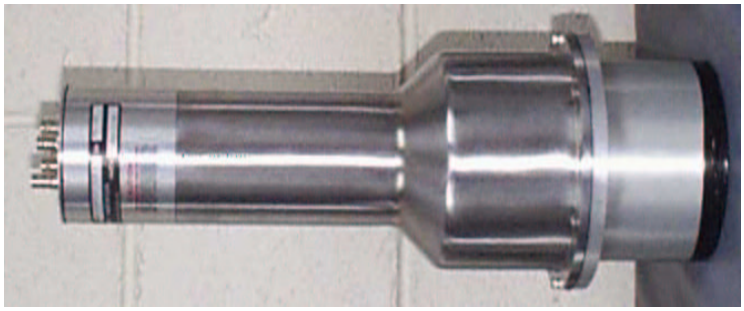

Figure 3.3: *Commercial Bicron C_6D_6 detector with improved neutron sensitivity.*

- Carbon fibre FZK-C_6D_6 detector. This is a handmade detector, designed and constructed at FZK[1]. An extreme reduction of materials has been adopted, resulting in a delicate but very light and improved detector. The detector

Figure 3.4: *Neutron sensitivity optimized C_6D_6 detector.*

(figure 3.4) consists basically of a carbon fibre cylinder, which contains approximately 1 L of C_6D_6, coupled to the window of an EMI 9823QKA photomultiplier tube.

It does not have the conventional quartz window between scintillation liquid and PM window, which is the main source of captured neutrons from E_n ∼20 keV upwards. The aluminum housing is also not present and only a μ-metal cylindrical cover (not shown in the picture of figure 3.4) surrounds the PM-tube during the measurement in order to reduce the influence of magnetic fields.

[1]Forschungszentrum Karlsruhe, Germany.

3.2.2 Sample changer

The sample whose (n,γ) cross section is going to be measured, is glued on thin mylar foil, which is attached by means of a light carbon fibre frame to a sample holder strip made also from carbon fibre (figure 3.2). Any of the ten samples in the holder can be placed in beam by remote control, thus avoiding to break the vacuum between measurements. The holder strip is placed inside the vertical tube of the sample changer, which is made also from carbon fibre. At each extreme of the sample changer cross is a piece of aluminum (top and bottom flanges and right and left rings), but all of them subtend a small solid angle from the sample (see figure 3.2).

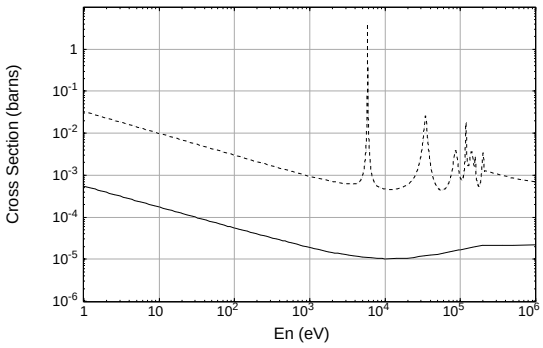

Figure 3.5: *Comparative plot of the (n,γ) cross sections of ^{27}Al (dashed curve) and ^{12}C (solid line).*

The reason to substitute any conventional aluminum component by carbon fibre is because the (n,γ) cross section of Carbon is more than one order of magnitude lower than that of aluminum, which shows also some strong resonances in the keV region, as can be observed in figure 3.5.

However, the carbon fibres are glued together with a commercial resine, whose composition was not available. The glue may have some elements with an undesired high neutron capture cross section which should be avoided. In order to obtain a quantitative composition of the carbon fibre, an R.B.S. analysis of the material was carried out. A detailed description can be found in reference [37]. The result of this analysis is summarized in table 3.1. The material with highest neutron capture cross section is Bromide, however it amounts to less than 1%.

Element	Atomic abundance (%)
C	83.76
O	8.4
N	6.7
Ca	0.5
Br	0.67

Table 3.1: *RBS determined composition of the carbon fibre.*

3.2.3 Neutron flux monitor

The time integrated neutron fluence is necessary in order to perform a relative normalization between two measurements done at different times.

In principle, this relative normalization could be carried out by utilizing the information of the calibrated Wall Current Monitor (see section 3.1), recording the total number of protons impinging on the lead spallation target. However, a more reliable monitoring of the neutron flux can be performed by using a neutron flux monitor [39] mounted in the neutron beam line, at a small distance from the sample.

The flux monitor used at n_TOF consists of a small mass device designed to be as less interferent as possible with the neutron beam and with scattered neutrons. The detection mechanism is based on the ^{6}Li(n,α)^{3}H reaction, detecting the outgoing triton and alpha particles by means of four silicon detectors placed off the beam but covering a high solid angle. A transversal view is shown on the left part of figure 3.6.

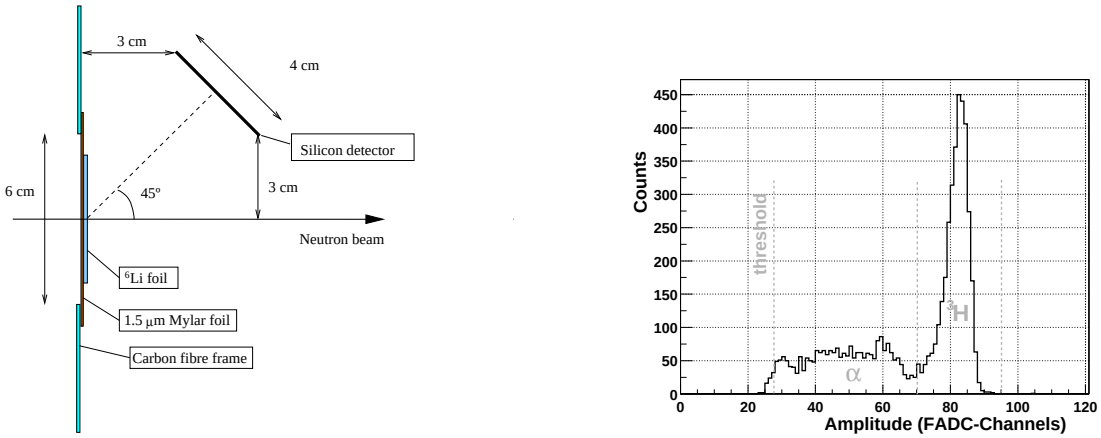

Figure 3.6: *(Left) Schematic view of the flux monitor. (Right) Typical observed Si-detector spectrum, where the triton peak can be clearly identified at higher energy.*

The $200\mu g/cm^2$ thickness chosen for the ^{6}Li deposit corresponds to a compromise between the need of a high count-rate and good resolution to clearly separate the triton's peak, as shown in the right part of figure 3.6.

A further minimization of the background due to scattered neutrons is achieved by constructing the vacuum chamber hosting the device in carbon fibre.

Using the ^{6}Li(n,α)^{3}H reaction cross section and its angular distribution, it was possible to determine the absolute neutron flux at the position of the silicon monitor. The result of this flux determination is in good agreement with dedicated flux measurement as will be shown later in section 4.5.

3.3 Data processing system

The pulsed PS proton beam used for the production of neutrons at n_TOF, has permitted the design and implementation of a zero deadtime acquisition system [38]. A flow diagram of the whole acquisition process is shown in figure 3.7.

The DAQ is based on the use of Flash Analog to Digital Converter (FADC) modules, which record the digitized detector pulses for each event or neutron bunch. The main difficulty of this acquisition procedure is the very large amount of accumulated data, thus requiring high storage capabilities and transfer rate.

Most of the front-end electronics (preamplifiers, time and energy amplifiers, ADCs, etc) are no longer needed and the relevant quantities like signal amplitude, time of flight, etc are extracted by means of an offline pulse shape analysis. The recording of all detector signals also allows to reprocess afterwards the whole experiment with minimum loss of information, enabling us to check for systematic uncertainties related with detectors performance during each run. Experimental effects like pileup, baseline fluctuations and noise can be effectively treated during the pulse shape analysis as shown in section 3.3.2.

3.3.1 Raw data acquisition system

The FADC modules available for these experiments had a resolution of 8 bit per channel, a buffer memory of 8 MByte per channel and a sampling rate capability between 100 MHz and 2 GHz. Each FADC module has either 4 or 8 channels and corresponds to one *data stream*.

The anode signal of each C_6D_6 detector was directly plugged into a channel of one FADC module. In the case of the flux monitor, the charge produced in each silicon detector is collected by a preamplifier and shaped by a Fast Timing Amplifier. The outgoing signal was then plugged into one FADC channel for each silicon detector.

When a proton bunch impinges onto the lead target, the pickup signal induced in the Wall Current Monitor (WCM), appropriately delayed, is used to trigger all the FADC modules. Then, data at a rate of 500 MHz are acquired for the C_6D_6 FADC channels until the 8 MByte buffer-memory has been filled 16 ms later. This fixes a time of flight window which ranges from the very energetic neutrons down to 0.7 eV neutrons. Lower neutron energies can be also studied by lowering the sampling rate or increasing the trigger delay. The silicon detector FADC channels are operated at a lower rate of 200 MHz.

The beginning of the movie of pulses is shown in figure 3.8 for each C_6D_6 detector. The first particles arriving to the experimental area are gamma rays and relativistic particles, produced also in the spallation process. They are what we call *Flash*. The time tagged as t_{Flash} in figure 3.8 corresponds to the time needed by a gamma-ray to fly through the 185 m distance between the lead target and the C_6D_6 detectors, i.e., 0.617 μs. The sharp Flash edge is therefore an accurate and absolute time reference for the rest of pulses in each 16 ms movie.

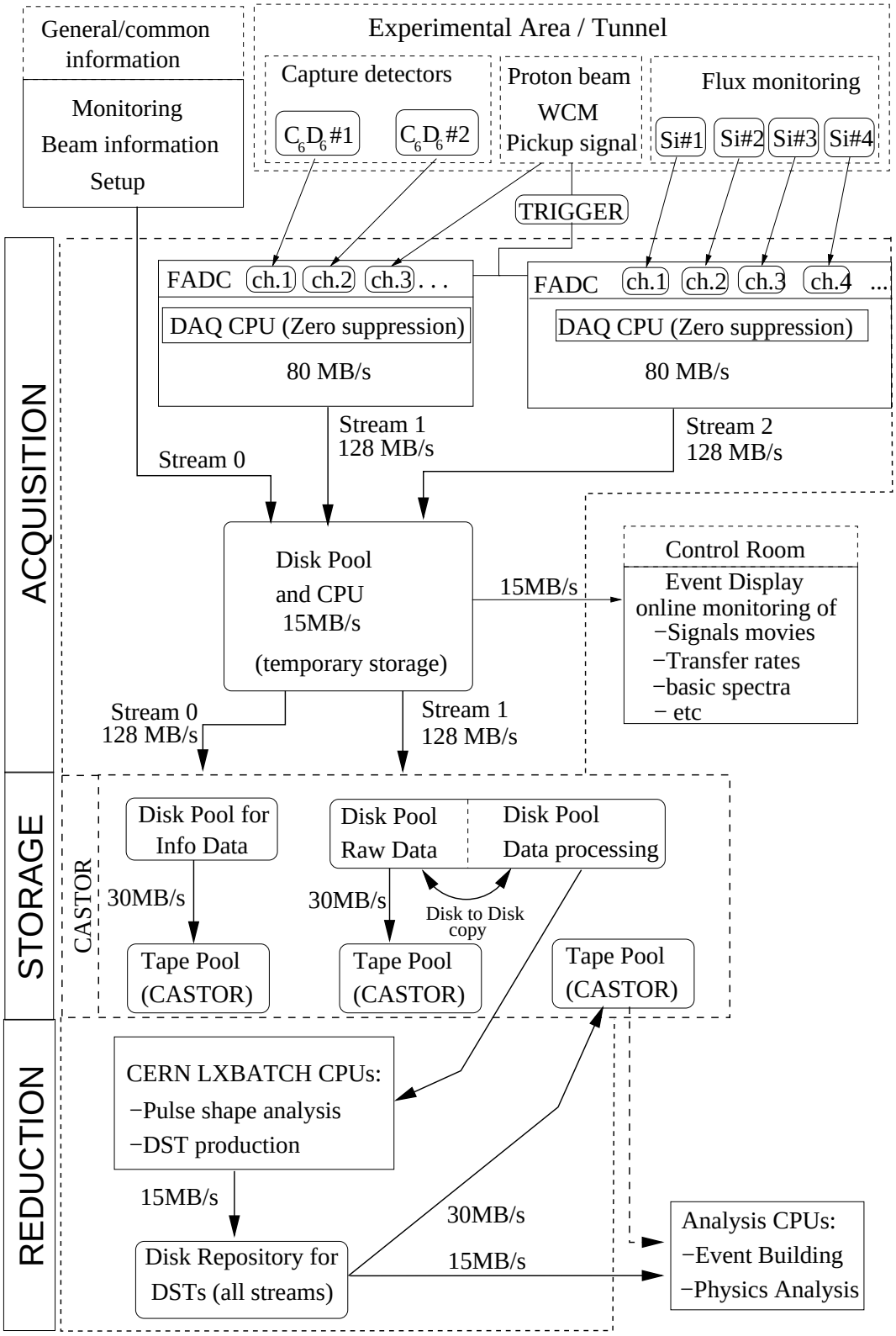

Figure 3.7: *Flow diagram of the data acquisition, storage and sort systems.*

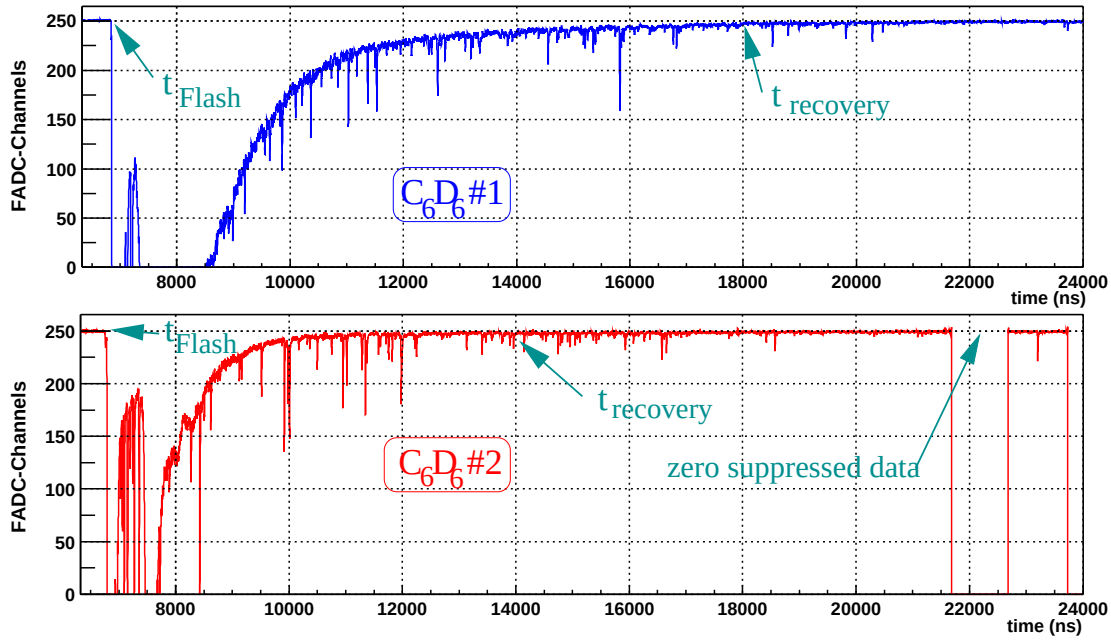

Figure 3.8: *First 24 μs of the movie of pulses for C_6D_6#1 (top) and for C_6D_6#2 (bottom).*

But the Flash saturates the C_6D_6 detectors, which need a considerable time interval to recover ($t_{recovery}$). This determines the highest neutron energy that can be used in capture experiments with this type of detectors. The value of $t_{recovery}$ depends mainly on the intensity of the proton bunch, but also on the gain of the detectors. It becomes also slightly different for each detector, as it can be observed in figure 3.8. The largest recovery time occurs in dedicated pulses of 7×10^{12} protons and is usually of about 14-15 μs, which corresponds to a top neutron energy limit of about 1 MeV.

Each *data stream* is coupled to one readout PC (figure 3.7), where a zero suppression algorithm prevents the storage of useless information corresponding to time intervals where no signal crossed a certain threshold value. This effect can be observed in figure 3.8, at a time of flight of about 22 μs in C_6D_6#2.

Along the signals buffer of 16 ms, each pulse is saved with a given number of presamples and postsamples (usually 256). This is a useful information for the pulse shape analysis routine in order to fit a pattern signal or extract the relevant parameters as baseline level, amplitude, area, etc. This will be explained in more detail in subsequent sections.

The zero suppressed data buffers are then transfered via GigaBit ethernet to a disk pool (see figure 3.7). This temporary storage is used for two different issues. *i*) Online monitoring of the experiment. Using a dedicated software called *Event-Display* the movie of signals of each FADC channel or detector can be visualized on

a PC at the Control Room or elsewhere. This is a very useful tool, since permits to check online the performance of each detector during the whole experiment and detect systematic errors, like incorrect triggering or artifacts in the proton beam structure. Moreover, basic histograming can be also made at the same time, which allows for a permanent control of the current count rate or statistics in the measurement and other relevant effects like backgrounds, baseline and gain shifts in the detectors, etc. *ii*) The zero suppressed data is also sent from this second disk pool to the CASTOR mass storage system for permanent storage (see figure 3.7), by using the Central Data Recording (CDR) system of CERN. CASTOR handles files of a minimum size of 2 GByte, therefore this size was also adopted for the n_TOF data acquisition system (DAQ) as maximum data file size in order to minimize data losses due to occasional file corruption.

3.3.2 Raw data sort system

The data sort consists of extracting the useful information for analysis, from the zero suppressed raw data. The zero suppressed raw data are the movies of pulses for each detector and for all the events or bunches accumulated for an experiment, which have been saved in tape. The useful information for analysis are a list of predefined quantities for each detector type, which have to be determined for each recorded pulse, as amplitude, time of flight, area, etc. This list is what we call Data Summary Tape (DST).

For this purpose a program was written in C, which access the required tape information at CASTOR via `rfio` (Remote File Input/Output) protocols. Once the information is accessed, this program allocates memory dynamically to hold the raw data. This is possible because the raw zero suppressed data has been recorded by the DAQ following a logical record based on an internal structure of headers called BOS Banks [39]. A generic description of a BOS Bank is shown in table 3.2.

offset	size (bytes)	type	content
0	4	4 char	bank name
4	4	int	revision number
8	4	int	reserved
12	4	int	number of data words following
16	1	byte	data
17	1	byte	data
⋮	⋮	⋮	⋮

Table 3.2: *General definition of a BOS Bank.*

With this logical record format, each zero suppressed raw data file starts with a *run header* (RCTR bank), which contains the run information like run number, segment number, time start of the run, date, comments, etc. Then, a *module header*

(MODH bank) follows for each flash ADC channel, where the general information of this channel is stored: chassis number, module number, channel number, sample rate, threshold, presamples, postsamples, etc. Finally, an *event header* (EVEH bank) contains each event's zero suppressed data for the flash ADC channel specified by the preceding module header. The last two modules are repeated as many times as needed, depending on the number of flash ADC channels acquiring data and events in the same run.

The fourth entry of each header (table 3.2) specifies the volume of data which follows, thus enabling an effective memory allocation for each event.

At this stage, a data sort program can be run to perform a pulse shape analysis routine over each detector signal's buffer and returns the predefined list of parameters for each detector, which are saved as the DST. The DST are recorded as permanent backup in tape, but they are also saved into a disk repository (see figure 3.7), which permits to have a faster access to this information during the data analysis.

For the C_6D_6 detectors and the Silicon monitor, two different pulse shape analysis routines have been developed. They are described in the two following subsections.

Pulse shape analysis routine I

This routine is based on a derivative procedure in order to find the *start time* of each pulse. To do this, the statistical fluctuations are smoothed by rebinning the signal. The derivative is then calculated and the *start time* determined by the time, at which this derivative is negative and its absolute value higher than a given empirical constant value.

Once the time of flight corresponding to the start of the signal has been determined, the level of the *baseline* is computed as the average of all the presample values. At the same time, the *baseline fluctuation* (RMS) is calculated.

The absolute minimum value of the signal determines the *peak time*. The *amplitude* of the signal is calculated as the difference between the baseline calculated before and the signal value at the absolute minimum or peak time.

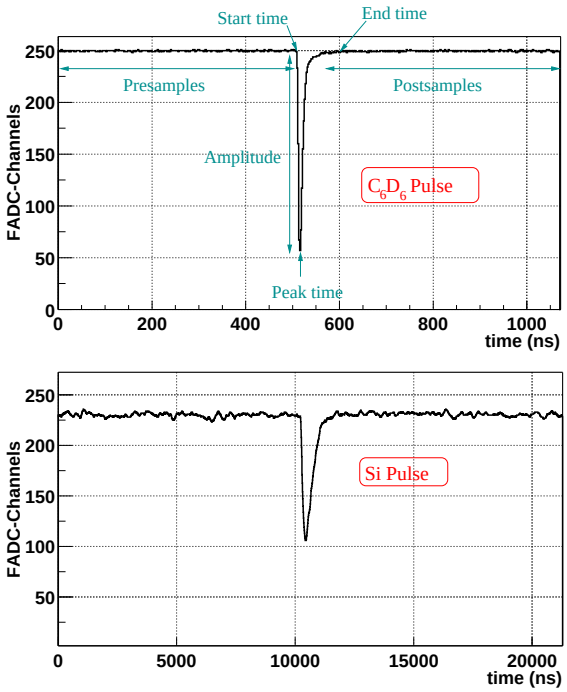

Figure 3.9: *Pulse of a C_6D_6 detector (top) and a Si detector (bottom).*

The *end time* of the pulse is given by the time, at which the derivative reaches again the value of the baseline plus its RMS

fluctuation. Finding this parameter, specific checks are made in order to *i*) detect a pileup (defined as a second pulse occuring within 100 ns after the start time of the first pulse), or *ii*) detect if the pulse has an extension longer than usual, tagging it as a *long peak*.

Once the pulse baseline and inflection points have been determined, the area of the first 16 ns and the total area (64 ns) of the pulse can be computed by integrating the signal.

An example of the information saved in the DST is given below in table 3.3. The first 3 entries are integers and correspond to detector number, segment number and event (bunch) number inside this file or run. The next 2 float entries stand for the proton intensity and the accumulated proton intensity (in the present run). They are saved from the slow control or stream 0 (figure 3.7). The following 5 float entries are finally those extrated by the pulse shape analysis routine. They are the amplitude of the signal, the level of the baseline, fluctuation of the baseline (RMS), area of the first 16 ns of the signal, total area of the signal, start time, peak time, end time, number of peaks in the same threshold-trigger, number of pileups, flag to tag peaks which extend longer than 100 ns and threshold used in the analysis (whose minimum value is the electronic threshold level set in the corresponding flash ADC channel for the zero suppression algorithm).

Detector Number	Segment Number	Event Number	PS intensity	Acc. intensity	Amplitude	Baseline	Baseline fluc.	Rise Area	Total Area	Start Time (ns)	Peak Time (ns)	End Time (ns)	Number of Peaks	Pileup Order	Long Peak	Threshold
... 67	... 0	... 1	... 5.8E12	... 5.8E12	... 160.23	... 252.23	... 0.42	... 844.0	... 4711.5	... 3948	... 3954	... 4138	... 1	... 2	... 1	... 250
68	0	1	5.8E12	5.8E12	90.4	252.3	0.52	476.1	2658.1	4021	4026	4210	1	2	1	250
...	...	...	...	...	...	...	...	...	...	...	...	...	...	...	...	...

Table 3.3: *Parameters extracted by the pulse shape analysis routine I, as they are saved in the DST.*

Only some of the variables extracted by the pulse analysis routine are needed for posterior analysis. In the case of the silicon detectors, only the time of flight of the pulse and the amplitude were necessary in order to derive the neutron flux and fluence.

In the case of the C_6D_6, this routine was also able to extract the information needed for analysis. However, a more accurate determination of the signal characteristics was achieved with the pulse shape routine described in the following section.

Pulse shape analysis routine II

This algorithm [40] is based on the fitting of a pattern to each signal. The pattern has been obtained by averaging a large number of signals. Since each detector has a slightly different pulse shape, a different pattern was determined for each C_6D_6 detector.

A polynomial fit of the baseline, permits the reconstruction of pulses at higher energy in the region affected by the flash. Moreover, an specific algorithm is included in order to accurately detect if the Flash is present in the movie and to tag its time, which is then used as time reference for the rest of pulses in the same event buffer. The detection of the Flash proves the arrival of the neutron bunch in the experimental area and that both C_6D_6 detectors have been properly triggered. In some cases, it may happen that there is a false trigger given by the WCM, but there is no beam coming into the sample. Such events are effectively rejected by setting the analysis condition that the flash must be present in both C_6D_6 detectors. Systematic artefacts or electronic reflexions due to the voltage divider can be now treated, since the whole accurate shape of the pulse is well defined in the pattern used for the fits. Figure 3.10 shows an accurate reconstruction of the complete signal of an FZK-C_6D_6 detector, including a systematic reflexion at about 500 ns after the main signal has occured.

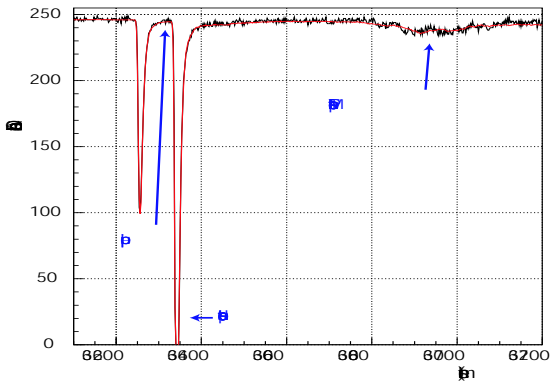

Figure 3.10: *Pileup of two signals being reconstructed by the pulse shape analysis routine.*

A more accurate determination of the pulse characteristics (time, amplitude, etc) is now achieved with the fitting procedure. As is shown in figure 3.10, pileups occuring 20 ns after the first pulse are effectively detected and reconstructed by this routine.

Saturated pulses are better reconstructed than with the previous pulse shape routine, since the pattern can still be fitted with less amount of data points defining the signal. However, the gain of the detectors has been adjusted in these measurements in order to not have any gamma ray of the capture cascade exceeding the FADC range of 256 channels. Hence, saturated pulses must correspond to cosmic rays and can be rejected afterwards in the analysis stage.

A list with the parameters extracted by this pulse shape analysis algorithm is

given in table 3.4. In the data analysis sections of posterior chapters (5, 6 and 7), we will refer to this table in order to describe the different cuts set for effective filtering of the raw information.

Parameter	Meaning
Order	Order of the polynomial baseline calculation
Baseline	Flag indicating successfull baseline fitting
Detector	Detector number
Saturation	Flag indicating if the pulse is saturated
Flash TOF	Time of Flight of the Flash
Tail Pulse TOF	Time of Flight for pulses sitting on the flash tail
Pulse TOF	Time of Flight of the pulse (ns)
Amplitude	Pulse Amplitude
Area	Total area of the pulse
Low Chi2	Lowest χ^2 of the pattern pulse fit
High Chi2	Highest value of the χ^2
Fast area	Integral of the signal during the first 16 ns
Slow area	Integral of the signal during its first 40 ns
Threshold	Internal largest threshold used by the algorithm for peak identification

Table 3.4: *Description of the parameters extracted by the pulse shape analysis routine II.*

Chapter 4

n_TOF raw capture data reduction

The reliable transformation of the raw measured count rate into experimental capture yield implies the knowledge of several elements related with the beam characteristics and the detection system. These experimental features have been carefully characterized at the n_TOF installation and they are briefly described in this chapter.

A detailed description of the data reduction process together with the study of the different uncertainties is also essential in order to allow evaluators construct the covariances matrix for an update of the existing information.

4.1 Experimental yield

The capture reaction yield is defined as the fraction of the neutron beam particles which undergoes a capture reaction in the sample. We call *data reduction* to the transformation of the registered number of counts into yield.

The raw number of counts registered in one measurement, N, can be written in the simplest form as a 2-tuple depending on the time of flight (t_{TOF}) and the pulse height (A) of each measured signal,

$$N = N(t_{\mathrm{TOF}}, A). \tag{4.1}$$

This 2-tuple can be built from the DST information as will be briefly described in section 4.2. In practice, it will depend also on many other parameters which will be a valuable information for the selection of "true" capture events. Indeed, one capture experiment lasts typically several days or weeks and different sources of systematic error, like drifts in the gain of the detectors or the electronics may arise. Therefore, the consistency between data corresponding to different proton bunches, detectors and runs has to be checked. These consistency tests are shown in section 4.2.1. This process of obtaining a collection of compatible data runs from the registered count rate is what we call *Event Building*.

Since we want to obtain the yield as a function of the neutron energy E_n, an accurate *time of flight calibration* has been carried out at n_TOF. This is shown in

section 4.3.

In order to express the measured number of counts as a function of the energy deposited in the C_6D_6 detectors rather than the pulse height A, the precise relationship between these two quantities is needed. This calibration becomes necessary for the posterior weighting of the count rate because the weighting function is obtained from simulations as a function of the deposited energy. The method employed to obtain an *energy and resolution calibration* of the liquid scintillator detectors is described in section 4.4.

With these two calibrations and after applying the consistency checks mentioned at the beginning, the clean number of counts can be written as the product of the capture yield Y, incoming number of neutrons N_n and detection efficiency ε,

$$N(E_n, E_{dep}) = Y \times N_n(E_n) \times \varepsilon(E_{dep}). \tag{4.2}$$

The neutron intensity dependence with the energy has been determined from two independent measurements, as it is explained in section 4.5. In general, N_n designates the time integrated neutron flux ϕ_n crossing a sample of a certain surface S,

$$N_n = \int_S \int \phi_n \, \mathrm{d}S \, \mathrm{d}t. \tag{4.3}$$

In equation 4.2, the dependency on the efficiency must be avoided since it means a cascade detection probability dependent on the actual deexcitation path. As it was described in detail in chapter 2, this can be effectively worked out by applying the PHWT,

$$N^w(E_n) = \sum_{E_{dep}} W(E_{dep}) \times N(E_n, E_{dep}). \tag{4.4}$$

The weighting function, $W(E_{dep})$, is in general different for each particular capture sample. This will be discussed in section 5.4. From equation 2.4, after the weighting process, the efficiency to detect a capture event becomes now equal to the energy of the cascade, $E_C = S_n + E_n$,

$$N^w(E_n) = \sum_{E_{dep}} W(E_{dep}) \times N(E_n, E_{dep}) = Y \times N_n(E_n) \times E_C(E_n). \tag{4.5}$$

If the count rate is high, it might be affected by pileup effects. The weighted count rate has been corrected in these cases following the procedure described in section 4.7.

From the last equation, the yield can be finally expressed as,

$$Y(E_n) = \frac{N^w(E_n)}{N_n(E_n) \times (S_n + E_n)}. \tag{4.6}$$

Nevertheless, the absolute value of the efficiency ε required for the calculation of $W(E_{dep})$ is not trivial to obtain since it depends on the exact positioning of the

detectors with respect to the samples and on the exact volume of scintillation liquid in each detector. Variations in these two quantities with respect to the simulated values would introduce only a proportionality constant in the simulated efficiency ($\alpha \neq 1$ in equation 2.4). Furthermore, the absolute value of the neutron flux is more difficult to obtain than just its relative dependence with the energy.

For the two reasons mentioned just above, the capture yield is always measured relative to a reference sample, as explained in section 4.6. This is the usual procedure to determine cross sections using the PHWT and it is usually based on the *saturated resonance method*. The corresponding correction factor will be denoted as f^{Sat}.

But there are two additional sources of systematic uncertainty which must be considered in the previous formula in order to determine the experimental yield reliably.

On one side, capture measurements are sometimes affected by a time of flight dependent background, due to the *neutron sensitivity* of the detection system. The corresponding correction, f^{ns}, for the resonances analyzed in this work will be discussed in section 4.8.

The second correction, $f^{t,s,ce}$, is mainly due to the loss of low energy counts below the threshold of the detectors and also, in less extent, to the summing of prompt gamma rays and the internal electron conversion process. The method that we have developed to account for these effects will be shown in the section 5.6 of next chapter.

The corrected yield, $Y'(E_n)$, can be finally calculated as,

$$Y'(E_n) = f^{ns} \times f^{t,s,ce} \times f^{Sat} \times Y(E_n). \tag{4.7}$$

Other experimental effects like self shielding and multiple neutron scattering in the sample, usually known as sample thickness effects, will be calculated with an appropriate code at the posterior stage of resonance analysis, as well as the Doppler broadening (see section 5.7.1 for a detailed description). The yield broadening due to the *resolution function* of the neutron beam will be also included in the final analysis of the resonances. However, for sake of simplicity, the n_TOF beam resolution function will be described in the section 4.9 of this chapter.

4.2 Event building

A software tool was written in order to access the DST, process the information, select "valid" events by applying specific cuts and save histogramed information for the posterior yield or cross section calculation and final analysis of it.

The C++ based analysis framework ROOT [41] was chosen for this purpose. The `TTree` class of this framework permitted the definition of an Event Class to hold the specific information of each detector type. Using `TTree` to store the information has the advantage of a very high compression level. The information is stored inside a `TTree` using a hierarchy of branches. Since each branch can be accessed and read

independently from any other branch, this further enhances the access speed. This event building software was written in the interpreted language ROOT-CINT [42].

Basically, the Event Building is performed in three stages, *i*) save the DST information as ROOT formated files of trees or *n*-tuples *ii*) cross checks between different detectors and *iii*) final data sort and histograming by applying definitive cuts.

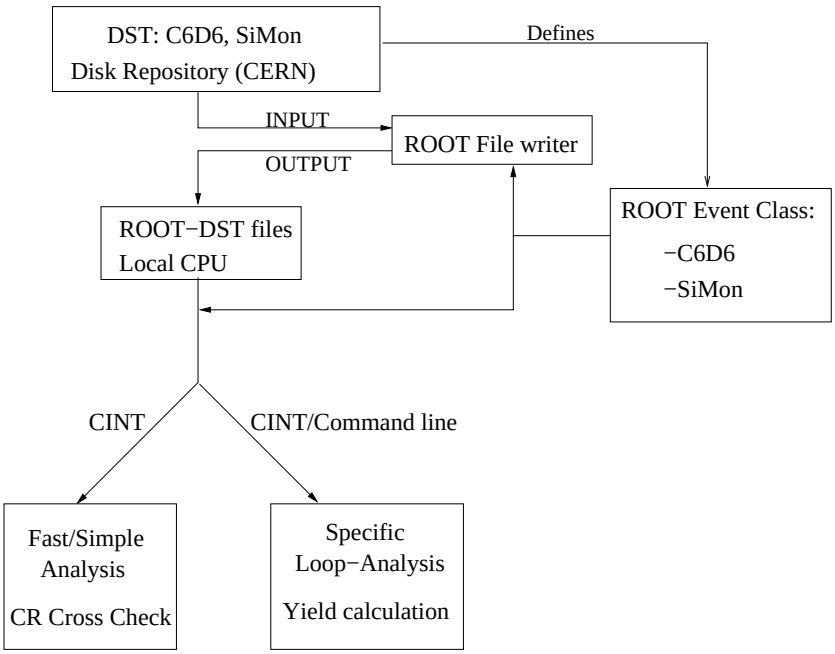

Figure 4.1: *Flow diagram of the final data reduction process for analysis.*

For the first capture measurements performed at n_TOF, described in chapter 5, only the pulse shape analysis routine I (section 3.3.2) was available. Hence, similar Event Classes were constructed for the silicon and the C_6D_6 detectors, provided both with the data members of the pulse shape analysis routine I (see table 3.3).

For the posterior measurements, chapters 6 and 7, the more accurate pulse shape analysis routine II (section 3.3.2) was written [40]. Therefore, a different Event Class was defined for the C_6D_6 detectors in order to hold and access the data members of this routine, which were shown in table 3.4.

4.2.1 Cross checks between detectors

The consistency between the count rates of the detectors involved in the capture measurements was systematically checked in order to exclude runs which are affected of certain systematic errors.

In order to compare better the count rates of the different detectors, it is convenient to apply some specific cuts in the data.

The counting of the C_6D_6 detectors (in these cross checks only) corresponds to neutron energies between 1 eV and 100 keV. This condition has been set to exclude the possibility of large baseline fluctuations in the high neutron energy region (or equivalently short time of flight) due to an intense Flash.

In the case of the silicon detectors only counts corresponding to neutrons with energies between 1 eV and 10 keV were accumulated in their count rate histograms. The range of amplitudes accepted corresponds to those belonging to the triton peak. This time of flight-amplitude window is shown in the right part of figure 4.2 for one of the detectors. The alpha particle signals were excluded in order to avoid the effect of the electronic threshold.

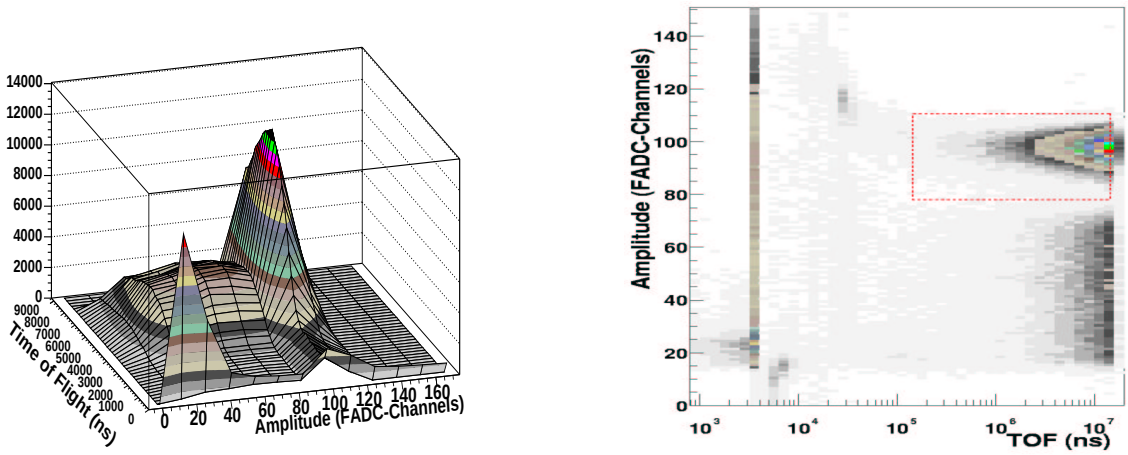

Figure 4.2: *(Left) Time of flight-amplitude distribution of a Si-detector. (Right) Time of flight-amplitude cut for selecting only counts in the triton peak and in a given neutron energy interval.*

In figure 4.3 the count rate of two FZK C_6D_6 and four silicon detectors during several runs is shown. For comparison, the proton intensity registered by the PS-Wall Current Monitor is also shown, scaled to the sum of all the Si-detectors (SiMon). In this example, a deposited energy threshold of 200 keV and 310 keV has been set respectively for C_6D_6#1 and C_6D_6#2. The higher count rate of detector C_6D_6#1 is due to its lower threshold level. However, the relevant information is that both detectors show a proportional counting along the events or measuring time.

The proportionality in the counting of the involved detectors is better shown in the bottom part of figure 4.3 by plotting the relative ratios. In this way, the adequate performance of the detectors involved in the capture experiment could be better controlled. Indeed, deviations of the proportionality between the count rates have been eventually experienced at n_TOF. Some of the situations causing a noticeable deviation in the counting rates are enumerated in the following.

i) Baseline drift. Since the threshold level is an absolute fixed value for each FADC channel, variations of the baseline level imply a different relative thresh-

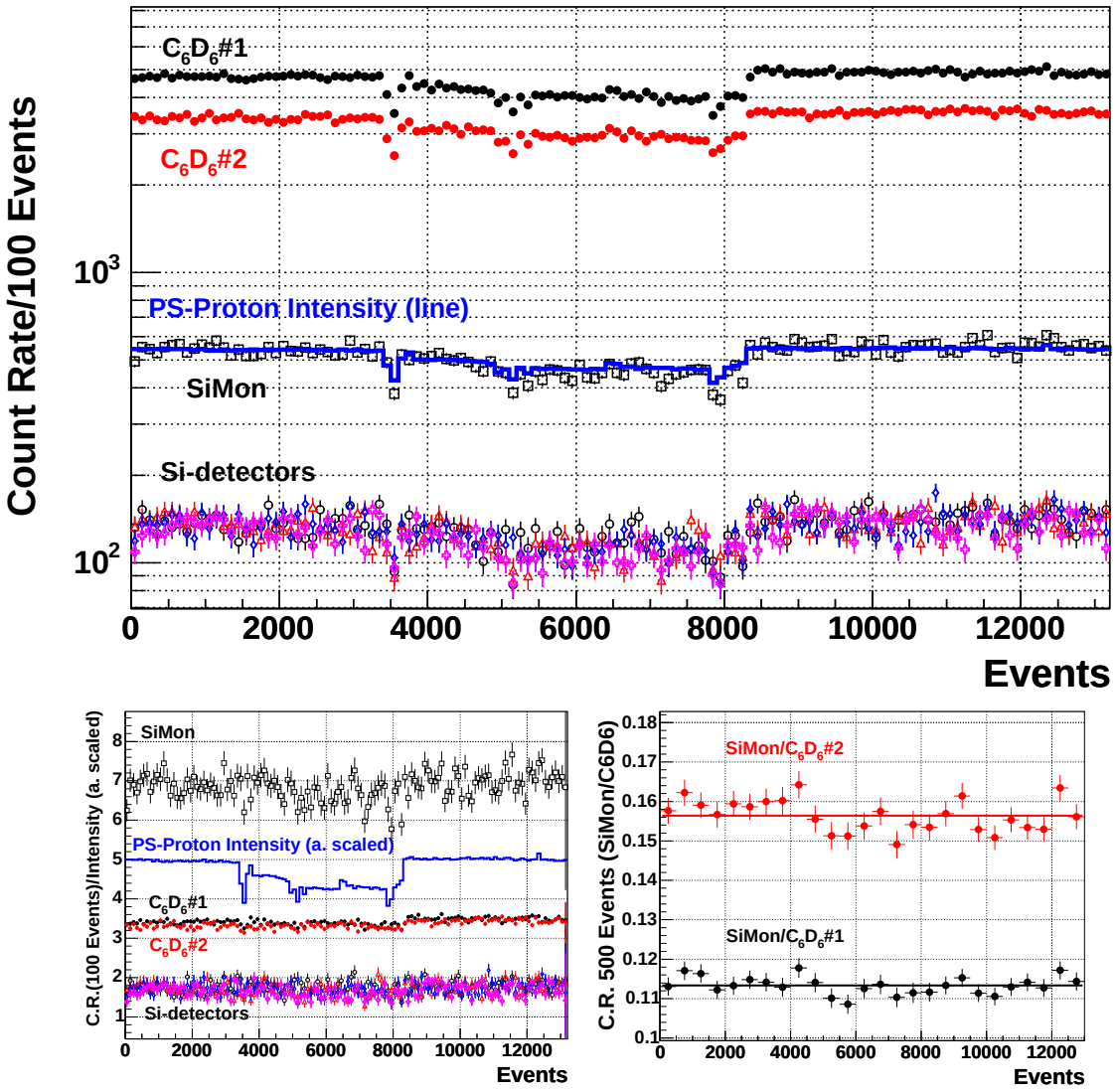

Figure 4.3: *(Top) Count rate of all detectors involved in the capture experiments. Open squares labelled with SiMon correspond to the sum of all the Si-detectors (open symbols below). (Bottom left) Ratio between the counting of the detectors and the PS-Intensity. (Bottom right) Ratio of the count rate between the Si-flux monitor and the C_6D_6 detectors. (See text for a detailed description).*

old level, which will be reflected as a change in the count rate of that particular channel.

ii) Accidental displacement of one C_6D_6 detector. If the geometry of the experimental setup suffers an accidental change, the geometric efficiency is modified and this is also reflected in the corresponding count rate. These runs can still be used performing an independent analysis of them.

iii) Possible electronic failure of a silicon detector or preamplifier. This effect is clearly noticed as a sudden suppression of the count rate of the corresponding silicon detector.

iv) False trigger. Eventually a proton intensity was read from the PS-WCM, although no proton bunch impinged on the lead target. Those cases could be clearly identified and excluded since the average count rate of all the detectors is due to ambient background and therefore is much lower than for the rest of "true" events.

The previous checks, permitted to identify systematic deviations arising in a relatively large time scale, i.e., along the PS-events or runs. However, specific errors may occur within one particular event or proton bunch. Therefore, some additional data sort conditions were required,

- Proton bunch intensity higher than zero. In some cases, the acquisition system was accidentally triggered by an external source. These kind of events, which do not correspond to a real proton bunch, have been successfully identified and rejected since there is no beam intensity recorded in the corresponding DST event.

- C_6D_6 detectors:

  – The Flash of gamma rays and relativistic particles must be present in both detectors at each event or proton bunch (see figure 3.8). This condition ensured the correct triggering of the two FADC channels were the C_6D_6 detectors were plugged in.

  – The time of the Flash, t_{Flash}, must be within a previously determined time window.

    As can be observed in figure 4.4, the time distribution of the Flash is different depending on the type of bunch (parasitic or dedicated), but in both cases it is a finite distribution. In some cases, an inadequate performance of the pulse shape algorithm may lead to a completely incorrect Flash time (out of this window). As the Flash serves as reference time for the rest of pulses, these type of events must be rejected.

    Since the trigger delay can change from one measurement to another, the time distribution of the Flash has to be histogramed for each run and the Flash time window appropriately adjusted prior to the final data sort.

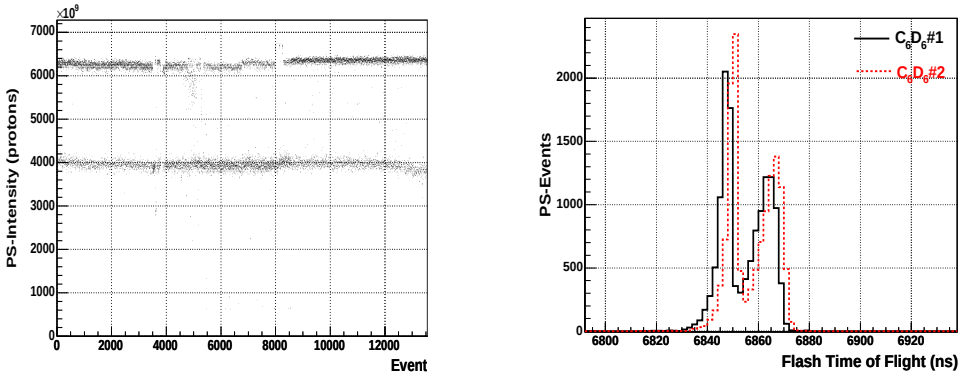

Figure 4.4: *(Left) PS-Proton intensity for dedicated and parasitic pulses.(Right) Flash time distribution of parasitic ($\bar{t}_{Flash} \approx 6847\ ns$) and dedicated ($\bar{t}_{Flash} \approx 6865\ ns$) events.*

- Low Threshold $< E_{dep}^{C_6D_6} <$ High Threshold.

  This condition is set for the final sort of the capture data. $E_{dep}^{C_6D_6}$ represents the energy deposited in each C_6D_6 detector. The Low Threshold value usually corresponds to the electronic threshold set in the FADC-modules for the zero suppression algorithm. The High Threshold value is set depending on the neutron separation energy S_n of the corresponding sample and the instrumental resolution of the detectors. It is used to exclude high energy signals, which are not related to the capture events, but to background or cosmic rays.

- Silicon flux monitor (SiMon):

  - This detector was systematically used for relative normalization of the neutron fluence between different measurements. The conditions for the final data sort correspond to those in signal amplitude and time of flight shown in figure 4.2.

4.3 Time of flight-neutron energy relation

In any time of flight experiment, one of the observables measured during the experiment is the time at which one event (neutron capture) occurs. This time is related with the energy of the neutron by means of the relationship,

$$E_n = \frac{1}{2} m_n v^2 = \left(\frac{72.2977 L}{t} \right)^2 , \tag{4.8}$$

where E_n is the non relativistic neutron energy (eV), L is the effective flight path (m) and t is the measured time of flight (μs).

The effective flight length L includes not only the geometrical distance between the neutron source and the sample, but also the moderation path followed by the neutron inside the lead block and the water moderator. Since the moderation process varies with the energy of the neutron, we have to take into account that the effective flight length depends also on E_n.

For convenience, L can be written as the sum of two terms,

$$L = L(E_n) = L_\circ + \Delta L(E_n) \tag{4.9}$$

where ΔL includes any dependence of the flight length on the neutron energy E_n, due to the moderation process. The constant term $L_\circ$ represents the geometrical distance between the outer face of the moderator and the sample but it includes also any constant term of the moderation distance.

The recursive dependence of the neutron energy E_n on itself is not a very practical situation from the computational point of view. However, it can be demonstrated [43] that in our case the addition of the ΔL energy-dependent term to the constant distance $L_\circ$ is equivalent to add a constant time offset, $t_\circ$, to the measured time of flight t,

$$E_n = \frac{1}{2} m_n v^2 = \left(\frac{72.2977 L_\circ}{t + t_\circ} \right)^2 . \tag{4.10}$$

Note that this equation is now much more practical than equation 4.8, since the recursive dependence on E_n is avoided.

In order to find the values of the calibration parameters $L_\circ$ and $t_\circ$, a set of standard resonances have been measured at n_TOF [43] as described in appendix A. From these measurements, the following values were obtained,

$$L_\circ = 185.20 \pm 0.01 \text{ m},$$

$$t_\circ = -68 \pm 13 \text{ ns}.$$

A summary of the measured resonances is given in table A.1. The average RMS deviation yields a calibration accuracy better than 0.01%.

4.4 Deposited energy and resolution calibration

A calibration which relates the area or amplitude of the registered signals with the energy deposited in the C_6D_6 cell of the radiation detectors is needed because the weighting function is obtained from a Monte Carlo simulation as a function of the deposited energy.

Furthermore, a resolution calibration is also necessary because the response functions obtained by Monte Carlo simulation have the zero width of an ideal detector. They need to be broadened with a realistic instrumental resolution (assumed Gaussian) in oder to obtain the weighting function.

The C_6D_6 detectors were calibrated using three different radioactive sources. ^{137}Cs, ^{60}Co and Pu/C-sources with gamma ray energies of 662 keV, 1.175 MeV & 1.33 MeV and 6.14 MeV respectively.

The deposited energy calibration was suppossed in general to depend linearly with the pulse height,

$$E_{dep} = a_0 + a_1 \times Amplitude, \tag{4.11}$$

although in some cases the energy range had to be divided in two subintervals with two different calibrations.

The instrumental resolution behaviour was found different depending on the type of detector. The commercial Bicron detectors were successfully fitted with a simple dependence on the energy,

$$\sigma^2 = b_0 E \tag{4.12}$$

with $b_0^{Bic.} = 6\ keV$, while the homemade carbon fibre C_6D_6 detectors needed an additional term,

$$\sigma^2 = b_0 E + b_1 E^2. \tag{4.13}$$

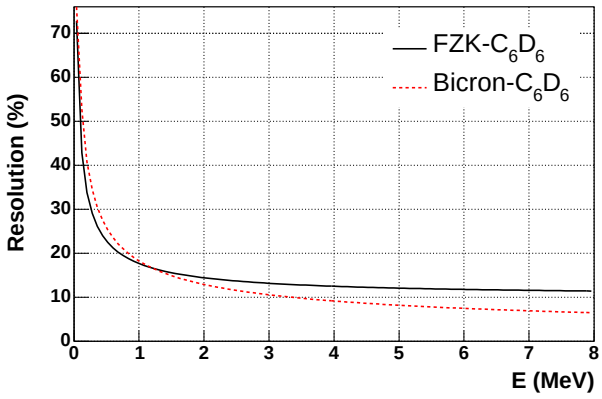

Figure 4.5: *Energy resolution of the two types of detector used in the capture measurements.*

with $b_0^{FZK} = 3.7469\ keV$ and $b_1^{FZK} = 1.8714 \times 10^{-3}$.

This resolution calibration was found to be independent of the gain of the detectors.

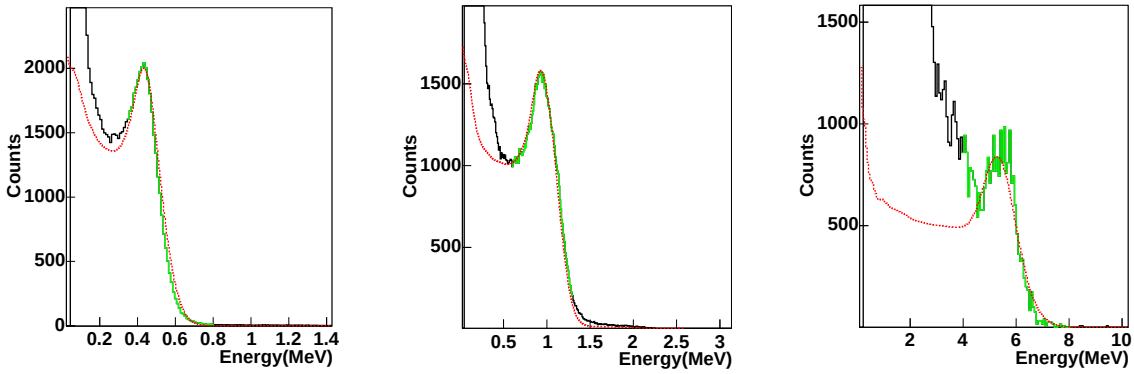

Figure 4.6: *From left to right: Cs, Co and Pu/C sources used for calibration.*

In figure 4.6 a general view of the calibration procedure is given. In order to accurately calculate the calibration coefficients, Monte Carlo simulations of the calibration setup were performed for each calibration source. The simulated deposited

energy histograms (dashed line) were recalibrated and convoluted in order to fit the measured spectra (solid line). The best coefficients (a_0, a_1, b_0 and b_1) were obtained by means of a simultaneous least squares fit. The part of the experimental histogram used in the least squares fit is shown in lighter colour. At the low energy region of these three spectra one can appreciate the exponentially decaying environmental background, which for sake of simplicity has not been included in the simulation. In the case of the Pu/C-source spectrum at lower energies contribute both, the environmental background and low energy gamma rays from the radioactive source itself.

The uncertainty introduced in the neutron capture experiment by the uncertainty in the energy and resolution calibration is practically negligible, as will be discussed in section 5.5 of the next chapter.

4.5 Neutron intensity

We will define the neutron intensity I_n as the number of neutrons per nominal PS-bunch (i.e., per 7×10^{12} protons). The dependence of I_n with the neutron energy has been determined from two independent measurements performed with the silicon flux monitor (section 3.2.3) and with the PTB-Chamber. The latter is described in the following subsection. The neutron intensity shape adopted in this work is showed below in subsection 4.5.1.

PTB[1]-Chamber[32]
It consists of a parallel plate chamber with fissile deposits of ^{235}U or ^{238}U, whose (n,f) cross sections are considered standard from 0.15 to 20 MeV and from 1-200 MeV respectively.

The detector has five platinum cathodes with the fissile material deposited on both sides, separated by 5 mm from tantalum anodes. The deposits have a diameter of 76 mm, thus wider than the neutron beam. When entering and exiting the chamber the beam crosses two tantalum windows too.

The measurement of the neutron intensity with this detector was performed in April 2001; a total number of 8.6×10^{17} protons were delivered by the PS in 155000 pulses with an average proton intensity of 5.5×10^{12} protons per pulse. A summary of the main parameters of this measurement is given in table 4.1.

Deposit	L_{TOF} (m)	Mass (mg)	Mass (μg/cm^2/plate)	Events
^{235}U	182.35	201.56(60)	444(18)	6.57×10^7
^{238}U	182.25	197.78(60)	436(18)	3.17×10^5

Table 4.1: *Relevant parameters of the neutron flux measurement at n_TOF with the PTB chamber.*

[1]PTB stands for Physikalisch-Technische Bundesanstalt Institut, Braunschweig, Germany.

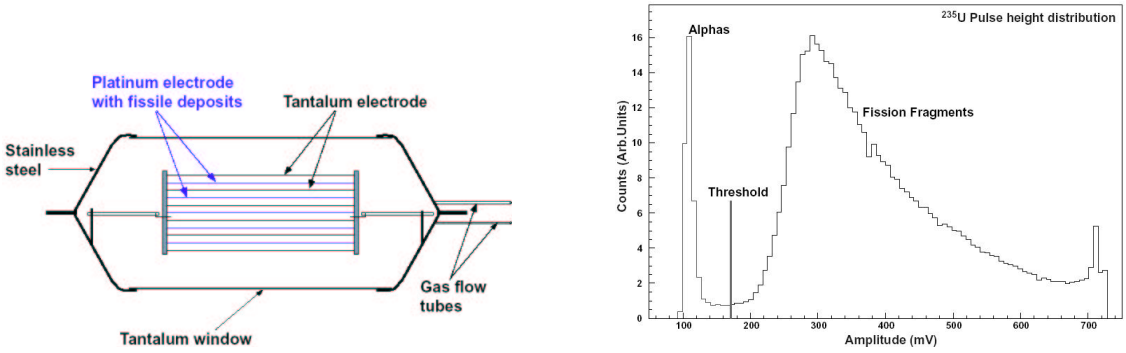

Figure 4.7: *(Left) Schematic view of the PTB chamber. (Right) Pulse height distribution in the fission chamber detector with the* ^{235}U *deposit.*

The neutron intensity as a function of the neutron energy was deduced from the measured fission yield, taking into account the corresponding cross sections and several corrections [46]. The obtained intensity will be shown in the following section.

4.5.1 Adopted neutron intensity

The two neutron intensity measurements available correspond to a silicon monitor (SiMon) measurement, based on the ^{6}Li(n,α)^{3}H reaction and to the PTB-measurement, described in the previous section. As can be observed in figure 4.8, the agreement between both data sets is good although there are evident systematic differences between both results.

The dip ocurring at 300 eV is due to absorption of neutrons in the manganese impurity of the aluminum alloy window crossed by the beam at the exit of the spallation target. However, it is visible only in the silicon data but not in the PTB measurement. The higher energy dips occuring at 6 keV, 30 keV and 80 keV are also due to transmission through the aluminum window, as was obtained from a calculation [47]. However, the dips in the PTB-data just above 10 keV may be real or not (only statistical fluctuations). They may be related to the oxygen, but the effect of the water moderator is more difficult to take into account in the calculations, since it is a source of moderated neutrons and a filter for fast neutrons.

The products of the ^{6}Li(n,α) reaction can be considered to have isotropic angular distribution up to about 1 keV. Above that energy, the angular distribution is not well known, and the silicon detectors curve looses accuracy.

For the reasons mentioned above, instead of fitting a parameterization to these two intensity measurements, the *best* pointwise intensity shape was adopted by weighting more one measurement or another, depending on the reliability of the data at a given neutron energy region. Proceeding in this way, we could overcome some systematic errors of each measurement, which would rather difficult the least squares approach.

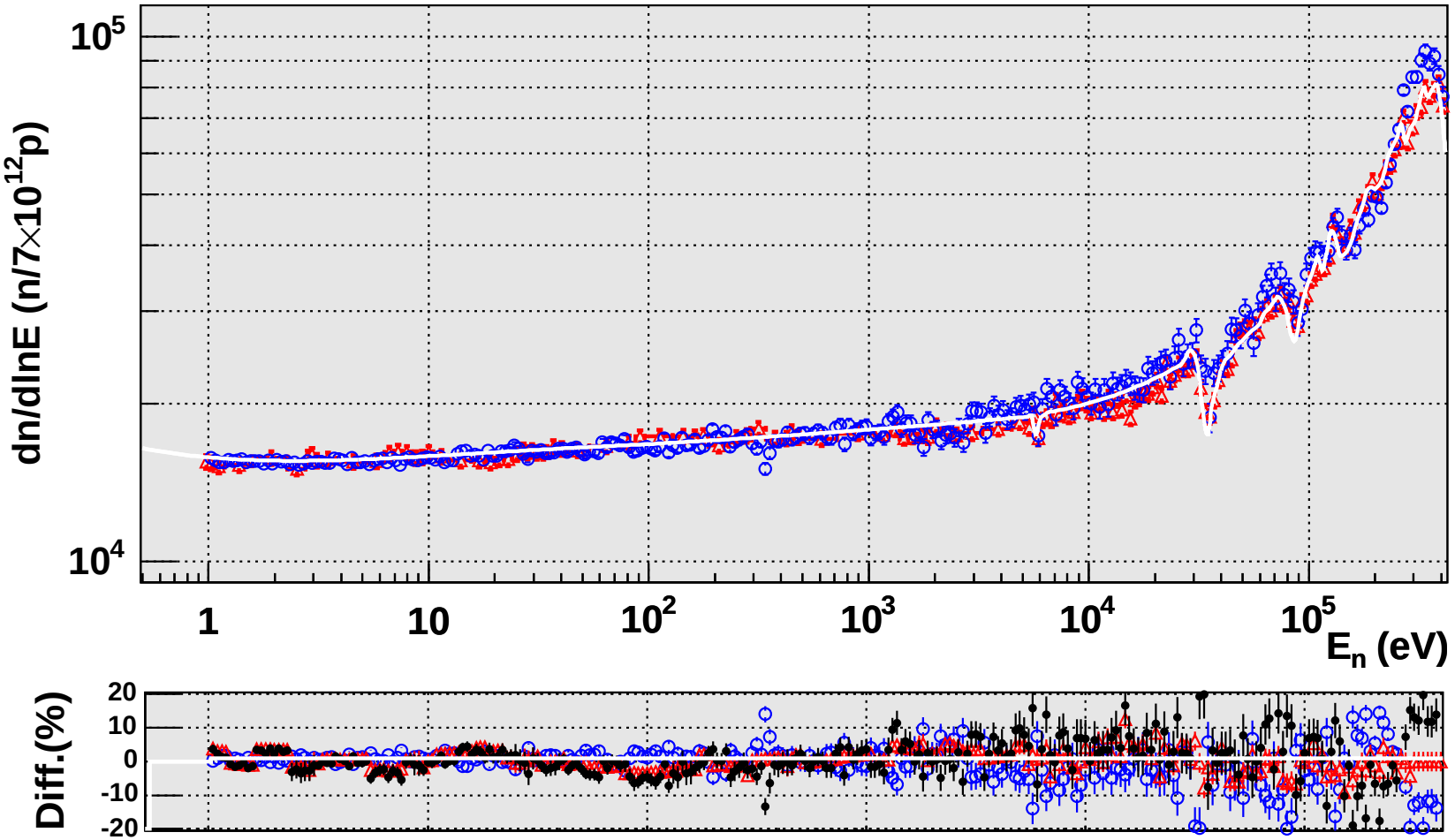

Figure 4.8: *Adopted neutron intensity (solid line) from several measurements (open circles correspond to the Si-flux monitor, open triangles stand for the PTB measurement). On the bottom pannel, relative differences with respect to the adopted intensity shape are shown for the two measurements. Solid symbols correspond to relative differences between both measurements.*

In the energy interval from 1 eV up to 1 keV, a smooth intensity-curve was averaged from both data sets following the formula $a \times E_n^b$. This parameterization does not fit at all the 300 eV dip, but that energy is completely unimportant for any analysis performed in this work and for sake of simplicity it was omitted in the fit. Beyond ∼200 keV only the PTB data was considered for the adopted intensity curve.

In order to estimate the systematic uncertainty of this intensity curve adopted for the capture measurements we have calculated the RMS differences between the SiMon and PTB measurements. Assuming that the adopted intensity is the best curve fitting both data sets, one could consider that its systematic uncertainty can be approximated by the RMS deviation of these two independent measurements. In figure 4.9 the RMS differences are shown versus the neutron energy.

Between 1 eV and 3 keV the uncertainty estimated by means of this approach lies below 2%. From 3 keV to 100 keV the RMS-deviation reises up to $\sim 3\%$, although this effect can be ascribed to angular distribution effects in the ^{6}Li(n,α) reaction, as was mentioned above. Beyond 100 keV, the neutron intensity and hence, its uncertainty, is determined only by the PTB-measurement. The latter measurement shows an uncertainty of $\pm 1.5\%$[32].

From these considerations, we have adopted a systematic uncertainty of 2% for the neutron intensity curve.

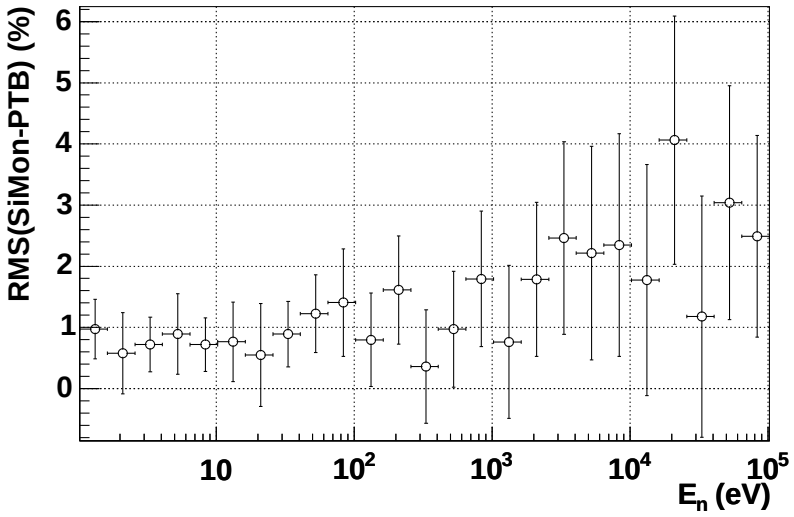

Figure 4.9: *RMS deviation between the SiMon and the PTB neutron flux measurements versus the neutron energy.*

4.6 Saturated resonance method

The determination of the capture yield (equation 4.6) depends on the detection efficiency ε and the neutron intensity I_n. But the absolute value of the simulated detection efficiency ε, unlike its relative dependence with the gamma ray energy, depends on several parameters whose exact values are difficult to keep under control such as, e.g., the volume of C_6D_6 liquid in the cells (which may vary with the temperature) and the relative distance between sample and detector. Furthermore, in the determination of the absolute neutron intensity, the analysis of the fission yield in the case of the PTB chamber or the ^{3}H products of the ^{6}Li(n,α) reaction for the silicon monitor, depends on the precise knowledge of cross sections, angular distributions and monitor efficiency.

Performing an inter-calibration measurement with respect to a well known resonance at a given energy $E_\circ$, one can avoid these uncertainties related to absolute intensity and efficiency values [48]. One usually chooses a reference sample of small thickness n (at/barn) with a resonance such that $\sigma \approx \sigma_\gamma$ and large $n\sigma$. Then, the yield at the resonance is saturated and it can be determined very accurately in the plateau region.

From equation 4.6, the experimentally determined yield for the reference resonance Y_{ref}^{exp} can be obtained as,

$$Y_{ref}^{exp}(E_n) = \frac{N_{ref}^{w}(E_n)}{N_n(E_n) \times (S_n^{ref} + E_n)}. \tag{4.14}$$

On the other side, the yield at this resonance can be precisely calculated Y_{ref}^{th} if its cross section is very well known and the sample is indeed thin (to avoid large thickness effects corrections). As the transmission is very small, the multiple scattering becomes the main source of loss neutrons. $Y_{ref}^{th}(E_n)$ must be therefore calculated with an appropriate code which accounts for those effects.

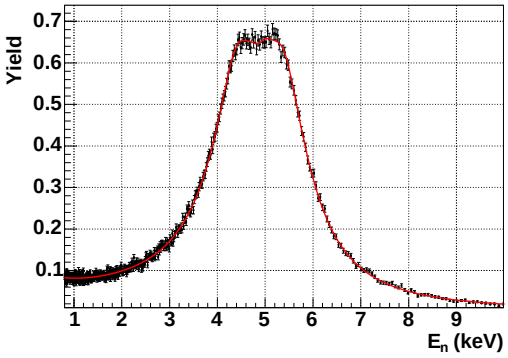

Figure 4.10: *4.9 eV ^{197}Au+n resonance used for inter calibration.*

An example of the reference resonance at 4.9 eV in ^{197}Au+n is shown in figure 4.10. The data points correspond to the experimental yield $Y_{ref}^{exp}(E_n)$. The solid line corresponds to a function with the form, $AY_{ref}^{th} + B$. The parameters A and B were fitted to have,

$$Y_{ref}^{exp}(E_n) = AY_{ref}^{th}(E_n) + B \;\rightarrow f^{Sat} = 1/A. \tag{4.15}$$

The calculated yield Y_{ref}^{th}, as well as the fit, were obtained with the SAMMY code [49], which will be described in more detail in section 5.7.

B is a constant term which accounts for the background. The value of the yield normalization constant, f^{Sat}, is given by the inverse of the fitted parameter A.

At n_TOF we have used different reference samples of ^{197}Au and ^{109}Ag which fulfill the requirements of high and well known peak cross section and small thickness.

Since the gold is monoisotopic, the pure Au sample was preferred for the yield calibration in the measurement of the ^{207}Pb and ^{209}Bi cross sections.

When the reference sample has a different diameter than the sample under study, the neutron beam profile is also needed in order to correct for the different flux seen by the sample in each case. The n_TOF neutron beam profile has been accurately determined by using dedicated neutron detectors as is shown in the subsection 4.6.1.

4.6.1 Beam profile

An accurate knowledge of the neutron beam profile at the sample position is necessary in order to compare between measurements of samples with different sizes.

The neutron beam profile at the n_TOF measuring station has been measured with the MicroMegas detector [50], based on the microstrip gas chamber (MSGC) technique. It consists of a gaseous detector, with two gaps: a first one of 3 mm where radiation produces ionization electrons, and a second thin (100 μm) amplification gap with printed strip-electrodes which collect the electrons from the avalanche. Both are separated by a 5 μm thick grid or micromesh.

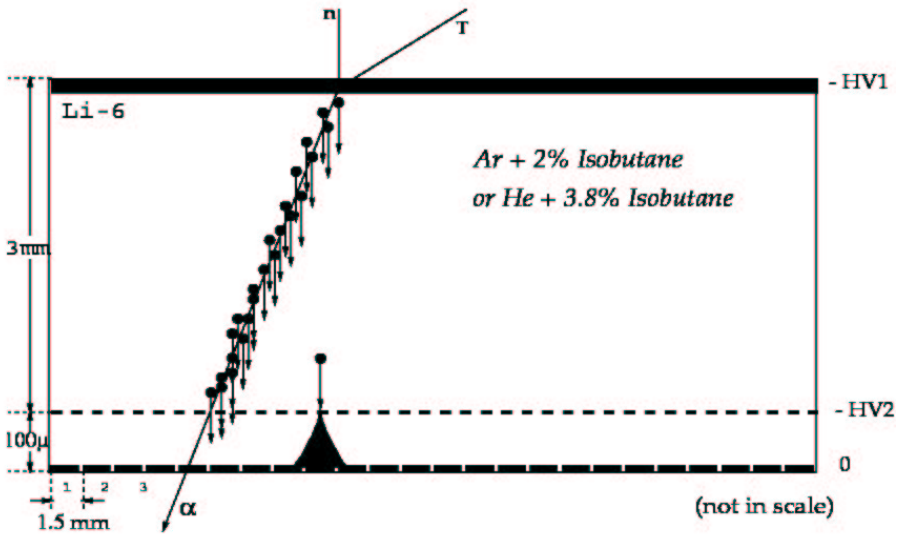

Figure 4.11: *Schematic view of MicroMegas, the 3 mm conversion gap and the amplification gap separated by the micromesh and the anode strip electrode.*

In order to operate the MicroMegas as a neutron beam profile detector at n_TOF, an appropriate neutron/charged particle converter must be employed which can be

either the filling gas of the detector or a deposited target on its entrance window. For neutron energies below 10 keV, the ^{6}Li(n,α)^{3}H reaction is used. Above that energy, the recoil due to elastic scattering of a neutron on a gas nucleus is detectable in addition to the tritons and alpha-particles.

At n_TOF, for the beam profile measurement, the gas filling the detector was He + C_4H_{10} (3.8%) or Ar + C_4H_{10} (2%). Only a small quantity of isobutane is permitted for safety reasons of flammability. The measurement lasted during one week and the acquisition rate was of about 100 signals per proton bunch with the detector placed at 186 m from the spallation source.

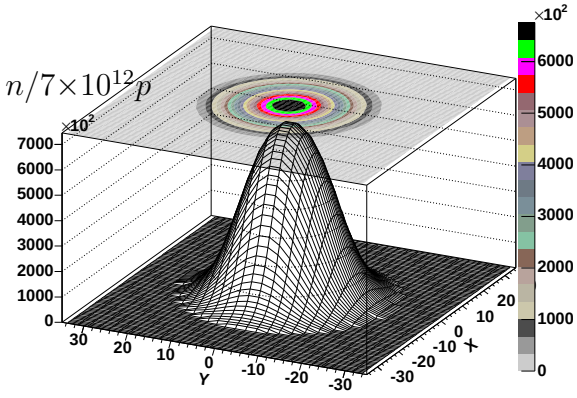

Figure 4.12: *Plot of the n_TOF beam profile [52] in the neutron energy range from 10 eV up to 100 eV.*

The projected beam profile was measured in the neutron energy interval from 10 eV to 20 MeV, with the strip-electrodes in horizontal position (vertical profile), 90° rotated (horizontal profile) and 30° rotated. From these measurements, a beam profile has been reconstructed [51]. At the distance of the capture measurements, 185.2 m, the beam profile was extrapolated by combining the information of the MicroMegas measurement at 186 m with that from the n_TOF neutron beam simulations [53]. The obtained value of the beam diameter at the capture sample position is of 4 cm and has an approximate Gaussian shape with σ =7 mm, slightly off centered in the horizontal direction, $\Delta_x = 1.5\ mm$.

A detailed description of the analytical approximation used to fit the beam profile can be found in appendix B.

4.7 Pileup corrections

We call pileup to the experimental situation where two signals occur within a given time interval, τ, in which they can not be distinguished as two independent pulses by the corresponding pulse shape analysis routine and are treated as a single pulse.

The time τ corresponds therefore to a blindness period related with the pulse shape analysis routine, and can be treated as a dead time.

As shown in figure 4.13, one should distinguish between paralyzable and non paralyzable systems. In the first case, the arrival of a second event during a dead time period extends this period by adding on its dead time τ starting from the moment of its arrival. If the system would not be sensitive during the dead time,

non paralyzable, the arrival of a second signal during the dead period τ would not be noticed and after a time τ the system becomes active again.

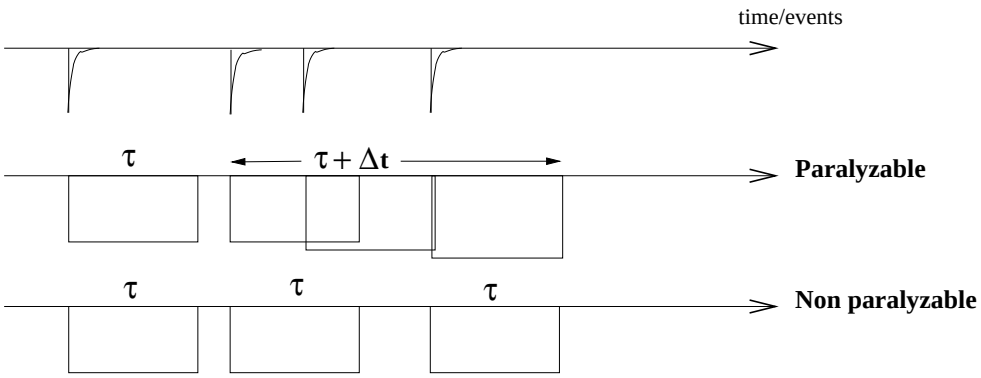

Figure 4.13: *Schematic representation of the two types of dead time systems.*

In figure 4.14 the time between each two consecutive pulses is shown for a capture measurement with low count rate (left part) and for another measurement with much higher count rate (right part). A time gap of $\tau \approx$18-28 ns can be observed between consecutive pulses. As was mentioned before, this time gap, similar to the dead time of a detection system, is related with the inability of the pulse shape analysis algorithm to identify two pulses which are too close with each other.

The pulse shape analysis algorithm behaves as a paralyzable system. Indeed, the non sharp drop at ∼20 ns indicates the extendable dead time $\tau + \Delta t$.

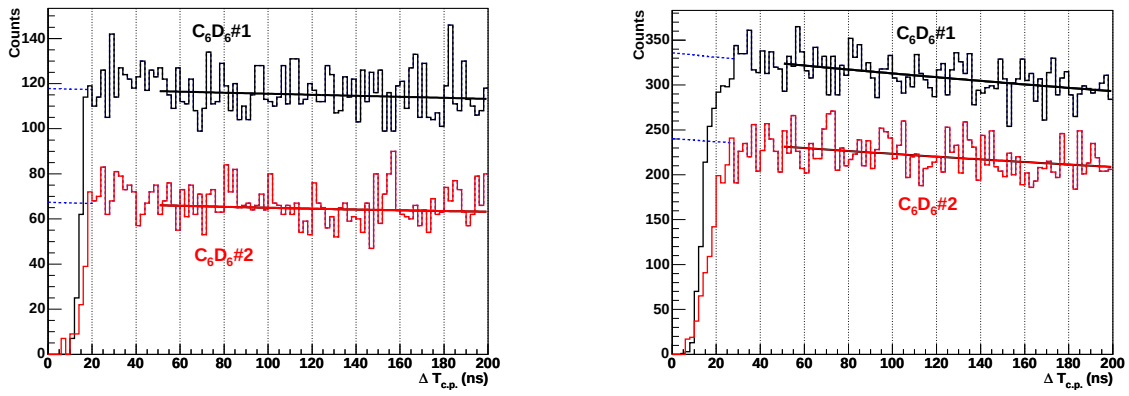

Figure 4.14: *Time distribution of each two consecutive pulses for a measurement with low pileup rate (left) and for another with higher pileup (right). The solid line corresponds to a polynomial fit in order to extrapolate the counts lost below τ (dashed line).*

In order to express the correction factor, let us define
m' = true count rate.
m = measured experimental counts in time T.
τ = "dead time" engendrated by each registered count.

In a paralyzable system, the true count rate m' must be solved numerically from the equation [54],

$$m = m'Te^{-m'\tau}. \tag{4.16}$$

This rather complicates the pileup correction. Nevertheless, it can be demonstrated [54] that if the pileup correction is small, it is approximately the same correction for both paralyzable and non paralyzable systems,

$$f^{Pileup}_{Paralyzable} \approx f^{Pileup}_{NonParalyzable}. \tag{4.17}$$

The correction to apply in a paralyzable system is simpler to calculate. During a measuring time T, a total number of $m'm\tau$ counts are lost in a non paralyzable system, so that the true number of counts registered during the time T would be:

$$m'T = m + m'm\tau \quad \rightarrow \quad m' = \frac{m/T}{1 - \tau m/T}. \tag{4.18}$$

Experimentally we have i-binned neutron energy or time of flight histograms. The N_i counts in the bin i can be corrected as,

$$N'_i = \frac{N_i}{1 - \tau N_i} = f_i^{Pileup} N_i, \tag{4.19}$$

where the count rate N_i can be expressed as counts per second, counts per proton bunch, etc. For practical reasons we prefer to perform this correction after the weighting of the histograms. As is demonstrated below, the correction to apply in that case will be the same.

In a weighted histogram, the number of counts at each bin i has been set as:

$$N^w_i = \sum_j w_j N^j_i \tag{4.20}$$

where the index j stands now for the pulse height or deposited energy. Let's consider now the true number of counts for signals of a given amplitude j,

$$m'^j T = m^j + m'^j m\tau \quad \rightarrow \quad m'^j = \frac{m^j/T}{1 - \frac{m}{T}\tau}. \tag{4.21}$$

Note that the total dead time $m\tau$ is independent of the amplitude of the signals j. Hence, the corrected counts of a given amplitude j to set now at the bin i would be:

$$N_i^{corr.,j} = \frac{N^j_i}{1 - \tau N_i} = f_i^{Pileup} N^j_i \tag{4.22}$$

and the corrected weighted content for the bin i,

$$N_i^{w,corr.} = \sum_j w_j N_i^{corr.,j} = \sum_j w_j f_i^{Pileup} N_i^j = f_i^{Pileup} \sum_j w_j N_i^j = \frac{1}{1-\tau N_i} N_i^w. \quad (4.23)$$

It means, that the pileup correction f_i^{Pileup} to apply in a weighted histogram is the same as that of the raw count rate histogram, and can be calculated from the corresponding raw count rate N_i and dead time τ.

Nevertheless it is important to note, that for a given sample, the count rate at a certain neutron energy or time of flight i, N_i, depends only on the proton intensity and hence the pileup correction depends also on the proton bunch intensity. During the experiment there are normally both low intensity parasitic pulses of 4×10^{12} protons and higher intensity dedicated pulses of around 7×10^{12} protons. Thanks to the discretized structure of the proton intensities pattern (see figure 4.4), the pileup correction was calculated in good approximation computing it separately for the average counting of high intensity pulses and for the lower average count rate of the parasitic bunches.

The pileup correction was found to be completely negligible for the highest count rates during a Pb or Bi sample measurement. The highest pileup corrections calculated were of about 1-2%, for the 4.9 eV saturated resonance of the ^{197}Au sample. These very small corrections lend further confindence that the assumed approximation 4.17 is valid.

4.8 Neutron sensitivity correction

The neutron sensitivity of the n_TOF capture setup is a key improvement with respect to previous measurements. A thorough investigation [5] has been carried out in order to develop a radiation detector as much optimized as possible in terms of low sensitivity to neutrons. It resulted on the carbon fibre FZK-C_6D_6 detector described in section 3.2.1.

The neutron sensitivity is defined as the ratio between the probability to detect a neutron and the probability to register a gamma ray. It is shown in figure 4.15 as a function of the neutron energy for the two types of detectors employed in this work (section 3.2.1) and also for the original commercial detector of Bicron (without any kind of sensitivity improvement). As can be observed, the neutron sensitivity of an FZK-detector ranges between a factor of 3 and 30 lower than that of the original Bicron detector. These results have been obtained by means of Monte Carlo simulations and have been also confirmed experimentally [5].

Now we want to evaluate how does the neutron sensitivity of the n_TOF optimized detection system affect to the neutron capture measurements carried out in this work.

Obviously, the radiation detector itself is the most critical element in the detection setup, since any capture reaction occuring in its volume subtends a relatively

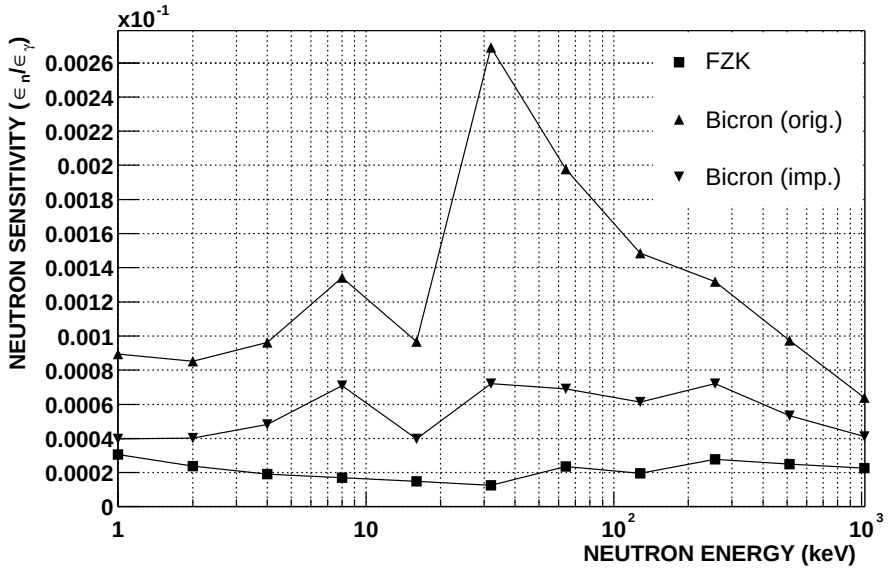

Figure 4.15: *Comparison of the simulated neutron sensitivities of the improved commercial detector of Bicron, and the carbon fibre detector.*

high geometric efficiency. Appart of the detectors, the other element in the setup which might be cause of concern is the sample changer. However its effect can be neglected due to the thin carbon fibre walls (2 mm) and to its very low, resonance free, capture cross section (see figure 3.5). The detectors are hanging from the ceiling by means of thin nylon cords, thus avoiding the conventional aluminum profile holders. The effect of these cords, in terms of neutron sensitivity, can be certainly neglected too. With these considerations, one can assume that the neutron sensitivity of the detection system is due to the C_6D_6 detectors only.

At a given capture resonance, the probability that a registered signal is due to a neutron captured in the detector material rather than to a gamma ray coming from a capture process in the sample can be expressed as

$$P^{ns} = \left(\frac{\varepsilon_n}{\varepsilon_c}\right)\left(\frac{\Gamma_n}{\Gamma_\gamma}\right), \tag{4.24}$$

where ε_n designates the neutron detection efficiency due to the probability for a sample scattered neutron to be captured in the detector's material and for one of the outgoing capture gamma rays to be registered in the detectors. ε_c is the probability to detect a cascade, and Γ_n and Γ_γ are the probabilities for a neutron to be scattered and captured respectively. The yield measured at this resonance should be then corrected by a factor,

$$f^{ns} = \frac{1}{1 + P^{ns}}. \tag{4.25}$$

The ratio $\varepsilon_n/\varepsilon_c$ is not directly the quantity shown in the vertical axis of figure 4.15, where ε_γ means the simulated detection efficiency for a gamma ray of 600 keV energy. The cascade efficiency, ε_c, following equation 2.4, can be approximated by the sum of the efficiencies of each gamma ray in the cascade, $\varepsilon_c \approx \sum_i \varepsilon_{\gamma,i}$, (which is in general larger than ε_γ).

The equation 4.24, can be rewritten as,

$$P^{ns} = \left(\frac{\varepsilon_\gamma}{\varepsilon_c}\right)\left(\frac{\varepsilon_n}{\varepsilon_\gamma}\right)\left(\frac{\Gamma_n}{\Gamma_\gamma}\right) = f^{gc}\left(\frac{\varepsilon_n}{\varepsilon_\gamma}\right)\left(\frac{\Gamma_n}{\Gamma_\gamma}\right), \tag{4.26}$$

where $f^{gc} = \varepsilon_\gamma/\varepsilon_c$ is the ratio between the probability to register a gamma ray of 600 keV and the probability to detect the prompt cascade of the corresponding capture resonance.

In order to obtain a realistic value of f^{gc}, one can generate nuclear cascades and simulate them for the corresponding capture setup by using a Monte Carlo code. A description of the cascades generator and the simulation will be given in section 5.5. Obviously, simulations have to be carried out for each specific resonance whose neutron sensitivity wants to be estimated.

From the different nuclides measured in this work, the *s*-wave resonances of the heavy isotopes ^{207}Pb and ^{209}Bi are the most critical cases. In table 4.2, we show the two resonances of these isotopes, measured in the present work (chapters 6 and 7), which have the largest scattering to capture ratio. In the same table, we show also the parameters of the calibration resonances and of the 1.15 keV resonance in ^{56}Fe+n.

Nuclide	E_r (eV)	J	l	Γ_n (eV)	Γ_γ (eV)	$R = \Gamma_n/\Gamma_\gamma$
^{56}Fe	1150	1/2	1	6.17×10^{-2}	5.74×10^{-1}	0.107
^{109}Ag	5.2	1	0	1.273×10^{-2}	1.36×10^{-1}	0.094
^{197}Au	4.9	2	0	1.52×10^{-2}	1.225×10^{-1}	0.124
^{209}Bi	12098	4	0	2.5889×10^{2}	1.17×10^{-1}	2213
^{207}Pb	41126	1	0	1.22×10^{3}	3.33	366

Table 4.2: *Parameters from reference [55].*

The 12.1 keV *s*-wave resonance of ^{209}Bi+n shows the largest scattering to capture ratio $R \approx 2.2\times10^3$. The f^{gc} value obtained from the Monte Carlo simulation of nuclear cascades mentioned above for this resonance is $f^{gc} \approx 0.446$. Taking the value of $\varepsilon_n/\varepsilon_\gamma$ from figure 4.15 at the neutron energy of 12.1 keV, the neutron sensitivity effect becomes,

$$P^{ns} = f^{gc}\left(\frac{\varepsilon_n}{\varepsilon_\gamma}\right)_{12keV}\frac{\Gamma_n}{\Gamma_\gamma} = \begin{cases} 25\% & \text{Original Bicron } C_6D_6 \\ 1.5\% & \text{Carbon fibre FZK } C_6D_6 \end{cases} \tag{4.27}$$

The accuracy of this correction is due to the uncertainty on $\epsilon_n/\epsilon_\gamma$, which is of about 12% [5], plus the uncertainty on the factor Γ_n/Γ_γ, which for this particular

resonance is of about 14%, yielding a final uncertainty on the correction of less than 20%.

The final correction factor for the 12.1 keV resonance of ^{209}Bi will be calculated through an iterative procedure by *i*) deriving the value of Γ_γ from the experimental yield and *ii*) calculating the corresponding f^{ns} correction using the resonance parameters obtained in the previous step.

For any other resonance of ^{207}Pb or ^{209}Bi the neutron sensitivity correction obtained was below 0.7%. For the calibration resonances of silver and gold samples and for the 1.15 keV ^{56}Fe resonance, the corresponding correction becomes also negligible.

4.9 Resolution function

Neutrons with the same energy at the capture sample position may have a different time history. This is due to two different causes, *i*) the 14 ns FWHM temporal width of the PS-proton beam and *ii*) the reflexions and moderation experienced by the neutrons inside the lead spallation block and in the water layer before exiting through the time of flight tube. See section 3.1 for details about the installation.

In a capture experiment, the measured capture yield $Y(t_{\rm TOF})$ is affected by these effects, becoming the true observable,

$$\bar{Y}(t_{\rm TOF}) = \int RF(E_n, t_{\rm TOF}) Y(E_n) {\rm d}E_n, \tag{4.28}$$

where $RF(E_n, t_{\rm TOF}){\rm d}E_n$ is the probability that an event observed at the time of flight $t_{\rm TOF}$ was actually due to a neutron with an energy in the interval $E_n + {\rm d}E_n$. A function describing this probability distribution is referred to as Resolution Function (RF). In a general way, at a given neutron energy E_n, it is defined as the time distribution of all neutrons arriving at the sample position (185.2 m) with energy E_n emitted by the target-moderator assembly as a consequence of a sharp delta pulse of the particle accelerator.

The n_TOF resolution function has been determined by means of Monte Carlo simulations [56]. It has been also validated and fine tuned experimentally by measuring narrow *p*- and *d*-wave capture resonances on a sample of $^{\rm nat}$Fe, as is described below.

Two Monte Carlo simulation codes, CAMOT [57, 58] and FLUKA [59], have been used to calculate the particles and gamma ray production and transport. A description of the neutron beam simulations is given in reference [56]. The simulation includes a detailed reproduction of the lead target-water moderator assembly, together with the aluminum alloy exit window and the 185 m long tunnel with the two collimators as described in section 3.1. In the simulation each incident proton is followed in its path inside the lead block and the neutrons (and all other particles) generated by interactions inside the target are Monte Carlo transported. Neutrons are transported inside the target as well as in the water moderator and through

the aluminum window. Given the large flight path of 185 m, only one neutron out of $\sim 10^7$ emerging from the lead target will finally reach the detector station at the end of the neutron tube. Hence, in order to accumulate enough statistics, the time distribution of the neutrons within a given energy range ΔE is calculated. It results in an asymetric curve due to the large dimensions of the lead target and the high number of neutron collisions before exiting outside. In figure 4.16 we show an example of simulated time distributions for neutrons in two different energy ranges, ΔE=1-3 keV and ΔE=18-22 keV.

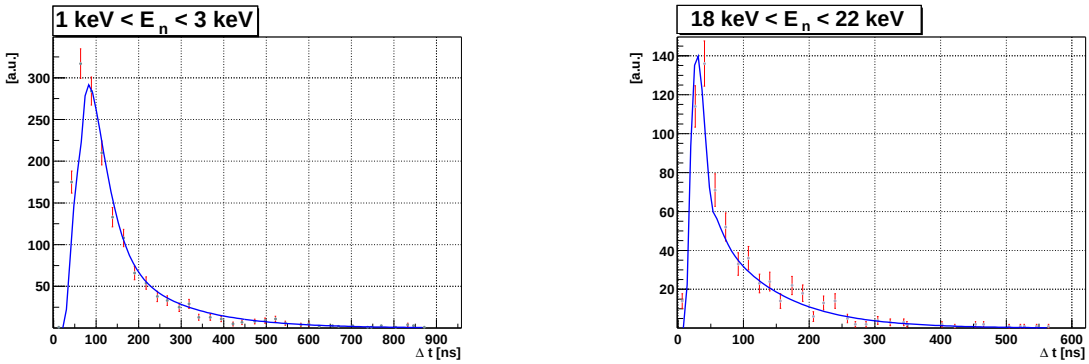

Figure 4.16: *Two simulated time distributions for neutrons in the energy ranges 1-3 keV (left) and 18-22 keV (right). The curve corresponds to the fitted RPI resolution function of SAMMY.*

A good description of the resolution function is of crucial importance in the analysis of resolved resonances (n,γ) cross sections. The analysis of capture data presented in this work is performed with the multilevel R-matrix analysis code SAMMY [49], which will be described in some more detail in section 5.7. In this code several parameterizations have been included to describe the resolution function of different facilities like ORELA or GELINA. We have found that the RPI[2] [60] resolution function is able to appropriately reproduce the simulated neutronic time distributions of the n_TOF installation. A brief description of this RPI-function is given in appendix C.

By using the neutron time distributions for several energy intervals, covering the whole neutron capture energy spectrum from 1 eV up to 1 MeV, an adequate parameterization of the RPI function has been found. Furthermore, it has been experimentally validated by fitting well isolated and narrow resonances present in ^{54}Fe and ^{56}Fe over a wide energy region, from 1 keV up to ~200 keV. Figure 4.17 shows the good agreement obtained with the experimental data, thus enabling us to analyse reliably narrow resonances at high energy, where the effect of the resolution function broadening dominates.

[2]RPI stands for Rensselaer Polytechnic Insitute, NY, USA.

The final parameterization adopted in this work for the n_TOF RPI resolution function is shown in appendix C.

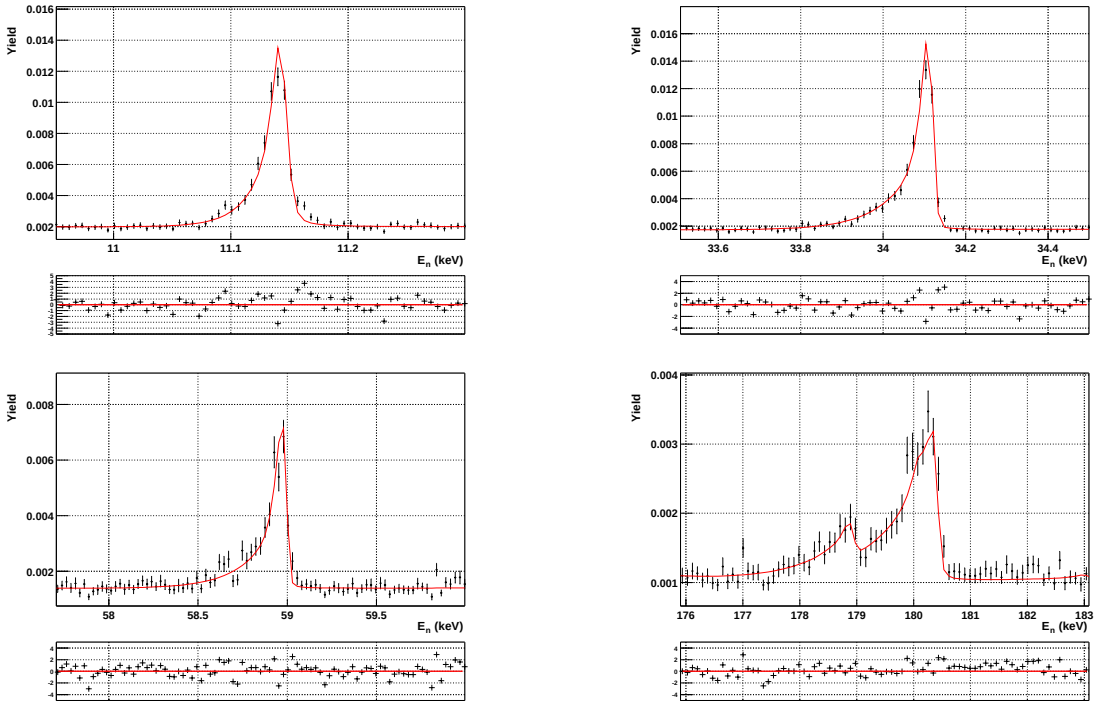

Figure 4.17: *SAMMY fit of the resolution function. The resonances are 11.2 keV* ^{54}Fe $l = 2$, *34 keV* ^{56}Fe $l = 1$, *59 keV* ^{56}Fe $l = 1$ *and the doublet 178-179 keV with* $l = 1$.

Chapter 5

Validation and accuracy of the Pulse Height Weighting Technique

The PHWT has been historically a source of uncertainty and controversy as it will be explained in section 5.1. For this reason, prior to the measurement of neutron capture cross sections at n_TOF, we decided to study in deep detail this measuring technique and the systematic accuracy which can be achieved with it.

From the analysis viewpoint, the Monte Carlo technique enabled us not only to determine accurate weighting functions, but it became also a prolific and efficient tool in order to account for several sources of systematic uncertainty.

At the same time, the present chapter aims to give a thorough description of the successful approach developed here in order to analyze this type of nuclear data.

5.1 Overview

Since the PHWT was firstly applied by Macklin and Gibbons [23] in 1967, the response distributions needed for the calculation of the weights were obtained by means of numerical calculation (using a very simplified picture of the experimental setup) and later by means of Monte Carlo simulations. However, in the early 80's a large discrepancy between transmission and some radiative capture measurements was found for the neutron width Γ_n of the 1.15 keV resonance in ^{56}Fe+n. It was considered at the International Conference on Nuclear Data for Science and Technology (1982) as one of the four major outstanding neutron data problems in the field of fission reactor neutronics [26].

Although some measurements based on MC simulated WF (using the EGS-code) yielded satisfactory results [61], the situation with another radiative capture data was still contradictory [62], showing discrepancies as large as $\sim$20%.

Exhaustive investigations at Geel [26] revealed that the problem had its origin in the Monte Carlo simulated response distributions. Moreover, an alternative method of obtaining the response functions was proposed, based on the coincidence technique for two-step cascades populated in (p,γ) resonance reactions. One of the two gamma

rays was registered in the conventional (n,γ) detection setup, while the other one was measured with an extra Ge detector. In this way, efficiencies and response functions were obtained for a set of thirteen gamma ray energies, by using targets of ^{26}Mg, ^{30}Si and ^{34}S at different proton energies. The experimental WF determined from these response distributions applied to capture data measured with thin samples (0.5 mm) gave a satisfactory result for the 1.15 keV ^{56}Fe resonance cross section. Nevertheless, it was also deduced from this experiment, that the materials surrounding the sample have a strong influence, by producing secondary radiation. Obviously, the sample itself becomes at the same time the first source of secondary radiation, thus casting doubts on the validity of this experimental approach and the experimental WF.

In view of this unclear situation we have re-investigated the issue of the accuracy of the MC simulation [63, 7], in particular whether the differences between simulation and measurement could be due to insufficient detail in the description of the measuring setup or rather to the poor implementation in the MC code of the relevant physical processes in the generation, interaction and transport of the secondary radiation.

Furthermore, as it will be shown in the following sections, the Monte Carlo technique becomes an essential analysis tool in this type of neutron capture measurements in order to account for several experimental sources of systematic deviation and derive reliable experimental yields.

5.2 Experimental validation

The 1.15 keV ^{56}Fe resonance constitutes an ideal accuracy test for a radiative neutron capture measurement. This resonance is strong and well isolated, and its capture width Γ_γ is about ten times larger than its neutron width Γ_n, thus becoming the radiative capture measurement sensitive to Γ_n. The value of this neutron width is very well known from transmission measurements.

Moreover, as it was described above, the detector response function has been found to be particularly sensitive to the details of the detection setup, including the sample itself [63]. Hence, the MC simulation seems to be the only reliable way to determine a realistic detector response for monoenergetic gamma radiation.

With these considerations, a good experimental approach to validate this technique would be the measurement of the 1.15 keV ^{56}Fe resonance. Using different sample geometries, normalization samples and detection setups, the ability of the Monte Carlo code to reproduce realistic response functions can be also experimentally demonstrated.

Iron samples of three different dimensions were measured at n_TOF using two different materials, gold and silver, for the yield normalization. Furthermore, two different detection systems were conceived by using the two types of C_6D_6 detector described in section 3.2 (in short Bicron and FZK), resulting in the eight different experimental setups listed in table 5.1. The number of protons dedicated to each measurement is also shown in the right column of this table.

Setup	Sample/ thick.×diam. (mm)	Thickness (atoms/barn)	Number of protons
Bicron	Au 0.1×45	6.32×10^{-4}	1.23×10^{16}
2×C_6D_6	Fe 0.5×45	4.18×10^{-3}	2.59×10^{17}
90°	Ag 0.2×20	1.19×10^{-3}	8.72×10^{15}
	Au 1.0×20	5.58×10^{-3}	5.27×10^{16}
	Fe 1.5×20	1.25×10^{-2}	2.05×10^{17}
FZK	Au 0.1×45	6.32×10^{-4}	6.71×10^{15}
2×C_6D_6	Fe 0.5×45	4.18×10^{-3}	1.37×10^{17}
90°	Fe 2.0×45	1.71×10^{-2}	5.69×10^{17}

Table 5.1: *Samples measured at n_TOF for the PHWT validation experiment.*

The experimental setup consisted of two detectors placed in horizontal position at 90° with respect to the beam line as is shown in figure 3.2 for the Bicron detectors and figure 5.1 for the FZK detectors. The frontal side of the C_6D_6-cell was set in both cases at approximately 4.2 cm from the sample's center. Both detectors, attached from the PM-tube, were hanging from the ceiling by means of thin nylon cords in order to minimize dead material and background sources close to the detector-sensitive volume. In this configuration, the calculated efficiency for a 1.27 MeV gamma ray was of 3.3% and 4.7% respectively for each Bicron and for each FZK detector.

5.3 Monte Carlo simulation of the response function

In order to learn which Monte Carlo package is better suited for our problem and to check for code-related systematic differences, a simplified test setup was simulated by employing four different codes, GEANT3 [64], GEANT4 [65], MCNP [66] and PENELOPE [67].

As we are interested in an accurate description of the electromagnetic processes, photons in the energy range of the capture energy (0-8 MeV) were sent perpendicularly to the sample and either the primary or secondary particles produced were registered by means of two C_6D_6 liquid scintillator cells. Two different samples of carbon and lead were simulated. This small benchmark test yielded compatible results for all the four codes.

Finally GEANT3 and GEANT4 toolkits were chosen to simulate each n_TOF setup. They permit to easily handle complex geometries, thus enabling us to carefully model the whole experimental setup in detail [37]. The high fidelity of the geometrical description can be appreciated in figure 5.1. This geometric input for the Monte Carlo calculation includes the sample in the central position, the sam-

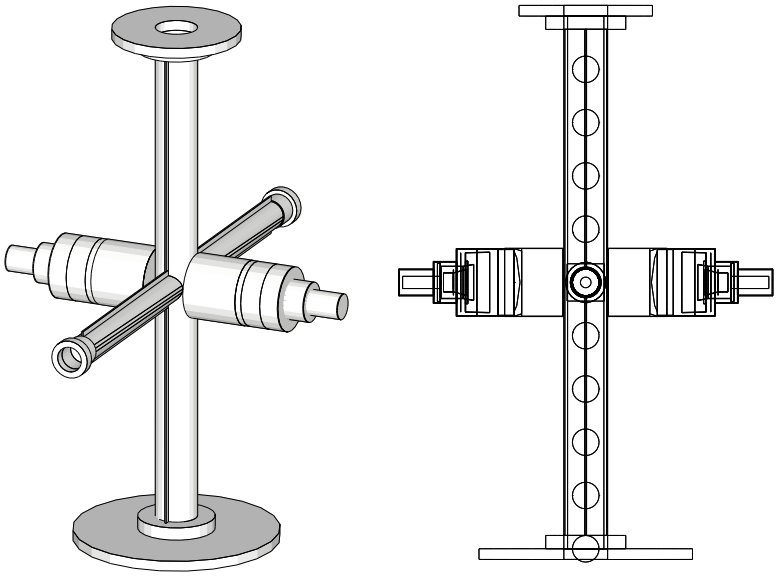

Figure 5.1: *(Left) General 3-D view of the experimental setup with the sample changer and the FZK-C_6D_6 detectors. (Right) Cross section of the same picture showing the details of the geometry as it has been implemented with* GEANT4.

ple's carbon fibre frame and holder strip, the sample changer with aluminum top and bottom flanges and front and back rings, and the detectors with the C_6D_6-cells and PM tubes as they are described in section 3.2. The carbon fibre elements where included with the chemical composition found in an RBS analysis (section 3.2.2).

In the case of GEANT3 the automatic tracking option (AUTO=1) was employed since it was verified that a more detailed and time consuming tracking of the secondary electrons produces negligible differences in the response. For the simulations carried out with GEANT4, the Standard Electromagnetic Package was used and the tracking cut length was lowered to 0.01 mm, when a stable result was achieved. Tests performed with the much slower Low Energy Extension package revealed no improvement or variation in the results.

The deposited energy distribution in the sensitive detector volume was recorded for $j = 1, \ldots, 12$ gamma-ray energies E_j in the range from 0.2 to 9 MeV. For each energy, $5{\times}10^6$ photons were sequentially and isotropically emitted starting randomly from the sample volume with a radial probability distribution following the neutron beam profile (see section 4.6.1). A depth probability distribution was also included, considering the magnitude of the isotope's cross section. It was verified that the depth distribution had in general a minor effect on these results, although in principle this distribution is very different for weak resonances (practically uniform) and strong resonances (surface peaked) in the capture experiments.

The deposited energy spectra were histogramed using a bin width of $\Delta E = 50$ keV. The instrumental resolution of the detectors was included in the sim-

ulated response functions by performing a convolution with a Gaussian function of appropriate width σ. Details on the instrumental resolution are given in section 4.4. In order to obtain $R_{i,j}$, the calculated response distributions were then normalized to the efficiency.

To illustrate the effect of the sample size in the response functions, the last have been plotted in the top part of figure 5.2 for the thinnest and thickest iron samples used in these measurements. Of course, for samples with different geometries but also different materials, e.g. like gold and iron, larger differences can be observed in the response distributions, as it is shown below in the same figure.

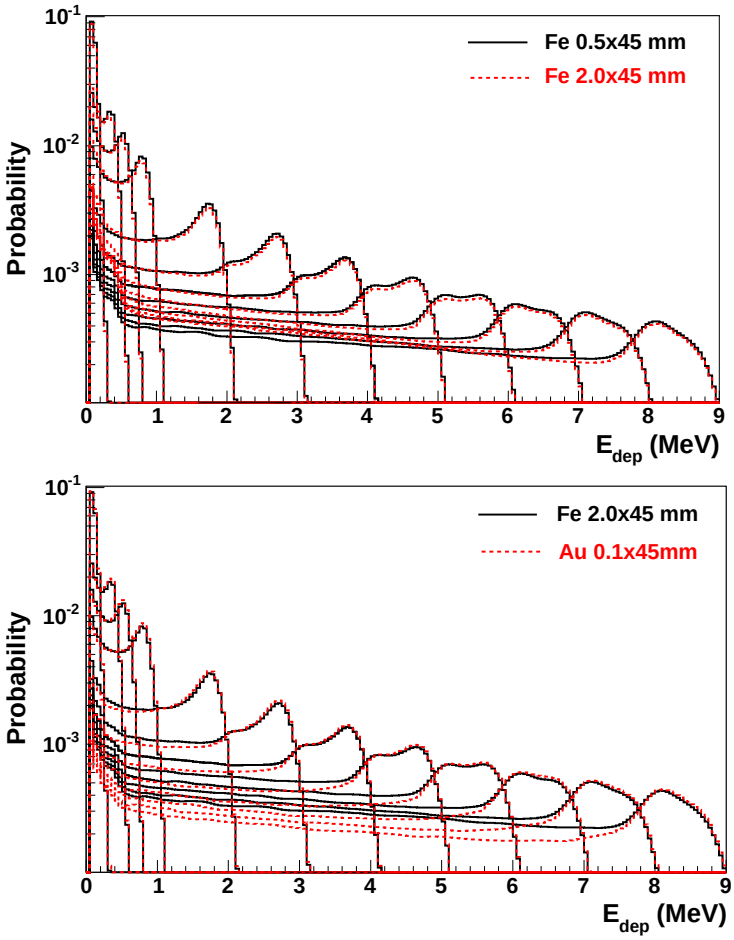

Figure 5.2: *(Top) Response functions calculated with* GEANT4 *for the iron samples of 0.5 mm (solid line) and 2.0 mm (dashed line). (Bottom) Response distributions for Au 0.1×45 mm and for Fe 2.0×45 mm.*

The sensitivity of the response distribution to the particular sample in the setup is clearly reflected in figure 5.2. Therefore, it becomes also a clear evidence that the Monte Carlo simulation is the unique approach to obtain realistic response distributions.

5.4 Polynomial weighting function calculation

To obtain the WF, we follow here the procedure described in section 2.2 for the calculation of a polynomial WF,

$$W_i \approx \sum_{k=0}^{4} a_k E_i^k. \tag{5.1}$$

Using the simulated, broadened and efficiency normalized response functions $R_{i,j}$, (see figure 5.2), one can calculate the coefficients a_k by performing a least squares minimization, as indicated by equation 2.9. Taking the proportionality factor between efficiency and energy α=1,

$$min\left(\sum_j \left(\sum_i \sum_k^n a_k E_i^k R_{i,j} - E_j\right)^2\right). \tag{5.2}$$

An example of WF obtained for the iron samples is shown in figure 5.3.

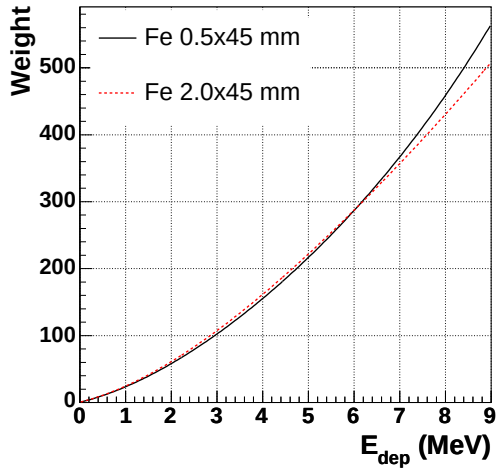

Figure 5.3: *Example of two polynomial WF obtained for the thinnest and thickest iron samples.*

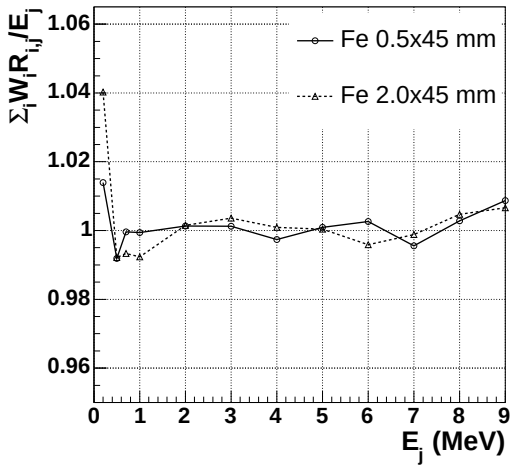

Figure 5.4: *Proportionality check at the simulated gamma-ray energies E_j of 0.2, 0.5, 0.7, 1,...9 MeV.*

One should check now the obtained result for each WF, by substitution of it back in equation 2.5. Equivalently, we have plotted in figure 5.4 for each simulated gamma ray E_j the ratio,

$$\frac{\sum_i W_i R_{i,j}}{E_j}, \tag{5.3}$$

which for an *exact* result of the WF should be equal to one. The last figure shows a good performance of the WF along the whole energy range of interest. Small local deviations between 1.5-4% are found for gamma rays of low energy. The

RMS deviation is 0.16% and 0.36% respectively for the thin and the thick samples. A similar behavior was obtained for the gold and silver samples used for calibration.

Fulfill equation 5.3 means that the approximation of the weighting factors by a polynomial WF (equation 2.8) is valid in the sense that the proportionality condition 2.2 is satisfied with a negligible RMS deviation.

About the calculation of the uncertainty related with the WF itself is going to be discussed in the following section.

5.5 Weighting function uncertainty

The conventional procedure to determine the statistical uncertainty related with the WF would consist of introducing the covariance matrix of the simulated responses into equation 2.9. But this uncertainty is not the relevant one, as it can be done arbitrarily small by increasing the number of simulated events. The relevant uncertainty is the systematic one. In order to determine the latter, we have developed a new procedure [7], which has been already introduced in section 2.1.

Let us assume $R_i^C = \sum_{c=1}^{N} R_{i,c}$ to be the detection system's total response distribution for N neutron capture events or capture gamma ray cascades of energy E_C. According to the principles of the PHWT, it should be fulfilled that the ratio

$$\frac{\sum_i W_i R_i^C}{N E_C} \tag{5.4}$$

is equal to one. Thus deviations of this value indicate the uncertainty introduced in the capture experiment due to the WF itself. Using a generator of realistic nuclear cascades we were able to obtain, by means of the Monte Carlo method, the detection system's response distribution R_i^C needed by this approach.

Note that the WF have been constructed in the previous section choosing a proportionality constant $\alpha = 1$, that is why it does not appear any more in the previous formula.

To give a clear overview of the procedure, we will describe first the code used to calculate realistic nuclear cascades. The performance of this code will be shown afterwards by applying it to the 1.15 keV ^{56}Fe resonance and the normalization samples.

Nuclear gamma-ray cascade code

A program was written to serve as an efficient event generator for Monte Carlo GEANT simulations. This program was designed to be easy to implement and fast in the calculation of the cascades.

To generate the prompt gamma rays which follow the capture process, the nuclear cascade is divided in two parts as sketched in figure 5.5.

The lower energy range corresponds to completely known levels, energy, spin, parity, transitions and intensities are obtained from experimental data. This known level scheme can be retrieved for example from the Evaluated Nuclear Structure Data Files (ENSDF), reference [68]. The lower energy part of the branching ratio matrix is therefore exactly computed with this information.

The conversion electron process can be included in the discrete experimental part of the cascade, given the binding energies of the K-, L- and M-shells, fluorescence yields and internal conversion coefficients.

The cutoff energy, E_{cut}, corresponds to the excitation energy up to which the discrete level scheme can be considered completely known.

The upper part, ranges from E_{cut} up to the capture energy E_C. The last determines an additional level, whose spin and parity are normally known too. This unknown interval, $E_{cut} - E_C$, is going to be modelled by means of the statistical model of the nucleus, as it is explained in the following.

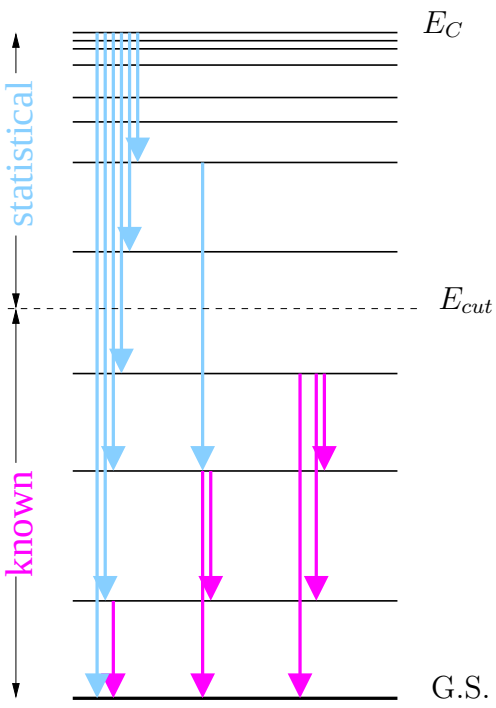

Figure 5.5: *Scheme of the Monte Carlo generation of cascades.*

First, the "statistical" interval is divided or discretized into 50 keV steps. This procedure enables a fast calculation of the transitions, reducing the total computing time. The details of this continuum have little effect on the capture gamma spectrum because the transition probabilities strongly favor high-energy gamma transitions, i.e., transitions to the ground state or to the near known experimental levels.

The part of the branching ratio matrix corresponding to transitions from these statistical 50 keV levels to the known lower energy experimental levels will be filled with the transmission coefficients $T_{XL}(E_\gamma)$, described in reference [69],

$$T_{XL} = 2\pi E_\gamma^{2L+1} \times f_{XL}. \tag{5.5}$$

The multipole type XL is defined by the usual selection rules, given the known spin and parity of the experimental levels and considering only transitions of type E1, M1 and E2.

The strength function for XL multipolar transitions, derived from the Giant Dipole Resonance (GDR) model has the form of a standard Lorentzian [70],

$$f_{XL}^{SLO}(E_\gamma) = \frac{26 \times 10^{-8}}{2L+1} \sigma_\circ \Gamma E_\gamma^{(3-2L)} \frac{\Gamma_\circ}{(E_\gamma^2 - E_\circ^2)^2 + E_\gamma^2 \Gamma_\circ^2} \qquad [\mathrm{mb}^{-1}\mathrm{MeV}^{-2}]. \tag{5.6}$$

where the Lorentzian parameters ($\sigma_\circ$,$E_\circ$,$\Gamma_\circ$) respectively stand for peak cross section, energy and width of the GDR. The single particle model and the improved generalized Lorentzian model, have been also included in this code (table 5.2).

Transition	Gamma strength parameterization	Parameters
E1	GDR, Generalized Lorentzian (1 or 2 resonances)	$E_\circ^{E1}, \Gamma_\circ^{E1}, \sigma_\circ^{E1}$
	GDR, Standard Lorentzian (1 or 2 resonances)	$E_\circ^{E1}, \Gamma_\circ^{E1}, \sigma_\circ^{E1}$
	Single Particle	k (strength factor)
M1	GDR, Standard Lorentzian	$E_\circ^{M1}, \Gamma_\circ^{M1}, \sigma_\circ^{M1}$
	Single Particle	k (strength factor)
E2	GDR, Standard Lorentzian	$E_\circ^{E2}, \Gamma_\circ^{E2}, \sigma_\circ^{E2}$
	Single Particle	k (strength factor)

Table 5.2: *Parameterizations tested for the gamma ray strength function. The possibility to add a second (pigmy) resonance for E1 transitions is available.*

The rest of the branching ratio matrix, corresponds to the relatively less likely transitions within the statistical range, $E_{cut} - E_C$. In this region the gamma ray spectrum is determined by the product [69]

$$T_{XL} \times \rho(E - E_\gamma, I, \Pi), \tag{5.7}$$

where $\rho(E - E_\gamma, I, \Pi)$ designates the density of final levels with excitation energy around $E - E_\gamma$, with spin I and parity Π.

The three models for the level density shown in table 5.3 were included in this code with the aim of studying density parameterization related differences in the generated spectra.

Lev. Density Parameterization	Parameters	Ref.
Back shifted Fermi Gas (Dilg et al.)	a (MeV^{-1}), Δ (MeV)	[71],[72]
Constant temperature (Egidy et al.)	T, $\mathrm{E}_\circ$ (MeV)	[72]
Combined CT+BSFG (Gilbert-Cameron)	T, $\mathrm{E}_\circ$,Δ, E_x (MeV), a(MeV^{-1})	[73]

Table 5.3: *Level density parameterizations tested with the cascades generator code.*

Starting at the top, known, capture level, a Monte Carlo sampling is performed in order to generate N random cascades in a sequential way. The statistical part of the branching ratio matrix is completed considering E1, M1 and E2 transitions to the underlying "statistical" levels. Once the full branching ratio matrix is available, the first transition is MC generated. For transitions within the statistical interval the branching ratio matrix is re-calculated again for the rest of statistical and experimental levels and the next transition is MC generated. The program proceeds sequentially in this way until finally the ground (or a metastable) state is reached.

Performance of the cascade generator

The code described in the previous section was implemented into the GEANT code as Monte Carlo event generator in order to generate random cascades in the 1.15 keV resonance of ^{56}Fe+n. The geometry included in the simulation corresponds to the n_TOF capture setup described in section 5.3.

The instrumental resolution of the C_6D_6 detectors was included in the simulated spectrum by convoluting it with a Gaussian function of appropriate width (section 4.4). The obtained result, could be then compared with the deposited energy spectrum measured for this resonance.

The experimental spectrum of deposited energy was obtained by setting an adequate time of flight window around the 1.15 keV resonance. For testing the code, we have chosen the measurement of the 2 mm thickness iron sample, where more statistics were accumulated (see table 5.1). As this resonance is well isolated, we were able to accurately substract the background by puting a similar window beside the resonance.

In figure 5.6 the experimental deposited energy spectrum is compared with that obtained from the MC simulation of the nuclear cascades.

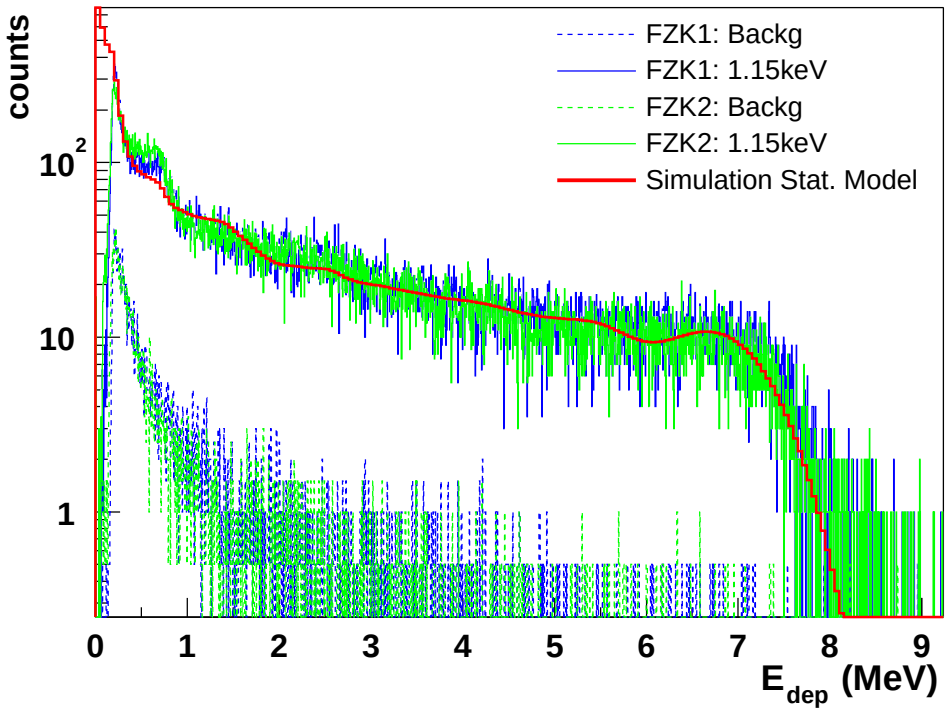

Figure 5.6: *MC simulation of the deposited energy spectrum for the 1.15 keV ^{56}Fe resonance and comparison with the spectrum measured with the FZK-C_6D_6 detectors.*

For this resonance, we studied in detail the performance of the different level density parameterizations by comparing them on one side to the known experimental

levels and on the other hand to the experimental deposited energy spectrum.

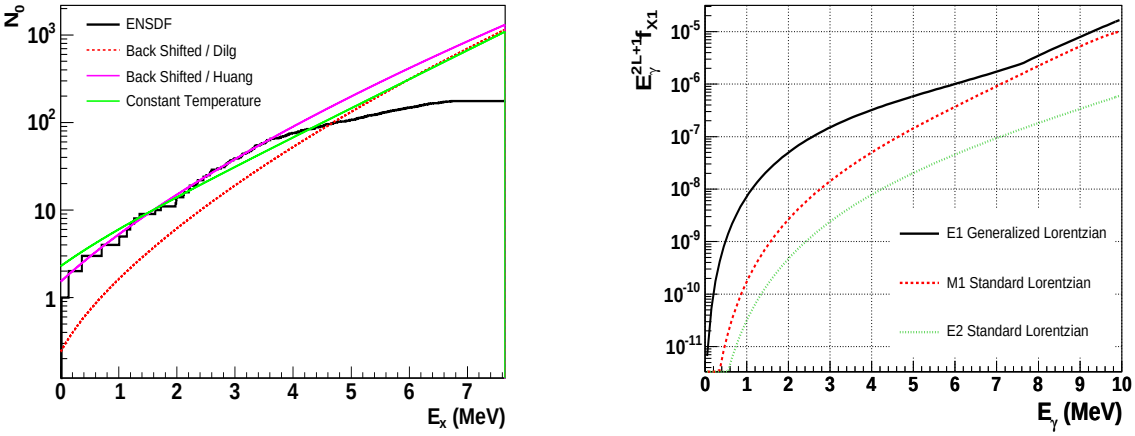

Figure 5.7: *(Left) Cumulative number of levels versus the excitation energy in* ^{56}Fe*. (Right) GDR model for electromagnetic strengths.*

In the left part of figure 5.7, the cumulative number of levels predicted by the parameterizations considered here are compared with the number of experimentally known levels. It can be observed that some of the parameterizations coincide with the experimental value up to about 3.5 MeV. This is an upper limit of the cutoff value, E_{cut}, since the number of completely known levels (spins, branchings, etc) is usually lower. In the case of iron, the E_{cut} limit is given by $\sim$2 MeV. This figure indicates also that the Back Shifted (BS) model calculated with the Huang et al. parameters from reference [74] seems to fit better the experimental level density data, although all of them predict similar density of levels.

Test simulations with the different level density parameterizations of table 5.3 confirmed no strong dependency on the model and parameterization used when comparing with the experimental spectrum of deposited energy. In figure 5.6 the simulated histogram has been calculated using the BS-level density formula.

The gamma strength was better reproduced by using a generalized Lorentzian for the electric dipolar E1 transitions, and a standard Lorentzian for M1 and E2 transitions. Indeed, the single particle model has been found to overestimate the E1 strength, as well as the standard Lorentzian [69]. The relative intensities of the transitions can be appreciated in the right part of figure 5.7, where they have been plotted against the energy of the gamma ray.

In general we tried to use the recommended compilations of GDR parameters derived from experimental data [75]. In many cases where this information is not available, a general parameterization of $E_\circ$, $\Gamma_\circ$ and $\sigma_\circ$ as a function of the atomic mass is also available [75] for E1, M1 and E2 transitions. In some cases however, the agreement with the experimental response distribution was not completely satisfactory and only $\sigma_\circ$ for the M1 giant resonance was varied in a reasonable magnitude.

The final agreement between calculated and measured spectra (figure 5.6) is striking, thus lending confidence that the calculated deposited energy distribution can be used to determine the uncertainty of the WF as is our purpose.

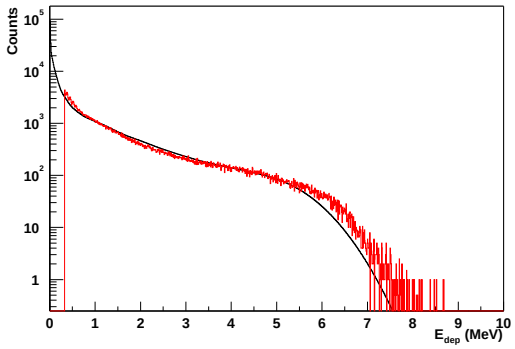

Figure 5.8: *Comparison between calculated and measured deposited energy spectra for the 4.9 eV ^{197}Au resonance.*

In a similar way, nuclear cascades were generated for the 4.9 eV ^{197}Au and the 5.2 eV ^{109}Ag resonances. In figure 5.8 the resulting deposited energy spectra for gold, both from the simulation and the measurement are compared.

The obtained result is also satisfactory and the small differences between simulation and experiment obtained at higher energy will have a negligible influence in the result, as will be seen in the following section.

Calculation of the weighting function uncertainty

Generating the gamma rays of the calculated nuclear cascade sequentially in the MC simulation, one avoids the possibility of having more than one prompt gamma ray registered at the same time in the detectors. With this "ideal" capture experiment, deviations of equation 5.4 can be explained only as uncertainty of the WF due to *i*) the statistical uncertainty of the simulated response distributions and *ii*) the mathematical accuracy of the polynomial approximation (note that the proportionality condition is not exactly fulfilled as can be observed in figure 5.4).

About the systematic deviation introduced by the summing of two or more prompt gamma rays and other experimental effects will be discussed in the next section.

A total of $N = 5 \times 10^5$ capture cascades were generated for each sample-setup configuration of table 5.1. The gamma rays of these cascades where then emitted in a sequential way in the GEANT Monte Carlo simulation. The whole response distribution for each setup was recorded, i.e., for a deposited energy threshold of 0 keV. As usual, the zero width simulated spectra, are convoluted with a Gaussian of appropriate width to include the effect of the instrumental resolution (section 4.4). An example of the obtained spectra can be seen in figures 5.6 and 5.8.

Finally, the uncertainty of the WF can be computed from equation 5.4 using the weighting functions obtained in section 5.4 and the ideal capture cascade response distributions described here. The results are listed in the last column of table 5.4.

In all the cases the deviations are below 0.8%. The obtained uncertainties for the WF show an RMS deviation of 0.17%. This result is compatible with both *i*) the statistical uncertainty of the response functions $R_{i,j}$ used to compute the WF, which varies between 0.1-0.2% and *ii*) the systematic deviation of the proportionality

Setup	Sample thick.×diam. (mm)	$\sum_i W_i R_i^C$ (weighted counts)	$\frac{\sum_i W_i R_i^C}{N E_C}$
Bicron	Au 0.1×45	6520969 (24781)	1.0014(38)
2×C_6D_6	Fe 0.5×45	7639933 (33390)	0.9910(44)
90°	Ag 0.2×20	6810364 (23183)	1.0002(34)
	Au 1.0×20	7638539 (33400)	0.9989(44)
	Fe 1.5×20	6563164 (25442)	1.0079(39)
FZK	Au 0.1×45	6551329 (21044)	1.0060(32)
2×C_6D_6	Fe 0.5×45	7650365 (28475)	1.0004(37)
90°	Fe 2.0×45	7628292 (28386)	0.9976(37)

Table 5.4: *Estimated uncertainty on the WF.*

condition whose RMS is of about 0.2-0.4% (section 5.4).

The same method was used to estimate the effect of the instrumental resolution used to convolute the MC simulated response function, showing variations of only a few per mil for reasonable width shifts. Small variations of the deposited energy calibration have a considerable effect on the value of $\sum_i W_i R_i^C$, however, this deviation is cancelled out when computing the ratio with respect to the Au or Ag reference sample.

Finally a 0.3% was adopted as the uncertainty associated with the polynomial WF of the samples listed in table 5.4.

5.6 Experimental sources of systematic error: threshold, γ-summing and conversion electrons

The procedure described above to determine the accuracy of the Weighting Function, can be employed also to calculate the uncertainty due to several experimental effects which take place in any capture measurement.

- During a capture measurement, the detectors register counts only above a certain electronic **threshold**. At the n_TOF experiment, a digital threshold is set at each FADC-channel for the zero suppression algorithm. Signals with smaller amplitude, coming from prompt gamma rays of low energy, are not recorded but have to be taken into account for the final determination of the capture cross section. This effect may be particularly important in the case of high multiplicity cascades or isotopes showing a soft spectrum. Given a threshold corresponding to t channels in the i-binned response distribution R_i^C for N simulated prompt cascades, the weighted count rate is given by

Sample	$\sum_{0\ keV}^{\infty} W_i R_i^C$	$\sum_{250\ keV}^{\infty} W_i R_i^C$	f^t
Au 0.1×45	6583164	6142547	1.072(5)
Fe 0.5×45	7709233	7560570	1.020(5)
Fe 2.0×45	7740907	7563170	1.023(5)

Table 5.5: *Deviation in the experimental yield due to an instrumental threshold of 250 keV. Quoted uncertainties represent the statistical deviation of the MC simulation, in which $N = 5 \times 10^6$ capture events were generated.*

$\sum_{i=t}^{\infty} W_i R_i^C$, while for an ideal zero threshold detection system, this quantity would be higher, $\sum_{i=0}^{\infty} W_i R_i^C$. The deviation between these two values, $f^t = \sum_{0\ keV}^{\infty} W_i R_i^C / \sum_{250\ keV}^{\infty} W_i R_i^C$ is shown in table 5.5 for a threshold level of 250 keV. As the weighted count rate is proportional to the yield (equation 4.5), this deviation gives an estimate of how much the calculated experimental yield is affected by the counts lost below the threshold.

As the cross sections are always measured with respect to a reference sample (gold or silver), the common practice of assuming that the counts lost below the threshold in the measurement of a given material, cancel out with the corresponding of the reference sample is invalid as can be deduced from table 5.5, and may introduce uncertainties of several per cent in the final result.

- Another experimental effect which has to be taken into account, is the **summing** of two or more signals. It happens when two or more gamma rays of the same cascade are detected at the same time. Given the low detection efficiency, this effect is generally small, but it also depends on the particular isotope under study and its multiplicity.

  This effect can be estimated by generating the prompt gamma rays of each cascade *simultaneously* in the Monte Carlo simulation instead of sequentially. If $\Sigma W_i R_i^{C,Sim}$ is the corresponding weighted response distribution, then deviations with respect to the sequential case, $\Sigma W_i R_i^C$ (table 5.4), will be necessarily due to the summing of two or more gamma rays. This effect is indeed small as can be observed in table 5.6, where the ratio $f^s = \Sigma W_i R_i^{C,Sim} / \Sigma W_i R_i^C$ is shown for three samples of the measured samples.

Sample	f^s
Au 0.1×45	1.017(5)
Fe 0.5×45	1.010(5)
Fe 2.0×45	1.018(5)

Table 5.6: *γ-summing effect estimation for the three samples measured with the FZK-C_6D_6 detectors.*

- The internal **Conversion Electron (CE)** process can lead to a slight underestimation of the experimental yield. In this process, a gamma-ray transition

of the nuclear cascade can be substituted by an electron emission. This electron and the emitted X-rays can be easily stopped in the sample material, delivering less energy or no energy at all in the detectors.

Sample	f^{ce}
Au 0.1×45	0.996(5)
Fe 0.5×45	0.998(5)
Fe 2.0×45	1.007(5)

Table 5.7: *Effect of the conversion electron process.*

The conversion electrons can be taken into account for the known lower energy part of discrete levels sketched in figure 5.5, by including the fluorescence yields in the simulation and the atomic electron binding energies. In particular, we considered K-, L-, and M-shell transitions. The estimated influence of the conversion electron process in the Yield is indeed very small as can be appreciated in table 5.7.

Global correction factor

It is more convenient and realistic to consider all these three sources of systematic error together and compute a unique yield correction factor which includes them altogether.

This can be achieved by *i*) generating a large number of cascades, N, which include the conversion electron process and *ii*) simulate them with simultaneous emission of the prompt cascade gamma rays (and conversion electrons), $R^{C,Sim}$. The correction factor to apply to the experimental yield will then be given by,

$$f^{t,s,ce} = \frac{\sum_{i=0}^{\infty} W_i R_i^C}{\sum_{i=t\ keV}^{\infty} W_i R_i^{C,Sim}}, \tag{5.8}$$

where R_i^C is the response function for the same number of cascades N, where no conversion electron process has been included and the cascade gamma rays have been sequentially generated.

The resulting correction factors for the samples measured in this validation experiment are summarized in table 5.8. The threshold level set for the Bicron detectors was of 150 keV, while the higher electronic noise of the FZK detectors required a threshold of 250 keV.

The uncertainty given is just the statistical uncertainty of the normalized weighted sum. It is not straightforward to assign a value for the systematic (model dependent)

Setup	Sample	$f^{t,s,ce}$
Bicron	Au 0.1×45	1.045(4)
	Fe 0.5×45	1.002(4)
	Ag 0.2×20	1.026(4)
	Au 1.0×20	1.060(4)
	Fe 1.5×20	1.009(4)
FZK	Au 0.1×45	1.056(4)
	Fe 0.5×45	1.009(4)
	Fe 2.0×45	1.018(4)

Table 5.8: *Final yield correction factors.*

uncertainty associated with this correction, but in view of the magnitude of the corrections a value of 1% was assumed.

5.7 Resonance analysis

In the analysis of resonance cross section data the yield is parameterized by means of nuclear reaction theory. In the thermal and resolved energy regions, the R-matrix theory is most conveniently employed. The parameters of this model are level energies, level spins and partial widths.

The advantage of using the R-matrix formalism to describe cross section data resides on the reduced number of parameters needed to describe the cross section over a wide energy range as well as to ensure consistency with physical constraints [76].

There are several approximations of the R-matrix formalism to describe the cross sections, the most important of them are Blatt-Biedenharn, single-level (multi-level) Breit-Wigner, multi-level Adler-Adler and multi-level Reich-Moore. The last of them is considered to be a better approximation than the other variants [76].

An iterative fitting procedure can be used in the analysis, varying one or more of the parameters describing the "theoretical" yield until the *best* parameterization has been found for the measured yield.

Nevertheless, as was already pointed out in section 4.1, there are some experimental effects, contributions to the yield and broadenings, which are difficult to correct for in the experimental data. It is easier to include them into the calculation of the theoretical yield, and moreover it is also more accurate from the analysis viewpoint.

Sample thickness effects

The experimental capture yield Y_γ is the sum of several contributions from multiple-collision events where the neutron undergoes zero, one, two etc. collisions before it finally induces the recorded reaction,

$$Y_\gamma = Y_{\gamma,0} + Y_{\gamma,1} + Y_{\gamma,2} + \dots . \tag{5.9}$$

The first collision term is the product of the interaction probability of the incident neutron times the ratio σ_γ/σ of the number of (n,γ) events to the total number of interactions,

$$Y_{\gamma,0} = (1 - T)\,\frac{\sigma_\gamma}{\sigma}, \tag{5.10}$$

where $T = e^{-n\sigma}$ is the fraction of neutrons of given energy which traverses the sample of thickness n (nuclei/barn) without interaction.

For very thin samples $n\sigma << 1$, the capture reaction yield can be approximated by the first term, $Y_\gamma \approx Y_{\gamma,0} \approx n\sigma_\gamma$. But in general the multiple-collision terms have to be considered. These can be written as,

$$
\begin{aligned}
Y_{\gamma,1} &= (1-T)\,\frac{\sigma_n}{\sigma}\left\langle (1-T_1)\frac{\sigma_{\gamma,1}}{\sigma_1}\right\rangle_1, \\
Y_{\gamma,2} &= (1-T)\,\frac{\sigma_n}{\sigma}\left\langle (1-T_1)\frac{\sigma_{n,1}}{\sigma_1}\left\langle (1-T_2)\frac{\sigma_{\gamma,2}}{\sigma_2}\right\rangle_2\right\rangle_1, \\
&\vdots
\end{aligned}
\tag{5.11}
$$

The numerical subscripts indicate the number of preceeding collisions. The brackets denote spatial and angular averages over all possible 1st, 2nd,... collisions. As can be noted from the last equations, the multiple-collision yields $Y_{\gamma,1}, Y_{\gamma,2}, \ldots$ are increasingly complicated functionals of the cross sections σ_γ, σ_n and σ. Hence, the only reliable method to calculate them [76] is by means of a Monte-Carlo simulation of multiple collision neutron histories based on the detailed resonance cross sections, on the appropriate probability distribution for free paths and angles, and on the exact sample geometry.

Thermal broadening

Thermal broadening (also referred to as Doppler broadening) in nuclear reactions is caused by the thermal motion of target nuclei. A method for the calculation of this broadening consists on assuming that the target nuclei have the same velocity distribution as the atoms of an ideal gas, which follow the Maxwell-Boltzmann distribution. Following some approximations [76], it can be demonstrated that this broadening can be included as a Gaussian broadening of the reaction rate on the energy scale with a width given by the so called Doppler width,

$$\Delta = \sqrt{\frac{4EkT}{M/m}}. \tag{5.12}$$

In this formula, M is the mass of the target nucleus, kT the gas temperature in energy units and m the neutron mass.

R-matrix code SAMMY

The SAMMY code [49] was chosen for the analysis of the capture data, because it permits to include all the effects mentioned above in a detailed way.

For the reproduction of the cross section we have used the Reich-Moore approximation, although several variants are included in this code.

The sample thickness effects are implemented within SAMMY using a numerical calculation technique. The exact geometry and dimensions of the sample are therefore given as input in SAMMY for this calculation. The multiple scattering is

computed assuming the approximation of neutrons uniformly distributed within the sample after the second scatter.

Several thermal broadening options are possible in SAMMY, although the free gas model described above is recommended for metallic samples.

The n_TOF neutron beam resolution can be succesfully implemented by using the RPI parameterization, as it was described in section 4.9.

Using Bayes' theorem, SAMMY generates a set of *a posteriori* resonance parameters and a covariance matrix from the given *a priori* parameters and experimental data. In general, input resonance parameters from reference [55] were used in the present work for the calculation of the theoretical yield with SAMMY. Parameters for different isotopes, as well as the atomic sample composition, can be also included in SAMMY in order to account for impurities in the sample.

5.7.1 Analysis of the 1.15 keV resonance of ^{56}Fe

Following the procedure described in chapter 4, the experimental (uncorrected) capture yield is obtained from the measured and weighted count rate N^w as

$$Y(E_n) = \frac{N^w}{N_n(E_n) \times E_C(E_n)}. \tag{5.13}$$

The neutron number N_n can be calculated as the product of the neutron intensity parameterization (section 4.5.1) times the number of proton bunches of 7×10^{12} protons employed in the measurement (table 5.1). However, the total proton pulse intensity registered by the Wall Current Monitor showed too large deviations for some proton pulses and therefore, the silicon monitor information was used to renormalize between measurements (section 3.2.3). This introduces an additional correction factor f^{Si} whose uncertainty is mainly statistical. For the samples with diameter of 20 mm the neutron number is multiplied by a factor 0.59 obtained from the n_TOF beam profile described in section 4.6.1.

The experimental yield was analyzed using the SAMMY code described above. The function used to fit the yield had the form

$$Y = AY^{th} + B, \tag{5.14}$$

where Y^{th} is the yield calculated with SAMMY from the resonance parameters, A is a yield normalization factor and B is a polynomial function to reproduce the background. The last two parameters, A and B where allowed to vary in the fit. It was found that the background was succesfully fitted with a constant term. An example of the fit obtained with SAMMY for the 1.15 keV resonance of ^{56}Fe+n with the thickest iron sample (2×45 mm) is shown below in figure 5.9.

All the relevant information is contained in the yield normalization factor A. It relates directly the measured yield Y with the calculated yield Y^{th}. Hence, A becomes sensitive to the systematic deviations due to the accuracy of the WF and the

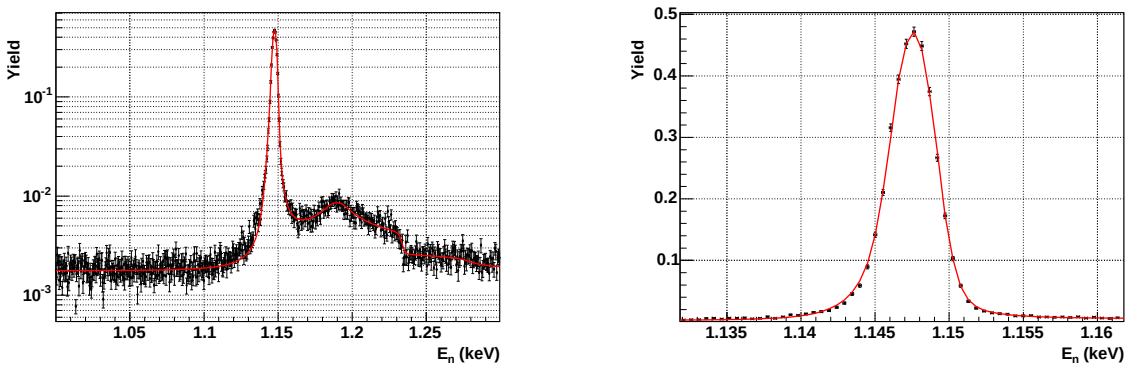

Figure 5.9: *SAMMY fit of the 1.15 keV resonance measured with the thick iron sample. It is shown on the left side in a logarithmic scale for better observation of the multiple scattering effect.*

other experimental sources of systematic uncertainty. Therefore, in order to extract information on the former, the rest of systematic corrections must be accounted for.

It can be observed in figure 5.9 how accurately the multiple scattering is reproduced by the SAMMY code, thus lending confidence that this effect is appropriately accounted for in the calculation of the yield Y^{th}. The rather symmetric shape of the resonance shown in the right part of figure 5.9 indicates that the main broadening at this energy is still due to the thermal motion of the nuclei (thermal broadening). The free-gas model used in this SAMMY analysis is considered to be vey accurate [49] and the uncertainty related with it can be certainly neglected.

The other sources of systematic uncertainty are those already introduced in section 4.1. The neutron sensitivity correction, f^{ns} can be absolutely neglected in our case given the very small scattering to capture ratio (Γ_n/Γ_γ) of all the resonances treated here and the very low neutron sensitivity of the detection setup (see section 4.8 for details).

The threshold, conversion electrons and summing of gamma rays are the experimental effects which introduce the highest correction factor as has been described and calculated in section 5.6. These correction factors are listed in table 5.8.

Finally, the value of the normalization factors A obtained from the fit, the different correction factors and the final corrected value of the normalization constant, $A' = f^{Si} f^{t,s,ce} A$, are shown in table 5.9. The quoted uncertainties include the 0.3% uncertainty from the weighting function plus the assumed 1% uncertainty from the threshold correction method. The systematic effect of the particular Monte Carlo simulation package, GEANT3 or GEANT4, in these results is within 1%.

Once the yield normalization factors of each sample have been appropriately corrected by the threshold effects and inaccuracies in the proton intensity readout, we will apply now the saturated resonance method in order to cancel out other systematic effects. By comparing relative values of the 1.15 keV resonance with respect to the reference Au and Ag samples, systematic effects like absolute neutron flux

Setup	sample	$E_\circ$	A	f^{Si}	$f^{t,s,ce}$	A'
Bicron	Au 0.1×45	4.9 eV	0.811(3)	1.000(9)	1.045(4)	0.847(9)
	Fe 0.5×45	1.15 keV	0.780(10)	1.020(7)	1.002(4)	0.817(12)
	Ag 0.2×20	5.2 eV	0.812(3)	1.023(10)	1.026(4)	0.852(10)
	Au 1.0×20	4.9 eV	0.802(2)	0.997(7)	1.060(4)	0.847(10)
	Fe 1.5×20	1.15 keV	0.827(8)	1.001(7)	1.009(4)	0.856(11)
FZK	Au 0.1×45	4.9 eV	1.024(4)	1.000(22)	1.056(4)	1.081(25)
	Fe 0.5×45	1.15 keV	1.034(10)	1.011(16)	1.009(4)	1.082(20)
	Fe 2.0×45	1.15 keV	0.933(5)	1.084(17)	1.018(4)	1.056(18)

Table 5.9: *Yield normalization factors A fitted with SAMMY, correction factors for each measurement f^{Si}, $f^{t,s,ce}$ and final corrected yield normalization factor A'.*

normalization are factorized out. The total detection efficiency, which depends on the exact positioning of the detector with respect to the sample, or the exact volume of the liquid scintillator, is also unimportant since these effects would introduce only a multiplicative factor in the weighting function and therefore cancel out in the ratio too. The yield or normalization correction introduced by this procedure can be then expressed as

$$f^{Sat} = \frac{1}{A'_{ref}}, \tag{5.15}$$

where A'_{ref} designates the corrected normalization factor of the corresponding normalization sample.

The values of the corrected normalization factor for the 1.15 keV resonance in ^{56}Fe+n relative to the respective reference sample values,

$$A^{rel} = f^{Sat}A' = \frac{A'}{A'_{ref}}, \tag{5.16}$$

are given for the different sample/reference sample combinations in figure 5.10.

The average value of the relative yield normalization factors, $\bar{A}^{\text{rel}} = 0.992(0.011)$, which is compatible with the neutron intensity uncertainty described in section 4.5. As was commented at the beginning, in order to exclude the uncertainty due to the flux intensity dependence with the neutron energy, only the relative values of A^{rel} will be compared. In this way the uncertainty due to the PHWT itself is better isolated. For this reason, the relative values in the plot shown in figure 5.10 have been normalized to the average value $\bar{A}^{\text{rel}}$ in order to enable a better inter comparison. This figure shows the uncertainty with which the integrated yield of the 1.15 keV ^{56}Fe+n resonance could be determined. All the values, including those corresponding to thick samples agree within the error bars of 2-3% and their RMS deviation is 1.7%.

It can be therefore concluded that the PHWT applied to C_6D_6 data with Monte Carlo calculated weighting factors is able to achieve an accuracy better than 2% [7].

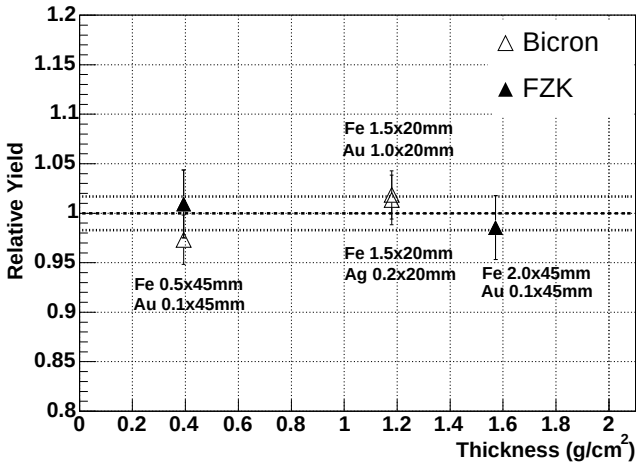

Setup	sample/reference	A^{rel}
Bicron	Fe 0.5/Au 0.1	0.965(22)
	Fe 1.5/Ag 0.2	1.005(22)
	Fe 1.5/Au 1.0	1.010(21)
FZK	Fe 0.5/Au 0.1	1.001(32)
	Fe 2.0/Au 0.1	0.977(30)

Figure 5.10: *Normalized ratio between theoretical and experimental reaction yields for the 1.15 keV resonance. The dotted line shows the RMS deviation.*

5.8 Summary and conclusions

The particular sensitivity of the PHWT to the 1.15 keV resonance in ^{56}Fe+n, makes it an excellent benchmark for testing the accuracy which can be achieved with this technique.

The experiment carried out at n_TOF, using two types of C_6D_6 detectors to measure samples of different sizes, yielded a result with an accuracy better than 2%. In this way, the ability of existing Monte Carlo packages to simulate realistic response functions, and obtain accurate weighting functions, has been experimentally demonstrated.

Nevertheless, it is important to note, that the mentioned accuracy would not be obtained if the different sources of systematic accuracy were not well under control. In this sense, the Monte Carlo technique becomes once more an essential tool in order to calculate accurate yield correction factors.

The same procedure presented here to analyze this capture data will be followed in the next two chapters, related with the measurement of the neutron capture cross section of ^{209}Bi and ^{207}Pb.

Chapter 6

^{209}Bi neutron capture cross section

The ^{209}Bi nuclide constitutes the heaviest stable isotope[1] build up by the s-process in the stars. Capture on this isotope determines its survival in AGB stars, but also the production of the unstable ^{210}Bi, which α-decays enhancing the abundance of ^{206}Pb. Accurate capture data on this isotope is also of primary interest in nuclear engineering, since it determines the radiotoxicity of an ADS reactor based on a lead-bismuth core.

Historically, the main experimental difficulty for the accurate measurement of this isotope's cross section was the neutron sensitivity of the experimental setup. Due to the large scattering to capture ratio of most of its resonances, contamination due to neutrons is of particular concern in this case. Furthermore, the neutron capture cross section of ^{209}Bi is very small due to the 126 neutron and 82 proton closed shell core, leaving only one loosely bound proton.

Taking advantage of the very optimized capture setup at n_TOF, we have performed an improved measurement of this isotope. Due to its soft gamma ray spectrum, threshold effect corrections are also particularly important. A detailed analysis of the resolved resonance region has been carried out taking under special consideration the different sources of systematic uncertainty. The obtained results are presented at the end of this chapter together with a comparison to previous experiments and evaluations.

6.1 Experiment

As was discussed in chapter 2, the accurate measurement of resonances with large scattering to capture ratio, needs of an optimized experimental setup in terms of very low sensitivity to neutrons. The n_TOF capture setup, with the FZK-C_6D_6 detectors, constitutes an excellent approach as has been discussed in section 4.8.

With the aim of reducing the in beam gamma rays induced background (appendix E), both FZK-C_6D_6 detectors were displaced backwards at 7.8 cm from the

[1] To be exact, ^{209}Bi has been recently found to be unstable with respect to α-decay [77], but its measured half life is of $1.9(2)\times10^{19}$yr.

sample's plane. This geometry also corresponds to an average detection angle with respect to the beam direction of ∼125°, thus minimizing the effects of the primary gamma ray angular distribution. Corrections due to the latter effect are certainly negligible in the analysis of this isotope due to its average high multiplicity of 4-5. A deeper study of the angular distribution effect will be presented with the analysis of the ^{207}Pb (n,γ) reaction in section 7.1.1.

Some relevant information about the ^{209}Bi sample has been summarized in table 6.1. The total number of protons invested in this measurement and the sample employed for the yield normalization are shown at the bottom of the table too. Assuming a nominal average rate of 5×10^{12} protons each 2.4 seconds, the measurement lasted for a total time of about 60 hours, in which $\sim87\times10^3$ proton bunches were used.

A	209
Z	83
S_n	4.60458(13) MeV
I^{Π} (target)	$9/2^-$
J^{Π} (GS compound)	1^-
Abundance	100 %
Sample mass	18.90453 g
Thickness	6.08 mm
Diameter	20.0 mm
Enrichment	100%
Nr. Protons	4.367828×10^{17}
Norm. Sample	Au 1 × 20 mm

Table 6.1: ^{209}*Bi sample and isotope properties.*

6.2 Data reduction

The ^{209}Bi(n,γ) capture data was sorted and reduced according to the general procedure shown in chapter 4 and the yield was calculated following the approach developed in chapter 5 for the 1.15 keV resonance of ^{56}Fe. The whole data reduction procedure will not be described here again, but only the two more particular and delicate stages. These are related with the calculation of the weighting function for the ^{209}Bi sample (section 6.2.1) and the yield correction factors (section 6.2.2).

6.2.1 Weighting function

The main obstacle in the analysis of this isotope was a difficulty found in the conventional procedure of obtaining the WF as a polynomial function. As was

already introduced in chapter 2, we have found that for thick samples of large Z isotopes a polynomial WF may not be appropriate.

In order to illustrate better this problem, we will show first the calculation of a polynomial WF, following the usual procedure described in section 2.2 (which was successfully employed for the validation samples in section 5.3). After checking the proportionality goodness and accuracy of the obtained polynomial WF, we will see that such a WF is not valid. The novel technique based on a regularization method will be applied in a subsequent section in order to obtain a better solution.

Polynomial weighting function

A set of 13 monoenergetic gamma rays were Monte Carlo simulated using the GEANT4 code, with energies 0.1, 0.2, 0.5, 0.7, 1,...,9 MeV. By minimizing the equation 2.9, one obtains the parameters of the WF given in table 6.2.

Sample	a_0	$a_1\ (MeV^{-1})$	$a_2\ (MeV^{-2})$	$a_3\ (MeV^{-3})$	$a_4\ (MeV^{-4})$
^{209}Bi	5.7100864	11.1721595	17.6742173	-2.07732342	0.0847137301

Table 6.2: *Coefficients of the polynomial WF for ^{209}Bi.*

The Monte Carlo simulated response functions together with the obtained polynomial WF are shown in figure 6.1.

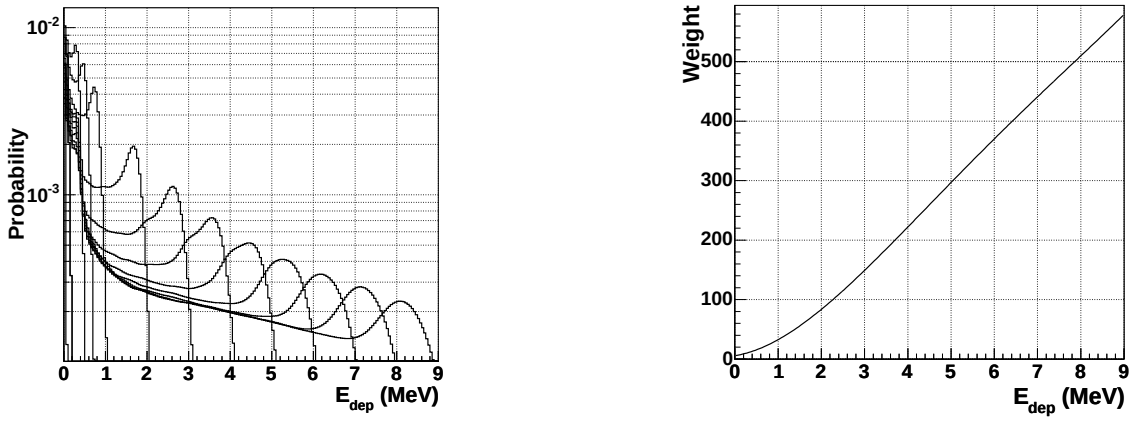

Figure 6.1: *(Left) Monte Carlo simulated response functions. (Right) Polynomial WF.*

Now, one must check if the obtained WF fulfills the proportionality condition between efficiency and energy (equation 2.2) by computing the ratio

$$\frac{\sum_i W_i R_{i,j}}{E_j}, \tag{6.1}$$

which should be close to one for each simulated gamma ray E_j. The result is shown in figure 6.2. In this figure, very high deviations between 80% and 40% can

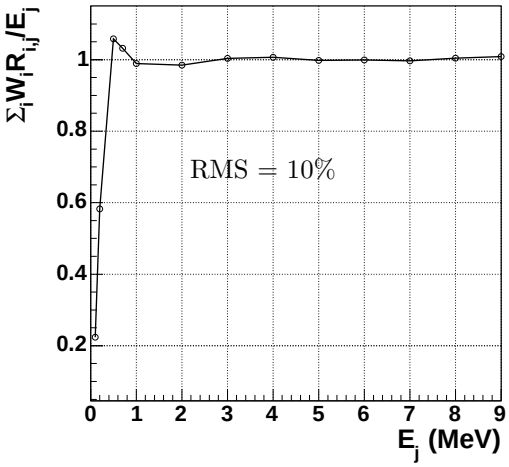

Figure 6.2: *Proportionality check for the polynomial WF.*

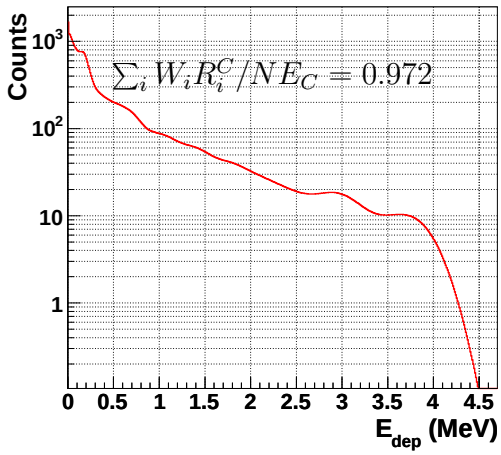

Figure 6.3: *Uncertainty of the polynomial weighting function.*

be observed for gamma ray energies below 500 keV. As a consequence, the RMS deviation of equation 6.1 is of ∼10%.

Let us show now, the deviation introduced in a capture experiment by such a weighting function. In a similar way as we did for the 1.15 keV resonance in ^{56}Fe+n, we obtain by Monte Carlo simulation the response distribution $R_i^C = \sum_{c=1}^{N} R_i^c$ for a large number ($N = 5 \times 10^6$) of realistic nuclear cascades corresponding to capture on the resonance of ^{209}Bi+n at 802 eV. The calculation of the nuclear cascades for this isotope will be shown in the next section. For a WF free of systematic deviation, the weighted sum of the nuclear cascade's response function, should be equal to the number of simulated cascades N times the cascade energy E_C, i.e., the ratio

$$\frac{\sum_i W_i R_i^C}{N E_C} \tag{6.2}$$

should be equal to one. Performing this calculation we obtain the result which is shown in figure 6.3.

This means that using this polynomial WF for the analysis of the capture data of ^{209}Bi+n, one would introduce an additional systematic deviation of about ∼3% (to be compared with the 2% systematic accuracy of the PHWT itself found in chapter 5).

At this point we tried to improve the polynomial WF calculation by simulating a larger number of gamma rays. Particularly at lower energy we calculated the additional responses for 10 gamma rays between 0 and 1 MeV with energies 0.1,0.2,...,0.9,1.0 MeV. We also studied the effect of having a higher degree polynomial WF, increasing it up to 8 (9 coefficients in total). Finally we investigated

the issue of the minimization procedure. Instead of applying the unweighted least squares estimation (equation 2.9 with $p_i = 1$) we tried several energy dependent weights, $p_i = E_i^n$, with n=1, 2, etc. But non of these exercises showed an improvement in the result of the polynomial WF. Both equation 6.1 and equation 6.2 showed still in all cases large deviations.

We were able to overcome this difficulty, by applying the mathematical method described in section 2.2.2. In the following section, we will apply it to the present problem, in order to obtain a WF with a negligible systematic deviation for the sample of ^{209}Bi.

Pointwise weighting function

According to the procedure described in section 2.2.2 we have to build the system of equations

$$(\mathbf{R}^T\mathbf{R} + \lambda\mathbf{H})\vec{W} = \mathbf{R}^T\vec{E}. \tag{6.3}$$

$\mathbf{R} = \{R_{ji}\}$ is the response matrix containing $j = 1, \ldots, m$ response distributions, histogramed with $i = 1, \ldots, n$ bins. Since the dimension of the solution $\vec{W}$ is the same as the number of columns n in the response matrix $\mathbf{R}$, we will histogram now the reponse distributions with a thinner binning of 10 keV, in order to obtain a weighting function with enough resolution. Given the thin binning, it is convenient to simulate now a large number of response distributions in order to have enough information across the whole energy range. On the other side, given the small neutron binding energy of bismuth, one needs (considering the instrumental resolution broadening and the kinetic neutron energy range between 0 and 1 MeV) a weighting function ranging only up to 5-5.5 MeV. Therefore, we simulate a total of $m = 120$ response distributions in energy steps of 50 keV, i.e., from $E_1 = 50$ keV up to $E_{120} = 6$ MeV. Each simulated response distribution, appropriately broadened by the instrumental resolution, is recorded in a historam of $n = 800$ channels. These response functions are shown on the left part of figure 6.4.

Once the appropriate dimensions $m \times n$ of the $\mathbf{R}$ matrix have been decided, one can construct the matrix $\mathbf{H}$ using the simple rule given by equation 2.17 and equation 2.18. The only information needed for this calculation is the horizontal dimension of the response matrix $\mathbf{R}$, which in this case was chosen as $n = 800$.

The last parameter to be determined in equation 6.3 is the Lagrange multiplier λ. The L-plot (see sec. 2.2.2) was drawn for a serie of λ values in order to find a good initial value. Through an iterative procedure one finally meets a value of λ which gives the best solution of $\vec{W}$. Of course, the goodness of the solution $\vec{W}$ can be always checked by substitution of it back into the original equation $\vec{W}\mathbf{R} = \vec{E}$. The solution of $\vec{W}$ shown in the right part of figure 6.4, was obtained for $\lambda = 9 \times 10^{-6}$.

With the pointwise WF, the proportionality condition given by equation 6.1 is much better satisfied than with the polynomial WF, showing a deviation of around 4% at 200 keV and a maximum discrepancy of 25% is found locally below 100 keV

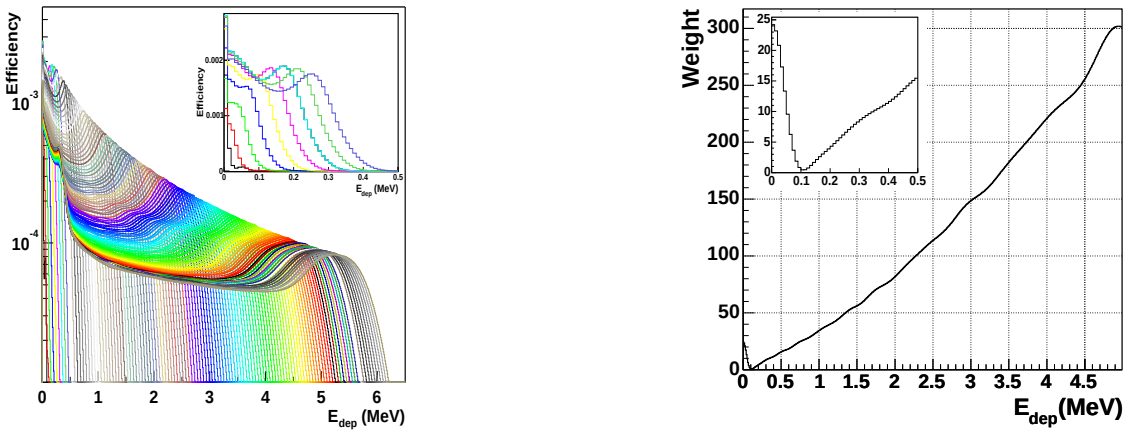

Figure 6.4: *(Left) 120 Monte Carlo simulated response functions in steps of 50 keV. (Right) Pointwise WF obtained with the linear regularization method.*

(figure 6.5). The RMS deviation is of 0.238%, much better than the 10% deviation of the polynomial WF obtained before.

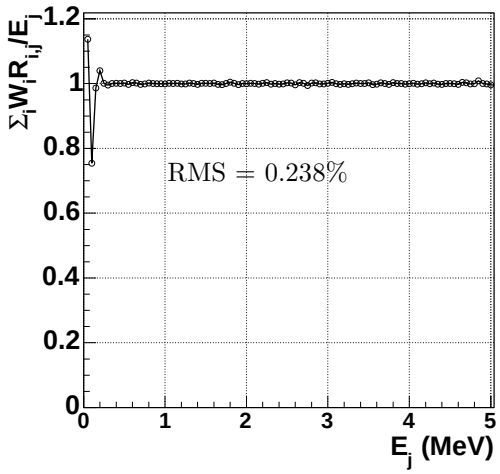

Figure 6.5: *Proportionality check for the pointwise WF.*

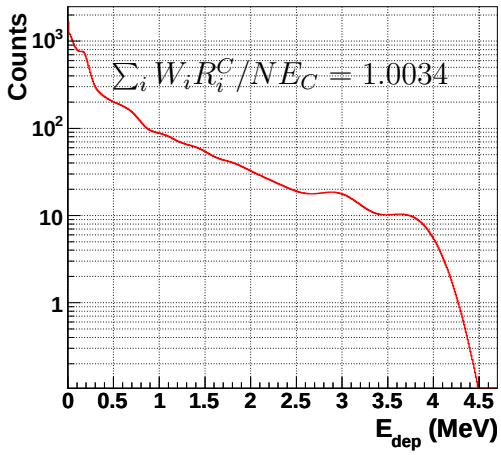

Figure 6.6: *Uncertainty of the pointwise weighting function.*

Furthermore, the systematic deviation (calculated with equation 6.2) introduced by the new pointwise WF is negligible, of about 0.34% (figure 6.6).

The inset shown on the right part of figure 6.4, shows the main difference found with respect to the polynomial WF. The abrupt change in the slope of the WF at ∼100 keV turns out impossible to be reproduced with a single polynomial WF in the energy range 0-5 MeV, as was found afterwards trying to fit a 9^{th} degree polynomial to the obtained pointwise WF. Several polynomial functions (in different

energy ranges) would be required in order to reproduce the pointwise WF with an equivalent accuracy.

The reason for the WF to increase going to lower energy is because the response function of the gamma rays below 100 keV decreases due to the increasing absorption in the target and dead materials. This effect can be appreciated in the inset shown in the left part of figure 6.4.

6.2.2 Correction of systematic effects

Threshold, γ-summing, conversion electron and isomeric state

As has been described in detail in section 5.6, any capture experiment employing total energy detectors is necessarily affected by three different experimental sources of uncertainty related with the threshold of the detectors, the summing probability of two or more gamma rays and the internal conversion electron process.

In the case of bismuth, there is an additional effect which needs to be considered. This isotope has an isomeric state at 271.31 keV with a half life of 3.04×10^6 years.

The procedure to account for the latter effect will be shown later. We will start the description of the correction due to the former three usual effects, which has been calculated using the nuclear cascades code described in section 5.5.

The 802 eV resonance of this nuclide was chosen for testing the different statistical model elements (level density model and gamma strength function), because this resonance shows the highest peak cross section and enabled us to obtain an experimental spectrum with enough statistics and substract the background in an accurate way.

Concerning the level density parameterization, the three different models listed in table 5.3 have been tested with ^{209}Bi. In figure 6.7, the results obtained with these parameterizations are compared with the experimental spectrum of the 802 eV resonance. The influence of the particular level density model or parameterization in the correction factor (calculated for a threshold of 250 keV) was of only 0.6% at maximum. Therefore, any of them would be valid and we took the Constant Temperature model (Egidy).

For the gamma ray strength function, the dominant E1 strength was calculated with a generalized Lorentzian, whereas for M1 and E2 strengths a standard Lorentzian was employed.

It is usually recommended [75] to adjust the Lorentzian parameters to experimental values of the GDR peak cross section ($\sigma_\circ$), but unfortunately there is no measurement performed on ^{210}Bi. In such cases, there exist a general parameterization of the GDR parameters as a function of the atomic mass A [75]. The latter is shown for the M1 strength in the right part of figure 6.8. However, the nominal value obtained with this parameterization for bismuth (open circle) did not reproduce well the experimental deposited energy spectrum. This is not surprising considering the high systematic uncertainty associated with this parameterization (about 300% at $A = 210$) and the large scattering in the measured M1 strengths for isotopes with

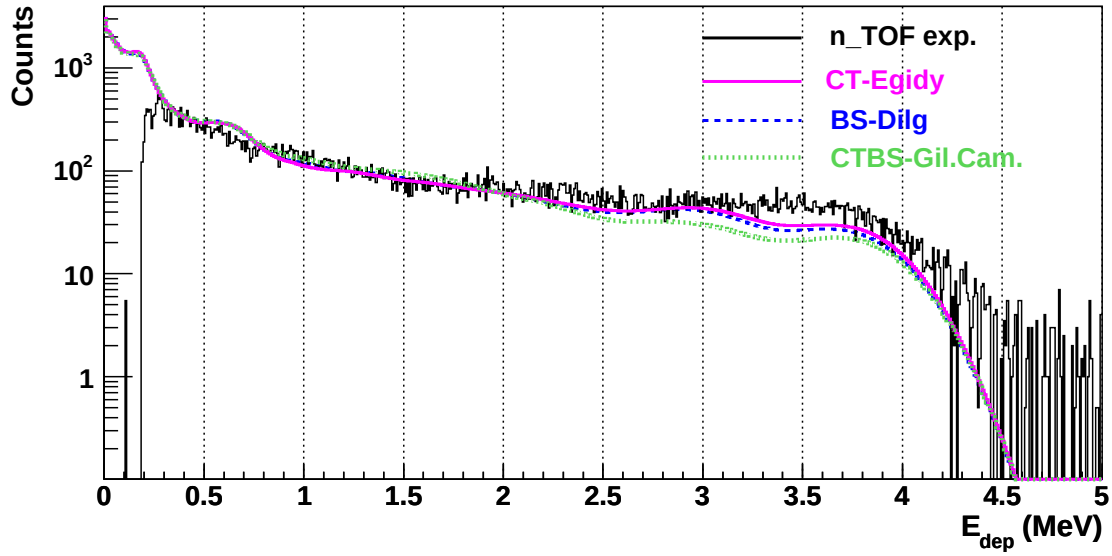

Figure 6.7: *Comparison between the deposited energy histogram predicted by several nuclear level density models and the spectrum measured at n_TOF for the 802 eV resonance.*

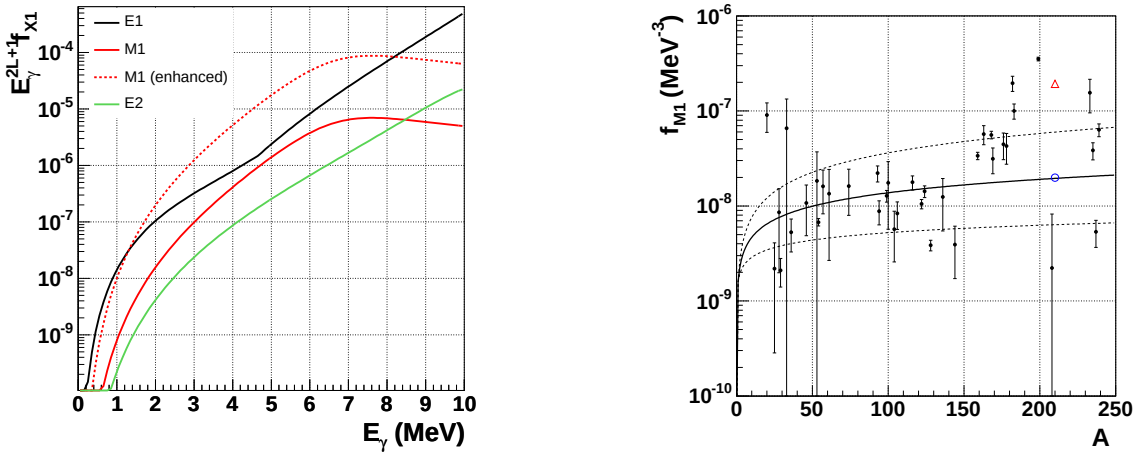

Figure 6.8: *(Left)* ^{210}*Bi electromagnetic strengths, generalized Lorentzian for E1 and standard Lorentzian for M1 and E2 transitions. The dashed curve stands for the enhanced M1 value adopted in this work. (Right) Comparison of M1-strength measurements plotted against the atomic mass. The solid line represents the RIPL-parameterization. The open triangle stands for the value adopted here, whereas the open circle corresponds to the strength predicted by the parameterization.*

high A (see again right part of figure 6.8). Therefore, one has relatively high freedom in adjusting manually the parameterized intensity of the M1 strength at least. We went from the original value of 1.55 mb to 19.5 mb (open triangle), which reproduced much better the shape of the experimental histogram.

Finally, the electromagnetic strength parameters are summarized in table 6.3. Appart of the adjusted M1 strength $\sigma_\circ$, the rest of values correspond to the parameterization recommended in reference [75]. The corresponding Lorentzian functions describing the E1, M1 and E2 transitions strengths are shown in the left part of figure 6.8.

	$E_\circ(MeV)$	$\Gamma_\circ(MeV)$	$\sigma_\circ(mb)$
E1	13.693	3.852	625.64
M1	6.898	4	19.503
E2	10.6	3.59	5.08

Table 6.3: *Electromagnetic strength parameters for* $^{209}Bi+n$.

The other resonances beyond 802 eV have lower neutron capture cross section and unfortunately the accumulated statistics in this experiment did not suffice to perform a similar detailed comparison for capture levels with different spin and parity. Therefore, for the yield correction calculation of the higher energy resonances, we had to rely on the statistical model parameters adjusted as shown above to the 802 eV resonance.

In order to account for the 9^- metastable state at 271 keV, we included this isomeric level in the discrete experimental part of the bismuth cascade. The exact amount of correction depends on the particular spin and parity of the resonance under analysis. For higher spins, the population of the isomeric state increases, thus enhancing the corresponding correction factor too. Using the statistical model of the nucleus, we estimated only a 6% population for 3^+ resonances whereas for deexcitations from 6^+ levels the isomeric state would be populated to about 44%.

In table 6.4, the calculated yield correction factors (using a reference threshold of 200 keV) are shown. They have been classified by spin and parity of the resonance. In the second column the estimated population of the metastable state is shown. In the third (fourth) column the yield correction factor not including (including) the isomeric effect is given. The ratio of the last two is shown in the fifth column in order to illustrate the effect of the isomeric state in the yield. In the last two columns of this table, the correction factor and the relative change in the yield are shown for the hypothetic case that the isomeric state is 100% populated. We can conclude, that the influence of the isomeric state in the yield correction factor is indeed small, but for the higher spin resonances at least it needs to be included.

In order to estimate the uncertainty associated with $f^{t,s,ce,m}$, let us compare this quantity with the hypothetic case $f^{t,s,ce,100\%m}$ for 4^- and 5^- resonances. These resonances are populated in thermal neutron capture reactions. In a recent mea-

Reso. J^π	popul. (%)	$f^{t,s,ce}$	$f^{t,s,ce,m}$	Δ^m (%)	$f^{t,s,ce,100\%m}$	$\Delta^{100\%m}$ (%)
3^+	6	1.125(2)	1.124(2)	0.1	1.103(2)	2.0
4^-	8	1.136(2)	1.131(2)	0.4	1.118(2)	1.6
4^+	9.3	1.144(2)	1.143(2)	0.1	1.116(2)	2.5
5^-	23.4	1.145(2)	1.137(2)	0.7	1.109(2)	3.2
5^+	22	1.151(2)	1.142(2)	0.8	1.119(2)	2.8
6^+	44	1.155(2)	1.134(2)	1.8	1.114(2)	3.7

Table 6.4: *Yield corrrection factors for ^{209}Bi. Effect of the bismuth metastable state in the yield correction factor, calculated for a threshold of 200 keV. Shown uncertainty is only statistical.*

surement [78] of the isomeric state population using a thermal neutron flux, a value of 51(5)% was obtained. Comparing with the relative populations obtained with the statistical model and the effect in the correction factor, one can conclude that a systematic uncertainty of 1% should be appropriate for $f^{t,s,ce,m}$.

Finally, the resulting deposited energy spectra for different spin and parity resonances are shown in figure 6.9. As is to expect, the shape of these spectra (and therefore the correction factor too) is very similar for resonances of same spin and parity, independently of the resonance's energy. The threshold correction factor, is computed from these spectra using equation 5.8.

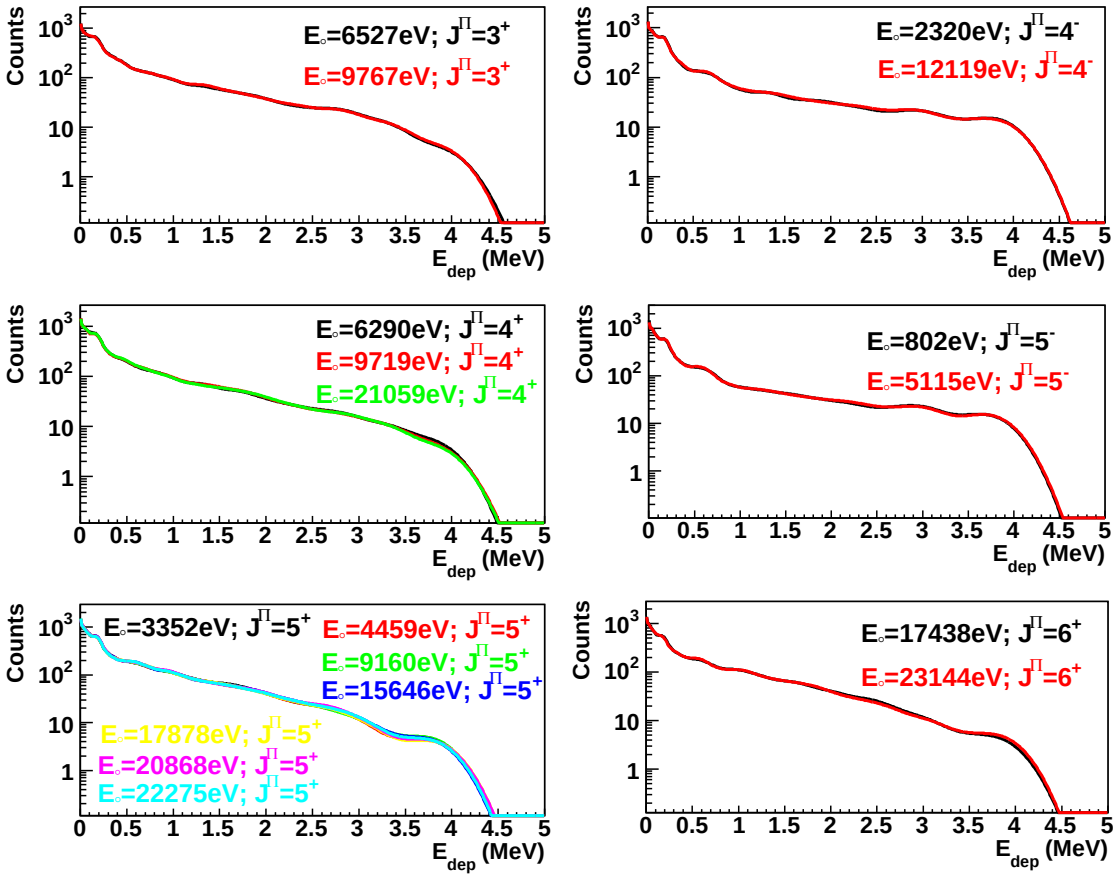

Figure 6.9: *Deposited energy histograms predicted with the statistical model of the nucleus for several resonances of* ^{209}Bi*. Similar shapes for* J^{Π} *resonances yield also similar correction factors (see table 6.4).*

6.3 Analysis

The yield is calculated as described in section 4.1,

$$Y'(E_n) = f^{ns} \times f^{Si} \times f^{t,s,ce,m} \times f^{Sat} \times Y(E_n), \tag{6.4}$$

where $Y(E_n)$ designates the uncorrected experimental yield, calculated as N^w/N_nE_c. Note that N^w refers now to weighted count rate using the pointwise weighting function obtained in section 6.2.1. N_n is the number of neutrons calculated as the product of the neutron intensity I_n (section 4.5) and the number of 7×10^{12} proton bunches (table 6.1). E_c is the capture energy. f^{ns} designates the neutron sensitivity correction factor (section 4.8). f^{Si} stands for the SiMon renormalization to correct the WCM proton intensity values. $f^{t,s,ce,m}$ accounts for the systematic effects due to the threshold, γ-summing, conversion electron and isomeric state, as described in section 6.2.2. Finally, f^{Sat} corresponds to the yield calibration constant obtained from the fit of the 4.9 eV saturated resonance of the gold sample (section 4.6).

In a resonance analysis of this capture yield, one usually evaluates the total capture area or integral capture cross section of each resonance. However, if some more information is provided, e.g. from other type of measurements, additional knowledge on the resonance parameters of each resonance can be derived.

Ideally, the resonance parameter analysis should proceed as follows [76],

1. From transmission data, one usually knows,

$$\begin{aligned} E_\circ, \Gamma_n, \Gamma, g \qquad & \text{for} \quad l = 0, \\ E_\circ, g\Gamma_n \qquad & \text{for} \quad l \geq 0. \end{aligned}$$

2. The previous information, can be used in capture data to determine,

$$\begin{aligned} E_\circ, \Gamma_\gamma \qquad & \text{if} \quad \Gamma_n,\ g \text{ are known}, \\ E_\circ, g\Gamma_\gamma \qquad & \text{if only} \quad g\Gamma_n \text{ is known}. \end{aligned}$$

3. Some thin p- and d-wave resonances have not been observed in transmission measurements. Hence, from the capture data one can derive only the area of the resonance,

$$E_\circ, g\Gamma_n\Gamma_\gamma/\Gamma \qquad \text{if} \quad g\Gamma_n \text{ is not known}.$$

The R-matrix analysis code SAMMY [49] has been employed to fit individually the corrected capture yield Y' of each observed resonance in bismuth. The procedure followed here was similar to that described in section 5.7.1. Double scattering, self-shielding and finite size corrections to single scattering were taken into account with this code.

A total number of 21 resonances were identified in the ^{209}Bi(n,γ) data, in the energy range from 800 eV up to 23150 eV. In this energy interval there are three additional resonances present in the Mughabghab compilation [79]. One s-wave resonance at 15510 eV, a very weak p-wave resonance at 9375 eV with a capture area or radiative kernel $K_r = 0.8(3)$ meV and finally another resonance of unknown orbital momentum l at 14860 eV with $K_r = 10.5(9)$ meV. Nevertheless, we did not expect to observe these three resonances since they are buried in the in-beam gamma ray induced background (see appendix E). The reason why we were not able to see resonances in bismuth beyond 23 keV is also due to the high in-beam gamma ray background. This gamma ray background is mainly originated (see appendix E) by capture on the water of the moderator/cooling of the spallation target. It has been the major limitation of the present measurement. Substitution of the water by heavy water is expected to reduce the background by two orders of magnitude. It is foreseen to extend the present measurements whenever this substitution takes place.

The background is better treated by fitting it to a constant term rather than substracting it. For this purpose each capture resonance was analyzed with a wide enough neutron energy window covering its both sides. The fitting function used in SAMMY had the form,

$$Y' = Y^f(E_\circ, \Gamma_n, \Gamma_\gamma) + B, \tag{6.5}$$

where Y' is the corrected experimental yield (equation 6.4). B is a constant term to describe the background. Y^f designates the yield curve fitted to the experimental one Y' and calculated by SAMMY using the Reich Moore formalism. In the last equation, $E_\circ, \Gamma_n$, and Γ_γ are the parameters describing the resonance under study. Following the analysis guidelines sketched before, for those resonances where one or several transmission measurements give an accurate value of Γ_n, we fixed this parameter to that experimental value and only the energy of the resonance and the gamma width are derived by SAMMY using the Bayes theorem. In some cases where the resonance is too broad (s-wave resonances) or the statistics are not high enough, the energy of the resonance was also kept fix.

The statistical and systematic uncertainties of the correction factors in equation 6.4 were taken into account in the resonance analysis by including the data covariance matrix in the fitting procedure. From this equation, the covariance matrix of the corrected yield Y' was calculated as,

$$\sigma_{Y'_i,Y'_j} = Y_i Y_j \sigma_f^2 + f^2 \sigma_{Yi}^2 \delta_{i,j}. \tag{6.6}$$

Where σ_f stands for the uncertainty of all the corrective multiplicative factors, $f = f^{ns} \times f^{Si} \times f^{t,s,ce} \times f^{Sat}$.

The value used for Γ_n and the derived $E_\circ$ and Γ_γ together with the computed radiative kernel for each observed resonance is given in table 6.5. The statistical spin factor g was calculated from the total spin J which was in general taken from the literature [79, 80].

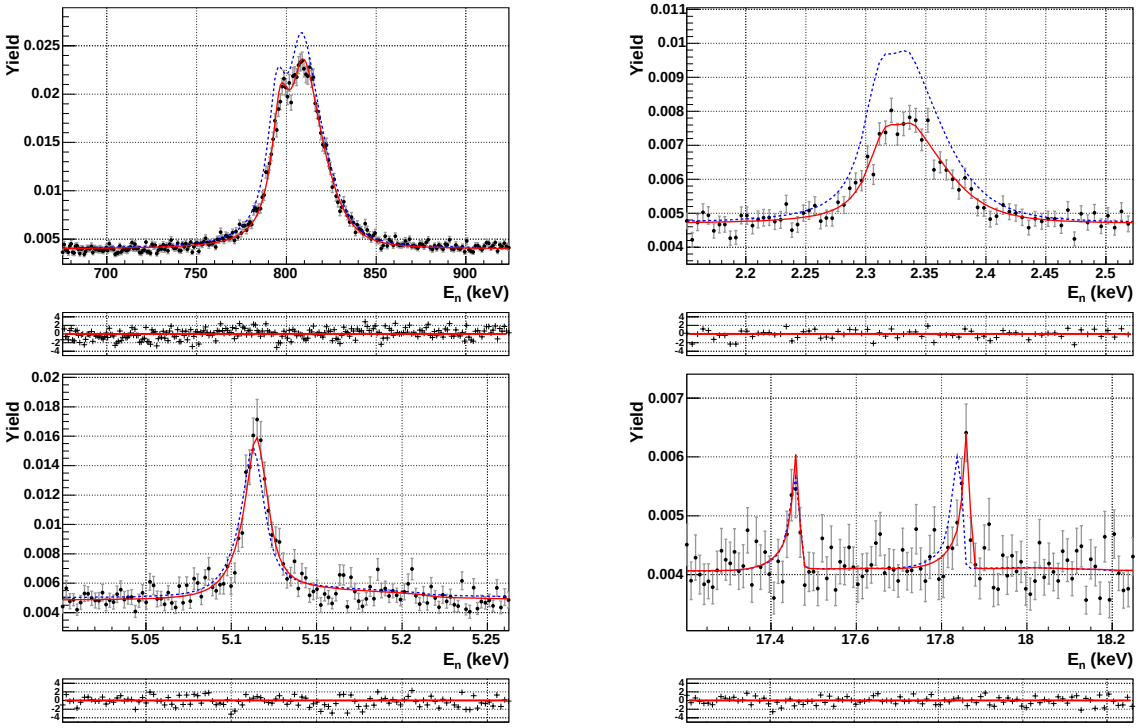

Figure 6.10: *First three s-wave resonances in ^{209}Bi+n and a doublet of p-wave resonances at ∼17 keV. The dashed line stands for the original ENDF cross section, whereas the solid curve corresponds to the yield, $Y^f + B$, fitted with SAMMY to the n_TOF experimental yield data points, Y'.*

The details of each resonance fit will be given in the following section, where the results obtained here are compared with those from previous experiments and the evaluated data files.

$E_\circ$ (eV)	l	J	Γ_n (meV)	Γ_γ (meV)	$g\Gamma_\gamma\Gamma_n/\Gamma$ (meV)
801.6(1)	0	5	4309(145)	33.3(12)	18.2(6)
2323.8(6)	0	4	17888(333)	26.8(17)	12.0(8)
3350.83(4)	1	5	87(9)	18.2(3)	9.5(2)
4458.74(2)	1	5	173(13)	23.2(22)	11.3(11)
5114.0(3)	0	5	5640(270)	65(2)	35.3(11)
6288.59(2)	1	4	116(18)	17.0(17)	6.7(7)
6525.0(3)	1	3	957(100)	25.3(14)	8.6(5)
9016.8(4)	1	6	408(77)	21.1(14)	13.0(9)
9159.20(7)	1	5	259(45)	21.4(21)	10.9(11)
9718.910(1)	1	4	104(22)	74(7)	19.5(21)
9767.2(3)	1	3	900(114)	90(8)	28.7(26)
12092.2(8)	1	5	1000	59(5)	31(3)
12118.6	0	4	258888(20000)	52(5)	23(2)
12285(3)	1	5	5273(272)	20(2)	11.0(10)
15649.8(1.0)	1	5	1000	47(4)	20.2(17)
17440.0(1.3)	1	6	1538(300)	32(3)	20.4(18)
17839.5(9)	1	5	464(181)	43(4)	21.7(20)
20870	1	5	954(227)	34.4(33)	18.3(17)
21050	1	4	7444(778)	33(3)	14.8(13)
22286.0(9)	1	5	181(91)	33.6(32)	15.1(15)
23149.1(1.3)	1	6	208(154)	25.3(25)	14.7(15)

Table 6.5: *Resonance parameters and radiative kernel determined for* ^{209}Bi.

The values reported for the radiative kernel of each resonance (last column in table 6.5) include only the uncertainty on the fitted parameter Γ_γ.

6.4 Results and discussion

The results obtained in this work for the radiative kernel are shown in table 6.6 compared with those yielded by two previous experiments due to Mutti et al. [81] and Macklin et al. [24]. The latter two are briefly described below.

With the aim of giving a clear overview and general comparison of the several experimental data sets mentioned above, these have been plotted in figure 6.11.

The radiative kernels computed from the resonance parameters provided in the Mughabghab compilation [79] and the evaluated data files ENDF and JENDL, have been also included in table 6.6 for comparison. This information is compared with the capture areas measured at n_TOF in figure 6.12.

Below follows a description of the experimental and evaluated information mentioned above, which will be compared later with the results obtained in this work.

- Mutti et al.: this information corresponds to an experiment performed in 1997 and was extracted from reference [81]. In this experiment, the PHWT was also used to determine the neutron capture cross section. The method to obtain the WF was the experimental technique [82] based on (p,γ) reactions rather than the MC simulation to obtain response functions. The measurement took around 800 hours and was performed at 59 m from the neutron source, the Geel electron linear accelerator (GELINA). The setup used in this experiment consisted of four commercial C_6D_6 liquid scintillators with Al-canning and a carbon fibre vacuum pipe to host the 4×80mm bismuth sample. The detectors were placed perpendicularly to the neutron beam direction. The neutron flux was measured simultaneously using an ionization chamber. For the relative calibration the 5.2 eV Ag resonance was measured at a 30 m distance from the neutron source. The measured capture yield spectrum was analysed using the R-matrix shape fitting code FANAC. Errors for the capture area are only statistical, except in the case of *s*-waves, for which an uncertainty of 50% of the correction for resonance scattering was also considered. The correction due to the isomeric level of bismuth at 271 keV is apparently not included, but as was described in section 6.2.2, this may amount 2% at maximum.

- Macklin et al.: information concerning this experiment was taken from reference [24]. The original results (radiative kernels) given in that reference had to be corrected by a factor $f = 1.0360$ according to a corrigendum [83]. This correction factor has an uncertainty of about 5%.

  In the experiment carried out at ORELA in 1976, two bismuth samples of 0.7 mm and 3.9 mm were measured at a distance of 40.123 m from the neutron source. The neutron energy resolution is then near $\Delta E/EFWHM = 1/600$. A set of two C_6F_6 liquid scintillators was used, and eventually scattered neutron sensitivity corrections were large ($\sim$50% for the 12.1 keV resonance).

  The measuring range at ORELA started at 2.6 keV, thus missing the first two

resonances of ^{209}Bi+n. The radiative kernel reported for the 2.3 keV resonance corresponds to an "estimation" made at ORNL by the authors of reference [24].

- Mughabghab [79]: compilation of previous existing experimental data, based mostly on the experiment of Macklin et al. described above.
- ENDF: (American) Evaluated Nuclear Data Files, Base VI release 8, available from IAEA. Evaluators A. Smith, D. Smith, P. Guenther, 1989.
- JENDL: Japanese Evaluated Nuclear Data Library, version 3.3, available from IAEA. Evaluators N. Yamamuro, A. Zukeran, September 2001.

Nr.	$E_\circ$ (eV)	l	this work	Mutti et al.	Macklin et al.	Mughabghab	ENDF-BVI	JENDL3.3
1	802	0	18.2(6)	16.5(9)	—	21.1	21.109	21.109
2	2324	0	12.0(8)	10(3)	21(10)[a]	20.6	20.647	20.647
3	3351	1	9.5(2)	10.30(3)	11.3(1)	11.3(1)	16.768	11.602
4	4459	1	11.3(11)	10.35(4)	11.20(20)	11.2(2)	12.179	12.179
5	5114	0	35.3(11)	29.7(1.1)	42.0(6)	33(2)	32.652	32.652
6	6288	1	6.7(7)	6.19(4)	6.6(2)	7.1(2)	13.283	9.684
7	6525	1	8.6(5)	8.78(6)	9.4(2)	12.3(2)	8.693	15.794
8	9017	1	13.0(9)	10.18(8)	11.0(4)	11.0(4)	14.152	12.074
9	9159	1	10.9(11)	8.75(8)	9.9(4)	9.9(4)	10.825	10.825
10	9719	1	19.5(21)	20.20(11)	22.5(6)	22.5(6)	21.264	21.265
11	9767	1	28.7(26)	21.41(11)	22.0(6)	22.0(6)	15.728	24.030
12	12092	1	31(3)	8.13[b]	8.0(9)	8.0(9)	—	—
13	12119	0	23(2)	15.23[b]	51(8)	52.8(10.4)	52.626	52.626
14	12285	1	11.0(10)	2.8[b]	3.7(7)	3.7(7)	—	—
15	15650	1	20.2(17)	18.1(2)	22.6(1.3)	22.6(1.4)	—	—
16	17440	1	20.4(18)	14.5(2)	17.3(1.0)	17.3(1.0)	22.368	18.992
17	17839	1	21.7(20)	18.9(2)	22.5(1.0)	22.5(1.0)	24.554	20.447
18	20870	1	18.3(17)	13.6(2)	13.3(9)	13.3(9)	14.598	14.598
19	21050	1	14.8(13)	14.1(3)	16.4(1.2)	16.4(1.2)	14.784	18.052
20	22286	1	15.1(15)	17.8(3)	18.9(1.1)	18.9(1.1)	—	—
21	23149	1	14.7(15)	6.1(2)	11.6(1.1)	11.6(1.1)	14.659	12.615

Table 6.6: *Values obtained for the capture area of ^{209}Bi compared with other works. (a) Estimated, not measured. (b) Private comunication.*

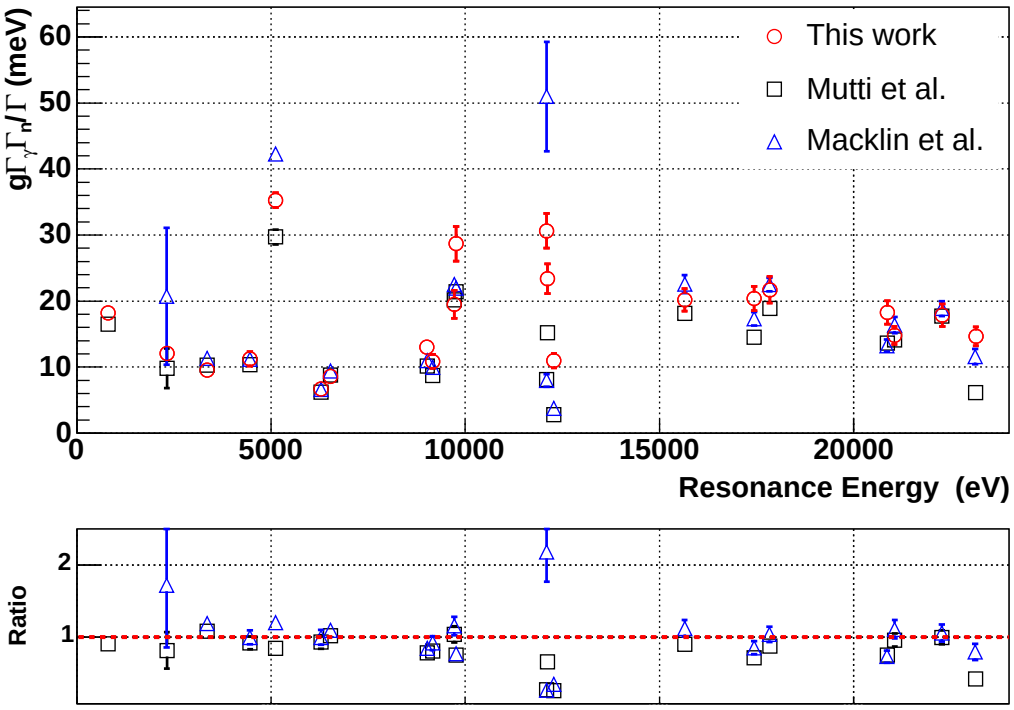

Figure 6.11: ^{209}*Bi experimental radiative kernels from n_TOF, GELINA and ORNL.*

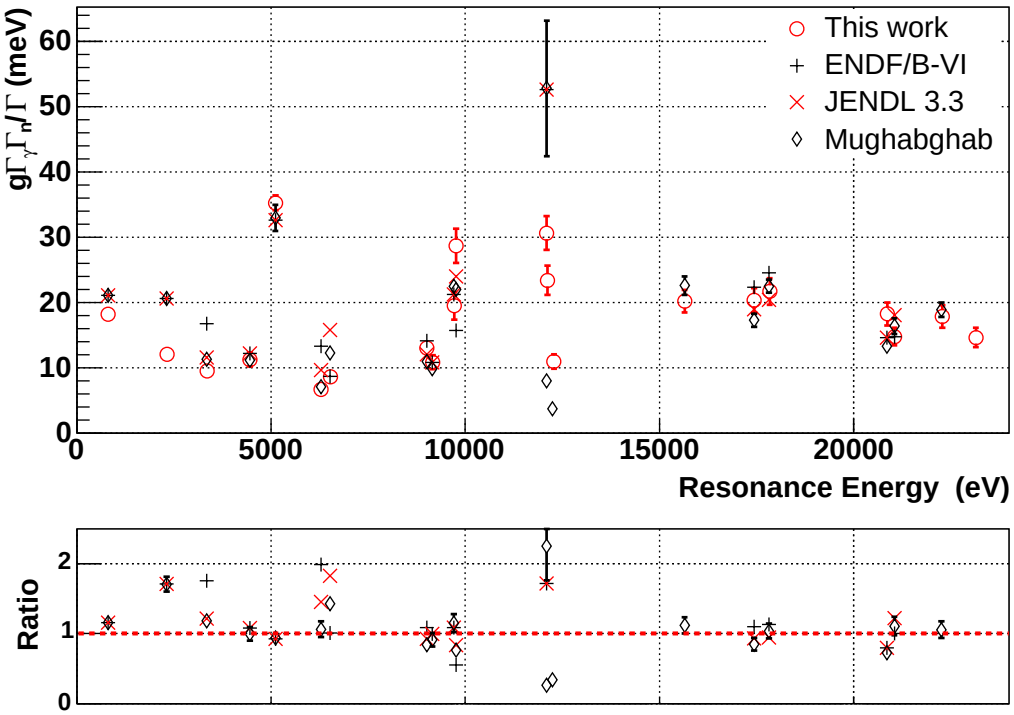

Figure 6.12: ^{209}*Bi n_TOF radiative kernels compared with ENDF, JENDL and Mughabghab compilation.*

Resonance 1: 801.6 eV

For this *s*-wave resonance, the neutron width values existing in the literature differ by ∼8%, as can be observed in table 6.7.

Author	Musgrove et al. [84]	Singh et al. [85]	Firk et al. [86]
$\Gamma_n(meV)$	4655(50)	4600(400)	4300(150)

Table 6.7: *Transmission values for the neutron width of the 802 eV resonance.*

Nevertheless, since $\Gamma_n \gg \Gamma_\gamma$ the value of the radiative kernel becomes insensitive to the exact value of the neutron width.

The analysis presented here has been performed with a fix $\Gamma_n = 4300$ meV [86]. Allowing both Γ_n and Γ_γ to vary, we obtain a compatible $\Gamma_n = 4320(50)$ meV. Using the value of $\Gamma_n = 4600$ meV provided by Mughabghab, the fit becomes slightly worse, but the resulting value for the radiative kernel is still in perfect agreement with that given in table 6.6.

It is interesting, that the result found here for this *s*-wave resonance is compatible with that of Mutti et al., but both lie approximately 20% below the values given by both the Mughabghab compilation and the evaluated data files. One should not forget, that there is no additional experimental capture data concerning this resonance, since the measurement range at ORELA starts beyond 2.6 keV. Therefore, it seems that the evaluated and compiled information for this resonance (based probably on theoretical assumptions) has been overestimated.

Resonance 2: 2323.8 eV

The value determined in our analysis is again in agreement with that of Mutti et al., but both are almost 50% lower than what is present in the evaluated files. The conclusion found for the previous resonance is also valid in this case. The evaluations seem to have been overestimated in this case, based probably on the radiative kernel reported by Macklin et al. The value given by Macklin et al. however is an estimation, not a real measurement [24].

The result obtained by us is affected of a lower uncertainty (less than 7%) than that provided by Mutti et al. (30%), because the latter needs to include also a neutron scattering correction whose estimated uncertainty is of about 50% the correction. It means that in this case, the correction itself applied to the GELINA's data was of about 60%.

Resonance 3: 3350.83 eV

The ENDF evaluation cross section for this resonance is clearly off, whereas the rest of information, including JENDL, show good agreement.

Resonance 5: 5114 eV

The neutron scattering correction made by Macklin et al. for the *s*-wave resonances, seems to be too small. In this case, as well as for their estimation of the cross section at 2.3 keV, the kernel is clearly overestimated when compared with the rest of experimental information (GELINA and n_TOF).

This is practically the only case where the Mughabghab compilation (which is based on the results reported by Macklin et al.) does not coincide with the results reported by Macklin et al. Apparently some additional correction, probably related with the neutron sensitivity, has been considered in the compilation. However, the resulting value from Mughabghab is in good agreement with the radiative kernel measured by us.

The capture areas obtained by Mutti et al. for the first two resonances and for this one, although compatible within the given uncertainties, lie systematically between 10% and 20% lower than our result. This may indicate that their correction for $l = 0$ resonances was probably overestimated in that measure (which is in agreement with the uncertainty of 50% that he attributes to the correction). Indeed, the radiative kernels obtained for the $l = 1$ resonances at 3.3 keV and at 4.4 keV show a much better agreement.

Resonance 6: 6288 eV

The JENDL (ENDF) evaluation lies 50% (100%) higher than our experimental result. However, the compilation reproduces the experimental information (this work, Mutti et al. and Macklin et al.), which is in agreement.

Resonance 7: 6525 eV

The three experimental results are in good agreement with each other, however, the values given by the compilation and JENDL are 30% and 60% larger respectively.

Resonances 10, 11: 9718.9 eV, 9767 eV

Results obtained for this doublet show good agreement. Only the value present in ENDF seems to be too low (30-40%).

Resonances 12, 13 and 14: 12092 eV, 12118.6 eV, 12285 eV

The situation in this region is difficult, because the s-wave resonance is overlaping on top of the other two p-wave resonances. There exist no transmission data for these p-wave resonances and they are also missing in the evaluated files.

The exact correction factor for the 12.119 keV resonance, due to the neutron sensitivity, was of $f^{ns} = 1.036(7)$. This value was found after recalculating the correction factor described in section 4.8 with the new fitted parameter of Γ_γ.

Comparing the three experiments, the results seem contradictory in this region. For the wide s-resonance, the result obtained at n_TOF is higher (by $\sim$50%) with respect to the value reported by Mutti et al., and about 50% of the value reported by Macklin et al. The trend is compatible with the systematic behaviour observed in previous s-wave resonances, thus confirming the excessive neutron sensitivity corrections in Mutti et al. and the underestimated corrections of Macklin et al. The results obtained here for both p-wave resonances, lie more than a factor of 3 higher than the self-consistent results of Mutti et al. and Macklin et al. Neverhteless, the total capture area for these 3 resonances is compatible between this work and Macklin et al. (65(4) meV versus 63(9) meV), whereas the total cross section reported by Mutti et al. lies more than a factor of 2 below (26 meV).

Resonances 15, 20: 15649.8 eV, 22286 eV

These resonances are not present in the evaluated files, although the experimental

information is compatible.

General remarks

Thanks to the neutron sensitivity optimized capture detection setup used in the present work, we were able to measure the resonances shown in table 6.5 with a negligible deviation due to this effect. The latter seems to have produced the main source of uncertainty in previous experiments for the case of *s*-wave resonances.

The deviation in the cross section due to the neutron sensitivity can be revealed by comparing the measured capture areas against the ratio of the neutron and gamma widths. This quantity is shown in figure 6.13, where the n_TOF results are compared with the other two previous experiments (Macklin et al. and Mutti et al.).

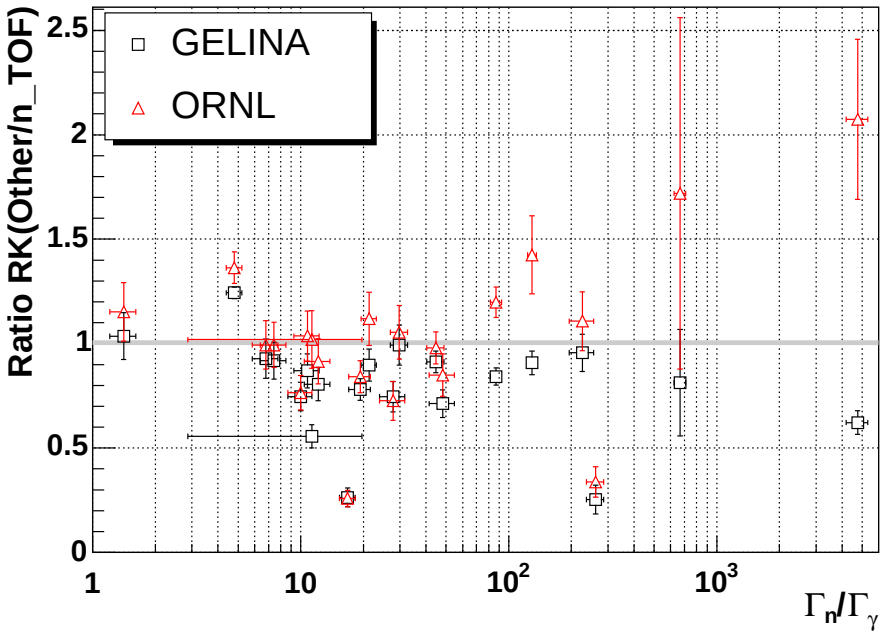

Figure 6.13: *Ratio of the capture area between previous experiments and n_TOF versus* Γ_n/Γ_γ.

The corrections due to the neutron sensitivity performed by Mutti et al., although slightly overestimated, seem to be in general reasonably compatible with the correctionless data of n_TOF (see figure 6.13). This agreement confirms that the corrections for scattered neutrons were properly treated by Mutti et al. However, the increasing capture area ratios obtained for higher Γ_n/Γ_γ with the data of Macklin et al., clearly indicate their deviation due to the neutron sensitivity effect. As the evaluations are mostly based on the latter, this deviation explains also the disagreement found before between the n_TOF data and the evaluated files.

The n_TOF results showing a higher disagreement with the rest of information are those at $\Gamma_n/\Gamma_\gamma \approx 17$ and 260, with capture ratios below 0.5. They correspond

to the 12.09 and 12.3 keV p-wave resonances which, as has been explained before, are overlaping with the wide s-wave resonance at 12.1 keV. We were not able to fit these p-wave resonances with the resonance parameters provided by Macklin et al. or Mutti et al.

The previous accounts, together with the comparison between n_TOF data and evaluations shown in table 6.6 and figure 6.12, clearly suggest an update of the evaluated data files. In general, discrepancies are evident mainly (although not only) for s-wave resonances as is the case of the 2.3 keV resonance, whose evaluated capture cross section deviates by almost a factor of 2. (See also figure 6.10).

Indeed, evaluators usually adjust or correct the parameters of some resonances, in order to obtain a compatible agreement with the thermal cross section.

The thermal neutron capture cross section, can be extrapolated as the sum of the contribution from the tails of all the individual Breit-Wigner resonances, both positive and negative. Near $E_n = 0$, the radiative capture cross section,

$$\sigma_\gamma = \sum_{i=1}^{N} g_n^i \frac{\pi}{k_n^2} \frac{\Gamma_n^i \Gamma_\gamma^i}{(E_n - E_\circ^i)^2 + (\Gamma/2)^2}, \tag{6.7}$$

where $N = N_\circ + N_1 + \ldots$ designates the total number of s-,p-resonances, etc. At thermal energy, assuming $E_\circ^i \gg E_n = 0.025\ eV$ and $E_\circ^i \gg \Gamma/2$, we can rewrite the previous equation as,

$$\sigma_\gamma^{th} \approx 4.099 \times 10^6 \left(\frac{A+1}{A}\right)^2 \sum_{i=1}^{N} g_n^i \frac{\Gamma_n^i \Gamma_\gamma^i}{(E_\circ^i)^2}. \tag{6.8}$$

Given that in s-wave resonances, $\Gamma \approx \Gamma_n$ is large, in the previous sum one can consider only the $l = 0$ resonances. If $N_\circ$ is the total amount of such resonances, then

$$\sigma_\gamma^{th} \approx 4.099 \times 10^6 \left(\frac{A+1}{A}\right)^2 \sum_{i=1}^{N_\circ} g_n^i \frac{\Gamma_n^i \Gamma_\gamma^i}{(E_\circ^i)^2}. \tag{6.9}$$

The result obtained from the n_TOF resonance parameters is in agreement with the value derived from the parameters reported by Mutti et al. from GELINA (see table 6.8). However, both values lie around 40% lower than the thermal cross section for this isotope, which has been accurately measured [78] and its value is of 33.8(5) mb.

The result obtained from the resonance parameters reported by Macklin et al. [24], clearly overestimates the thermal cross section due to the higher values reported for the capture areas.

The value predicted by the resonance parameters of the evaluated libraries is in agreement with the thermal capture measurement, most probably because evaluators have adjusted the s-wave resonance parameters by means of an expression like equation 6.9 in order to reproduce that value.

		$\sigma_\gamma^{th}(mb)$
In-pile measurement [79]		33.8(5)
From resonance parameters		
	This work	23.5 (9)
	Mutti et al. (GELINA) [81]	24.6 (9)
	Macklin et al. (ORNL) [24]	39.1 (17)
	ENDF	33.5
	JENDL	33.5

Table 6.8: *Thermal neutron capture cross sections predicted by the resonance parameters reported here, by Mutti et al. and by Macklin et al. At the bottom, the same calculation is shown for the resonance parameters of the two evaluated files ENDF and JENDL.*

In the present work, these s-wave resonances have been determined with a much better systematic accuracy. Hence, these new results call for the need to introduce subthreshold or negative energy resonance(s) in the evaluated data files[2].

6.5 Implications in stellar nucleosynthesis and ADS

At a given stellar scenario with a constant neutron density n_n, the stellar neutron capture rate is given by,

$$\langle \sigma v \rangle = \int_0^\infty \sigma v f(v) \mathrm{d}v, \tag{6.10}$$

where the velocity distribution $f(v)$ corresponds to the Maxwell-Boltzmann distribution. The Maxwellian-averaged stellar (n,γ) cross section can be calculated using the formula 6.11, which determines it as a sum of the $1/v$ extrapolation of the thermal value and the contributions of the resonances [88],

$$\langle \sigma \rangle_{kT} = \frac{\langle \sigma v \rangle}{v_T} = \sigma_{th} \sqrt{\frac{25.3 \times 10^{-6}}{kT}} + \frac{2}{\sqrt{\pi}} \sum_i A_r^i \frac{E_\circ^i}{(kT)^2} \exp\left(\frac{-E_\circ^i}{kT}\right). \tag{6.11}$$

The index i goes through all the resolved resonances. σ_{th}=33.8(5) mb is the thermal cross section of bismuth [79], kT the stellar temperature in keV, $E_\circ^i$ the resonance energy in keV and A_r^i the resonance area (mb keV).

At lower stellar temperatures kT the MACS is dominated by the broad s-wave resonances. For these resonances we have found important discrepancies with respect to the evaluated information and previous experiments, hence it is interesting to

[2]Estimation of the contribution of direct capture at thermal energies has been performed by G. Arbanas (ORNL, USA), resulting only on about 2.5×10^{-5} mb (private communication).

estimate which is the impact of the new capture data in the MACS and the stellar nucleosynthesis calculations. Using the previous formula, we have calculated the MACS for bismuth, which is shown in figure 6.14 (solid thick line). In this work, resonances have been analyzed for neutron energies from 800 eV up to 23 keV. This region corresponds to the main contribution to the MACS for stellar temperatures below 25 keV (dashed thin line). Above this temperature, the n_TOF data have been complemented with data from reference [81] up to 30 keV and from the Mughabghab compilation [79] up to 65 keV (dotted line). Average values of the cross section reported by Macklin et al. [24] (dash-dotted line) have been used to complete the calculation up to $E_n = 900$ keV.

Compared to n_TOF are shown the MACS reported by Mutti et al. in reference [81] (solid thin line) and in reference [87] (dashed thick line). The latter corresponds to the same data of reference [81] after analyzing the higher energy region (E_n >80 keV), therefore both coincide practically at lower temperature (kT < 10 keV). The MACS calculated with the parameters of the Mughabghab compilation [79] are also shown for comparison (see figure 6.14).

Table 6.9 summarizes all the MACS values mentioned above, plus the MACS calculated with the parameters reported by Macklin et al. [24] (not included in the figure).

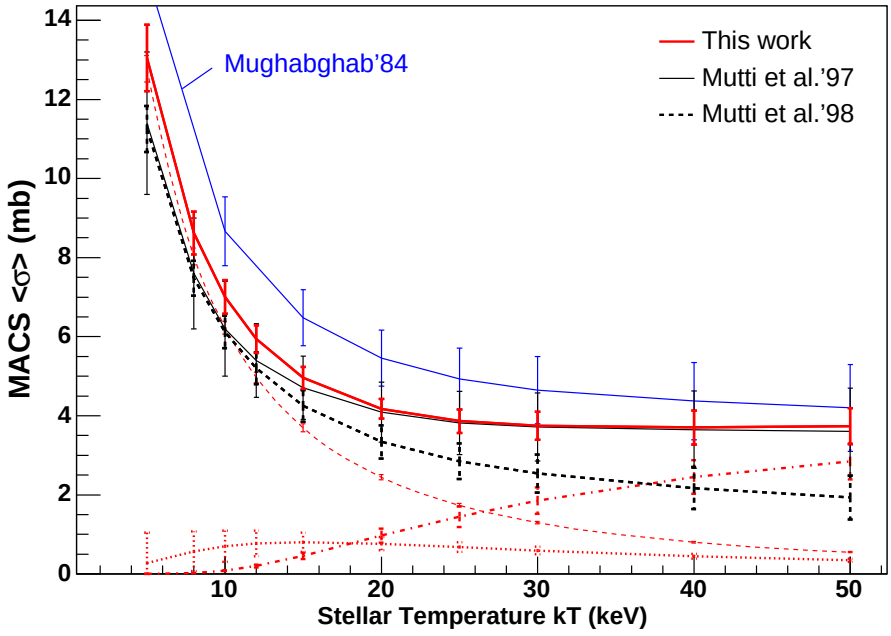

Figure 6.14: *Comparative plot of the ^{209}Bi-MACS versus the stellar temperature kT. See text for a detailed description.*

As was to expect, the result obtained for the MACS of Macklin et al. is overestimated due to the larger neutron sensitivity of the setup used at ORNL and to the

kT (keV)	This work	Mutti et al. [81]	Mutti et al. [87]	Mughabghab [79]	Macklin et al. [24]
5	13.05(0.84)	11.40(1.80)	11.25(0.58)	15.17(1.50)	16.40
8	8.62(0.54)	7.60(1.40)	7.48(0.44)		
10	7.01(0.43)	6.20(1.20)	6.12(0.41)	8.67(0.87)	12.40
12	5.94(0.35)	5.40(0.93)	5.20(0.40)		
15	4.96(0.27)	4.71(0.80)	4.25(0.40)	6.48(0.71)	
20	4.18(0.25)	4.09(0.76)	3.34(0.42)	5.46(0.71)	12.10
25	3.87(0.30)	3.82(0.80)	2.85(0.45)	4.93(0.78)	
30	3.74(0.35)	3.72(0.86)	2.54(0.48)	4.65(0.85)	10.7
40	3.70(0.43)	3.65(0.98)	2.17(0.53)	4.37(0.98)	9.3
50	3.74(0.46)	3.60(1.10)	1.93(0.55)	4.2(1.1)	8.2

Table 6.9: *MACS (mb) calculated in this work for ^{209}Bi compared to the values reported in the literature.*

insufficient correction applied in their analysis, as was discussed in section 6.4. The MACS calculated with the Mughabghab parameters is obviously overestimated too, since it is mostly based on the measurement of Macklin et al.

The results obtained in a previous experiment by Mutti et al. [81, 87], show a much better agreement with those reported here, as was also expected from the similar cross sections obtained in both works, shown in table 6.6. It is interesting the value of the 16% higher cross section obtained here for lower stellar temperatures (5-15 keV), as a consequence of the improved neutron sensitivity effect. On the other side, the MACS calculated by us (solid thick line) above $kT \approx 25$ keV is strongly influenced by the contribution of the average cross section values of Macklin et al. (dash-dotted line), with which our calculation was complemented at higher energy.

In terms of the *s*-process nucleosynthesis, a higher cross section in bismuth would be reflected firstly as a lower survival of this isotope (lower abundance) and secondly as a higher production through α-recycling of the ^{206,207}Pb isotopes.

Moreover, as was described in chapter 1, over the evolution of a thermally pulsing AGB star, in a tiny region (1/20) of the mass of the He intershell the major ^{13}C neutron source operates in the interpulse phase at temperatures around $T_8 \sim 1$ (in units of 10^8 K), which correspond to a thermal energy[3] $kT \approx 8 - 9$ keV. The lower stellar temperature part of the MACS (figure 6.14) could be therefore important for this stellar model, which has been proposed as a natural explanation of the observed overabundances of lead and bismuth.

The effect of the higher bismuth (n,γ) cross section measured here for a temperature of 8 keV, has been estimated[4] using a $M = 3M_{\odot}$ model of thermally pulsing AGB star with a metallicity [Fe/H] $= -1.3$. The resulting abundances for all the

[3]These two quantities are related by $kT = 8.62\ T_8$.

[4]R. Gallino (Università di Torino and Sezione INFN di Torino, Italy), private comunication.

lead isotopes and bismuth are compared in table 6.10 to the reference case computed with the values reported in the Bao et al. [88] compilation, which is based on the measurement of Mutti et al. [87].

Isotope	Abundance $< \sigma >^{Bao\,et\,al.}_{kT=8\ keV}$	Abundance ($\times 10^6$) $< \sigma >^{This\,Work}_{kT=8\ keV}$	Discrepancy (%)
^{204}Pb	0.08815	0.08815	0.00
^{206}Pb	0.5546	0.5532	-0.2
^{207}Pb	0.7493	0.7487	-0.08
^{208}Pb	9.473	9.481	0.1
^{209}Bi	0.4425	0.4174	**-6**

Table 6.10: *Calculated s-process abundances ($Si = 10^6$) in a low metallicity star model, for a reference case with the values of Bao et al. (second column) and with the ^{209}Bi cross section measured in this work (third column).*

Although the influence in the lead isotopes abundances is negligible, a remarkably 6% less survival (with respect to the reference case of Bao et al.) has been predicted for the bismuth isotope abundance.

With the aim of illustrating the performance of the nucleosynthesis calculations, one can use the "strong" s-process contributions from table 6.10 (from this work), in order to calculate the total s-process abundance by adding to it the well known main component from reference [1]. The s-only ^{204}Pb isotope can be used to renormalize the values of the third column in table 6.10. The total s-process abundances so obtained, can be complemented with detailed calculations of the r-process abuncances [13] in order to estimate the total abundance $N_s(\text{main}) + N_s(\text{strong}) + N_r$. The latter can be compared with the measured solar abundances $N_\odot$ of reference [1]. The result is shown in figure 6.15, which indicates that the theoretical calculations of the "strong" s-process abuncances obtained with the experimental input information of this work, show a good agreement with both the measured solar abundances and the calculated r-process abundances.

This result also turns out important, in order to estimate the radiogenic contribution of the Pb/Bi isotopes, due to the decay of the long lived uranium and thorium nuclides. As was introduced in chapter 1, the part of the lead and bismuth abundance due to the radiogenic contribution of the r-process sets a constraint for the age of old (first generations) metal poor stars, born at the beginning of their Galaxy.

In a recent study [12] the Maxwellian averaged capture partial cross section of bismuth into the ground state of ^{210}Bi has been measured with an uncertainty down to ~5% using the activation technique at an stellar temperature of $kT = 25$ keV. A bismuth sample was irradiated with the quasi-stellar neutron spectrum yielded by the ^{7}Li(p,n) reaction when 1991 keV protons are employed (see experimental histogram in figure 6.16). This new measurement was mainly motivated by the

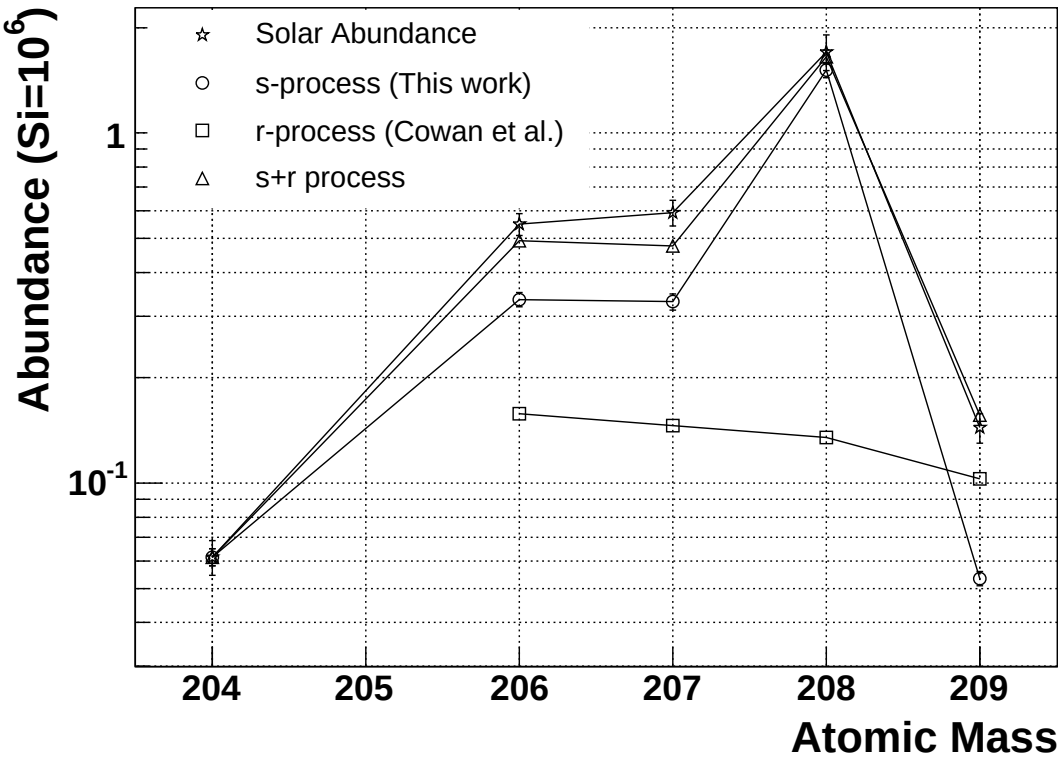

A	$N_s(main)$	$N_s(strong)$	N_r	$N_s + N_r$	$N_\odot$
204	0.0555(0.0034)	0.0060	0.0000	0.0615(0.0034)	0.0615(0.007)
206	0.2970(0.0154)	0.0376	0.1579	0.4925(0.0154)	0.55(0.04)
207	0.2790(0.0176)	0.0509	0.1462	0.4761(0.0176)	0.59(0.05)
208	0.8690(0.0756)	0.6447	0.1352	1.6491(0.076)	1.70(0.2)
209	0.0250(0.0025)	0.0284	0.1029	0.1563(0.0025)	0.144(0.014)

Figure 6.15: *Abundances predicted for the s-process and total abundances obtained as the sum of the s- and r-contributions (see text for details).*

renewed interest in the Th/U cosmochronometer, and the insufficient accuracy of previous measurements of this isotope which showed uncertainties between 9 and 14% [87]. As is shown in the same study, an accuracy of about 5% is required in order to reliably separate the radiogenic contribution of the lead and bismuth isotopes. Therefore, the uncertainty of about 6-7% achieved in the present work for the bismuth MACS, from kT=5 keV up to 15 keV, can be considered as a further step in the self-consistent determination of the s-process abundances of the lead and bismuth isotopes. It constitutes also an excellent complement at lower energies of the value measured in reference [12] at 25 keV.

The (n,γ) cross section of ^{209}Bi is also of relevance for ADS based reactors, since capture on bismuth produces the long term α-emitter ^{210m}Bi. The cross section of this reaction is up to date only known for thermal neutron energies ($\sim$0.025 eV) [79, 78], whereas accelerator driven transmutators based on a lead/bismuth spallation target [4] would operate at the higher energy range of 1 eV-0.5 MeV. Valuable information about the isomeric state feeding rate at the higher energy of 25 keV can be extracted by substracting the partial ground state cross section reported in reference [12],

$$\langle\sigma\rangle^{g}_{25\ keV} = 2.54(14) \quad \text{mb}, \tag{6.12}$$

from the total (n,γ) cross section measured in this work.

The latter to be compared with the partial one, needs to be appropriately convoluted with a Maxwellian distribution at kT = 25 keV. In order to calculate the metastable capture branching ratio of ^{210}Bi, the resonances measured at n_TOF (shown in figure 6.16 with an arbitrary vertical scale) have been convoluted with the same neutron quasi-stellar spectrum used to obtain the value (6.12) in reference [12] (see experimental spectrum in figure 6.16). Similar to the calculation of the MACS reported before, the resonances analyzed in this work have been complemented up to 65 keV with values from [81, 79] and up to 106 keV (the cut-off value of the Li(p,n) spectrum) with the average capture cross sections of reference [24].

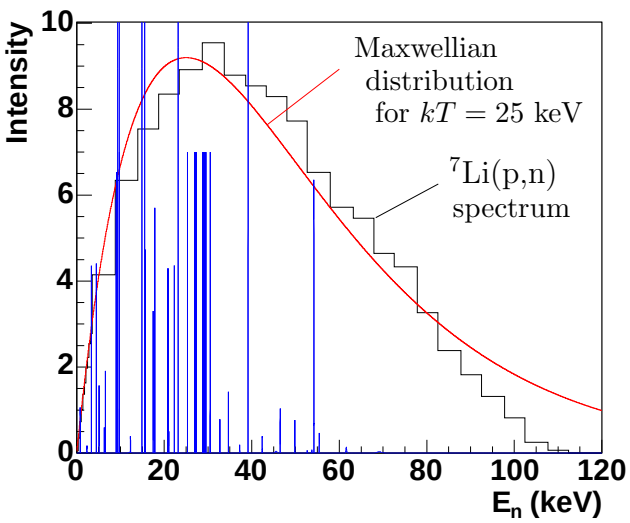

Figure 6.16: *Li(p,n) spectrum for calculation of the Bi MACS. The Bi isolated resonances are shown with an arbitrary scale.*

The result obtained in this way for the total averaged cross section is

$$\langle\sigma\rangle_{25\ keV} \approx 3.546 \quad \text{mb}, \tag{6.13}$$

thus resulting the metastable cross section

$$\langle\sigma\rangle^{m}_{25\ keV} \approx 1.0 \quad \text{mb}. \tag{6.14}$$

This means that at $kT = 25$ keV the branching ratio to the metastable (ground) state is of ∼28% (72%). This result is in agreement with the quantity that would be obtained from Mutti et al. [81] (see also figure 6.14), but it is in contrast with the value reported by Mutti et al. in reference [87]. The latter would lead to an average metastable state cross section of $\langle\sigma\rangle^{m}_{25\ keV} \approx 0.3$ mb or equivalently, to a metastable state population at $kT = 25$ keV of only ∼11%. In reference [87] this discrepancy is ascribed to a new experimental result for the unresolved resonance region, which in fact amounts to 35% of the value (6.13) in our case. On the other hand, the small value of 11% derived from reference [87] is to be compared with the thermal value of 28% [79] or even with the higher result of 49% from reference [78]. Considering the calculated metastable state population listed in table 6.4, it is not easy to understand why capture at $kT = 25$ keV would yield smaller isomeric state branching ratio than at thermal energy, since capture at higher energy leads to higher spin levels.

In order to solve this problem and obtain a more accurate value of $\langle\sigma\rangle^{m}_{25\ keV}$, the present measurement should be extended to higher energy with improved conditions of signal to noise ratio and statistics.

Chapter 7

^{207}Pb neutron capture cross section

This isotope is very close to the termination point of the stellar *s*-process, thus becoming its capture cross section interesting for the development of nucleosynthesis models.

On the other hand, given its ∼22% abundance and its neutron capture cross section higher than that of ^{208}Pb, this nuclide strongly influences the neutron balance in a lead-bismuth based ADS reactor.

Capture on ^{207}Pb leads to an excited state of the double magic ^{208}Pb, which shows a rather hard and simple deexcitation pattern. On one side the high energy prompt gamma rays are an advantage from the experimental viewpoint. On the other hand, the low multiplicity of the nuclear cascade can induce strong angular distribution effects in the measurement, which need to be accounted for.

7.1 Experiment and data reduction

The experimental setup used for this measurement, is exactly the same as that used for the ^{209}Bi. Basically both FZK-C_6D_6 detectors, placed 7.8 cm backwards at an angle of ∼125° with respect to the incident beam direction. This geometry was chosen in order to *i*) reduce the in beam gamma rays background and *ii*) minimize the effects of the primary radiation angular distribution. The latter effect will be discussed in section 7.1.1.

A sample enriched in ^{207}Pb was used in order to optimize the count rate and reduce contaminations. A description of the sample used in this experiment is given in table 7.1.

In the data reduction process, there were some particular differences with respect to the isotopes analyzed in previous chapters. These are related with the calculation of yield correction factors and the weighting function, as is described in the subsequent sections.

Atomic Mass A	207
Atomic Number Z	82
Neutron separation energy S_n	7.36782(9) MeV
I^{Π} (target)	$1/2^-$
J^{Π} (GS compound)	0^+
Abundance in nat. Pb	22.1(1) %
Sample mass	8.000 g
Thickness	2.21 mm
	7.408×10^{-3} atoms/barn
Diameter	20.05 mm
Enrichment in 207	92.40%
Impurity of 208	5.48%
Impurity of 206	2.16%
Impurity of 204	<0.02%
Number of protons	2.596925×10^{17}
Normalization sample	Au 0.1×20 mm

Table 7.1: *^{207}Pb sample and isotope properties.*

7.1.1 Correction of systematic effects

Detector's threshold

When ^{207}Pb captures a neutron, the target nucleus with $J^{\Pi} = 1/2^-$ goes to an excited state of ^{208}Pb. The capture of s-wave neutrons can lead therefore to 0^- or 1^- resonances, while p-wave neutrons lead to 0^+, 1^+ or 2^+ states. $J = 0$ resonances cannot deexcite to the 0^+ ground state of ^{208}Pb through one step emission of photons. Any resonance with total spin $J = 1$, undergoes E1 (for negative parity) or M1 (parity positive) transition to the ground state 0^+ [89], thus emitting a 7.37 MeV gamma ray. It has been also found experimentally [90], that the 2^+ resonances do decay both through an E1 transition to the 2.6 MeV 3^- first excited state of ^{208}Pb and to the 0^+ ground state by means of an E2 transition. But the branching to the ground state never exceeds 35%.

With such a simple level scheme and the well known spin-parity assignments of the ^{208}Pb levels, it was rather easy to calculate in this case the corrections due to threshold. Obviously, prompt gamma rays summing effect is impossible for $J = 1$ levels, and negligible in very good approximation for levels with spin $J = 2$.

The two types of transitions, respectively for resonances with $J = 1$ and $J = 2$, were Monte Carlo simulated using the GEANT4 code to implement the geometry of the experimental setup described in previous section. The obtained deposited energy spectra together with the corresponding nuclear level scheme are shown in figure 7.1. These spectra have been appropriately broadened to include the instrumental resolution of the FZK-C_6D_6 detectors.

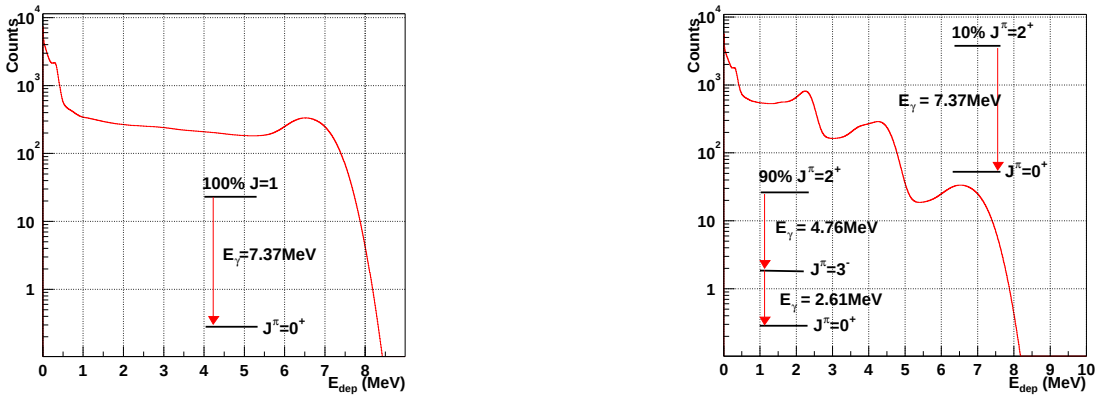

Figure 7.1: *Monte Carlo simulation of the deexcitation pattern of* ^{207}Pb*+n for resonances with spin* $J = 1$ *(left) and* $J = 2$ *(right).*

Unfortunately the statistics of the measurement were not high enough in order to make a good comparison between the simulated deposited energy cascades histograms and the measured ones. Nevertheless, a rough comparison of the two resonances with highest yield was performed accumulating their deposited energy histogram. The 3.3 keV with $J^\pi = 2^+$ and the 41 keV 1^- resonances were chosen for this comparison. A 10% branching ratio to the ground state for $J = 2$ resonances was included in order to reproduce the experimental histograms. This value is compatible with spectroscopic measurements of this nuclei [90]. As can be seen in figure 7.2, a good agreement is found between simulated and measured gamma ray spectra, thus lending confidence on the use of these spectra to calculate the threshold correction. This correction is shown in table 7.2 and has been obtained as was described in section 5.6 by computing the weighted sum of the cascades.

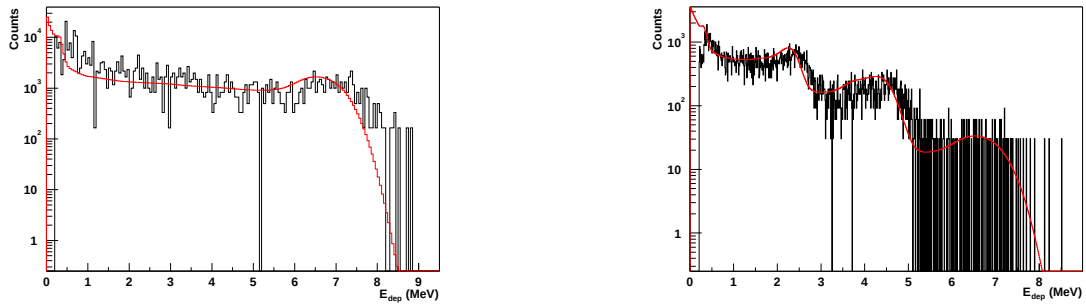

Figure 7.2: *Comparison between the simulated response functions for resonances with total spin* $J = 1$ *(left) and for resonances with spin* $J = 2$ *(right).*

Despite of having a rather high electronic threshold of 340 keV, the yield correc-

Resonance	f^t
^{207}Pb $1^{+/-}$	1.0174
^{207}Pb 2^{+}	1.0259
^{197}Au 4.9 eV	1.06828

Table 7.2: *Threshold correction factor for each type of resonance.*

tion factors are very low, of about 2%, due to the hardness of the spectrum. A 1% of systematic uncertainty was assigned to the obtained threshold correction factor.

Angular distribution

Due to the low multiplicity of the ^{208}Pb deexcitation pattern, the angular distribution of the primary radiation emitted is of concern in this case. Indeed, capture on $l > 0$ wave, leads to an aligned state of the compound nucleus, perpendicular to the incident direction of the neutron beam. This causes anisotropy in the angular distribution of the prompt gamma rays, which is in general given by,

$$W(\theta) = \sum_k A_k P_k(cos\theta) = 1 + A_2 P_2(cos\theta) + A_4 P_4(cos\theta) + A_6 P_6(cos\theta), \qquad (7.1)$$

where $P_k(cos\theta)$ are the Legendre polynomial of order k and A_k are coefficients which depend on the initial spin (J_i), final spin (J_f), the contributing transition multipolarities (L) and the degree of alignment.

For pure dipolar transitions ($L = 1$), $A_4 = A_6 = 0$ and the effect of the angular distribution can be minimized by setting the detectors at an angle θ such that $P_2(cos\theta) = 0$. This condition is fulfilled for $\theta \approx 55°$ and $\theta \approx 125°$. In the case of an ideal detector of negligible volume, the angular effect could be completely neglected by arranging the detector at those angles. But since the detector's volume is of about 1 L and it is rather close to the sample, the effect of the angular distribution has to be taken into account.

We have evaluated the effect of the anisotropic angular distribution for the two types of nuclear cascades occurring after the deexcitation of the compound nucleus ^{208}Pb*.

i) In the first case we will consider resonances with total spin $J = 1$ (gamma ray spectrum shown in the left part of figure 7.1). As was mentioned above, the compound nucleus is aligned only if the capture process takes place with $l > 0$. Capture in p-wave leads to a $J^{\Pi} = 1^+$ level, from which the emitted gamma ray corresponds to a pure M1 transition because the ground state is 0^+.

In the general case there is a channel spin admixture ($s = 0, 1$) which contributes to an incomplete alignment with unknown proportions of both $s = 0$ and $s = 1$. Each channel spin s produces a different alignment of the initial state. If only $s = 0$ contributes, considering $J_i = 1$, $J_f = 0$, $L = 1$, we have calculated using

the equations of reference [91], that in equation 7.1 the coefficients $A_2 = -1$ and $A_4 = A_6 = 0$. On the other side, if one has only $s = 1$, then $A_2 = 1/2$ and $A_4 = A_6 = 0$.

In the general case of unknown spin admixture, the angular distribution for a pure dipolar transition can be written [92],

$$W(\theta) = 1 + \frac{1-3a}{2} P_2(cos\theta) \tag{7.2}$$

where the coefficient a designates the relative contribution of channel spin $s = 0$ with respect to the total. This coefficient can be written as a function of the angular distribution ratio R,

$$a = \frac{\frac{9}{8}R - \frac{3}{4}}{\frac{3}{8}R + \frac{3}{4}}, \quad \text{being} \quad R = \frac{W(90^\circ)}{W(135^\circ)}. \tag{7.3}$$

The ratio R has been determined experimentally [93] for some of the resonances in ^{208}Pb. Hence, the angular distribution and the angular distribution correction factor can be calculated for those resonances.

The angular distribution of two out of the four M1 transitions measured in this work (see later table 7.5) has been determined experimentally [93].

E (keV)	W(90°)/W(135°)	a
30.2	1.41 ± 0.20	0.65 ± 0.14
37.5	0.64 ± 0.09	-0.03 ± 0.10

Table 7.3: Value of R reported in reference [93] for two M1 transitions in ^{207}Pb+n.

Including this angular distribution (see left part of figure 7.3) in the Monte Carlo simulation of the n_TOF capture experimental setup described in section 7.1, we can compare the obtained response function with that corresponding to an ideal isotropic angular distribution of the prompt gamma rays.

The effect of the anisotropy in the response function can be observed in the right part of figure 7.3.

For the 30 keV resonance, the corresponding weighted spectra show a deviation of ∼3.5%, and the correction factor becomes $f^{\theta,1^+}_{30\ keV} = 0.965(3)$.

In the case of the 37 keV resonance, $a \sim 0$ and the correction factor becomes $f^{\theta,1^+}_{37\ keV} = 1.037(6)$.

For the other two M1 transitions measured in this work, resonances at 90 keV and 128 keV, there is no angular distribution reported in reference [93], since these resonances were obscured by contaminants. In this case, we have studied the maximum deviation introduced by the angular distribution due to an arbitrary value of a between 0 and 1. The resulting correction factors range from 0.925(3) for $a = 1$ up to 1.037(6) for $a = 0$. Therefore, the systematic uncertainty of the capture area reported for these last two M1 resonances can be ascribed to be +3.7%/-7.5%.

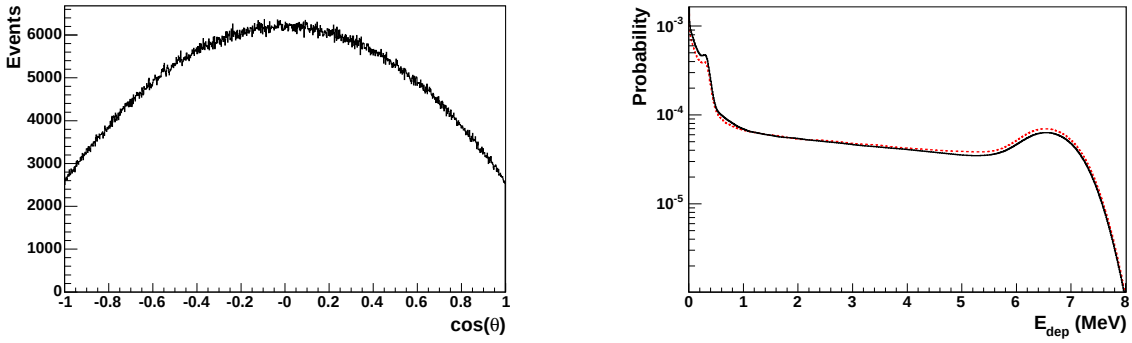

Figure 7.3: *(Left) Angular distribution used in a Monte Carlo GEANT simulation of 5×10^6 events for $a = 0.65$. (Right) Comparison of the response functions with isotropic angular distribution (solid line) and with the angular distribution shown on the left side (dashed line).*

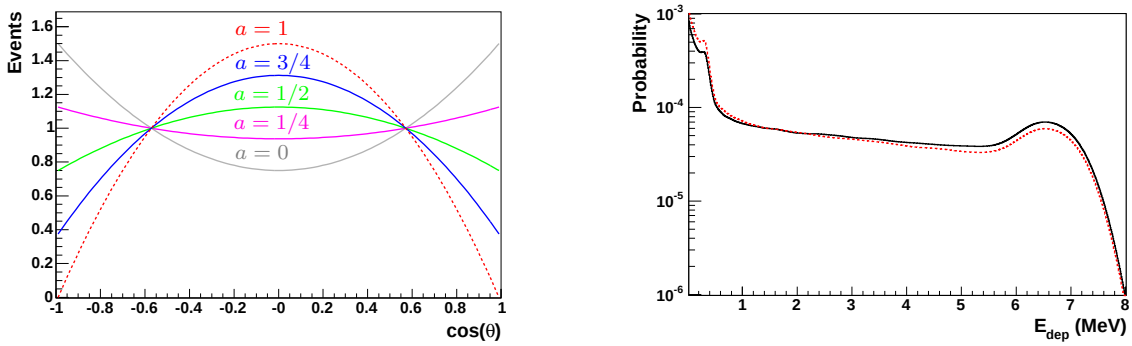

Figure 7.4: *(Left) Angular distribution for several values of the initial alignment a. (Right) Effect in the pulse height spectrum of the angular distribution for $a = 1$ (dashed line) compared versus an isotropic spectrum (continuous line).*

ii) Resonances with $J^{\Pi} = 2^+$ deexcite predominantly by means of a two step cascade (see right part of figure 7.1). The angular distribution of the second gamma ray emitted of 2.61 MeV is influenced by the re-alignement introduced by the previous gamma ray of 4.76 MeV.

The first gamma ray of this cascade, with 4.76 MeV energy, is a pure E1 transition since it connects a 2^+ state with the first excited state at 2.61 MeV with $J^{\Pi} = 3^-$. Using the formula of reference [91], the calculated coefficients for this first transition are $A_2 = -0.1$ and $A_4 = A_6 = 0$. This corresponds to a rather flat distribution as can be observed in the left part of figure 7.5. For the second gamma ray, emitted from a 3^- level to the 0^+ ground state, it can be also calculated [91] (considering also the quantum numbers of the previous transition), that the angular distribution coefficients are $A_2 = 0.6$, and $A_4 = A_6 = 0$. This takes into account the loss of the alignment induced by the first transition. The resulting angular distribution in this case is much more pronounced due to the octupole character of the transition, as can be observed in the right part of figure 7.5.

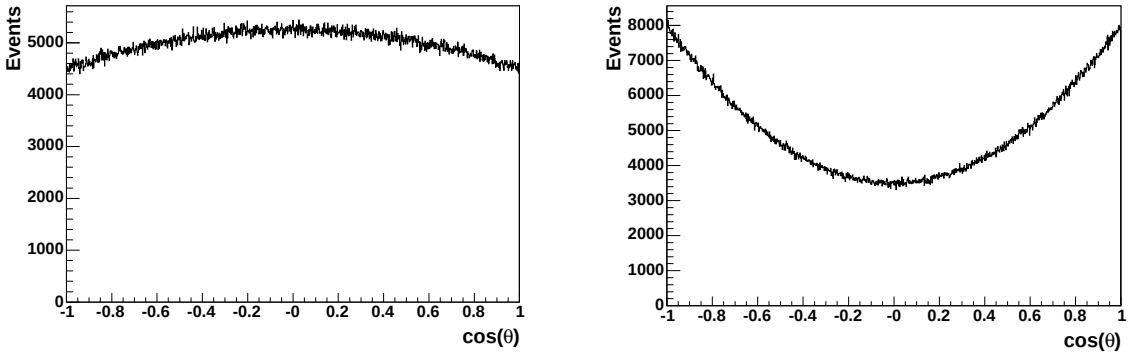

Figure 7.5: *Angular distribution included in a Monte Carlo simulation of* 5×10^6 *events, for E1 transitions connecting* 2^+ *and* 3^- *levels (left) and for E3 transitions from the* 3^- *level to the ground state* 0^+ *(right).*

The final yield correction factor for resonances with $J^{\Pi} = 2^+$ becomes $f^{\theta}_{2^+} = 1.015(3)$.

7.1.2 Weighting function

This is a very interesting case of WF. Thanks to the hard gamma spectrum of ^{207}Pb+n, an inaccurate (at least at low energy) polynomial WF is still able to introduce a negligible uncertainty in the capture experiment. Indeed, the polynomial WF obtained with the conventional procedure does fulfill only the proportionality condition with an RMS deviation as large as ∼6%. Both the polynomial WF and proportionality check are shown in figure 7.6.

However, the deviation in the capture experiment due to this WF is very small. In order to estimate this uncertainty we calculate, as usual, the weighted sum of

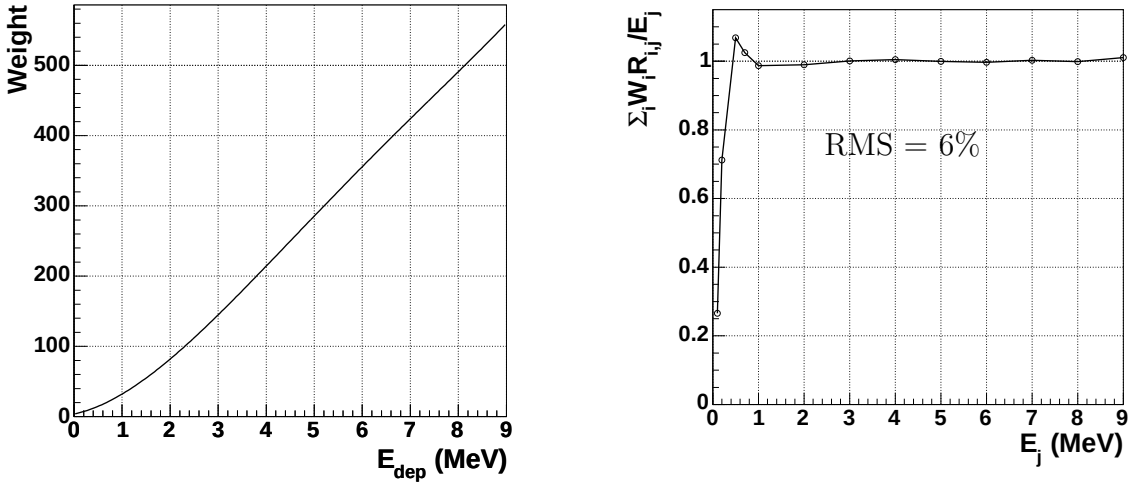

Figure 7.6: *(Left) Polynomial WF for the ^{207}Pb sample. (Right) Proportionality check of the individual simulated response functions.*

the deposited energy spectra obtained in the previous section (see figure 7.1). The corresponding weighted sum deviations are shown in table 7.4.

Level Spin	$\sum_i W_i R_i^c / N E_c$
$1^{+/-}$	0.998
2^+	1.002

Table 7.4: *Estimated uncertainty of the polynomial WF.*

Indeed, despite of the 6% RMS deviation of the proportionality condition due to the polynomial WF, the uncertainty introduced in the capture experiment is much lower, less than 0.3%. This is consequence of the hard gamma ray spectrum of this nuclide. The lower part of the WF has a negligible influence in the yield, since the weighted sum is dominated by the higher weights to apply to higher energy gamma rays.

Anyhow, a pointwise weighting function has been calculated for this sample, and we preferred to use this one for the data reduction of the ^{207}Pb (n,γ) data. A brief description of its calculation is given below.

Following the algorithm described in section 2.2.2, a pointwise WF is calculated starting from a set of 180 simulated response functions in steps of 50 keV, covering the energy range from 50 keV up to 9.0 MeV. The response distributions are histogramed with a 10 keV bin width. Using a regularization order equal to one and a multiplier $\lambda \approx 9 \times 10^{-6}$, we obtain the WF shown in the left part of figure 7.7.

Despite the really small proportionality deviation shown in the right part of figure 7.7, the uncertainty of the obtained pointwise WF for ^{207}Pb coincides however

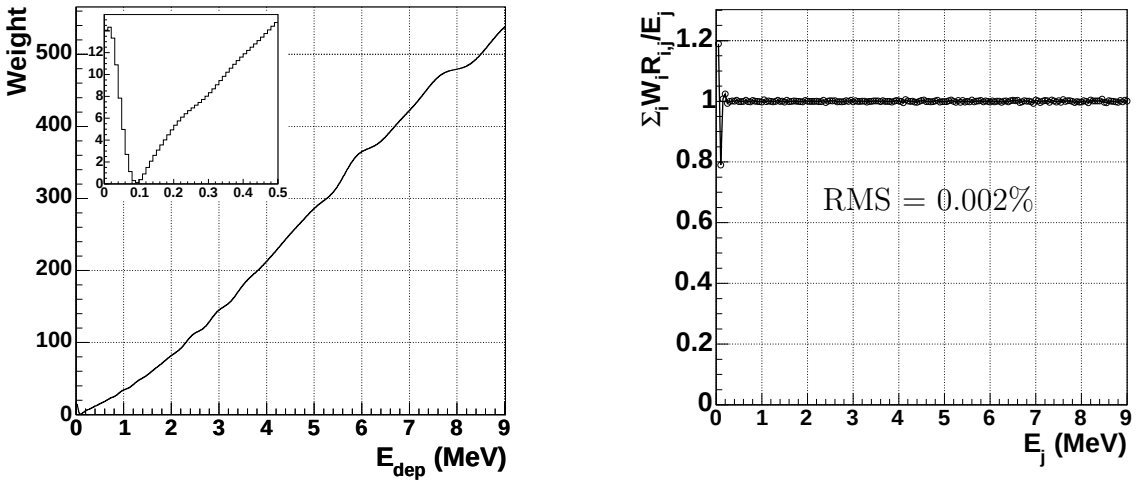

Figure 7.7: *(Left) Pointwise WF obtained with the regularization method for the ^{207}Pb sample. (Right) Proportionality check of the pointwise WF for the 180 simulated response functions in the energy range from 0-9 MeV.*

with that shown in table 7.4 for the polynomial WF. This is because this uncertainty is purely statistical, related with the statistics of the simulated response functions.

7.2 Analysis

The capture yield of ^{207}Pb can be calculated as,

$$Y'(E_n) = f^{\theta}_{J^{\Pi}} \times f^{Si} \times f^{t} \times f^{Sat} \times Y(E_n), \tag{7.4}$$

where $Y = N^w/N_n E_c$, being N^w the count rate weighted with the WF obtained in section 7.1.2. $f^{\theta}_{J^{\Pi}}$ is the correction factor due to the angular distribution effect, which is to be applied in this case only for $J^{\Pi} = 1^+$ resonances (section 7.1.1). f^{Si} is the SiMon renormalization factor to account for inaccuracies in the WCM proton intensity values. f^t designates the threshold correction factor obtained in section 7.1.1 and f^{Sat} is the yield normalization factor obtained from the measurement of the gold sample. The correction due to the neutron sensitivity f^{ns} has been omitted in the previous formula because it was found to be negligible for all the resonances of ^{207}Pb (section 4.8).

The corrected experimental yield Y' has been analyzed with the R-matrix analysis code SAMMY in the same manner as we did with the bismuth data in section 6.3. In the case of ^{207}Pb, impurities in the sample due to the other stable lead isotopes, ^{208}Pb, ^{206}Pb and ^{204}Pb (see table 7.1) were included in the SAMMY code in order to account for them in the calculation of the total yield.

A total of 16 resonances could be observed and analyzed in the energy range from 3 keV up to 317 keV. It is interesting that three of them are missing in the evaluated

data files and have not been observed in any transmission measurement either (two of these resonances are shown in figure 7.8). On the other side, we were not able to identify several of the resonances which are present in the ENDF evaluation: two s-wave resonances at 101.8 keV and 228.76 keV, most of the p-wave resonances (we could analyze only 7 out of 35 evaluated levels) and finally, from 7 evaluated d-wave resonances we could observe clearly three of them. This is to be ascribed to the in-beam gamma rays induced background in our measurement (see appendix E).

Some examples of resonances analyzed with the SAMMY code are shown in figure 7.8. As can be observed in this figure, small discrepancies in the energy of the resonance (with respect to the evaluated values) have been also found in some cases. The values derived for the resonance parameters $E_\circ$, Γ_γ, Γ_n and the radiative kernel are presented in table 7.5. The radiative kernels reported for resonances 1^+ and 2^+ have been corrected by the angular distribution effect, as described in section 7.1.1. Specific details about the analysis of each particular resonance are given in the following section, together with a comparison with other works.

$E_\circ$ (eV)	l	J	Γ_n (meV)	Γ_γ (meV)	$g\Gamma_\gamma\Gamma_n/\Gamma$ (meV)
3064.700(3)	1	2	111.0(8)	145.0(9)	78.6(9)
10190.80(4)	1	2	656(50)	145.2(12)	149(14)
16172.80(10)	1	2	1395(126)	275(3)	287(30)
29396.1	1	2	16000	189(7)	234(9)
30485.9(5)	1	1	608(45)	592(50)	225(30)
37751(3)	1	1	$50(10)\times10^3$	843(40)	620(30)
41183(30)	0	1	$1.220(30)\times10^6$	3972(160)	2970(120)
48410(2)	1	2	1000	230(20)	235(20)
82990(12)	1	2	$29(5)\times10^3$	360(30)	444(30)
90228(24)	1	1	$272(13)\times10^3$	1615(100)	1200(80)
127900	1	1	$613(60)\times10^3$	1939(150)	1449(120)
130230	1	2	$87(9)\times10^3$	923(80)	685(60)
181510(6)	0	1	57.3×10^3	14709(500)	8780(300)
254440	2	3	$111(20)\times10^3$	1219(90)	2110(150)
256430	0	1	1.66×10^6	12740(370)	9482(280)
317400	0	1	850×10^3	10967(480)	8120(350)

Table 7.5: *Resonance parameters and radiative kernel derived from the analysis of the ^{207}Pb(n,γ) data measured at n_TOF.*

The values reported for the radiative kernel of each resonance (last column of table 7.5) include only the uncertainty on the fitted parameters Γ_n and Γ_γ, or Γ_γ if the neutron width has been kept constant during the fit.

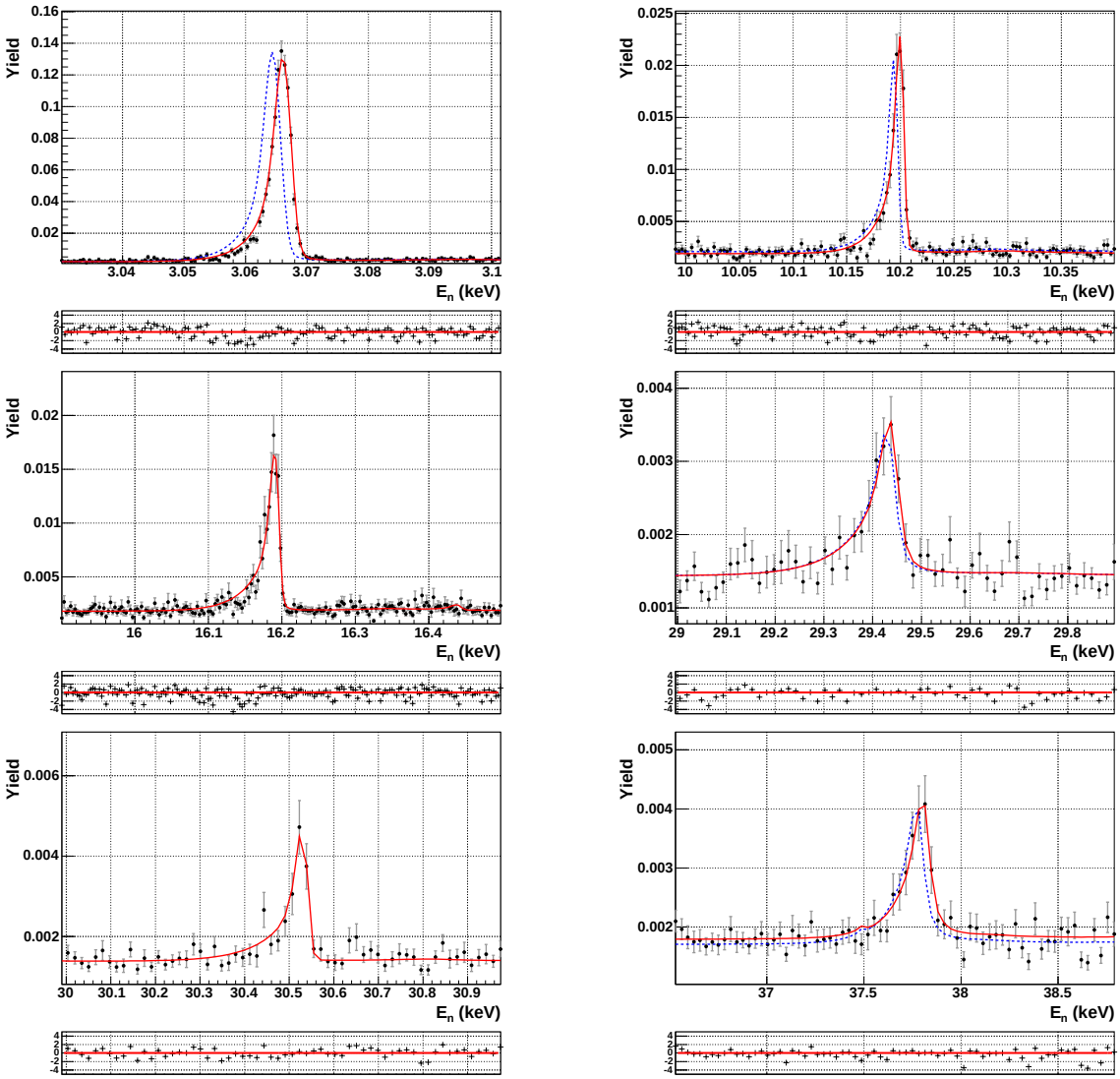

Figure 7.8: *Yield fit (solid line) performed with the SAMMY code, for several resonances of $^{207}Pb+n$ at 3 keV, 10 keV, 16 keV, 29 keV, 30 keV and 37 keV. The dashed line corresponds to the ENDF resonance parameters. Resonances at 16 keV and 30 keV are missing in the evaluations.*

7.3 Results and discussion

The radiative kernel or integrated capture cross section of the resonances measured at n_TOF is compared in table 7.6 with those obtained from another measurement due to Raman et al. [90, 94]. Few of the ^{207}Pb resonances analyzed in this work, have been also observed in measurements due to Allen et al. [95, 96]. However, the latter contains only information about 6 resonances and has been omitted in table 7.6. Both the Raman et al. and the Allen et al. measurements are briefly summarized below, specific information can be found in the corresponding references.

In order to give a better overview and show more clearly the differences between the results of the several measurements, all the experimental information mentioned above is shown in figure 7.9.

The kernels computed from the resonance parameters of two different compilations due to Sukhoruchkin et al. [80] and to Mughabghab [79] are also shown for comparison in table 7.6. Finally, the radiative kernels calculated from two representative evaluated data files, ENDF and JENDL, have been also included in this table.

The compiled and evaluated information is shown in figure 7.9 together with the results of this work.

Below follows a description of the experimental and the evaluated information mentioned above, which will be compared later with the results obtained in the present work.

- Raman et al.: information extracted from references [90] and [94] for resonances with total spin $J = 1$ and $J = 2$ respectively.

  A 92.4% enriched 249 g ^{207}Pb metal rectangular sample ($2.62 \times 5.05 \times 1.63 cm^3$) was measured at 40 m from the ORELA pulsed neutron source (neutron energy resolution 1/600). Data from a much thinner sample ($2.62 \times 5.05 \times 0.05$ cm^3) obtained in an earlier measurement were reanalyzed for resonances below 45 keV. The relative normalization of the cross section was carried out by using the 4.9 eV ^{197}Au resonance.

  The original results, have been corrected by a factor $f = 0.9655$ according to a corrigendum [83].

  The values of the radiative kernel for $J = 1$ resonances have been computed using the neutron widths given in the original reference [90]. These were taken mainly from an independent transmission measurement (reference [97]). The uncertainty of the computed value for the capture area, includes only the uncertainty due to the capture width.

  For resonances with total spin $J = 2$, only the gamma widths are given in the original reference and the kernels of table 7.6 have been computed using the Γ_n from reference [79] which are equivalent to those from reference [98].

- Allen et al.'73: information from reference [95]. It has not been included in table 7.6 since it contains only 4 resonances in the energy range considered here. The measurement was carried out at the Oak Ridge electron linear accelerator (ORELA). The measuring setup consisted on two C_6F_6 liquid scintillator based detectors and the neutron flux was monitored by utilizing a ^{6}Li glass.

  A posterior paper of the same author [96], cited here as Allen et al.'83, includes only two resonances. The latter measurement was carried out at the Australian 3 MeV van de Graaff accelerator, and the radiative widths were measured relative to gold in the 20-80 keV neutron energy range.

- Sukhoruchkin et al.: this is a recent compilation of experimental data [80], which is mostly based on an unpublished measurement performed at GELINA [25]. The latter experiment was similar to that described in section 6.4 for the Mutti et al. ^{209}Bi(n,γ) measurement. In this case, the ^{207}Pb sample was a disk of 2×80 mm enriched to 90.44% and the 4 C_6D_6 detectors were placed at 135° in order to minimize the effects of the angular distribution (although in principle 125° is a better direction as was described in section 7.1.1).

- Mughabghab [79]: compilation of experimental data, mostly based on the Raman et al. and on the Allen et al. measurements described before.

- ENDF: (American) Evaluated Nuclear Data Files Base VI release 8.0. Evaluators Chadwick, Young, Fu, 1996.

- JENDL: Japanese Evaluated Nuclear Data Libraries, version 3.2. Evaluator M. Mizumoto, July 1987. Information about this nuclide is not present yet in the newer version 3.3.

Nr.	$E_\circ$ (eV)	l	This work	Raman et al.	Sukhoruchkin et al.	Mughabghab	ENDF	JENDL
1	3064.7	1	78.6(9)	82.1(1.4)	84.3(1.4)	80.8(1.4)	80.77	80.77
2	10190.8	1	149(14)	129(4)	138(1.5)	126(4)	126.06	131.3
3	16172.8	1	287(30)	249(13)	329(4)	241(13)	—	—
			Γ_γ=275(3)	Γ_γ=232(12)	Γ_γ=224(12)			
4	29396.1	1	234(9)	224(9)	183(2)	216(9)	216.38	216.38
5	30485.9	1	225(30)	444(14)	220(8)	—	—	—
			Γ_γ=592(50)	Γ_γ=620(20)	Γ_γ=600(20)	Γ_γ=600(20)		
6	37751	1	620(30)	606(40)	677(7)	590(44)	590.55	590.55
7	41183	0	2970(120)	3958(220)	3656(24)	3800(220)	2491.6	3809.08
8	48410	1	235(20)	106(3)	103(4)	103(3)	—	—
			Γ_γ=230(20)	Γ_γ=93(3)	Γ_γ=98.2(36)	Γ_γ=90(3)		
9	82990	1	444(30)	231(4)	267(6)	223(4)	223	134
10	90228	1	1200(80)	1526(30)	1150(18)	1470(30)	1474.24	1474.3
11	127900	1	1449(120)	2200(45)	1368(30)	2127(450)	2128.7	2127.6
12	130230	1	685(60)	749(15)	751(20)	734(148)	728	727
13	181510	0	8780(300)	10384(3500)	8856(90)	7185(380)	7151	3243
14	254440	2	2110(150)	—	—	—	2460	192
15	256430	0	9482(280)	16162(300)	16144(300)	15554(296)	15540(?)	75
			Γ_γ=12740 (370)	Γ_γ=21700 (400)	Γ_γ=21700 (400)	Γ_γ=21000 (400)	Γ_γ=21000	
16	317400	0	8120(350)	8000(150)	7980(150)	7700(150)	7698.4	5944
			Γ_γ=10967 (480)	Γ_γ=10800 (200)	Γ_γ=10800 (200)			

Table 7.6: *Values obtained for the capture area of ^{207}Pb compared with other works.*

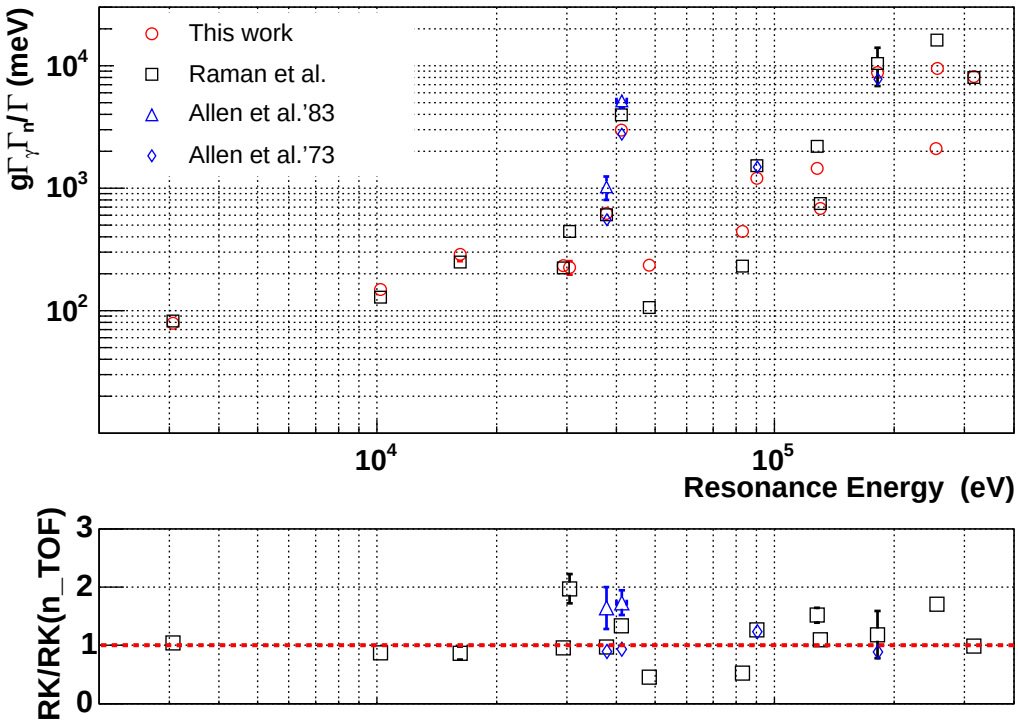

Figure 7.9: ^{207}Pb *radiative kernels measured at n_TOF and at ORNL.*

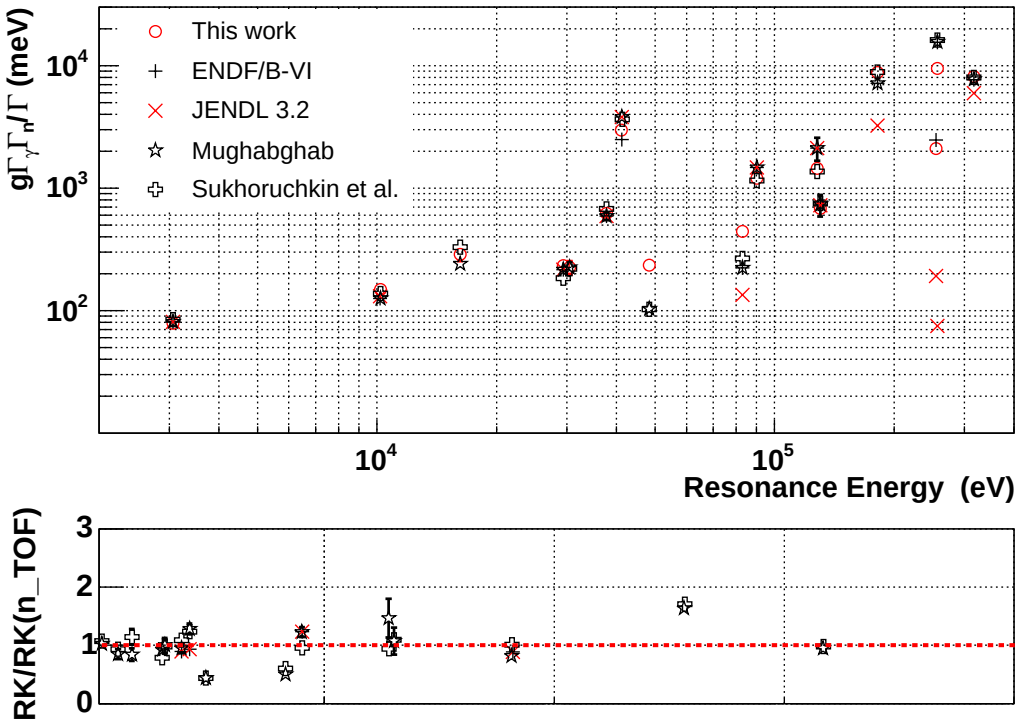

Figure 7.10: ^{207}Pb *n_TOF radiative kernels compared to ENDF, JENDL and the Mughabghab and Sukhoruchkin et al. compilations.*

Resonance 1: 3064.7 eV

The yield of this resonance measured at n_TOF is shown in figure 7.8 together with the ENDF evaluated parameterization. In the analysis of this resonance, we derived both $\Gamma_\gamma = 145.0(9)$ meV and $\Gamma_n = 111.0(8)$ meV. Nevertheless, if one fixes the neutron width to the value from reference Mughabghab, $\Gamma_n = 120(50)$ meV, the resulting capture area is still compatible with the value given in table 7.5. The first thing that one notices is the small change in the energy of the resonance with respect to the evaluated parameter $E_\circ = 3063$ eV.

The radiative kernel obtained here lies about 4% below the measurement due to Raman et al. and around 7% (4%) below the value of the Sukhoruchkin et al. (Mughabghab) compilation.

Resonance 2: 10190.8 eV

For this resonance the value of the neutron width is only approximately known, $\Gamma_n \approx 560$ meV [79]. However, the high peak cross section of this resonance (see figure 7.8) enabled us to derive both the capture and the neutron widths, shown in table 7.5. The result obtained for the capture area is also compatible with that obtained when fixing $\Gamma_n = 560$ meV.

The result obtained here is compatible with the others, specially considering that the uncertainties on the radiative kernel given for the rest of authors in table 7.6 do not include any uncertainty on Γ_n.

Resonance 3: 16172.8 eV

This resonance has not been observed in transmission measurements. For the analysis presented here, we adopted the spin parity value 2^+ from Sukhoruchkin et al. [80] and derived both Γ_n and Γ_γ. The fit of the experimental yield performed with the SAMMY code can be observed in figure 7.8.

As there is no value for Γ_n, in table 7.6 we show also the gamma widths. The corresponding radiative kernels have been computed with the neutron width derived by us, however the uncertainty on Γ_n has not been included in the other kernels.

The evaluations do not give any information about this resonance, although the capture information summarized here shows reasonable agreement.

Resonance 4: 29396.1 eV

In order to fit this resonance, the value of the neutron width $\Gamma_n = 16(3)$ eV was taken from the Mughabghab compilation [79]. The much lower value of the derived gamma width, makes the fit of this resonance mainly sensitive to the latter. The result obtained here of $\Gamma_\gamma = 189(7)$ meV, shown in table 7.5, is in perfect agreement with the value reported by Raman et al. [94] of 181(7) meV. Finally, the computed value for the radiative kernel shows also agreement with the compilations and evaluated files.

Resonance 5: 30485.9 eV

There exists almost no transmission measurement reported in the literature for this resonance, hence from our capture data we derived both the neutron and the capture widths. The result of the SAMMY fit, shown in figure 7.8, is given in table 7.5.

The unique value of a measured neutron width for this resonance was found in the paper of Raman et al. [90]. However, with such a large $\Gamma_n = 13$ eV, we obtain a worse fit to the n_TOF data and a value for $\Gamma_\gamma = 410(10)$ meV, not compatible with the $\Gamma_\gamma = 620(20)$ meV provided in the same reference. Therefore we conclude that the value provided for Γ_n in that reference (and the corresponding capture kernel of 444 meV) may not be correct.

The value obtained by us, $\Gamma_\gamma = 592(50)$ meV, is compatible with the value of Γ_γ from Raman et al. mentioned above, and with the values present in the compilations (see table 7.6).

Resonance 6: 37751 eV

Appart of the radiative kernels shown in table 7.6 for this resonance, there exists an additional measurement by Allen et al.'83 [96], which yields a radiative kernel value of $K_r = 1021(219)$ meV, not in agreement with the rest. However in another previous paper, Allen et al.'73 [95], a kernel value was obtained ($K_r = 554(0.14)$ meV), which would be in better agreement.

The capture width of this resonance, shown in figure 7.8, was fitted using a fix neutron width of 50(10) eV from Mughabghab [79]. The values obtained for the capture width (table 7.5) and the radiative kernel are in good agreement with the rest of measurements (table 7.6).

Resonance 7: 41183 eV

For this resonance there exists also two additional measurements due to Allen et al.'83 [96], $K_r = 5146(600)$ meV, and Allen et al.'73 [95], $K_r = 2766(0.08)$ meV. As in the previous resonance, the latter shows a better agreement with the rest of information presented in table 7.6.

Using a fix $\Gamma_n = 1220(30)$ eV from the Mughabghab compilation [79], we obtained a radiative kernel of about 20-30% lower than the two compilations and the measurement due to Raman et al. [90]. This might be related with the lower neutron sensitivity of the n_TOF capture setup.

Resonance 8: 48410 eV

This resonance has not been observed in any transmission experiment and therefore no data for Γ_n was available. We could see this resonance clearly, but the statistics were not enough to perform a fit of both Γ_n and Γ_γ. Therefore, starting from a fixed $\Gamma_n = 1$ eV the value of the gamma width and radiative kernel given in table 7.5 were derived.

The result obtained here is about a factor of two larger than the results obtained by Raman et al.

No resonance parameters are available for this resonance in the evaluations.

Resonance 9: 82990 eV

Starting from the neutron width provided by Horen et al. [97], the value of the capture width Γ_γ was derived. It is shown, together with the radiative kernel, in table 7.5.

The results reported by us for Γ_γ and the capture area are again a factor of two larger than those measured by Raman et al.

Resonance 10: 90228 eV

In order to analyze this resonance the value of the neutron width was fixed to $\Gamma_n = 272(13)$ eV from the Mughabghab compilation [79].

As has been described in section 7.1.1, an additional systematic uncertainty of +3.7%/-7.5% due to angular distribution effects, should be also considered for this 1^+ resonance.

The n_TOF result is in agreement with that reported in the Sukhoruchkin et al. compilation. However, these two results do not agree with an additional measurement due to Allen et al. [95], which yielded a radiative kernel $K_r = 1489(0.009)$ meV, compatible with the rest of values shown in table 7.6.

Resonance 11: 127900 eV

This resonance is overlaped with a smaller one of $J = 2$ at 127670 eV, with $\Gamma_\gamma = 469.88$ meV and $\Gamma_n = 125540$ meV. We were not able to distinguish the latter and therefore it was kept constant for fitting the bigger one at a fixed energy of 127900 eV. For a constant $\Gamma_n = 613(60)$ eV from the Mughabghab compilation [79], we obtained the value of Γ_γ shown in table 7.5, which is again in good agreement with the result reported in the compilation due to Sukhoruchkin et al. However, both are about 50% lower than the rest of capture areas shown in table 7.6.

As in the previous case, an additional systematic uncertainty of +3.7%/-7.5% should be considered for this resonance due to the unknown angular distribution of the emitted gamma ray.

Resonance 12: 130230 eV

Using a constant value of $\Gamma_n = 87(9)$ eV from Mughabghab [79], the capture width was fitted obtaining a result in good agreement with the rest (table 7.6).

Resonance 13: 181510 eV

This strong and broad s-wave resonance masks other p-wave resonances at about 181.15 keV, 182.29 keV and a d-wave resonance at 182.1 keV. The parameters of the latter three resonances were therefore kept constant to the values provided in the compilation due to Sukhoruchkin et al. [80], as well as the neutron width $\Gamma_n =$ 57.3 eV. Using the SAMMY code the main resonance's capture width was derived. The result obtained by us, shown in table 7.5, is in reasonable agreement with the two compilations and the measurement due to Raman et al. [90].

The two evaluated files, differ by about ∼50%, being the ENDF much closer to the result found here.

Resonances 14 and 15: 254440 eV, 256430

There is scarce experimental information concerning these two resonances. In particular, in Raman et al. [90] only about the latter is reported as one s-wave resonance at 256.11 keV with spin $J = 1$, $\Gamma_\gamma = 21.7(4)$ eV and $\Gamma_n = 3107$ eV. In the Sukhoruchkin et al. compilation, this resonance appears at 256.72(5) keV, with the same capture width but with $\Gamma_n = 2693$ eV, whereas in the Mughabghab compilation, a resonance at 256.43 keV is splitted into an s- and a d-wave resonance, the first having $\Gamma_n = 1666$ eV and $\Gamma_\gamma = 21$ eV and the second only $\Gamma_n = 1390$ eV (unknown Γ_γ).

We were able to observe one resonance at 254.44 keV plus another one at 256.43 keV. The latter was identified with the better known $l = 0$, $J = 1$ resonance. Fixing a $\Gamma_n = 1666$ eV from Mughabghab [79], the values for the capture width and area were derived (table 7.5). Using a $\Gamma_n = 3000$ eV (closer to the value reported by Sukhoruchkin et al. and by Raman et al.), we would obtain a $\Gamma_\gamma = 16770(490)$ meV and a radiative kernel $K_r = 12500(300)$ meV.

In order to fit the lower energy resonance at 254.4 keV, the neutron width was taken from the Mughabghab compilation [79], as well as the values of the quantum numbers $J = 3$ and $l = 2$. The values derived for the capture width and area are shown in table 7.5.

Regarding the first resonance at 254.4 keV, there is no other experimental information to be compared with. Concerning the *s*-wave resonance, a reduction of about a factor of two both in the capture area and width was obtained, probably due to the lower neutron sensitivity of the n_TOF experimental setup.

Resonance 16: 317400

In order to fit this *s*-wave resonance, the neutron width Γ_n was fixed to the value reported by Mughabghab [79]. The derived values of the radiative kernel and capture width are in good agreement with the other existing in the literature, as can be observed in table 7.6.

General remarks

A very interesting effect related with the WF can be observed when comparing with the results of Raman et al. (see figure 7.9). There is a clear good agreement for the capture areas measured below 45 keV, whereas above this energy the capture areas measured here differ considerably from those reported by Raman et al. in references [90, 94]. The results reported in the latter references, correspond to a thin sample measurement (of 0.5 mm thickness) for neutron energies below 45 keV, whereas in the high energy range, above 45 keV, a very thick sample of 1.6 cm was used, apparently employing the same WF as in the analysis of the thin sample data. In the chapter 5 of the present work, we have seen the importance of obtaining an specific WF for each experimental setup and in particular, for each sample. Therefore, the systematic deviations above 45 keV can be most probably ascribed to an incorrect WF in the analysis of the data reported by Raman et al. This hypothesis is farther confirmed by the fact, that above 45 keV the discrepancies follow a systematic relationship with the spin-parity of each resonance. For $J^\Pi = 2^+$ resonances, the values reported in reference [94] lie systematically lower. See for instance resonances at 48.4 keV and 83 keV in figure 7.9. On the other side, for resonances with $J^\Pi = 1^+$, as those at 90 keV and 127 keV, the opposite effect occurs. This systematic trend probably indicates that the WF used by Raman et al. to analyze the ^{207}Pb data beyond 45 keV is over-weighting the hard gamma rays of resonances with $J^\Pi = 1^+$ and on the other side, it is under-weighting resonances with $J^\Pi = 2^+$.

A further remark concerns the uncertainty on the neutron width Γ_n, which exceeds in general that on the capture width. This means, that in order to improve the capture cross section values in the resolved resonance region of ^{207}Pb, more accurate transmission measurements are needed.

Chapter 8

Discussion and outlook

The aim of the present work was to perform a measurement of the (n,γ) cross sections of ^{207}Pb and ^{209}Bi with a systematic precision down to few percent. In order to achieve such a goal, the experimental technique has been validated at n_TOF by measuring the particularly sensitive 1.15 keV resonance in ^{56}Fe+n. As a result of a thorough data reduction and the treatment of several experimental sources of systematic uncertainty, a systematic accuracy better than 2% was achieved. This is the first remarkable result since, despite the controversy in the past, it demonstrates that the PHWT can be successfully employed for the accurate measurement of radiative neutron capture cross sections. At the same time, an analysis procedure for this type of capture data has been developed based on the extensive use of the Monte Carlo technique. The latter has been employed for different issues. Firstly, detailed MC simulations have yielded realistic response distributions, needed for the calculation of the weighting functions. Measuring iron samples of different thicknesses, the sensitivity of the response function to the particular experimental sample-setup and the ability of the MC code (GEANT3 and GEANT4) to reproduce them, have been also proved. On the other hand, using the MC method with a statistical model of the nucleus we were able to reproduce successfully the shape of the prompt gamma rays spectrum for the measured capture resonances. This constitutes a new analysis approach for the determination of yield correction factors for several (unavoidable) experimental effects like threshold, gamma summing and internal conversion electrons. Furthermore, we have concluded from this study, that the common practice of assuming that these effects also cancel out by measuring with respect to a reference sample is wrong and can lead to inaccurate results.

Once the data reduction and analysis related with the PHWT are well under control, the measurement of the radiative capture cross section of ^{207}Pb and ^{209}Bi was tackled. As has been described in the present work, the main experimental difficulty in the measurement of these cross sections arises from the dominant elastic scattering channel of these isotopes. The present measurements were carried out with the aim of reducing as much as possible the contaminations due to scattered neutrons, which in previous experiments led to corrections larger than 50%.

Such large corrections imply necessarily large systematic uncertainties as well. An optimized detector, based on carbon fibre canned C_6D_6 and restricted materials, as well as a generally optimized detection setup, have been key in order to completely overcome the problem of having neutrons captured in the setup materials. From the experimental viewpoint, this constitutes an important improvement and demonstrates the ability of this new detector setup to obtain unbiased radiative capture cross sections.

In the case of the ^{209}Bi (n,γ) measurement, despite the limited statistics available and the in-beam gamma rays background, a further improvement in the determination of its cross section has been achieved when comparing with previous experiments. It is remarkable that the highest neutron sensitivity correction included in our analysis was of 3.6(7)% for the 12.1 keV resonance, whereas this correction was larger than 50% in any previous capture experiment. This is the most critical case, but not the only one since a total amount of four *s*-wave resonances have been analyzed in this isotope. The consequences of this measurement have been further extended to the evaluated information available. Indeed, the latter is based on previous experiments, which are affected by large uncertainties due to the neutron sensitivity effect. This result is evident when comparing the total cross section of the resonances measured in this work with those obtained from the evaluated data files. Important discrepancies are found, mainly for *s*-wave resonances, which suggest to update of the current evaluations using the newer experimental data available.

An additional issue has been discovered in ^{209}Bi after estimating the thermal capture cross section σ_{th} from the set of resonances measured in this work. The value obtained here, compatible with a previous radiative capture time of flight experiment [81], differ by $\sim$40% with respect to the value predicted by the evaluations, which coincides with accurate measurements of σ_{th} [78]. The reason for this apparent contradiction between the evaluated data files and the time of flight measurements, may be due to the fact, that evaluators usually adjust the evaluated cross sections, within the experimental uncertainties, in order to reproduce the well known value of σ_{th}. However, given that the lower energy *s*-wave resonances dominate the value of the extrapolated σ_{th}, and that their systematic uncertainties have been considerably reduced with the present work, we propose the inclusion of sub-threshold (negative energy) resonances in the evaluated files in order to obtain the thermal value, rather than adjusting the cross section of the *s*-levels.

The stellar nucleosynthesis implications of the measured (n,γ) cross section in ^{209}Bi have been also thoroughly investigated in chapter 6. The most remarkably result obtained here is the 6-7% uncertainty of the Maxwellian averaged cross section at stellar temperatures between 5 keV and 15 keV. It is worthy to emphasize that the systematic uncertainty however has been determined to be less than 3% (chapter 5), thus representing this technique an improvable way of obtaining accurate cross sections for nucleosynthesis calculations. Stellar cross section values with an improved accuracy down to $\sim$5% are relevant in order to determine self-consistent *s*-process abundances and isolate the radiogenic contribution to the lead and bismuth abun-

dances. The result obtained here constitutes, therefore, an excellent complement of the same quantity determined in another work [12] at the higher temperature of 25 keV by using the activation technique. In section 6.5, the latter quantity has been used, combined with the (n,γ) cross section measured in this work, in order to estimate the metastable state population for a neutron energy of 25 keV, resulting in a 28% feeding. However, it has been also found that a more accurate estimation requires to extend the bismuth measurement to higher energy and with improved signal to noise ratio and statistics.

In the measurement of the ^{207}Pb isotope, the discrepancies obtained with respect to previous measurements were smaller as was expected from the lower scattering to capture ratios of these resonances. Nevertheless, this measurement has revealed some inconsistencies with the evaluated data files and in addition, three resonances have been clearly seen in the present work, which do not exist in the evaluations.

The importance of the accurate measurement of the ^{207}Pb (n,γ) cross section for stellar nucleosynthesis calculations and the Th/U cosmochronometer, has been stressed in a recent study [12]. The measurement carried out in this work however, despite of an improved systematic uncertainty down to 3%, is affected by a higher than requested statistic uncertainty ($\sim$10%) due to the beam time available for the experiment and the in-beam gamma rays induced background. However, the demonstrated accuracy of 2% achievable in a time of flight measurement using total energy detectors (chapter 5), constitutes a call for future extension of this measurement.

At this point of the discussion, given the notable discrepancies found between the cross sections measured here and those present in the evaluations, we should comment about the qualitative impact of the ^{207}Pb and ^{209}Bi cross sections measured in this work in the design of future advanced hybrid reactors cooled with liquid Pb/Bi eutectic. A recent sensitivity study [18] has shown the consequences that inaccurate cross sections may have in the design of an ADS based nuclear reactor. In this study, the change in the neutron balance due to the discrepancies between evaluations has been investigated. The study, introduced in chapter 1, is based on one of the so far most developed designs of hybrid nuclear reactor called EADF. Concerning the ^{209}Bi (n,γ) cross section, the analysis revealed that the differences between the two evaluated data files, JENDL and ENDF, cause a discrepancy in the neutron multiplication coefficient $\Delta k/k = 207$ pcm, equivalent to a discrepancy of 12.5% in the neutron balance of the reactor. In the case of ^{207}Pb however, the discrepancy in the neutron balance due to the (n,γ) cross section was of only $\sim$2%.

The importance of the resolved resonance region for this prototype of ADS depends on the shape of the neutron energy spectra in the Pb/Bi volume of the machine, which acts as both spallation target and primary coolant. The neutron flux is shown in figure 8.1 (extracted from reference [18]). As can be observed in this figure, a large range of the neutron flux both in the spallation target and in the primary coolant, extends over the region of resolved resonances analyzed in this work. The flux, in the case of the primary coolant region, is a smooth distribution increasing less than one order of magnitude between 1 eV and 500 keV, with a maximum at

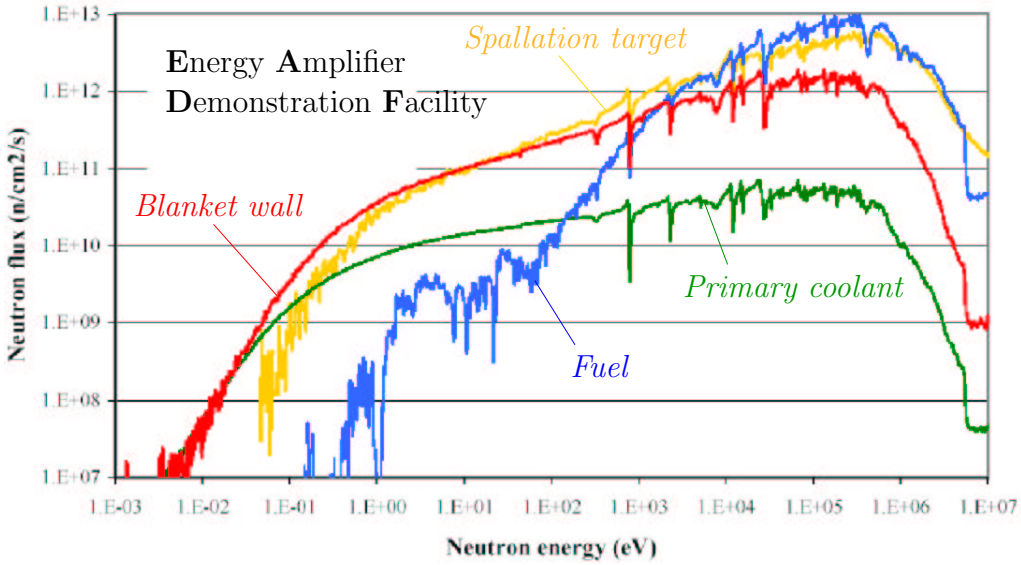

Figure 8.1: *Neutron flux spectrum in different parts of the EADF.*

about 300 keV. In the spallation target however, the spectrum is much faster increasing almost two orders of magnitude between 1 eV and 1 MeV. In particular, the absorption of neutrons due to the 802 eV resonance is clearly visible in both spectra, as well as some other higher energy resonances up to 1 MeV.

The discrepancy between the integrated cross section of the resonances measured in this work and those derived from ENDF (in which the sensitivity analysis [18] is based) can be calculated from table 6.6. In table 8.1 we present a summary of those resonances showing differences larger than 10%. In addition to those resonances shown in this table, it is worthy to mention here that in the present work we have found 4 and 3 resonances respectively for bismuth and ^{207}Pb, which do not exist in the evaluated data files.

A quantitative estimation of the influence in the ADS neutron balance due to the large differences shown in table 8.1, needs to be carried out with an appropriate neutron Monte Carlo simulation tool. This study is out of the scope of the present work, but from the differences shown in the previous table (some of these resonances are appreciable in figure 8.1), one may think that they could have a non negligible effect in the multiplication factor of the system.

Concerning future capture experiments at n_TOF, the optimized capture detection setup has been found to be very appropriate for the measurement of Γ_n-dominated resonances. Nevertheless, the measurement of a larger amount of nuclear resonances at higher energy as well as an improved statistical accuracy would be interesting for both *i*) stellar nucleosynthesis, where the MACS needs to be determined with an accuracy down to ∼5% up to ∼30 keV and *ii*) ADS, in particular for the Energy Amplifier project, where the neutron flux in the Pb/Bi spallation

$E_\circ$ (eV)	Isotope	Reso. area (meV) this work	Reso. area (meV) ENDF	Discrepancy (%)
801.6	Bi	18.2(9)	21.1	16
2323	Bi	12.0(8)	20.6	72
3352	Bi	9.5(9)	16.8	76
6289	Bi	6.7	13.3	98
6769	Bi	29(4)	15.7	-35
10191	^{207}Pb	146(16)	126.1	-16
12100	Bi	23(3)	52.6	230
41183	^{207}Pb	2970(390)	2491.6	-20
82990	^{207}Pb	436(125)	223(4)	-95
90228	^{207}Pb	1113(170)	1474.24	13
127900	^{207}Pb	1340(200)	2128.7	60
130230	^{207}Pb	624(100)	728	17
181520	^{207}Pb	8778(300)	7151	-23
256430	^{207}Pb	9482(280)	15540	63

Table 8.1: *Discrepancy between the integrated resonance cross section from ENDF and the present work. Only those showing differences larger than 10% are listed.*

target has its maximum at ∼300 keV.

A lower background at higher energy is also necessary in order to reliably analyze the unresolved resonance region of these isotopes.

These improved experimental conditions could be achieved at n_TOF by employing deuterated water as moderation liquid in the spallation source assembly. In this case, the background level is highly suppressed at higher energy as is described in appendix E. Indeed, the in-beam gamma rays have hindered the observation of a large number of resonances both in bismuth and in the lead samples. It is worthy to note here that replacement of the light water by deuterated water will affect the neutron flux shape, thus requiring a new measurement of it. The resolution function of the installation would be also affected by the new moderator. However, in this case both FLUKA and CAMOT packages have demonstrated already the ability to simulate realistic neutron distributions. Therefore, determine the new parameters of the RF should not be a big effort.

Resumen

Antecedentes

La medida precisa de secciones eficaces de captura neutrónica (n,γ) tiene dos motivaciones principales, *i*) la explicación de la producción de elementos pesados en las estrellas y *ii*) el diseño de reactores nucleares híbridos para la transmutación de residuos radiactivos y la producción de energía.

Astrofísica nuclear

El origen de los elementos constituye uno de los temas más fascinantes de la investigación en astrofísica nuclear. Aproximadamente la mitad de la abundancia isotópica por encima del hierro (A>56) que se observa en las estrellas es debida al denominado proceso de producción s [8]. Éste tiene lugar en escenarios estelares en los que existe un flujo de neutrones suficientemente bajo como para que el tiempo característico de captura neutrónica en los átomos de la estrella sea considerablemente inferior al de desintegración β. En estas circunstancias los elementos a lo largo del valle de estabilidad β se van sintetizando en el interior estelar a través de secuencias sucesivas de reacciones de captura neutrónica y de desintegración β. Por lo tanto, las abundancias de los elementos formados a lo largo del proceso s, están directamente ligadas con las secciones eficaces de captura (n,γ) de dichos isótopos. El camino del proceso s termina con los isótopos del plomo y el bismuto. La captura en bismuto conlleva la producción de isotopos que son inestables y se desintegran por emisión α, reciclándose de nuevo en isótopos del plomo, principalmente ^{206}Pb y ^{207}Pb.

La otra mitad de las abundancias observadas se debe principalmente al denominado proceso r. Éste ocurre en escenarios estelares donde existe un flujo de neutrones muy elevado, como en las explosiones supernova. En esta situación, la probabilidad de captura neutrónica suele ser mucho más elevada que la de desintegración β, de manera que se forman isótopos ricos en neutrones pero que son altamente inestables. Cuando estos decaen, tras sucesivas emisiones β alcanzan también el valle de estabilidad. Este proceso es el responsable exclusivo de la formación de los isótopos de uranio y torio, a los que el proceso s, como comentábamos anteriormente, no puede llegar. U y Th tienen vidas medias de desintegración muy largas, con lo cual la medida de las abundancias de los productos de dichas desintegraciones radiogénicas constituye a su vez una medida indirecta del tiempo en que dichos isótopos se formaron. Estos productos son precisamente los del plomo y del bismuto, de manera que conociendo la contribución radiogénica a las abundancias observadas se puede datar el origen de la estrella [12].

En base a las abundancias de los elementos observadas en las estrellas y a las secciones eficaces de captura neutrónica medidas experimentalmente se han conseguido elaborar sofisticados modelos estelares [10, 11], que permiten explicar con éxito las abundancias isotópicas en las estrellas a la vez que nos informan sobre los mecanismos internos y la evolución estelar y galáctica. Sin embargo, todavía no se ha alcanzado un escenario o modelo estelar fiable que permita predecir las abundancias observadas en el tramo final del proceso s, es decir, de los isótopos del plomo y del bismuto. En esta región, la situación es más compleja, puesto que además de las contribuciones debidas a los procesos s y r, existen también las contribuciones radiogénicas descritas anteriormente que se deben al decaimiento α de los isótopos de uranio y torio.

Para desarrollar un modelo estelar que permita describir las abundancias observadas de plomo y bismuto, es necesario conocer las secciones eficaces de captura neutrónica (n,γ) de dichos isótopos con una incertidumbre $\sim$5% [12]. Además, la medida precisa de estas secciones eficaces es relevante para poder separar la componente radiogénica de Pb y Bi, y utilizar esta información para la datación de los procesos r y del origen de las estrellas.

Diseño de reactores híbridos avanzados

La determinación precisa de las secciones eficaces de captura (n,γ), tiene por otro lado una aplicación práctica importante en el campo de la producción de energía por fisión nuclear. Como es generalmente conocido, los residuos radiactivos constituyen la principal desventaja de las centrales nucleares de producción energética. Actualmente, la idea predominante es que estos residuos van a ser almacenados sistemáticamente en repositorios geológicos profundos. No obstante, esta situación no es muy deseable por varios motivos, como puedan ser la posibilidad de reestructuración que implique criticidad y la utilización para la proliferación armamentística nuclear. Por estos motivos, desde hace años se está considerando la posibilidad de transmutar estos residuos utilizando el mismo mecanismo por el que fueron formados: reacciones inducidas por neutrones [3]. Mediante una reacción de captura (n,γ) o (n,f), se podrian convertir los residuos radiactivos de las centrales nucleares en elementos estables, a la vez que se produce energía.

Uno de los diseños de reactor-transmutador más desarrollados actualmente es el amplificador de energía (EA) [4]. Éste está basado en un blanco líquido de plomo y bismuto, sobre el cual se hace incidir un haz de protones para producir un elevado flujo de neutrones por el mecanismo de espalación. Inmerso en este líquido se encontraría el núcleo de este reactor híbrido conteniendo el combustible fisible (uranio, torio o plutonio) mezclado con los residuos radiactivos que se producen en un reactor convencional. Controlando la intensidad del flujo de neutrones, así como su distribución energética, se pueden producir reacciones de fisión (produciendo energía) tanto en el combustible fisionable del reactor como en los residuos radiactivos conocidos como transuránidos (TRU), ^{239,242,240}Pu, ^{241,243}Am, etc a la vez que

se eliminan éstos. La transmutación de los productos de la fisión con vidas medias largas (LLFF), ^{99}Tc, ^{129}I, etc se puede llevar a cabo efectivamente mediante reacciones de captura neutrónica (n,γ) a las cuales les sucede generalmente un decaimiento β, produciendo un nuevo isótopo que ya es estable o con un periodo de vida media mucho menor. Este mecanismo de incineración de LLFF ha sido demostrado experimentalmente en el experimento TARC [16], llevado a cabo en el CERN. Además, en dicho experimento se comprobó la utilidad de este mecanismo para la producción de radioisótopos de interés en medicina nuclear. En efecto, a partir de una muestra de molibdeno natural, se consiguió activar ^{99m}Tc, ampliamente utilizado como radiotrazador en medicina.

Las reacciones de captura neutrónica (n,γ), al contrario que otras como (n,f) o (n,xn) no tienen un umbral energético y por lo tanto pueden parasitar continuamente (consumiendo neutrones) las otras reacciones utilizadas para la producción de energía en el reactor. En un estudio [18] sobre la sensibilidad del balance neutrónico en el EA a las secciones eficaces de captura evaluadas, se encontró una discrepancia del 12% en el balance de neutrones, debida a las discrepancias que presentan las evaluaciones ENDF y JENDL en la sección eficaz (n,γ) del bismuto.

Un motivo adicional para la medida precisa de estas secciones eficaces se debe a que las reacciones de captura neutrónica en bismuto determinan la producción del isótopo inestable ^{210m}Bi, con un periodo de vida media de 3×10^6 a, el cual se desintegra emitiendo una partícula α. La acumulación de este isótopo en el Pb/Bi del EA determina la radiotoxicidad a largo término del blanco de espalación. Por otro lado, captura en bismuto también conlleva la producción de ^{210}Po, que es inestable α con un periodo de semidesintegración $t_{1/2}$=138 d, lo cual contribuye a la radiotoxicidad a corto plazo del blanco de espalación. Por estos motivos, las secciones eficaces de captura neutrónica radiativa en plomo y bismuto son relevantes para determinar el balance de neutrones en el EA así como el nivel de activación o radiotoxicidad del blanco de espalación empleado en este tipo de reactores híbridos.

Reto experimental

Desde el punto de vista experimental, la medida de estas secciones eficaces es complicada, puesto que muchas resonancias de estos isótopos presentan un canal de dispersión neutrónica dominante. En consecuencia, por cada reacción de captura (n,γ) en la muestra a medir, tienen lugar muchas otras de dispersión neutrónica. Estos neutrones dispersados, pueden ser fácilmente capturados en los materiales del dispositivo experimental y en el propio detector, dando lugar a reacciones parásitas (n,γ), que pueden a su vez ser registradas en los detectores dando lugar a una contaminación en la medida. Este efecto se conoce como sensibilidad neutrónica del dispositivo experimental y debe ser minimizado para evitar una incertidumbre sistemática elevada en el resultado de la medida.

La primera aproximación para reducir la sensibilidad neutrónica consiste en utilizar detectores de pequeño volumen y baja eficiencia, conocidos como detectores de

energía total. La técnica alternativa de emplear un calorímetro de absorción total 4π para estas medidas, mostraría una contaminación prohibitiva debido a capturas parásitas en el amplio volumen del detector.

No obstante, a pesar de la ventaja que suponen los detectores de energía total, en experimentos anteriores de captura en el isótopo ^{209}Bi [24, 87] fueron necesarias correcciones superiores al 50% en las secciones eficaces de algunas resonancias debido al efecto de la sensibilidad neutrónica. Esto conlleva necesariamente una incertidumbre sistemática alta, puesto que el factor de corrección no es sencillo de determinar de manera precisa. Estas incertidumbres sistemáticas altas en experimentos anteriores se reflejan además en discrepancias importantes en las bases de datos nucleares evaluadas.

Otro efecto experimental a considerar en estas medidas es que estos isótopos tienen una configuración nuclear próxima a la del doblemente mágico ^{208}Pb. Por este motivo, su sección eficaz de captura neutrónica es también muy baja. Esto es una dificultad experimental añadida, puesto que reduce la sensibilidad de detección, es decir, la relación señal/ruido es más baja que en la medida de otros isótopos.

Por otro lado, la técnica de los detectores de energía total requiere la obtención de funciones peso para corregir el efecto de la energía del rayo gamma en la eficiencia de detección. Esta técnica, así como la obtención de estas funciones peso, han sido fuente de controversia en experimentos anteriores [61, 62]. A principios de los años 80, el valor de Γ_n en la resonancia de 1.15 keV de ^{56}Fe+n determinado en algunos laboratorios utilizando la técnica de los detectores de energía total, difería entorno a un 20% respecto al resultado obtenido en medidas precisas de transmisión. Este hecho condujo a un replanteamiento de la precisión alcanzable con la técnica de los detectores de energía total.

En un primer intento de resolver este problema, en GELINA (Geel) se ideó un método puramente experimental [26], que permitía obtener las funciones peso necesarias en la técnica de los detectores de energía total. Este método consistió en utilizar una técnica de coincidencias con cascadas de dos transiciones pobladas en reacciones (p,γ). Mientras uno de los rayos gamma se detectaba en el dispositivo experimental convencional para medidas (n,γ), el otro se media con un detector de germanio. Utilizando diversos materiales como muestra, se obtuvieron funciones de respuesta para un conjunto de rayos gamma en el intervalo de energía de interés hasta $\sim$ 9 MeV. De esta manera se encontró una función peso experimental, que permitía obtener buenos resultados para la resonancia de 1.15 keV cuando se utilizaban muestras delgadas. No obstante, en dicho trabajo se concluyó que el material que rodea a la muestra influye considerablemente en la distribución de respuesta y por lo tanto en la función peso. Evidentemente la propia muestra de captura es a la vez la principal fuente de radiación secundaria y por lo tanto, la función peso experimental así como el propio método son bastante cuestionables. Además, con la finalidad de mantener el tiempo de haz total empleado para cada medida dentro de unos limites razonables, es normal emplear muestras de espesor considerable, para las cuales la precisión del método de la función peso experimental queda cláramente

en evidencia.

Objetivos

En vista de los antecedentes descritos en la sección anterior, en el presente trabajo nos hemos planteado los siguientes objetivos generales:

- Validación experimental de la técnica de medida para determinar la precisión sistemática que se puede alcanzar utilizando detectores de energía total. Para ello, como se explica en mayor detalle más adelante, se midió la resonancia de 1.15 keV en ^{56}Fe utilizando muestras de hierro con diferentes tamaños y empleando dos modelos de detector diferentes.

- Determinación experimental de las secciones eficaces de captura radiativa de ^{207}Pb y ^{209}Bi, con una incertidumbre sistemática baja ($\sim$3%). Para este objetivo, básicamente se emplearon detectores de energía total optimizados en términos de sensibilidad neutrónica y por otra parte se hizo un tratamiento exhaustivo de las diferentes fuentes de incertidumbre sistemática que puedan afectar a la medida.

- El trabajo se completa con una estimación y discusión sobre el impacto de las medidas realizadas tanto en el ámbito de la nucleosíntesis estelar como en el de la ingeniería de reactores nucleares avanzados.

A continuación se describirá el contexto experimental del presente trabajo a la vez que se desarrollarán en mayor detalle los puntos marcados arriba como objetivos.

Instalación n_TOF

La sección eficaz de la reacción (n,γ) se mide en función de la energía del neutrón. Para determinar la energía del neutrón, se utilizó la técnica del tiempo de vuelo (TOF). Esta consiste en la medida precisa del tiempo transcurrido desde el instante de producción del neutrón hasta que tiene lugar la reacción (n,γ). Midiendo este intervalo temporal y conocida la distancia de vuelo, se puede calcular la energía cinética que tenía el neutrón cuando tuvo lugar la reacción de captura radiativa. Estas medidas se llevaron a cabo en la instalación n_TOF del CERN (Ginebra) [6]. El dispositivo experimental completo se describe en el capítulo 3. n_TOF (figura 3.1) dispone de un túnel de 185 m de longitud, lo cual se refleja en una excelente resolución energética ya que ésta es inversamente proporcional a la distancia de vuelo. Para producir el haz de neutrones se utiliza el sincrotrón de protones del CERN (PS). Este haz tiene una energía de 20 GeV/c, una intensidad nominal de 7×10^{12} protones por pulso y una anchura de 6 ns (RMS). Cuando se hace incidir sobre un bloque de plomo, se producen reacciones de espalación que liberan aproximadamente unos 600 neutrones por cada protón incidente. Con la finalidad de evitar partículas

cargadas y fotones, que son dispersados preferentemente hacia delante, el haz de neutrones forma un ángulo de 10° con respecto al haz incidente de protones.

Dispositivo experimental y técnica de medida

En la estación de medida, a ∼185 m de la fuente de neutrones, se encuentra la muestra cuya sección eficaz de captura se desea medir.

Cuando tiene lugar una reacción de captura neutrónica, el núcleo compuesto formado se encuentra en un estado excitado que a continuación decae emitiendo una cascada de rayos gamma hasta llegar al estado fundamental (figura 1.3). En general, las reacciones de captura neutrónica (n,γ) se detectan registrando estos rayos gamma que suceden a cada evento de captura.

En las medidas de los isótopos del plomo y el bismuto, como se explicó anteriormente, la técnica de los detectores de energía total supone una ventaja en términos de minimizar la sensibilidad neutrónica. En particular, para estas medidas se utilizaron detectores de benceno deuterado, C_6D_6.

La técnica de los detectores de energía total [23] se describe ampliamente en el capítulo 2. Consiste en el empleo de detectores de muy baja eficiencia, de manera que en buena aproximación como máximo un único rayo gamma de la cascada nuclear va a ser registrado. Pero como la cascada de rayos gamma sigue en general caminos diferentes tras cada captura, la eficiencia de detección para cada evento (n,γ) va a depender de cada cascada o rayo gamma detectado en particular. Para evitar esto, se aplica un peso a la función de respuesta de los detectores de manera que la eficiencia de detección gamma se hace proporcional a la energía del rayo gamma registrado. Si además la eficiencia de detección es muy baja, se puede demostrar que la probabilidad de detectar una cascada o un evento de captura (n,γ), es proporcional a la energía de captura E_c (que es un valor conocido y constante para una energía del neutrón E_n) y por lo tanto es independiente del camino particular de desexcitación nuclear.

Por lo tanto, utilizando detectores de energía total, tenemos que hallar un peso W_i para cada señal de amplitud i, que al ser aplicado a la funcion de respuesta $R_{i,j}$ del sistema de detección para un rayo gamma de energía E_j, satisfaga la condición

$$\sum_i W_i R_{i,j} = kE_j. \tag{8.1}$$

Para poder calcular W_i, se necesitan un conjunto de ecuaciones como la anterior, en un rango de energías E_j que cubran la energía de captura, 6-9 MeV.

El método usado para obtener las funciones peso W_i es utilizando la técnica de simulación Monte Carlo. Simulando la emisión de un conjunto de rayos gamma E_j en el dispositivo de medida e histogramando sus funciones de respuesta $R_{i,j}$, se puede obtener el sistema de ecuaciones 8.1 deseado. No obstante, como se explicó en la sección anterior, en medidas anteriores de la resonancia de 1.15 keV del ^{56}Fe se encontraron desviaciones inaceptables utilizando este método. Actualmente existen no obstante potentes herramientas de simulación Monte Carlo que poseen librerias

amplias y detalladas para simular los procesos electromágneticos de manera precisa. En particular, en el presente trabajo hemos realizado un estudio de la capacidad de los códigos GEANT3 [64] y GEANT4 [65] para la obtención de funciones de respuesta realistas que permitan calcular funciones peso W_i válidas. El último de estos códigos está basado en el lenguaje de programación C++ y permite una implementación muy detallada y completa de la geometría del dispositivo experimental. En trabajos anteriores [63, 37] se pudo demostrar que ambos códigos permiten reproducir los procesos electromagnéticos subyacentes con fiabilidad.

Validación

Para validar la técnica de los detectores de energía total, también conocida como técnica de ponderación según la amplitud del pulso (PHWT), nos basaremos en la resonancia de 1.15 keV en ^{56}Fe [7]. En experimentos anteriores se ha encontrado que esta resonancia es especialmente sensible a los detalles de la función peso. Por otra parte, la anchura neutrónica Γ_n es aproximadamente 10 veces menor que la anchura de radiación Γ_γ. Esto hace que la medida de esta resonancia sea particularmente sensible a Γ_n, cuyo valor está bien determinado por medidas de transmisión.

Como se describió en el apartado anterior, esta técnica de medida requiere de unas funciones peso W_i para corregir el efecto de la baja eficiencia. En un estudio previo [63], se demostró que la técnica de simulación Monte Carlo es capaz de reproducir detalladamente las funciones de respuesta de un sistema de detección como el utilizado en n_TOF. Por este motivo, para obtener las funciones de respuesta $R_{i,j}$, se hizo uso principalmente de los códigos de simulación Monte Carlo GEANT4 y GEANT3. A partir de estas funciones de respuesta $R_{i,j}$, mediante un sistema de equaciones como 8.1, se calcularon las funciones peso W_i.

Por otro lado, para poder obtener una precisión sistemática alta en este tipo de medidas, es necesario mantener bajo control todas las fuentes de incertidumbre. Por este motivo se desarrolló un método que permita estimar y corregir diversos efectos experimentales como el umbral electrónico de los detectores, los procesos de conversión de electrones y el efecto suma que tiene lugar cuando se registran dos o más rayos gamma simultáneamente.

La validez de las simulaciones Monte Carlo para obtener las funciones peso W_i, y del método de corrección desarrollado, se comprobó aplicándolos a la resonancia de 1.15 keV del ^{56}Fe y comparando los resultados obtenidos con los valores de referencia que se conocen con gran precisión.

En particular, utilizando muestras de diferentes espesores y diámetros, se comprobó la capacidad de la técnica Monte Carlo para reproducir con precisión los detalles del dispositivo experimental.

Medida de la sección eficaz de ^{207}Pb y ^{209}Bi

Una vez validada la técnica de medida y establecida la incertidumbre sistemática asociada a esta, se procedió con la medida de dos de los isótopos más relevantes para

los temas mencionados en la primera sección de este capítulo.

Con el objetivo de reducir al máximo las contaminaciones debidas a captura de neutrones en los materiales del dispositivo de medida, se utilizaron detectores de C_6D_6 especialmente manufacturados [5] para este propósito.

En el análisis de estos datos se hizo uso del método desarrollado en el apartado de validación para obtener la función peso W_i. También se empleó un tratamiento exhaustivo de las otras fuentes de incertidumbre sistemática que afectan a este tipo de medidas, debidas al umbral electrónico de los detectores, la conversión de electrones y el efecto suma.

Una vez analizados los datos de captura y obtenidas las secciones eficaces de estos dos isótopos, se hizo un estudio comparativo de los resultados obtenidos en n_TOF frente a experimentos anteriores. Por otro lado, se estudió también las discrepancias con las bases de datos evaluados.

Finalmente se comprobó el impacto de los resultados obtenidos en los cálculos de abundancias en nucleosíntesis estelar así como su posible influencia en el diseño de reactores nucleares híbridos para la transmutación de residuos radiactivos y la producción de energía.

Discusión

Validación experimental y precisión de la técnica de medida

Para determinar la precisión sistemática de la PHWT se midió la resonancia de 1.15 keV en ^{56}Fe utilizando dos modelos diferentes de detector C_6D_6 y midiendo dos muestras distintas de hierro con cada tipo de detector [7]. Las características de las muestras medidas se resumen en la tabla 5.1.

Los datos obtenidos en estas medidas se analizaron utilizando la herramienta de análisis de datos ROOT [41] del CERN. Para este propósito se escribió una librería en C++ que permitiese por un lado escribir los datos en un formato de n-tupla con el cual ROOT puede operar de manera más efectiva y por otro lado procesar la información y analizar los resultados. La selección de eventos válidos se realiza aplicando las pruebas de consistencia descritas en el capítulo 4. Finalmente se calcúlan las tasas de rendimiento experimental.

Para dicho cálculo es necesario conocer los siguientes elementos:

- Calibrado en energía de los detectores de C_6D_6. Para este calibrado se utilizan tres fuentes radiactivas monoenergéticas de Cs, Co y Pu/C. (Sección 4.4).

- Calibrado en energía del neutrón [43]. Para determinar la energía $E_\circ$ de cada resonancia es necesario conocer la relación existente entre el tiempo de vuelo y la energía del neutrón. La determinación experimental precisa de esta relación viene descrita en la sección 4.3.

- Intensidad del haz de neutrones [46]. En particular, para estas medidas es necesario conocer únicamente la dependencia de la intensidad de neutrones con la energía. Ésta se ha determinado a partir de dos medidas independientes realizadas con dos detectores diferentes, como se explica en la sección 4.5.

- Perfil del haz de neutrones [51]. Esta información es necesaria para comparar medidas realizadas con muestras de diámetros diferentes. El perfil del haz se describe en la sección 4.6.1.

Además la tasa de rendimiento experimental puede estar afectada por efectos de solapamiento entre pulsos. Si la tasa de contaje es muy alta, los ficheros de rendimiento se pueden corregir siguiendo el procedimiento descrito en la sección 4.7.

Finalmente, en el cálculo de la tasa de rendimiento experimental, están implicadas las funciones peso cuya precisión queremos comprobar en el presente experimento. Para obtener las funciones peso en este trabajo hemos hecho uso de la técnica de simulación Monte Carlo. En particular se simuló la función de respuesta $R_{i,j}$ correspondiente a cada dispositivo experimental (detector-muestra). Utilizando el código de simulación GEANT4 hemos reproducido la geometría del dispositivo de medida con un elevado grado de detalle [37] (figura 5.1). El primer resultado importane que se obtiene del cálculo Monte Carlo, es que las funciones de respuesta y por lo tanto las funciones peso W_i, dependen de la muestra en particular, tanto del material como de sus dimensiones (figura 5.2). A partir de las distribuciones de respuesta obtenidas, se calculan las funciones peso W_i asumiendo un comportamiento polinómico y obteniendo los coeficientes de dicho polinomio mediante una minimización del sistema de ecuaciones 8.1.

Para evaluar la incertidumbre (estadística y sistemática) de las funciones peso obtenidas, se ha desarrollado un método basado en la simulación Monte Carlo de los procesos de desexcitación nuclear que ocurren tras una captura neutrónica [7] (sección 5.5). Como los estados cuánticos del núcleo compuesto son conocidos experimentalmente [68] solo hasta un cierto valor de la energía E_{cut}, por encima del último nivel experimental conocido se ha hecho uso de un modelo estadístico del núcleo que permita completar la cascada nuclear hasta la energía de captura E_c. La parte de la cascada nuclear correspondiente al modelo estadístico se puede calcular como se ha descrito en la sección 5.5. Básicamente se divide esta región en intervalos de 50 keV. La intensidad de las transiciones desde estos "niveles" a los experimentales reales a baja energía se pueden calcular utilizando el modelo de la resonancia dipolar gigante [69]. Para calcular transiciones entre los "niveles" de la región estadística hemos empleado varios modelos diferentes de densidad de niveles [75]. Este cálculo ha sido programado e implementado como generador de eventos en el código de simulación GEANT, en el cual hemos incluido una representación detallada del dispositivo experimental de medida. De esta manera se puede reproducir de forma completa la función de respuesta R_i^c de los detectores para una captura neutrónica en cada resonancia definida por los números cuánticos $E_\circ$, J^Π. Simulando un experimento ideal en el que no tienen lugar los efectos experimentales convencionales de

umbral electrónico, suma, etc y aplicando la función peso calculada anteriormente a la distribución de respuesta ideal obtenida en dicho cálculo, se puede determinar la incertidumbre debida exclusivamente a la función peso.

El método de simulación de cascadas descrito arriba, permite por una parte evaluar la incertidumbre debida a la función peso, y por otra estimar los factores de corrección debidos a varios efectos experimentales, como son el umbral electrónico de los detectores, la conversión de electrones y la suma de dos o más rayos gamma registrados en coincidencia. Estos efectos se pueden incluir también en la simulación. Comparando respecto al caso ideal en que no existieran, se puede calcular el factor de corrección a aplicar a la tasa de rendimiento experimental. El cálculo de estos factores de corrección se describe en la sección 5.6 de este trabajo.

Los ficheros de tasa de rendimiento experimental se analizaron con el código de análisis de reacciones con neutrones SAMMY [49]. Este código permite tener en cuenta diversos efectos experimentales como son la composición isotópica de la muestra, lo cual resulta particularmente útil no solo para las muestras de ^{nat}Fe, sinó también para la de Pb (enriquecida en ^{207}Pb). También calcula efectos debidos a la dispersión múltiple de neutrones dentro del volumen de la muestra y efectos de apantallamiento. Por otra parte permite incluir también el ensanchamiento debido a la agitación térmica de los núcleos, conocido también como ensanchamiento Doppler. Este ensanchamiento es importante para energías de hasta varios keV. Por encima de esta energía, principalmente para resonancias delgadas ($l > 0$), el principal ensanchamiento es debido a la función de resolución de la instalación. Esto nos lleva a un objetivo adicional del presente trabajo, que consiste en determinar la función de resolución de n_TOF. La función de resolución se define como la distribución temporal de neutrones con una energía concreta en la zona de medida (a la distancia de vuelo de la muestra cuya sección eficaz de captura se quiere medir). Esta distribución temporal se debe a la anchura inicial del haz de protones y a las reflexiones y moderación que sufren los neutrones dentro del bloque de espalación y en el moderador de agua que rodea a éste. De nuevo, la única vía para determinar la función de resolución fue haciendo uso de simulaciones Monte Carlo de las reacciones de espalación en el blanco de la instalación n_TOF. Por otra parte, la calidad de los resultados obtenidos se comprobó analizando resonancias finas a alta energía en la muestra de ^{nat}Fe como se describe en la sección 4.9.

Finalmente, para evaluar la precisión de la PHWT, se calculó para cada una de las muestras medidas el cociente entre la tasa de rendimiento analizada con SAMMY de los datos medidos en n_TOF y el valor de la tasa de rendimiento nominal para la resonancia de 1.15 keV. El resultado obtenido se muestra en la figura 5.10. La desviación cuadrática media es del 1.7%, lo cual demuestra que la precisión sistemática que se puede alcanzar con el método de los detectores de energía total es mejor del 2% [7].

En la obtención de este resultado cabe destacar principalmente, tanto el tratamiento exhaustivo que se ha hecho de las fuentes de incertidumbre, como el alto grado de detalle implementado en las simulaciones Monte Carlo. Estos dos

elementos resultan ser claves en la obtención de una precisión sistemática alta.

Sección eficaz de captura en ^{209}Bi

Este isótopo es el último eslabón de los núcleos estables sintetizados por el proceso s en las estrellas. Una medida precisa de su sección eficaz es importante para poder determinar cual es la producción de los isótopos del plomo y del bismuto debida al proceso s.

Por otro lado, la captura en bismuto determina la radiotoxicidad a largo término del blanco de espalación en un reactor híbrido para la transmutación de residuos radiactivos.

En este isótopo, al contrario de lo que sucedía con la muestra de hierro, existen muchas resonancias cuyo canal de dispersión neutrónica domina (uno o varios órdenes de magnitud) sobre el de captura radiativa. Experimentalmente esto se traduce en que por cada reacción de captura (n,γ) susceptible de ser medida, tenemos muchas de dispersión (n,n'). El neutrón dispersado puede entonces producir una reacción (n,γ) en los materiales del dispositivo de medida y el rayo gamma emitido se puede registrar en el detector. Éste no se puede distinguir de los que provienen de reacciones (n,γ) en la muestra y por tanto es una fuente de contaminación indeseable. Por este motivo, estas medidas se hicieron con el dispositivo experimental optimizado en el que se utilizaron detectores especiales de C_6D_6 [5]. Estos detectores se caracterizan por un contenedor del líquido C_6D_6 de fibra de carbono así como por una restricción máxima de materiales que no son absolutamente necesarios (sección 3.2).

Utilizando el método descrito en el apartado anterior para la muestra de Fe, hemos medido y analizado una muestra de ^{209}Bi. La principal diferencia en este caso radica en la incompatibilidad del método convencional para calcular la funcion peso. Éste consiste en asumir una función polinómica para W_i, y obtener los coeficientes del polinomio haciendo un ajuste por mínimos cuadrados de un conjunto de ecuaciones 8.1. Sin embargo, con la muestra de bismuto, la función peso obtenida de esta manera no cumplía la condición de proporcionalidad (figura 6.2). Por este motivo, se desarrolló un nuevo procedimiento matemático [27] que permitiese obtener una función peso válida. Para este propósito se utilizó el método de regularización lineal de Tikhonov, descrito ampliamente en el capítulo 2. El motivo de la insuficiencia de una función polinómica en la muestra de bismuto, radica en la gran absorción de rayos gamma de baja energía que tiene lugar en una muestra tan gruesa y de un número atómico tan elevado.

Los efectos experimentales en los detectores, debidos al umbral electrónico, conversión de electrones y suma de rayos gamma, fueron tenidos en cuenta de nuevo siguiendo el método desarrollado en el análisis de la muestra de hierro. Como se muestra en la figura 6.9, se encontró que el factor de corrección es aproximadamente el mismo para resonancias con igual espin y paridad, independientemente de la energía de la resonancia. Éste es un resultado interesante que facilita la reducción de

datos para obtener la tasa de rendimiento experimental final. Debido a que el espectro de rayos gamma del bismuto es blando, el factor de corrección es generalmente muy alto, mayor del 13% para un umbral de 200 keV.

Además, el bismuto tiene un estado isomérico a 271 keV que debe ser tenido también en cuenta en el factor de corrección. Utilizando el modelo nuclear descrito anteriormente se estimó el efecto de este nivel isomérico, afectando en el caso más crítico menos de un 2% al factor de corrección calculado. Este efecto también se incluyó en el cálculo del factor de corrección global.

Los resultados obtenidos tras el análisis con SAMMY de los datos medidos en n_TOF se muestran en la tabla 6.5. Para comparar con resultados obtenidos en experimentos anteriores, hemos calculado la integral de la sección eficaz de cada resonancia, que viene dada por la fórmula del *kernel* radiativo,

$$K_r = g\frac{\Gamma_\gamma \Gamma_n}{\Gamma}. \tag{8.2}$$

Los resultados de n_TOF se comparan en la gráfica 6.11 frente a dos medidas realizadas anteriormente en ORNL [24], Oak Ridge (EEUU) y en GELINA [81], Geel (Bélgica). Comparemos en primer lugar los resultados obtenidos en el presente trabajo con los publicados por Macklin et al. de ORNL. El primer resultado importante es que principalmente para las resonancias s a energías de 802 eV, 2.3 keV, 5 keV y 12.1 keV, en n_TOF se ha medido una sección eficaz de captura neutrónica considerablemente más baja. Esto es debido a la alta sensibilidad neutrónica del dispositivo experimental utilizado en ORNL y a una insuficiente corrección de sus datos (por este efecto) en el análisis de estas resonancias. Cabe decir que su resonancia a 12.1 keV fue corregida en un 50%, y que a pesar de ello, todavía queda más de un factor 2 por encima del resultado medido en n_TOF. En nuestro caso, la corrección debida a la sensibilidad neutrónica fue inferior al 4% (y esta fue la única corrección de sensibilidad neutrónica necesaria en los datos de n_TOF). Este excelente resultado es consecuencia del elevado grado de minimización de la sensibilidad neutrónica del dispositivo experimental utilizado en n_TOF.

Los resultados obtenidos en n_TOF muestran mucho mejor acuerdo en general con los resultados obtenidos en GELINA, lo cual refleja que en este caso se efectuó un tratamiento de las correcciones de sensibilidad neutrónica adecuado. No obstante, se puede apreciar una tendencia sistemática en los datos de GELINA tal que las resonancias s muestran una sección eficaz ligeramente menor que las medidas en n_TOF. Esto indicaría una ligera sobrecorrección del efecto de sensibilidad neutrónica, que por otra parte no es sencillo de calcular de manera precisa.

La mayor sensibilidad neutrónica de experimentos anteriores queda reflejada al comparar las áreas de las resonancias medidas, frente al cociente Γ_n/Γ_γ. La figura 6.13 refleja la elevada contaminación neutrónica presente en el experimento de ORNL, cuyos efectos fueron insuficientemente corregidos en las secciones eficaces analizadas. Por otro lado, los datos medidos en GELINA muestran mucho mejor acuerdo con los de n_TOF, aunque la ligera sobrecorrección queda patente en esta gráfica.

Comparando los resultados obtenidos en n_TOF frente a las evaluaciones (figura 6.12), se observan en general claras discrepancias, principalmente en el caso de resonancias s. Esto es debido a que las bases de datos evaluados están basadas sobre todo en el primer experimento realizado hace tiempo en ORNL, el cual esta afectado de una incertidumbre sistemática alta, como ya se ha comentado anteriormente. Este resultado sugiere cláramente una actualización de la información evaluada, considerando los resultados más recientes y precisos de n_TOF.

A partir de las secciones eficaces de la región de las resonancias resueltas, se puede calcular o extrapolar el valor de la sección eficaz de captura térmica σ_{th}. Utilizando los parámetros de las resonancias medidas en n_TOF y en GELINA, se obtiene un resultado compatible de aproximadamente 24 mb. Sin embargo, haciendo el mismo cálculo con los parámetros existentes en las bases de datos, se obtiene el valor medido experimentalmente [79] de $\sim$34 mb. Mientras que el resultado experimental se conoce con una incertidumbre muy baja, sabemos por otro lado que los parámetros de las bases de datos no son precisos. Esta aparente contradicción radica en el hecho de que los evaluadores, cuando existe un experimento con incertidumbres sistemáticas altas, ajustan los valores de los parámetros para reproducir entre otras cosas el valor de la sección eficaz térmica a baja energía. Sin embargo, basados en los resultados de GELINA y n_TOF, los evaluadores deberían incluir mejor resonancias por debajo del umbral (resonancias a energía negativa) para reproducir el valor de la sección eficaz térmica.

Las implicaciones en nucleosíntesis estelar debidas a la la sección eficaz de captura en bismuto medida en n_TOF han sido estimadas en primera aproximación. Para este propósito se ha calculado, a partir de las resonancias medidas, la sección eficaz Maxwell promediada (MACS), que es la cantidad relevante en los cálculos con modelos estelares. El resultado obtenido con los datos de n_TOF es ligeramente superior al valor de la MACS obtenida con los datos medidos en GELINA, en los cuales está basada la compilación de Bao et al. [88] que se utiliza actualmente como referencia para los cálculos de abundancias en las estrellas. Una sección eficaz mayor, indicaría en primer lugar una menor supervivencia del isótopo ^{209}Bi, debida a la mayor captura de neutrones, y en segundo lugar, podría reflejarse en una mayor producción de los isótopos del Pb, en partícular ^{206,207}Pb, debido al reciclaje α del ^{210}Po y ^{210m}Bi. Utilizando un modelo para una estrella pulsante AGB de baja masa y baja metalicidad, se ha obtenido[1] una abundancia de un 6% menor del isótopo estable del Bi, debida a la mayor sección eficaz de este medida en n_TOF. El resultado obtenido muestra que este modelo estelar presenta una buena compatibilidad con datos medidos de las abundancias solares, así como con las predicciones teóricas de las abundancias debidas al proceso r.

[1] R. Gallino (Univ. de Torino, Italia), comunicación privada.

Sección eficaz de captura en ^{207}Pb

La medida precisa de la sección eficaz (n,γ) de este isótopo es importante en nucleosíntesis estelar, para poder separar la contribución debida al proceso s de la contribucion r y la contribución radiogénica.

Cuando un núcleo de ^{207}Pb captura un neutrón, se convierte en el doblemente mágico ^{208}Pb. Este isótopo presenta un patrón de desexcitación muy sencillo y bien conocido, por lo cual en este caso, en lugar de hacer uso del modelo estadísitico nuclear para obtener los factores de corrección, se simuló la cascada nuclear completa. Los resultados obtenidos se compararon con resonancias medidas en n_TOF (figura 7.2), obteniendo un buen acuerdo.

La distribución angular de la radiación primaria emitida tras la captura debe ser considerada en este caso, ya que la multiplicidad de la cascada nuclear es muy baja. Cuando tiene lugar la captura neutrónica en onda $l > 0$, el núcleo compuesto queda alineado en el plano perpendicular a la dirección del neutrón incidente. Este alineamiento provoca anisotropía en la radiación primaria emitida tras la captura. En el caso de resonancias 1^+, la distribución angular puede ser calculada [91] de manera exacta como se muestra en la figura 7.3. Para resonancias de espin paridad 2^+, el núcleo se desexcita decayendo mediante una transición E1 pura al primer estado excitado a 2.76 MeV de $J^\Pi = 3^-$. La distribución angular de esta transición se muestra en el lado izquierdo de la figura 7.5. Esta primera transición afecta a la distribución angular de la segunda transición que tiene lugar hasta el estado fundamental (0^+). En este segundo caso, la distribución angular se muestra en la parte derecha de la figura 7.5. Para resonancias 1^+, el factor de corrección a aplicar a la tasa de rendimiento es de un 7%, mientras que en el segundo caso, para resonancias 2^+ es completamente despreciable.

Utilizando el código SAMMY, se analizaron un total de 16 resonancias. En los casos en los que existen medidas de transmision precisas, el parámetro Γ_n se fijó a ese valor, y se hizo un ajuste de Γ_γ. Los resultados obtenidos así como la sección eficaz integrada para cada resonancia se muestran en la tabla 7.5. En la tabla 7.6 los resultados obtenidos con los datos medidos en n_TOF se comparan con previos experimentos [90, 94, 95, 96], con los ficheros de datos evaluados (JENDL y ENDF) y con las compilaciones de Mughabghab [79] y Sukhoruchkin et al. [80]. En este isótopo, las discrepancias obtenidas respecto a previos experimentos son menores. Esto era de esperar, puesto que en este caso, el canal de dispersión neutrónica de las resonancias no es tan dominante como en el bismuto. Por otro lado, la sección eficaz es mayor y esto siempre favorece el cociente señal/ruido. No obstante, a altas energías ($E_n > 100$ keV) si que se aprecian diferencias importantes respecto a medidas anteriores. Estas diferencias son comparables a las obtenidas con las bases de datos evaluadas (figura 7.10), puesto que éstas están basadas en los experimentos anteriores.

Lo que resulta más destacable en esta medida es que en n_TOF se han podido medir y analizar tres resonancias que no se hayan en las bases de datos evaluados. Dos de estas resonancias se muestran en la figura 7.8. Esto, junto con las discrepan-

cias mostradas en la figura 7.10, cláramente sugiere una actualización de las bases de datos del ^{207}Pb, basada en estos resultados más recientes.

Conclusión

El primer resultado remarcable que se ha alcanzado en el presente trabajo ha sido la validación experimental del método de medida de los detectores de energía total. En particular, hemos comprobado la validez de la técnica de simulación Monte Carlo, para obtener distribuciones de respuesta de los detectores precisas, las cuales han permitido la obtención de funciones peso correctas.

Paralelamente, se ha conseguido desarrollar un método de análisis que permite tener en cuenta de manera precisa diversos efectos experimentales asociados con el umbral electrónico de los detectores, los electrones de conversión interna y la suma de dos o más rayos gamma en coincidencia.

Midiendo la resonancia de 1.15 keV en ^{56}Fe en varias muestras de hierro, se consiguió una incertidumbre final mejor del 2%, lo cual demuestra tanto la capacidad de la simulación Monte Carlo para obtener las funciones peso, como la precisión del método de corrección de incertidumbres sistemáticas utilizado.

En la medida de la sección eficaz de captura en ^{209}Bi se han obtenido discrepancias importantes respecto a medidas anteriores existentes en la literatura. Los resultados obtenidos en n_TOF son más precisos desde el punto de vista de las incertidumbres sistemáticas gracias al dispositivo experimental optimizado en términos de baja sensibilidad neutrónica. Principalmente para resonancias en onda s, que tienen un canal de dispersión neutrónica dominante, se ha reducido considerablemente la sección eficaz con respecto al primer experimento realizado en ORNL. Puesto que las bases de datos actuales todavía están basadas en dicho experimento, se han obtenido también discrepancias importantes con respecto a dichas evaluaciones. Además, a raíz del estudio comparativo que hemos llevado a cabo en este trabajo, hemos concluido que sería conveniente incluir resonancias a energías negativas en las evaluaciones del ^{209}Bi para reproducir el valor de la sección eficaz térmica.

Por otra parte se ha estudiado el impacto de las medidas realizadas en el ámbito de la nucleosíntesis estelar. La MACS obtenida con los datos medidos en n_TOF, está por encima del valor de la compilación Bao et al. tomado actualmente como referencia. Utilizando un modelo de estrella pulsante AGB, de baja metalicidad y baja masa, se ha estimado que, debido a la MACS medida en n_TOF la abundancia de bismuto sería un 6% menor con respecto al valor de referencia. Se ha comprobado que el resultado obtenido es compatible con las abundancias observadas en el Sol, así como con cálculos detallados y precisos de la abundancia r.

La medida de la sección eficaz del ^{207}Pb ha confirmado a baja energía ($E_n <$ 100 keV) los datos medidos anteriormente en ORNL, mientras que a energías superiores se han encontrado discrepancias considerables. Estos resultados reflejan la necesidad de actualizar las bases de datos existentes con esta información.

Appendix A

TOF calibration

In order to accurately determine the parameters $L_\circ$ and $t_\circ$, a set of eight resonances adopted as energy standards [44, 45] was measured at n_TOF. By comparing with the tabulated resonances energies, the best values for $L_\circ$ and $t_\circ$ were derived [43]. The ^{238}U resonances were used to determine the value of the constant

Reaction	$E_\circ$ (eV)	Deviation (%)
^{238}U(n,γ)	6.673(1)	-0.03
^{238}U(n,γ)	20.864(3)	0.005
^{238}U(n,γ)	36.671(6)	0.02
^{238}U(n,γ)	66.015(10)	0.008
^{32}S(n,γ)	30388(23)	0.0
^{32}S(n,γ)	97550(7)	0.055
^{32}S(n,γ)	513330(100)	-0.035
^{32}S(n,γ)	819340(180)	0.0061

Table A.1: *Energy standards measured at n_TOF to perform the time of flight calibration.*

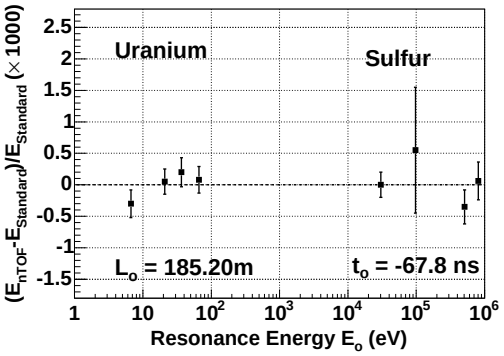

Figure A.1: *Deviation between measured and tabulated energies of the standard resonances.*

independent term $L_\circ$= 185.20±0.01 m. The energy dependent term ΔL, or equivalently the time offset $t_\circ$, is more sensitive to the higher energy resonances of the ^{32}S+n reaction, where the energy resolution of the beam dominates. A value of $t_\circ$= -68±13 ns was obtained. table A.1.

Table A.1 summarizes the resonances measured at n_TOF. The second column shows the standard energies as they are tabulated and the third column shows the deviations between standard and n_TOF measured energies of the resonances[1]. The latter are shown also in figure A.1. The average RMS deviation yields a calibration accuracy better than 0.01%.

[1]N. Colonna (INFN, Italy), private communication.

Appendix B

n_TOF beam profile

A suitable analytic function, $B(x, y)$, to reproduce the n_TOF beam profile and its best parameters have been calculated by J. Pancin et al. [51].

A correlated gaussian function was convoluted with a step function in order to account for possible misalignment of the collimators, which would have an effect on the centering and the beam orientation.

$$B(x, y) \propto \frac{1}{2a}(\mathrm{Erf}(a + g(x, y)) - \mathrm{Erf}(g(x, y) - a)) \tag{B.1}$$

where

$$\mathrm{Erf}(u) = \frac{2}{\sqrt{\pi}} \int_0^u e^{-t^2} \mathrm{d}t \tag{B.2}$$

and

$$g(x, y) = \sqrt{\frac{1}{2(1-\rho^2)} \left(\frac{(x-\mu_x)^2}{\sigma_x^2} + \frac{(y-\mu_y)^2}{\sigma_y^2} - 2\rho \frac{(x-\mu_x)(y-\mu_y)}{\sigma_x \sigma_y} \right)} \tag{B.3}$$

$B(x, y) = 0$ for $r = \sqrt{(x-\mu_x)^2 + (y-\mu_y)^2} > R_{max}$

The beam profile measurement was carried out at 186 m from the neutron spallation source. The obtained result, compared with that from a simulation [53], showed a good agreement, thus validating the latter. New profile function parameters corresponding to other flight lengths, could be then determined from simulations at those distances.

A summary of the beam width and mean value in both Cartesian axis is given in the following table for a flight distance of 185.2 m in several energy ranges:

Energy	σ_x(mm)	σ_y(mm)	μ_x(mm)	μ_y(mm)
10-100 eV	4.97(4)	4.83(4)	0.63(1)	0.05(1)
0.1-1 keV	4.95(4)	4.92(4)	0.54(1)	0.04(1)
1-10 keV	5.09(4)	5.05(4)	0.86(1)	0.13(1)
10-100 keV	4.99(3)	4.93(3)	0.80(1)	0.17(1)
0.1-1 MeV	4.87(1)	4.83(1)	0.79(1)	0.07(1)

Table B.1: *Parameters of the beam profile function for a flight length of 185.2 m in several energy intervals.*

Appendix C

Resolution function

The RPI-function consists basically of the sum of three components: a chi-squared function with six degrees of freedom and two exponential terms. This particular function, was derived initially for the LINAC at RPI [60] and depends on 25 parameters. By fitting some of these parameters to the simulated distributions, we could adapt this function to successfully describe the n_TOF neutron beam resolution. A unique parameterization in the whole energy range (1 eV-1 MeV) was not possible and three different energy intervals had to be used, 1 eV-200 eV, 200 eV-50 keV and 50 keV-1 MeV. Also an energy dependent parameterization was required for the parameter `A5` in the latter two intervals.

$$\texttt{A5} = \begin{cases} -6.603 \times 10^{-5} log\,(E_n)^2 + 0.0027737 log(E_n) - 0.010461 \\ \qquad\qquad\qquad\qquad\qquad\qquad \text{for 200 eV} < E_n < \text{50 keV} \\ 2.088 \times 10^{-14} E_n^2 + 9.4398 \times 10^{-9} E_n + 0.01152 \\ \qquad\qquad\qquad\qquad\qquad\qquad \text{for 50keV} < E_n \end{cases}$$

A new parameterization will be available in the next version of SAMMY, in order to include the `A5` parameter as an energy dependent function.

A summary of the best parameters for this function over the three neutron energy intervals follows.

```
1 eV < En < 200 eV
------------------

RPI RESOLUTION FUNCTION parameters follow
BURST0          6.100      0.600
TAU  00000    -1095.3       0.55     -232.0  0.026918     -56.42
TAU            000.00    0.00000     0.0000   0.00000      0.000
LAMBD000        537.0    -180.72     17.163
LAMBD          0.0000     0.0000     0.0000
A1    00000    0.0000     0.0000     0.0000   0000000      0.100
```

```
A1               0.0       0.0       0.0       0.0     0.000
EXPON00000    -40.00      -1.0     0.010        1.     0.820
EXPON           0.00       0.2     0.400      0.01     0.001
CHANN 000       0.00     0.000     0.000

-------------------------------------------------------------

200 eV < En < 50 keV
--------------------

RPI RESOLUTION FUNCTION parameters follow
BURST0          6.100     0.600
TAU  00000    -47.938  0.001599   -14.496 0.0000915   -8.6329
TAU            000.00   0.00000    0.0000   0.00000     0.800
LAMBD000       198.62   -36.517    1.7538
LAMBD          0.0000    0.0000    0.0000
A1   00000    -0.0127  0.000628    0.0000     0.000    0.0112
A1               0.0       0.0       0.0       0.0     0.015
EXPON00000    -40.00      -1.0     0.080        1.   A5INPUT
EXPON           0.00       0.0     0.000      0.00     0.000
CHANN 000       0.00     0.000     0.000

-------------------------------------------------------------

50keV < E < 1MeV
----------------

RPI RESOLUTION FUNCTION parameters follow
BURST0          6.100     0.600
TAU  00000    -2.529 0.0000045    -13.22   0.00003    -5.002
TAU            000.00   0.00000    0.0000   0.00000     0.000
LAMBD000       66.728   -7.8290    0.2274
LAMBD          0.0000    0.0000    0.0000
A1   00000    -0.0757 0.0000056    0.0013-0.0000047    0.0822
A1               0.0       0.0       0.0       0.0     0.000
EXPON00000    -10.00      -1.0     0.170        1.   A5INPUT
EXPON           0.00       0.0     0.000      0.00     0.000
CHANN 000       0.00     0.000     0.000
```

Appendix D

Commercial C_6D_6 detector

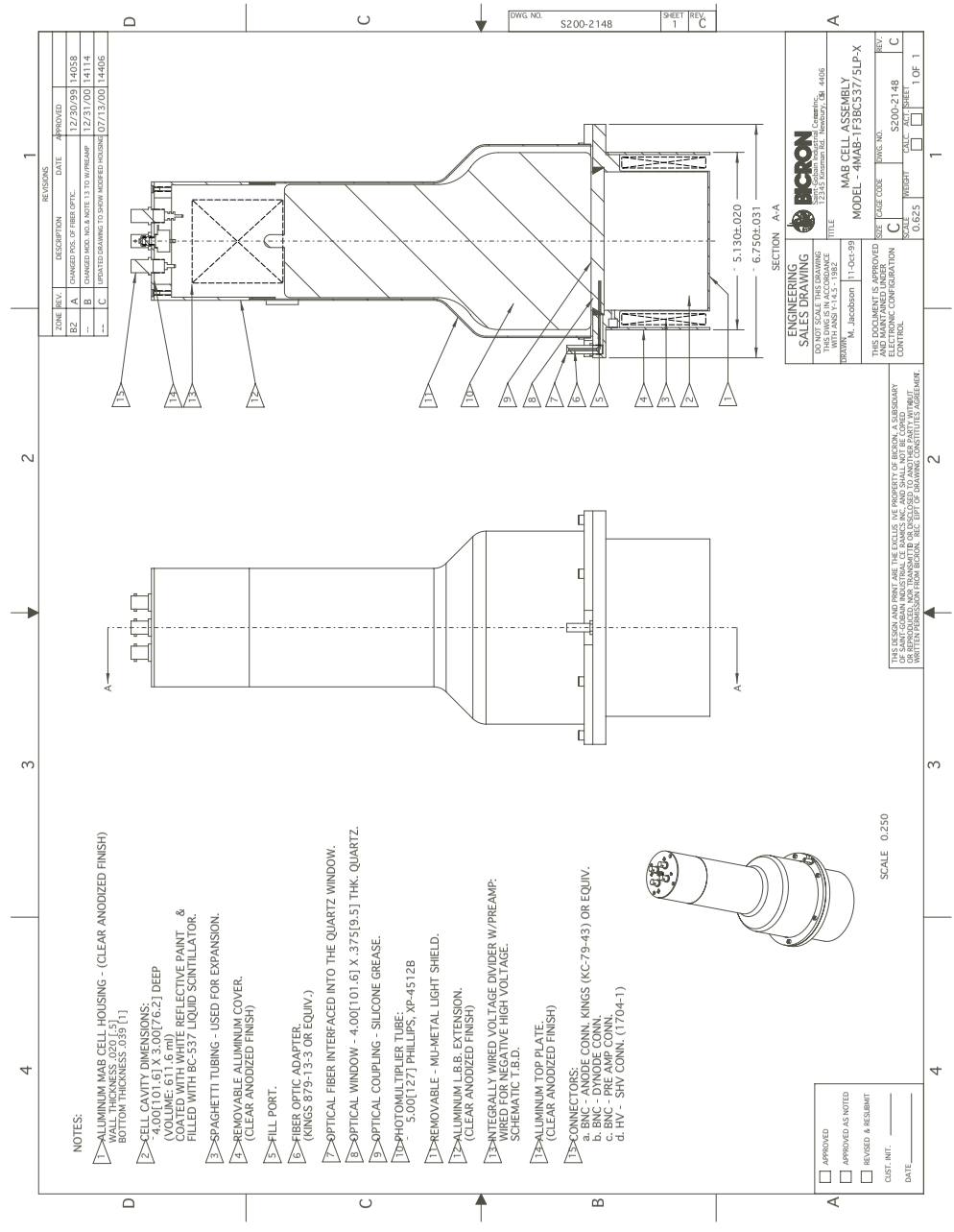

Figure D.1: *Bicron detector scheme.*

Appendix E

Background at n_TOF

The sources of background in the measuring station have been thoroughly identified and investigated at n_TOF [99]. To illustrate the different background contributions we show in figure E.1 the raw and the weighted neutron energy spectra of a bismuth measurement.

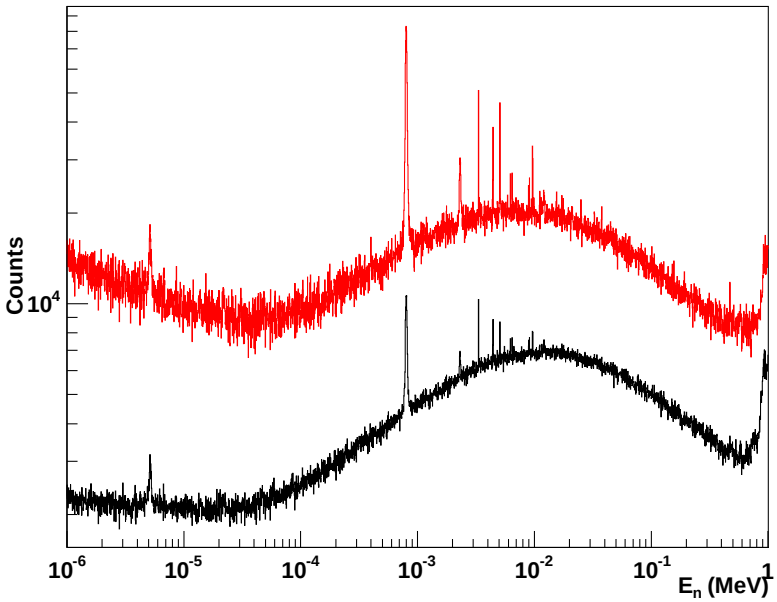

Figure E.1: *Raw and weighted neutron energy spectra of* ^{209}Bi.

At the low energy part of the spectrum 1-100 eV, the background is mostly due to environmental radiation caused by stray neutrons which are thermalized and captured in the walls of the experimental area or material therein. The tiny resonance which can be observed at ∼5 eV is due to a small silver impurity in the bismuth sample. Between 100 eV and 500 keV, the background is dominated by in-beam delayed gamma rays, which are scattered in the sample and registered in

the C_6D_6 detectors. This contribution is highly reduced after weighting the raw histogram, as can be appreciated in the much better signal to noise ratio of the upper spectrum in figure E.1. However, this background hindered the observation of the weaker resonances in this energy range.

At higher energies, $E_n > 0.8$ MeV, the count rate increases steeply due to inelastic neutron collisions in the Bi-sample, whose γ-rays are registered by the C_6D_6 detectors.

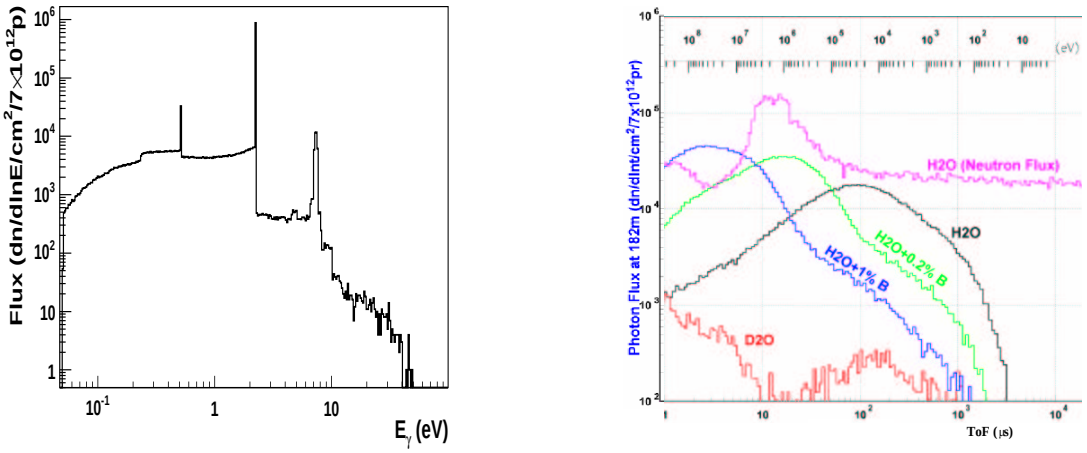

Figure E.2: *(Left) Energy distribution of the in beam gamma rays with a light water moderator. (Right) Time of flight (neutron energy) distribution of the in beam gamma rays for different moderators.*

In the energy region of interest for the present work, between 1 eV and 1 MeV, the background at the measuring station is a smooth function of the time of flight or neutron energy. For this reason, in the analysis of the resolved resonances the background has been simply adjusted to a polynomial of degree 0 or 1, by analyzing a wide enough region around the resonance.

A way of reducing the dominating in-beam gamma ray component has been investigated with the aim of improving future measurements. The in-beam gamma rays are produced mainly by capture of thermalized neutrons in the hydrogen of the water moderator surrounding the spallation target (2.2 MeV). In much lower amount there are also contributions due to capture in the spallation target assembly materials, Pb, Al, etc (7-7.5 MeV) and to pair production (511 keV). The complete gamma ray spectrum is shown in the left part of figure E.2. This causes a delayed distribution of hard gamma rays (mostly of 2.2 MeV) flying outside with the neutrons and reaching the sample 185 m upstream at a neutron energy of about 10 keV. These gamma rays are preferably scattered in the forward direction and therefore, its contribution is minimized by setting the detectors backwards with respect to the sample. It was found by means of Monte Carlo simulations, that the best compromise between efficiency and background is achieved by setting the detectors at ∼7.8 cm backwards with respect to the sample, and they were arranged in that

way for the measurement of bismuth and lead. The scattering of in-beam gamma rays is also increased in the case of thick and high Z samples like bismuth or lead.

Considering the origin of this problem, a solution has been proposed based on the use of heavy water or borated water instead of the light water currently being used as moderator. The in-beam gamma rays time of flight distribution for the different cases is shown in figure E.2. Whereas the borated water represents a considerable improvement at energies above 1 keV, the best situation is achieved by far with the employment of heavy water.

Acknowledgements

I am very grateful to my mentor José Luis Taín, who gave me the opportunity to work with him at the *Grupo de Espectroscopía Gamma* and constantly supervised my PhD work. Looking backward to the beginning of my PhD I realize that I have learnt a lot during these years thanks to the frequent discussions, sharp corrections and fruitful suggestions of José Luis.

I want to acknowledge sincerely all the Committee members, who kindly accepted to judge this PhD work. My thanks to A. Ferrer (Universidad de Valencia), E. González (CIEMAT), F. Käppeler (FZK, Germany), F. Gunsing (CEA, France) and H. Leeb (TUW, Austria).

I acknowledge financial support from *Consejo Superior de Investigaciones Científicas*.

Before starting my PhD work in Valencia, I spent more than two years at the "Institut für Kernphysik" in Mainz (Germany), where I left many good colleagues and friends like Oliver, Erik, Michael Lang, Michael Seimetz, Victor, Mimoun, Giovanni, Ilya, Matthias, Dirk and Rudolf. I thank them for their friendship and for teaching me the first words in experimental nuclear physics.

In Valencia, I had the good luck to met another very enjoyable, interesting and motivated group (*Grupo de Espectroscopía Gamma*) leaded by Berta Rubio and José Luis Taín. They have constantly communicated enthusiasm and professionalism in our daily work and scientific business. I am also very grateful to the other colleagues of this group, Kike Nácher, Luis Caballero, Alejandro Algora, Ana Pérez, Jorge Agramunt and Juan Carlos Pacheco for their help at any time and the nice atmosphere.

Many other friends and colleagues at IFIC have been also part of the enjoyable working environment of this institute. Here I would like to acknowledge my nice mates Juan de Dios, Noriel, Nerina, Christoph, Gustavo, Marcos and Azedine.

In the first trip to my second working place, at CERN, I met first Carlos Paradela and Daniel Cano. They became during the long stays in Switzerland my main colleagues and friends outside home. With Carlos I had the opportunity to share many night shifts, but also nice coffees, pizzas, galician dinners and some walks in Geneva and to the Jura mountains. To Daniel I am indebted for many things. His working endless energy, professionalism and above all, nice and sharp humour, made of my stays at CERN a very enjoyable and fruitful experience. It was also a pleasure for me to work at n_TOF with many other people like Ralf Plag, Michael Heil and

Stefano Marrone. I also would like to thank Shawn O'Brien and Saed Dababneh for their friendship, enthusiasm and nice talks in that sweet and charming studio at St. Genis Pouilly.

The stays at n_TOF, despite the many shifts to cover by few people, were very enjoyable thanks to the contribution of many colleagues like Carlos Guerrero, Laure, Christophe, Julian, Adonai, Christos, Andreas, Gaelle, Pino, Marita, Luc, Eric, Guillem, Paolo, Pierfrancesco, Dimitri, Vasilis, Strahinja, Hector, Marco, etc. I do not want to forget our nice colleague Nicola Bustreo who joined us at the beginning, as well as the Portuguese colleagues Francisco and Americo.

Our work was constantly guided by experienced people. In this sense I would like to acknowledge, in addition to J.L. Taín mentioned above, E. González, N. Pavlopoulos, A. Mengoni, F. Käppeler, F. Gunsing, N. Colonna, P. Calviño, P. Vaz and N. Durán for their enormous effort to make the n_TOF experiment take off.

I am particularly grateful to F. Käppeler, F. Gunsing, E. González, A. Mengoni and N. Colonna for their very helpful comments, discussions and suggestions during these years of PhD work and also about this manuscript.

My several travels to attend meetings and conferences have been an excellent experience, which allowed me to learn about Paris, Lisbon, Prague, Vienna, Les Houches, Flachau, Darmstadt, Santa Fe and of course, Geneva. In these attractive scenarios, I also got the nice opportunity to interact and learn from many other scientists, whose comments and discussions have been very fruitful for this work. In this sense, I would like to thank R. Gallino, G. Arbanas, M. Krtička, P. Schillebeeckx and P. Mutti.

Finally I will go into a more personal scope, which I think it is essential in order to enjoy ones job and professional achievements. My family fortunately is too big to list all of them here, but at least I want to thank all of them for their constant support. Special mention deserve my parents Ernesto and Marisa, who have always taken care of my education and happiness. My brother Marcos (an excellent fishing mate and chess player) and my sisters (and fans) Eva and Laura made me always feel extremely fortunate. I also would like to thank the Escat Paricio family for their understanding and encouragement. Rafael Ramirez deserves also an special mention in this family section, thus he is like a brother for me and I am indebted to him for so many things.

I want to acknowledge my appreciated friends from Carcaixent, Adrian Palomares, Daniel Santacreu, Jorge Iñigo as well as others from outside Spain, Yin Weijun, Agnieszka Grohodska and Mâdâlina Sandu for their friendship.

One person has followed me closer than anyone else during all these years. I want to thank her help, patience and love (tested experimentally when I pretended to dedicate this work *"To my bicycle."*). Berta, to you my thanks, my love.

Bibliography

[1] F. Käppeler et al., *s-process nucleosynthesis - nuclear physics and the classical model*, Rep. Prog. Phys. **52** (1989), pag. 945.

[2] C.D. Bowman, *Accelerator-Driven Systems for Nuclear Waste Transmutation*, Annu. Rev. Nucl. Part. Sci. **48** (1998), pag. 505.

[3] L.C. Hebel et al., *Report to the American Physical Society by the study group on nuclear fuel cycles and waste management*, Rev. Mod. Phys. **50** (1978) No. 1.

[4] C. Rubbia et al., *Conceptual Design of a Fast Neutron Operated High Power Energy Amplifier*, CERN/AT/95-44 (EET), CERN, Geneva, 1995.

[5] R.Plag et al., *An optimized C_6D_6 detector for studies of resonance-dominated (n,γ) cross-sections*, Nucl. Instr. and Meth. in Phys. Res. A **496** (2003), pag. 425.

[6] The n_TOF Collaboration, *Proposal for a Neutron Time Of Flight Facility*, CERN/SPSC 99-8, SPSC/P 310, CERN, Geneva, 1999.

[7] U. Abbondanno et al. (The n_TOF Collaboration), *New Experimental validation of the Pulse Height Weighting Technique for Capture cross-section measurements*, Nucl. Instr. and Meth. in Phys. Res. A **521** (2004), pag. 454.

[8] E.M. Burbidge et al., *Synthesis of elements in stars*, Rev. Mod. Phys. **29** (1957), pag. 547.

[9] H. Beer et al., ^{198,199,200,201,202,204}*Hg(n,γ) cross sections and the termination of s-process nucleosynthesis*, Phys. Rev. C **32** (1985), pag. 738.

[10] C. Travaglio et al., *Galactic chemical evolution of heavy elements: from barium to europium*, The Astrophys. Journal **521** (1999), pag. 691.

[11] C. Travaglio et al., *Lead: asymptotic giant branch production and galactic chemical evolution*, The Astrophys. Journal **549** (2001), pag. 346.

[12] U.Ratzel et al., *Nucleosynthesis at the termination point of the s process*, The Astrophys. Journal (in press).

[13] J.J. Cowan et al., *r-process abundances and chronometers in metal-poor stars*, The Astrophys. Jour. **521** (1999), pag. 194.

[14] J.P. Revol, *Nuclear Waste Removal Using Particle Beams Incineration with Fast Neutrons*, DPG (1997) CERN-PPE/97-142.

[15] C.D. Bowman et al., *Nuclear energy generation and waste transmutation using an accelerator-driven intense thermal neutron source*, Nucl. Instr. and Meth. in Phys. Res. A **320** (1992), pag. 336.

[16] A. Abánades et al., *Experimental verification of neutron phenomenology in lead and transmutation by adiabatic resonance crossing in accelerator driven systems. A summary of the TARC Project at CERN*, Nucl. Instr. and Meth. in Phys. Res. A **463** (2001), pag. 586.

[17] C. Rubbia et al., *Sensitivity Analysis of Neutron Cross Sections Relevant for Accelerator Driven Systems*, in the 1$^{\text{st}}$ Management Report of the n_TOFND-ADS EC programme under contract no. FIKW-CT-2000-00107.

[18] A. Herrera-Martinez et al., *Importance of Neutron Cross-Sections for Transmutation*, Conference Proceedings "International Workshop on Nuclear Data for the Transmutation of Nuclear Waste", Editors: A. Kelic et al., GSI-Darmstadt, Germany, 2003, ISBN 3-00-012276-1.

[19] A. Foderaro, *The Elements of Neutron Interaction Theory*, The MIT Press, 1971.

[20] *Neutron Radiative Capture*, Vol. 3, Editors A. Michaudon, S. Cierjacks and R.E. Chrien, 1984.

[21] A.M. Lane et al., *R-Matrix Theory of Nuclear Reactions*, Reviews of Modern Physics **30** (1958) No.2, Part I.

[22] M.C. Moxon et al., *A gamma-ray detector for neutron capture cross-section measurements*, Nucl. Instr. and Meth. in Phys. Res. A **24** (1963), pag. 445.

[23] R.L. Macklin et al., *Capture-Cross-Section Studies for 30-220-keV Neutrons Using a New Technique*, Phys. Rev. **159** (1967), pag. 1007.

[24] R.Macklin et al., *Resonance neutron capture by* ^{209}Bi, Phys. Rev. C **14** (1976), pag. 1389.

[25] P.Mutti et al., *Stellar capture rates for s-process strong component elements*, Conference Proceedings Vol. 59, "Nuclear Data for Science and Technology", Editors G. Reffo et al., SIF, Bologna, 1997.

[26] F. Corvi et al., *An experimental method for determining the total efficiency and the response function of a gamma-ray detector in the range 0.5-10 MeV*, Nucl. Instr. and Meth. in Phys. Res. A **265** (1988) pag. 475.

[27] C. Domingo-Pardo et al., Nucl. Instr. and Meth. in Phys. Res. A (in preparation).

[28] F. Rau, *Entfaltung des mit einem Szintillationsspektrometer beobachteten Impulshöhenspektrums zum Energiespektrum der γ-Strahlung*, Nucleonik **5** (1963), pag. 191.

[29] *Numerical Recipes in C: The art of scientific computing*, Cambridge University Press, 1988-1992.

[30] C. Rubbia et al., *A high Resolution Spallation driven Facility at the CERN-PS to measure Neutron Cross Sections in the Interval from 1 eV to 250 MeV*, CERN/LHC/98-02 (EET), CERN, Geneva, 1998.

[31] C. Rubbia et al., *A high Resolution Spallation driven Facility at the CERN-PS to measure Neutron Cross Sections in the Interval from 1 eV to 250 MeV*, CERN/LHC/98-02 (EET)-Add.1, CERN, Geneva, 1998.

[32] C.Borcea et al., *Results from the commissioning of the n_TOF spallation neutron source at CERN*, Nuc. Instr. and Meth. in Phys. Res. A **513** (2003), pag. 524.

[33] D.J. Simon, Conference Proceedings, "5th European Particle Accelerator Conference", Sitges, Barcelona, Spain, 10-14 June 1996, IOP, Bristol (1996) pag. 295.

[34] A.Ferrari et al., *A comprehensive study of the nTOF Background*, CERN/SL-EET/2001-036, CERN, Geneva, 2001.

[35] The n_TOF Collaboration, *Study of the Background in the Measuring Station at the n_TOF Facility at CERN: Sources and Solutions*, CERN/SL/2001-046, CERN/INTC/2001-038, CERN, Geneva, 2001.

[36] D.Cano-Ott et al., *Proposal for a two-step cylindrical collimation system for the n_TOF facility*, CIEMAT Ref: DFN/TR-04/II-00, 2000.

[37] C. Domingo Pardo, *Diploma thesis*, CSIC-University of Valencia, 2001.

[38] U. Abbondanno et al., *The data acquisition system of the neutron time of flight facility n_TOF at CERN*, Nucl. Instr. and Meth. in Phys. Res. A **538** (2005), pag. 692.

[39] The n_TOF Collaboration, *Technical Report*, CERN/INTC 2000-018, CERN, Geneva, 2000.

[40] D.Cano-Ott, Nucl. Instr. and Meth. in Phys. Res. A (in preparation).

[41] R. Brun et al., *ROOT - An Object Oriented Data Analysis Framework*, Conference Proceedings "AIHENP'96 Workshop", Lausanne, 1996. Nucl. Inst. & Meth. in Phys. Res. A **389** (1997), pag. 81.

[42] M. Goto, C++ Interpreter - CINT, CQ publishing, ISBN4-789-3085-3 (Japanese)

[43] G. Lorusso et al., *Time-energy relation of the n_TOF neutron beam: energy standards revisited*, Nucl. Instr. and Meth. in Phys. Res. A **532** (2004), pag. 622.

[44] C. Coceva et al., *Neutron energy standards for white neutron sources*, IAEA-TECDOC-410, Leningrad, USSR, 1986, pag. 56.

[45] C. Coceva et al., *Neutron energy standards*, In: H.Condè (Ed.), Nuclear data standards for nuclear measurements, NEA-OECD Report, NEANDC-311"U",INDC (SEC)-101, 1992, pag. 83.

[46] CERN SL-ECT Group, PTB group, *n_TOF neutron fluence with the PTB Fission Chambers*, CERN/SL/ECT/2002, CERN, Geneva, 2002.

[47] G. Aerts et al., *The capture yield of the ^{232}Th(n,γ) reaction measured at n_TOF-CERN*, preliminary report, 9 April, 2004.

[48] R.L. Macklin et al., *Absolute Neutron Capture Yield Calibration*, Nucl. Instr. and Meth. in Phys. Res. A **164** (1979), pag. 213.

[49] N.M. Larson, "SAMMY: Multilevel R-matrix fits to neutron data using Bayes equations", ORNL/TM-9179, Oak Ridge NL, 2000.

[50] Y. Giomataris et al., *MICROMEGAS: a high-granularity position-sensitive gaseous detector for high particle-flux environments*, Nucl. Instr. and Meth. in Phys. Res. A **376** (1996), pag. 29.

[51] J. Pancin et al., *Measurement of the n_TOF beam profile with a micromegas detector*, Nucl. Instr. and Meth. in Phys. Res. A **524** (2004), pag. 102.

[52] J. Pancin, private communication.

[53] V. Vlachoudis et al., *Particle distribution entering the vacuum tube from a 80×80×60 cm^3 lead target*, CERN/SL-NOTE-2000-029 EET, CERN, Geneva, 2000.

[54] W.R. Leo, *Techniques for Nuclear and Particle Physics Experiments*, Springer Verlag, 1987.

[55] Cross Section Evaluation Working Group, ENDF/B-VI Summary Documentation, BNL-NCS-17541 (ENDF-201), 1991

[56] C. Coceva et al., *On the figure of merit in neutron time-of-flight experiments*, Nucl. Instr. and Meth. in Phys. Res. A **489** (2002), pag. 346.

[57] A. Bignami et al., Euratom Report EUR 5157, 1974.

[58] C. Coceva et al.,*CAMOT: A Monte Carlo Neutron Transport Code*, unpublished.

[59] A. Fassó et al., Proceedings "1st Workshop on Simulating Accelerator Radiation Environments (SARE 1)", Santa Fe, New Mexico, 1993, Los Alamos Report LA-12835-C, 1994, pag. 134.

[60] B.E. Moretti, *Molybdenum Neutron Transmission Measurements and the Development of an Enhanced Resolution Neutron Target*, Ph.D. Thesis in Nucl. Engineering & Science, Rensselaer Polytechnic Institute, Troy NY, 1996.

[61] F.G. Perey et al., *Responses of C_6D_6 and C_6F_6 gamma-ray detectors and the capture in the 1.15 keV resonance of ^{56}Fe*, Conference Proceedings "Nuclear Data for Science and Technology", Mito, 1988, pag. 379.

[62] G. Rohr, *Proc. NEANDC/NEACRP Specialists' Meeting on Fast-Neutron Capture Cross Sections*, Argonne, Illinois, ANL-83-4, Argonne National Laboratory, 1982, pag.394.

[63] J.L. Tain et al., *Accuracy of the pulse height weighting technique for capture cross section measurements*, Jour. of Nucl. Sci. and Tech., Supplement 2 (2002), pag. 689.

[64] *GEANT: Detector description and simulation tool*, CERN Program Library W5013, 1994.

[65] Agostinelli et al., GEANT4-*a simulation toolkit*, Nucl. Instr. and Meth. in Phys. Res. A **506** (2003), pag. 250.

[66] J.F. Briesmeister (Ed.), *MCNP-a general Monte Carlo N-particle transport code*, Version 4B, LA-12625-M, 1997.

[67] F. Salvat et al., *PENELOPE-a code system for Monte Carlo simulation of electron and photon transport*, NEA/NSC/DOC-2001-19, 2001.

[68] M.R. Bhat, *Evaluated nuclear structure data file (ENSDF)*, in: S.M. Qaim (Ed.), Nuclear Data for Science and Technology, Springer, Berlin, 1992, pag. 817.
`http://www.nndc.bnl.gov/ensdf/`

[69] J. Kopecky et al., *Test of gamma-ray strength functions in nuclear reactor model calculations*, Phys. Rev. C **41** No. 5 (1990), pag. 1941.

[70] J. Kopecky et al., *Observation of the M1 Giant Resonance by resonance averaging in* ^{106}Pd, Nucl. Phys. A **468** (1987), pag. 285.

[71] Dilg et al., *Level Density Parameters for the back-shifted Fermi gas model in the mass range* $40 < A < 250$, Nucl. Phys. A **217** (1973), pag. 269

[72] T. von Egidy et al., *Nuclear Level Densities and level spacing distributions: PartII*, Nucl. Phys. A **481** (1988), pag. 189.

[73] A. Gilbert et al., *A composite nuclear-level density formula with shell corrections*, Can. Jour. of Phys. **43** (1965), pag. 1446.

[74] Z. Huang et al., *New sets of back-shifted level density parameters*, *Chinese Jour. Nucl. Phys.* 13 (1991), pag. 147.

[75] IAEA-TECDOC, *Reference Input Parameter Library*, Handbook for calculations of nuclear reaction data, 1998.

[76] F.H. Fröhner, *Evaluation and analysis of nuclear resonance data*, JEFF Report18, 2000.

[77] P. de Marcillac et al., "Experimental detection of α-particles from the radioactive decay of natural bismuth", Nature **422** (2003), pag. 876.

[78] A. Letorneau et al., Conference Proceedings "11^{th} International Symposium on Capture Gamma-Ray Spectroscopy and Related Topics", pag. 734, World Scientific, Prage, 2003.

[79] S.F. Mughabghab, *Neutron Cross Sections: Neutron Resonance Parameters and Thermal Cross Sections*, Academic press, 1984.

[80] S.I. Sukhoruchkin et al., *Low Energy Neutron Physics, Subvolume B Tables of Neutron Resonance Parameters*, Landolt-Börnstein series, Vol. 16, Springer, 1998.

[81] P. Mutti, *s-Process implications of ^{136}Ba, ^{208}Pb and ^{209}Bi stellar capture rates*, Ph.D. Thesis, Gent University, 1997.

[82] F. Corvi et al., *Nucl. Sci. Eng.***107** (1991), pag. 272.

[83] R.L. Macklin et al., *Corrigendum-Stable Isotope Capture Cross Sections from the Oak Ridge Electron Linear Accelerator*, Nucl. Sci. Eng. **78** (1981), pag. 110.

[84] A.R. Del Musgrove et al., Aust. Jour. **31** 1978, pag. 47.

[85] U.N. Singh et al., *Neutron resonance spectroscopy: ^{209}Bi*, Phys. Rev. C **13** (1976), pag. 124.

[86] F.W.K. Firk et al., *Resonances in the neutron cross section of bismuth*, Nuc. Phys. **44** (1963), pag. 431.

[87] P. Mutti et al., *s-process implications of ^{207}Pb and ^{209}Bi neutron capture cross sections*, Conference Proceedings "Nuclei in the Cosmos", Volos (1998), pag. 204.

[88] Z. Bao et al., *Neutron cross sections for nucleosynthesis studies*, Atomic Data and Nuclear Data Tables **76** (2000), pag. 70.

[89] J.A. Biggerstaff et al., *Radiative Transitions in 207Pb and 208Pb Following Resonance Neutron Capture in ^{206}Pb and ^{207}Pb*, Phys. Rev. **154** (1967), pag. 1136.

[90] S. Raman et al., *Fine Structure of the Magnetic Dipole Giant Resonance in ^{208}Pb*, Phys. Rev. Let. **39** (1977), pag. 598.

[91] A.J. Ferguson, *Angular correlation methods in gamma-ray spectroscopy*, North-Holland Publishing Company-Amsterdam, 1965.

[92] R.W. Carr et al., *Table of Angular-Distribution Coefficients for (Gamma, Particle) and (Particle, Gamma) Reactions*, Nuclear Data Tables **10** (1971), No. 2.

[93] C.D. Bowman et al., *M1 Giant Resonance in ^{208}Pb From Threshold Photoneutron Measurements*, Phys. Rev. Let. **25** (1970), pag. 1302.

[94] S. Raman et al., *Observation of Primary E2 Transitions in the Reaction $^{207}Pb(n,\gamma)$*, Phys. Rev. Let. **40** (1978), pag. 1306.

[95] B.J. Allen et al., *Neutron-Capture Cross Sections of the Stable Lead Isotopes*, Phys. Rev. C **8** (1973), pag. 1504.

[96] B.J. Allen et al., *Radiative Widths of Neutron Scattering Resonances* Jour. Phys. G **6** (1983), pag. 1173.

[97] D.J. Horen et al., *Doorway states in s-, p-, and d−-wave entrance channels in ^{207}Pb+n reaction*, Phys. Rev. C **18** (1978), pag. 722.

[98] D.J. Horen et al., ORNL Report No. ORNL-5137, 1976 (unpublished), pag.8.

[99] The n_TOF Collaboration, *CERN n_TOF Facility: Performance Report*, CERN/INTC-O-011 INTC-2002-037 CERN-SL-2002-053ECT.